U.PORTO

MITPortugal

FEUP **FACULDADE DE ENGENHARIA**
UNIVERSIDADE DO PORTO

UNIVERSITY OF PORTO

FACULTY OF ENGINEERING, MIT-PORTUGAL PROGRAM
"Engineering design and advanced manufacturing"

Understanding the challenges of high injection pressure resin transfer moulding

by

Masoud Bodaghi

Thesis submitted to the University of Porto for the
degree of Doctor of Philosophy in LTI-Leaders for Technical
Industries
Supervisor:

Nuno Curado Correia (INEGI)

Co-supervisor:

António Torres Marques (FEUP)
November 2017

Abstract

Since the introduction of Resin Transfer Moulding (RTM) in the production of commercial aircraft in the 1980s the scope and quantity of advanced continuous fibre polymer composites used has significantly grown. The same composite take-up trend is observed in automotive OEMs (Original Equipment Manufacturer) where large advanced manufacturing programmes on resin transfer moulding and similar technologies (Liquid Composite Moulding), are increasingly getting these materials out of exotic high end segments and into more "standard" product lines. While these technologies are allowing the industry to push capacity and module while improving part quality and production reliability.

However, the overall cost and the quality of composites, and production waste remain important issues. In a possible answer to these requirements, one was introduced manufacturing process, high injection pressure resin transfer moulding (HIPRTM), to reduce the impact of the aforementioned issues in an approach that is relevant to the two industries mentioned (aeronautical and automotive) drawing from the experience and positioning of both in quality, safety and cost drivers. In order to obtain high performance composite parts, this process utilises a press to compress the dry fibrous medium to desired fibre volume fraction (60%-65%) in a constrained way and the resin is injected at high pressure (thereby reducing energy consumption when compared with autoclave). This manufacturing process is complex as the resin has to be injected at high pressure while the preform undergoes deformation.

To achieve a reliable, reproducible and qualitatively robust HIPRTM process, several parameters have to be appropriately adjusted. In this context, both process development and process handling are not trivial. The quality of composite parts is dominated by preform deformation, where the tow reinforcement shows irregularities. Additionally, high pressure resin injection may pose the problem of voids as well as inadequate preform wetting. One must include not only the local variation of permeability due to the complex compaction stage and natural variability in preform but also the injection strategy as well as the compaction to prevent some possible processing defects such as voids and the analysis of void formation throughout the process. A fundamental knowledge is required towards the solution of these challenges associated with high injection pressure resin transfer moulding.

One challenge associated with the application of HIPRTM- as is the aim of the first part of this thesis- is an accurate prediction of the permeability of the fibrous media. Several models have been developed to predict permeability. The validity of these models is limited due to assumption of (i) regular and parallel arrangements of fibres, (ii) ideal tow path. The application of these models is further limited due to the significant scatter in the experimentally determined permeability of equivalent fabric under equivalent conditions.

Here, a multiscale approach is presented to propose not only an appropriate statistical model for the characterisation of permeability variations but also the spatial variation of permeability due to the internal geometry variation of the fibrous medium. It is believed

that the scatter in measured permeability are not only induced by experimental difficulties, but are also induced by internal geometry variations of the fibrous medium.

The multiscale permeability evaluation is demonstrated for a 2/2 twill woven carbon fabric. The permeability is shown to be influenced not only by the statistical distribution model but also by the internal geometry variation of the fabric. The variations of permeability are largely dominated by fabric heterogeneity while the contribution of the measurement tools with proper control will be insignificant. Furthermore, it was observed that local permeability in a real fabric varies continuously and reporting permeability by an average value are not completely represent the fabric.

The second challenge associated with the application of HIPRTM- as is the aim of the second part of this thesis- is the achievement of autoclave part quality (void content less than 1%) with high fibre volume fraction using high injection pressure resin. High injection pressure (20 bar) is required to obtain cost-effective composite components with the current resin transfer moulding. A major issue of increasing the injection pressure in this new variant of RTM is the formation of processing defects such as voids and dry spots that undermine the mechanical performance of produced composite parts. Mechanisms of void formation and analytical predictions of detrimental effects of dry spots on the structural integrity of produced composite parts have been well documented. In addition, several void removal strategies have been proposed. However, little helpful technical information is present regarding HIPRTM for the proper choice of injection strategies at high pressure.

Here, the study of HIPRTM variables introduces the ways to propose not only a proper injection strategy but also to produce a comparable autoclave-part quality. It is believed that the void formation in final composite parts are not only induced by the spatial variation of permeability over the medium, but are also induced by improper injection strategy.

Accordingly, a correlation between injection strategy and void formation is formed. The interaction between the two is important. In addition, the effect of compaction and adjusting the gap between the upper mould and preform - the main mechanism of void removal strategy- on the void content is considered, highlighting a correlation between the compaction force and void content.

Finally, an experimental study is established to examine the effects of the presence of a gap between the upper mould and the preform consisting of a number of 2/2 twill woven carbon fabrics on fibre volume fraction and void content as well as void size distribution of a wing spar. To substantiate this work, a comparative study is presented by considering autoclave and conventional RTM. Results showed that the composite part produced without the gap in which the preform is continuously compacted is comparable with the autoclave results. In both fibre volume fraction and void content, HIPRTM assisted with external compaction pressures yields a composite wing spar with the lowest void content of all studied process providing a better component than it is possible to obtain from autoclave processing.

Nomenclature

1   LIST OF SYMBOLS

ϕ	Porosity	-
K	Permeability	m^2
V	Volume-averaged superficial velocity	m / s
ρ	Density	kg / m^3
μ	Viscosity	$Pa . s$
P	Volume-averaged pressure	Pa
x	Flow front position	m
k_c	Kozeny constant	-
τ	Tortuosity	-
L_e	Effective average flow path length	m
L	Shortest flow path distance	m
r_f	Mean radius of circular solid fibre	m
P	Pressure	Pa
K_{eff}	Effective permeability	m^2
K_s	Permeability of solid tows	m^2
K_L	Intra-tow permeability along a tow path	m^2
K_T	Intra-tow permeability perpendicular to a tow path	m^2
x, y, z	Rectangular coordinates	m
α	Anisotropy Index	-
γ	Semivariogram function	-
h	Lag distance	m
N	Number of experimental pairs of points	-
C_0	Maximum semivariogram	-
a_0	Maximum lag distance	m
$\mu(X)$	Mean value of X (statistical)	-
r_{inj}	Radius of injection tube	m
P_{inj}	Injection pressure	Pa
c_1, c_2	Gebart permeability constants	m^2
a	Major axis of tow ellipse	m
b	Minor axis of tow ellipse	m
d_f	Diameter of cylinder	m
w_{gap}	Width in warp direction	m
h_{gap}	Height in weft direction	m

P_c	Compaction pressure	Pa
P_{out}	Pressure in the surrounding environment	Pa
P_{in}	Pressure within the vacuum bag	Pa
V_c	True void content	-
V_c^*	Estimate void content	-
V_v	Volumetric void content	-
A_v	Total void area	m^2
A	Area of image	m^2
d_{eq}	Equivalent diameter	-
V_f	Global fibr volume fraction	-
V_f^{tow}	Intra-tow fibr volume fraction	-
σ	Standard devation	-
R^2	Coefficient of determination	-
σ^2	Variance	-
n_t	Number of fibres per tow	-
u_{x0}	In-plane flow velocity	m / s
u_{z0}	Through thickness flow velocity	m / s
U	Standard uncertainty	-

2   LIST OF ABBREVIATIONS

AC	Autoclave Curing
ACF	Auto-correlation Function
CFD	Computational Fluid Dynamic
CK	Carman-Kozeny
COV	Coefficient of Variation
CSR	Complete Spatial Randomness
ECDF	Empirical Cumulative Distribution Function
FEA	Finite Element Analysis
GEV	Generalized Extreme Value
HIPRTM	High Injection Pressure Resin Transfer Moulding
KSS	Kolmogorov-Smirnov Statistcs
LCM	Liquid Composite Moulding
MCM	Monte-Carlo Method
Micro-CT	X-Ray Micro-Computed-Tomography
MLE	Maximum-Likelihood Estimation
OEM	Original Equipment Manufacturer
OoA	Out-of-Autoclave
PDF	Probability Distribution Function
RTFI	Resin Infusion under Flexible Tooling
RTM	Resin Transfer Moulding
RVE	Representative Volume Element
UAV	Unmanned Aerial Vehicle
UD	Unidirectional
VBP	Prepreg/Vacuum Bag Processing
VI	Vacuum Infusion

This thesis is dedicated to:

Elham

and

Toranj

Without their patience, understanding, support, and most of all love, the completion of this work would not have been possible.

Acknowledgment

My advisor, Dr. *Nuno Correia*, was instrumental in encouraging me to pursue my doctoral degree, and I am extremely thankful for his patient guidance and belief in me as a student.

Besides my advisor, I would like to thank Prof. *Torres Marques* for his insightful comments and encouragement.

Helpful discussions and resources lent to me by Prof. *Stepan Lomov*, who provided me an opportunity to join their team as visiting scholar, was invaluable, and I am appreciative of his assistance and guidance.

I thank all the people from the jury, especially Dr.*Juan García Manrique*, Dr.*Raul Fangueiro* and Dr.*Alexandre Afonso* for the careful reading of the text. Their corrections and suggestions greatly improved the readability of the thesis

I could not have completed this degree without the support and love of my wife *Elham*, and I cannot thank her enough for standing behind me and my studies. The word also goes for *Toranj*, my daughter, who has been the light of my life for the last two years and who has given me the extra strength and motivation to get things done.

I am also indebted to my parents, who taught me how to live life to the fullest with a balance of discipline, hard-work, and fun. My parents-in-law are a source of enjoyment and fulfilment, and I love spending time with them.

Some special words of gratitude go to my friends who have always been a major source of support when things would get a bit discouraging: *Hesam Zolfonun ,Rui Gomes, Cláudia Cristovão, Pedro Mimoso, Hooshiar Zolfagharnasab, Mahoor MehdiKhani,* and *Amin Davarpanah*. I am indebted to each and every one of the aforementioned individuals, and I thank God daily for their presence and influence in my life.

Contents

Chapter 1

Overview of the thesis

Introduction

Over the last decades, an increasing number of functional and structural metal parts have been progressively replaced by continuous fibre polymer composites (CFPC). The main drivers for this replacement are weight reduction and a higher degree of complexity in forming process [1].

CFPC are formed by a fluid flow through the fibrous medium, whether to make a pre-impregnated that is further consolidated or to directly produce parts from dry fibre reinforcement. Based on these two forming concepts, most advanced manufacturing processes for CFPC can be classified in two main groups: Hand lay-up\autoclave curing (AC) and Out-of-Autoclave (OoA) processes.

AC is a robust technique for manufacturing high performance composite components. However while time and energy consuming AC is still the main process for aerospace, providing process and material reliability in high fibre volume fraction components from pre-preg materials. While several groups looked into improving autoclave curing in order to reduce cycle times as well as labour cost [2] autoclave curing was never able to become a mass production process due to highly labour-intensive process, high cycle time and high capital cost [3]. Given the increasing use of CFPC, the working hypothesis of this thesis is that substituting AC with OoA manufacturing methods, in particular those that deliver autoclave-quality components, will become a major industry driver of composite materials.

Liquid Composite Moulding (LCM) is one of the most relevant OoA technology families and experience with this technology has shown that it is possible to manufacture autoclave-quality components. In this family of processes, a liquid thermosetting resin is injected into a dry fibre preform. The LCM family thus includes Resin Transfer Moulding (RTM), vacuum-assisted RTM (VARTM) and, when flexible membranes or shells are used, vacuum infusion (VI) or other resin infusion under flexible tooling (RIFT) variants.

RTM has the potential advantages of cost competitiveness, class A finish of the parts, and production rates over autoclave process. In this push towards OoA, RTM has seen significant developments - some coming from the R&D community- that have enabled the manufacturing of complex turbine blades for aeroengines and automotive components such as car doors, roofs and side panels. Table 1-1 shows the use of RTM for manufacturing polymer composite components in the automotive industry over five years [1]. However, quality concerns, strength, surface quality and durability significantly influence the potential application of RTM. Most relevantly the entrapment of volatiles, air, or other non-

solid foreign materials leads to void formation, and limits the effective structural stress transferring between fibres and the applicability of these materials in critical applications.

Table 1-1: Examples of composite components used in automotive industry, adopted from [1].

OEM-Model	Application	Material	Drive to use composites	Manufacturing method	Year
Daimler AGT-Mercedes	Fluid filter module	CFPC	Weight and cost reduction	RTM	2010
Faurecia Jeep Liberty SUV	Door module	CFPC	Weight reduction	--------	2010
Land Rover-Evoque	Instrument panel, inner door modules	CFPC	Weight and fuel consumption reduction	--------	2012
Lamborghini Aventador LP700-4	Front and rear bumpers, body aerodynamics kit	CFPC	Weight reduction	RTM, Forged composite	2012
Lexus LFA	Cabin, floor, roof, pillars, hood	CFPC	Weight reduction	RTM, Prepreg lay up	2012
Callaway Corvette	Body aerodynamics kit	CFPC	Weight reduction	RTM, Forged composite	2012
Daimler Smart 3rd generation electric	Wheel rims	CFPC	Light weight, stunning look	RTM	2012
BMW M6 Coupe	Car roof	CFPC	Weight reduction	RTM	2012
BMW M6 convertible	Roof compartment cover, trunk lid	CFPC	Weight reduction	RTM	2013
McLaren MP4-12C Spider	Car roof, chassis, bodywork	CF monocell, lightweight CF body panels		RTM	2013
Alfa Romeo 4c	Bumpers and mudguards	CF+PUR-RIM	20% less weight compared to aluminum	RTM	2013
	Outer body	SMC			2013
	Chassis	Prepreg (CF, epoxy)			2013
BMW i3	Passenger cell	CFPC	Weight reduction	RTM	2013
BMW i8	Passenger cell	CFPC	Weight reduction	RTM	2014

To sum up, a manufacturing process by which one would be able to produce components outside an autoclave, yielding high quality laminates with high fibre volume fraction as well as low content void without prepregs, cleaner than wet lay-up, would go a long way in creating further markets and applications for composites. The author believes that the proposed combination of the best items of both LCM and Autoclave curing process can contribute to the achievement of this goal.

1.1 The state of art

Resin transfer moulding (RTM) is being currently used to manufacture high performance aerospace components. However, production rate is low and manual work is inevitable, being a significant part of the total cost. In automotive manufacturing RTM parts are mostly used for their aesthetics and then only in small quantities. Potential markets and applications of high performance composites would exist if a fast reliable and

automated RTM production line would be developed (as is currently the case with RTM in BMWs carbon fibre reinforced polymer manufacturing plant).

Owing to concerns about fibre washing and the use of a static mixing system (Table 1-2), the regular RTM processes are done in a relatively low injection pressure (lower than 15 bar) taking up to 10 min to inject a part. Realizing that this can be changed, Dieffenbacher, Krauss-Maffei and Fraunhofer recently developed the high injection pressure resin transfer moulding (HIPRTM) process for use in automotive industry at injection pressures above 50 bar [4]. In HIPRTM, the preform is placed in the mould, vacuumed, injected at a high pressure (60-100 bars) with high reactivity epoxies and polyurethane systems and, at the end, pressed to complete the production cycle. Importantly, when compared to RTM this technology yields a polymer composite part with less void-content and air entrapment, excellent surface properties and low dimensional variations.

Table 1-2: Comparison of high and low pressure RTM configurations [5]

Tooling	Standard RTM	High pressure RTM
Mixing configuration	Static mixer	Mixing chamber
Mixing pressure	<15 bar	>15 bar
Mould pressure	<15 bar	>15 bar
Typical total cycle time	>15min	<15 min

1.2   Progress beyond the state of art

The combination of high injection pressure and high compaction pressure introduces possible processing drawbacks such as fibre wash-out, filling defects, high porosity and poor mechanical performance. The author was only able to find a small number of published scientific studies that investigated HIPRTM: experimental works such as those of Barraza [6] on void content as a function of various pressure levels, Khoun *et al.* [7] on the experimental effect of process parameters, such as injection flow rate, vacuum assistance sequence, mould gap control and binder concentration, on mechanical performance of composites part made by HIPRTM [7] and numerically, on isothermal model with a highly reactive resin by Siddiqui [8] who reported a non-isothermal model for HIPRTM model and have correlated their results with actual processing data for production of unidirectional carbon fibre composites.

The work that remains in this field is, however, still significant. One must include not only the non-isothermal rheo-kinetics but also due to the high injection pressure and compaction, issues with permeability at very high fibre volume fraction and its variability within the preform [9], the squeeze flow phase (compression moulding) and the analysis of void formation throughout the process are increasingly important.

1.3 Challenges

The HIPRTM is a multi-step process with a strong correlation between the different steps, which one must consider in order to push HIPRTM towards a robust manufacturing technique. This also reinforces the need to perform studies, which allow a full characterization of the process and its most relevant parameters. Considering the dual stage HIPRTM injection (high pressure in-plane flow) and the interesting phenomena regarding void formation (and reduction under pressure), one can argue, based on the limited number of studies on this process and the inexistence of tools for highly variable materials, that there is significant requirement for the understanding of the interaction between flow and inherent material variabilities.

Also, as HIPRTM parts need to be high quality and low cost, fundamental knowledge on the HIPRTM process has a key role. Fundamental knowledge allows a better control on the manufacturing process, and subsequently a higher, as well as a more reproducible part, quality. Therefore, the whole HIPRTM process needs to be understood while optimisations of the individual steps of the manufacturing process only to partially address the optimisations of the whole process.

Figure 1-1 shows the steps of the HIPRTM process that influence the final quality of composite parts and summarises the correlation among the process variables, fibrous media behaviour and final part quality. The critical steps in HIPRTM is to inject resin into a fibrous medium as fast as possible while minimising defects such as void content, nonhomogeneous wetting of reinforcements. The permeability of the fibrous medium and the injection strategy[1] are two important variables that relate to the fibre wetting and the impregnation rate of the fibrous medium.

These steps are often performed separately. However, the parameters of different steps are mutually dependent. For instance, for the first step: preform deformation is mainly caused by high compaction pressure and also depends on the textile pattern (architecture) as well as the fibre properties (such as arrangement inside a tow). On the other hand, the fibre arrangements and local arrangements of tow paths are influenced by the deformation of the preform. Similarly, flow behaviour inside the preform depends on the deformation of the preform as well as fibre arrangements. For the second step, injection pressure depends on the preform thickness, which depends on compaction pressure. Conversely, the preform can be influence by the injection pressure and compaction pressure.

Based on the above discussion, two main challenges are distinguished:

(1) Permeability scatter due to heterogeneous nature of fibrous media and imperfection in experiment set-up. It is interesting to know where the scatter comes from, what the implications are, and how it can be reduced. In this sense, this is an important topic and effort to put forward an appropriate distribution model for simulation of its variability in this thesis is systematic. More specifically, inherent material variability causes spatial

---

[1] Injection strategy evolves adjusting different process variables such as mould gap, compaction pressure, and injection point towards a comparable autoclave composite part.

variations in permeability; the experiment measurements at macroscale level (mould scale) present an aggregated result influenced by this local variability. This fact has to be part of the analysis for the selection of an appropriate distribution model. Similarly, permeability at micro and mesoscale is directly affected by the geometric features of the reinforcement, which involve significant uncertainty.

(2) Injection strategies govern the imperfections due to voids and dry spots. To support the use of HIPRTM, in addition to concentrating on the material variability which is a necessary input for process simulations, studies concerning the effects of process variables on high fibre volume faction composites are lacking. It is important to know what improvements are obtained over hand lay-up/autoclave processes, how the process variables affect the final quality of composite parts (void content) produced by HIPRTM.
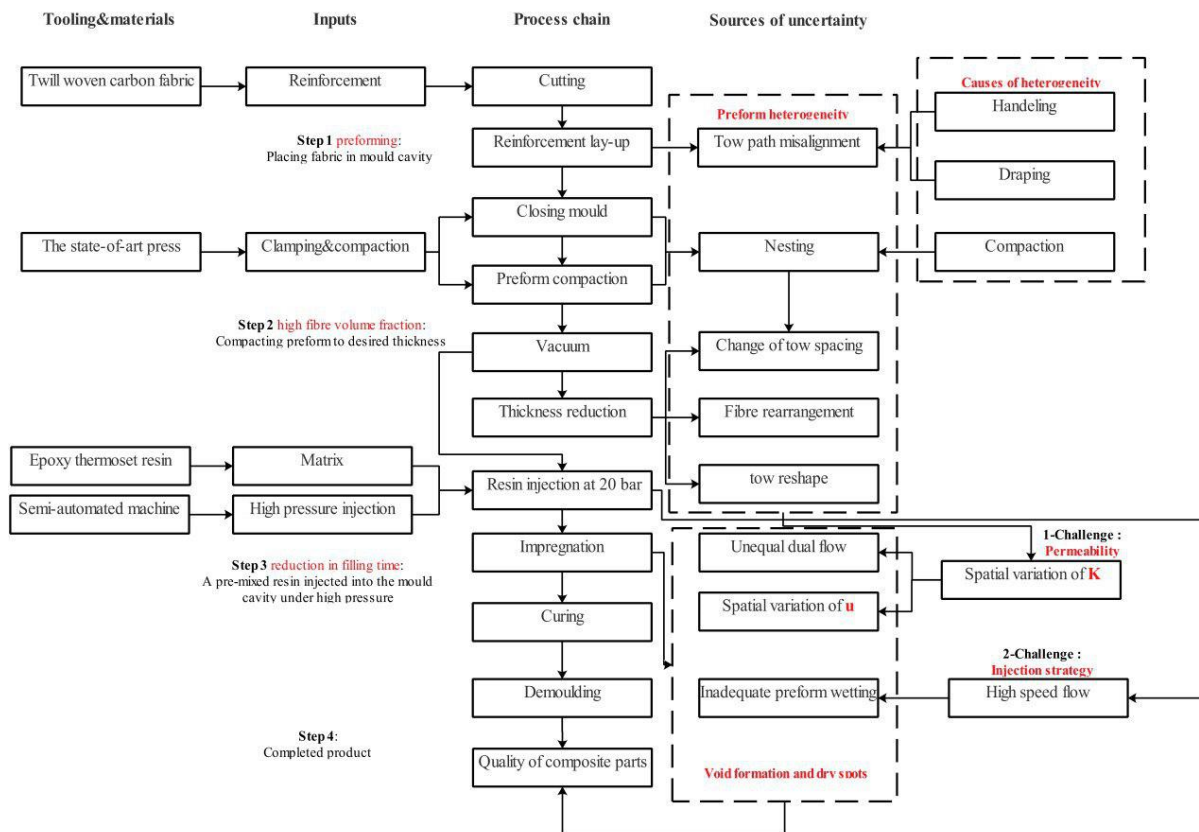
Figure 1-1: Relationships between HPRTM manufacturing steps and material behaviour

1.4   Context

As technology for the production of composite materials has evolved significantly with higher pressures used in thermosetting resins geared to higher processing speeds, these materials are finding an ever-increasing place in the automotive and aeronautical sectors, research has also had to evolve. With the application of these materials in an ever-increasing number of products (from the Boing787 fuselage and wings to the BMW i8 chassis) it has become even more pressing to fully understand the physical and chemical phenomena underlying the manufacturing of composites materials.

Tow placement, hot stamping, High Injection Pressure Resin Transfer Moulding are three of the most promising manufacturing processes for composite materials in terms of industrial uptake for the automotive and aeronautical sectors. It is the author's aim to continue the development of the high injection pressure resin transfer moulding and provide both relevant data sets for the validation of models and a sustainable development in this technology.

This thesis aims to expand fundamental knowledge in the phenomena that dominate the HIPRTM and provide a strong scientific basis for the technological research that is being performed at INEGI. The focus of thesis is on out of-autoclave technologies: while autoclave curing has dominated the manufacturing of high quality components (due to its inherent high quality, low void content and repeatability), it is also extremely expensive because it suffers from issues such as high energy consumption (20MJ/kg of composite vs. 3-5MJ/kg in resin injection processes is a typical number), prohibitive equipment costs and high manual labour involved. For this reason, both the academic and industrial technologies communities have pushed, in the last 10 years, to move component production out of the autoclaves and all of the work discussed here is following that important trend. Composites manufacturing processes are challenging. The difficulty in assessing experimental data, the low reproducibility of these processes and leads to difficulties in the relevance of advanced theoretical studies in this field and reliable process models are essential to the practical establishment of each of the manufacturing techniques in the composites industry. Optimized industrial processes, able to support specific technological applications and economies, depend on that. Relevant changes are continuously occurring in composites processing at material, machinery and control levels. As such, the overall modelling approach remains the same but the laboratorial and industrial equipment and capabilities evolve.

This work is carried out in the first place as part of SciTech project in INEGI. Secondly, the research project was supported by the *Fundação para a Ciência e a Tecnologia* (FCT). Finally, the work was partly done in SciTech project at the KU Leuven.

In the high injection pressure resin transfer moulding activity I will study the process whereby resin is injected at high pressures into a mould containing dry formed fibres. This technology family, that has recently upgraded from standard RTM, is a recent development that has taken place due to two needs: higher processing speed (faster flow, higher resin reactivity) and better laminate quality (lower voids and higher fibre volume fraction). This is being achieved through a combination of high pressure resin injection (from the typically

500 kPa up to 6MPa) which allows both higher fibre compression (that reduces permeability) and lower voids (because further compression leads to lower void size in direct perfect gas law relation). The experiments so far show that it is possible to achieve up to 65% fibre volume fraction (up from the typical 55% of standard processes) and void contents below 1% (down from typical 2-4%). However, it was identified that a more fundamental knowledge was needed to solve manufacturing process related to challenges. The challenges encountered comprised several issues, including the textile preform deformation and the subsequent impregnation behaviour using HIPRTM. Therefore, this activity aims to experimentally research process improvements and upgrades to the existing pilot line which will be designed and implemented in view of enforcing:

a- In-house capabilities to develop and manufacture increasingly complex shapes and high-quality continuous fibre polymer composites (CFPC) parts and

b- Use different concepts of high pressure flow, be it in-plane flow in a fully consolidated blank or through thickness flow where a gap is used to enhance flow and where a subsequent pressure is used to fully consolidate the injected part.

c- Perform characterization of the materials so that data are available to modelling (within the multiphysics modelling activity).

In this thesis I will look into the injection strategy approaches for very high pressure injection RTM in order to understand the flow and void formation mechanisms. I will also implement an uncertainty based approach to take variability effects into account explicitly be based on stochastic simulations of composites manufacturing.

The two central challenges in modelling Darcy's flow are: 1) model the material uncertainties and provide a mechanism to generate statistically accurate permeability estimates at different scales; and 2) relate the micro/meso scale material uncertainties to macro-scale permeability of fibrous media. This thesis addresses the first problem and propose ways for the quantitative uncertainty evaluation of permeability at different scales.

Also, as textile reinforcements show a hierarchical structure, different length scales have to be taken into account in permeability (micro, meso and macro scales). The experiment samples (mould scale) have spatial dimensions on the order of centimetres which are 100 times larger than the spaces between tows (mesoscale) and 1000 times larger than spaces between fibres (microscale). The meso- and micro-scale permeability represents properties near the characteristic length of the gaps (100 μm space between tows on the mesoscale and 1 μm space among fibres within a tow on the microscale). On the other hand, permeability determined from the laboratory experiments represents a rough average of the intrinsic properties (fibre arrangement, tow spacing, and tow path). Therefore, the statistics of global scale measurements does not represent directly the statistics of the local micro-scale variations. The distribution of local properties needs to be involved in determination of these local variations. Therefore, the uncertainty propagation of permeability is a multiscale approach. In this thesis, the numerical solution of fluid flow is carried out in the separate scales to obtain the statistics of permeability on the each scale. Separating scale will help to know where the scatter comes from, what the implications are, and how the statistics of permeability vary with the scales.

The linking of microscale properties to the macroscale properties needs upscaling that allows the essence of physical processes at one level to be summarized at the larger level. However, the understanding of upscaling process from microscale to macroscale are not focus of this thesis.

With this work we aim to strengthen the research group in this advanced process and prepare future work for the automotive and aerospace sectors. The ability to provide regional and national actors with such a technology, both in equipment and in the modelling of such processes, may also bring substantial advantage and ultimately lead to improved business competitiveness.

1.5   Permeability

To help the more efficient and cost-effective design and to improve the quality of composite materials, both understanding and modeling of several important aspects of flow phenomena in LCM process are important. This work is aimed at contributing to the scientific basis for understanding of how LCM process variables affect the final quality of composite components. Its prime goal is to contribute to the development of the knowledge and engineering equipment to control fluid flow inside fibrous media to ensure homogeneous flow pattern, to minimize dry spots as well as voids, and control fibre volume. This need led to in the past to models to accurately predict the influence of key LCM process variables on mould filling in such a way as to adjust parameters such as injection pressure, flow rates, gate location and preform placement and temperature. Such models already provide helpful guidelines regarding creating and improving tooling design.

These commercially available simulation packages like PAM-RTM (PAM-RTM, 2010), RTM-Worx (Polyworx, 2010), LIMS (Advani and Bruschke, 1994) or SimLCM (Kelly and Bickerton, 2009) have been developed based on finite element / finite volume techniques. These softwares need a comprehensive characterisation of textile reinforcements. Hence, one main aspect of understanding the flow behavior in the LCM process is related to textile reinforcement permeability. The accuracy of permeability data is key for the reliability of the numerical mould filling simulations to avoid void formation during impregnation process. Because of its major contribution to the result of flow models, the determination of permeability is an object of continuous intensive research for the scientific community and, as Advani *et al.* [10] pointed out already in 1994, the state of the art of flow modeling is much more advanced than the techniques to determine textile reinforcement permeability. In my opinion this statement is still valid today. One main challenge associated with permeability measurement is the scatter of experimental data: variations of up to two order of magnitude have been observed. This scatter is caused by the various uncertainties associated with permeability determination which can be thought as in two groups: (i) natural variation in preform structure and (ii) experimental difficulties. Permeability values in preform present significant stochasticity due to the heterogeneous nature of the reinforcements. This is further complicated by experimental difficulties as well as a lack of standard measurement methods. Evidently, quantifying these sources of uncertainties can improve the quality of permeability measurements.

1.5.1 Preform heterogeneity

The problem of calculating average permeability on the basis of small scale (i.e micro, and meso-scale) numerical approach is a common practice. If preform were completely homogenous, this average value would be a representative value of the whole geometry where the permeability would be constant and not vary through the preform. However, in HIPRTM, preform contains different types of heterogeneity, which affect the average value of permeability. The heterogeneity is caused in part by compaction, which is a very important stage in HIPRTM process. This stage is carried out through a hydraulic compression press, leading to microstructural alterations in fibre arrangements and changes in the preform. Hence, compaction results in the spatial distribution of fibre tows and nonlinear viscoelastic behaviour in the fibrous media. These variations change the permeability of the preform and affect the impregnation step. Hence, the knowledge of the effect of tow spacing, tow cross section and distortions of the tow centerlines on the preform permeability is an important step towards better designs and control of the HIPRTM process.

Several researchers pointed out that spatial variations in the local permeability originate in the spatial micro-level variations of the reinforcement geometry. Hence, a reliable study of permeability needs the identification of the uncertainties associated with internal geometry of preform. When all these uncertainties are adequately described, the quality of permeability data is improved and flow simulations can be carried out with higher confidence.

The scientific community recently focused more attention on the stochastic simulation of resin flow during LCM processes in order to consider the imperfections in the textile reinforcement. Nevertheless, several steps still need to be carried out since sources of uncertainties have not been well understood and numerical approaches are lacking in the accurate prediction of the effects of variation on permeability. Most studies are limited to local features, neglecting the spatial dependency of permeability (permeability variation with a mould cavity) across the textile reinforcement which is necessary for adequately simulate fluid flow. Analysts have to impose a number of assumptions regarding the statistical characterisation of the permeability, leading to inaccurate approximations of the actual limits of textile reinforcement properties. Further, spatial variability is well analysed by advanced methods developed in the area of stochastic structural mechanics. However, there is no systematic method to apply internal geometry variations of textile reinforcements to flow simulation procedure in combination with realistic experimental data. Charmpis et al. [11] explained these requirements for experimental data and proposed an appropriate multiscale method. First experimental data on the spatially correlated random fluctuations of uncertain properties should be collected and subsequently used to derive probabilistic information for macroscopic permeability from the lower level. Only when dependencies between permeability and other properties of a textile reinforcement are adequately explained, can we replicate virtually flow advancement in a real fibrous medium for liquid composite moulding can be simulated. The subsequent step in this development should involve the prediction of permeability that takes into account variation at the different scales and is calibrated with experimental work. Therefore, the inclusion of uncertainties at different preform scales is a key tool towards the reproducibility of

permeability values determined. This is necessary to obtain results in mould filling simulations.

1.5.2   Experimental statistics

As was mentioned above, the experimental difficulties and lack of a standard approach for permeability determination, has meant that permeability values determined by laboratories with differing set-ups have produced contradictory data. This fact has led to a number of permeability benchmark exercises [12]–[14]. Nonetheless, even with these results, some issues still remain regarding our understanding of the fundamentals of variability and uncertainty behind permeability experiments.

As with other properties, so too has the uncertainty of permeability been characterized by using probability density functions to describe its variability, in which, an appropriate statistical distribution model to permeability data is a key part of data analysis. The most commonly used statistical models for permeability are the Gaussian and log-Gaussian distribution: they have been frequently used to model the statistics of experimentally determined permeability data. One major limitation of the proposed statistical models is that they were validated for a particular experimental design and fibrous medium. There is no guarantee that they can be used over the different types of fabric with various experimental set ups. To validate the proposed statistical models, permeability experiment has to be repeated several times. The previous study by Hoes *et al.* [15] shows that 75-100 experiments are required to obtain an appropriated statistical distribution model. Although recent efforts reveal a shift towards propagating the uncertainties in statistical model predictions, which implies that the validation of a statistical model should encompass all possible sources of uncertainties, little work has been done in this field [16] [20]. However, there remains the shortage of experimental statistics, which is an important part of the interpretation of permeability data.

The state of the art, explained above, reveals a need for the uncertainty propagation for an appropriate statistical distribution model of permeability. Since a realistic statistical model of permeability should reflect these uncertainties, the validity of a statistical model must be assessed based on measurements of permeability. The accuracy of measured permeability is then a function of experimental uncertainty. With an error in an experimental measurement, there is a possibility that this error can propagate to permeability. Identifying where errors propagate in a measurement system is important for development of a robust permeability measurement. Uncertainty propagation helps reveal the significant parameters in a measurement system, and to establish how different input variables associated with errors affect the magnitude of permeability. Additionally, this uncertainty propagation also provides insight into how to improve the measurement system to reduce or eliminate these errors.

The author believes that knowing the sensitivity of permeability distribution to uncertainties and incorporating their influences into the statistics of permeability data could substantially increase the quality of permeability data.

In summary, the inclusion of uncertainties is a key towards the reproducibility of permeability values determined by either measurements or simulations. This is necessary

to obtain reliable results in the mould filling simulations. When the sources of uncertainties are fully characterised, permeability values can be revisited, resulting in better industrial processes with a less scrap at a reduced cost.

1.6 Injection strategy

The use of high injection pressure with this new, fast process (HIPRTM) poses several new scientific as well as technical challenges. In HIPRTM, such a high injection pressure may cause preform deformation and as a result of that mould filling times become longer with increasing fibre volume fraction. In addition, proper impregnation can be an issue because of the possibly inadequate wet-out due to high-speed resin flow. Therefore, without addressing and overcoming these technical challenges, there is no guarantee that one can obtain autoclave-quality composite components.

Every aspect of the RTM process has been widely examined over the two last decades from the preforming step to the mould filling and consolidating step, showing the importance of controlling the process variables such as injection pressure, compaction pressure, thermal histories to obtain quality-autoclave composite components. Similarly, several RTM computational works have been performed to explain physico-chemical phenomena during the impregnation process (i.e. heat transfer, preform compaction, and consolidation) by simulation of the mould filling step.

With the intent of increasing production rates, several studies focused on compression RTM. In these studies, the effects of mould gap, the gap closure rate, injection pressure, and compaction pressure and preforming on the mould filling time, composite component quality, and void content were examined. However, the injection pressure and packing pressure used (6 bar) is lower than one expects to use in HIPRTM. Very few experiments have been reported that present part quality results of these processing conditions. Existing studies do not cover the questions of moulding conditions which affect void content of final composite pats. In this sense, at high pressure resin injection, a lack of a dedicated analysis would result to some quality concerns such as dry spot, formation fibre roving and low fibre volume fraction of the produced components. Therefore, a robust design of the process to manufacture composite parts at the shortest possible impregnation time with the highest quality is essential.

1.7 Objectives and contributions

It follows from the above that to be assured of the quality of fibre-reinforced composites, it is important to properly address the physics and material aspects of two important parameters in high injection resin transfer moulding HIPRTM: uncertainty in permeability data and injection strategy. This thesis addresses these needs following this rational. Hence, research and its objectives were divided into two different parts: uncertainty in permeability, focusing on preform properties for reliable flow simulations and injection strategy, focusing on process optimization for autoclave-part quality in terms of void formation.

Uncertainty in permeability data

Various sources of uncertainties associated with permeability can be classified into two groups:

Type I: Uncertainty associated with the inherent variation in permeability due to internal geometry variations of preform (Figure 1-2, left panel).

Type II: Uncertainty associated with error due to imperfection in measurement instruments (Figure 1-2, right panel)
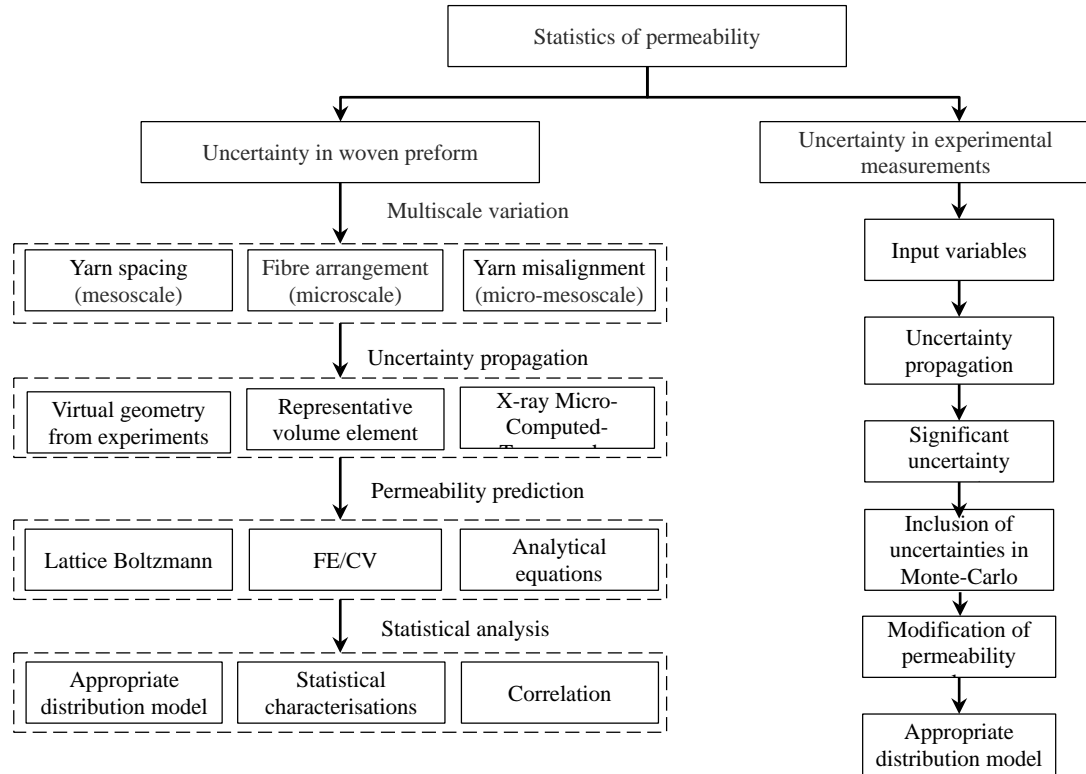

Figure 1-2: Uncertainty propagation of permeability

1.7.1   Internal variation

The textile reinforcements of interest in automotive and aerospace applications are woven textiles. Woven textiles have a dual porosity scale: porosity among fibres which are gathered together to form a tow (e.g. intra-tow porosity) at a scale of 10^{-5}m, and another porosity between tows which are separated by relatively large gaps (inter-tow porosity) at a scale of 10^{-3}m. Then these textiles are compacted in layers into the mould. Such media promote the non-homogenous advancement of fluid flow and can result in void formation and dry spots between tows or among inside tows. Hence flow modelling of injection-based manufacturing process such as Resin Transfer Moulding (RTM) inside the such media involves capturing both porosity scales. Additionally, tow cross-section shape is an important variable as the global fibre volume fraction increases as the tow shape become more elliptical. Furthermore, the intra-tow properties will have significant impact on the

global flow at high degrees of compression. This is relevant to HIPRTM where high pressure injections ($>10^6$ Pa) combined with dynamic fibre compaction using state-of-the-art presses has opened a possible window for jumps of the current 50-55% to over 65% fibre volume in Resin Transfer Moulding.

Hence, it is fundamental that one takes into account this multiscale nature of uncertainty in the evaluation of permeability. Simulating fluid flow inside woven textiles is not only a challenging task due to the dual porosity characteristic but the simulating this process simultaneously at intra- and inter-tow can be computationally expensive [19]. One common way to deal with these difficulties is to carry out the simulation of fluid flow at three separate scales.

Three distinct scales are considered, namely, those of the textile, the tow, and the fibres. The desired reinforcement parameters (fibre arrangements, tow centroid coordinates, and tow aspect ratio) must be correctly identified, while a statistical analysis describes the suitable distribution model, distribution parameters and possible correlation. Subsequently, advanced numerical techniques involve multi-scale modelling in order to adequately predict the variation of permeability. For this purpose, methods from stochastic mechanics were applied (Figure 1-3, left panel). At the micro scale, an RVE-based stochastic numerical model is used to predict the permeability of randomly generated media. At the tow level, based on the statistical information of tow geometry data, a relationship between the width (w) and thickness (t) of tows is derived to obtain the variance of the tow-level fibre volume fraction (V_f^{tow}). V_f^{tow} is calculated for each pair of w and t. Subsequently, local distributions of intra-tow permeability along the fibres (K_L) and perpendicular to the fibres (K_T) are predicted with the Gebart's equation along tow paths. Using statistical analysis of the permeability data, a mathematical model is proposed for the spatial variation of permeability along the tow path. At the mesoscale, a virtual geometry of a 2/2 twill carbon fabric based on the previous work of Vanaerschot *et al.* [20]–[24] is used to mathematically represent internal geometry variations including yarn spacing, width and thickness and distortions of the yarn centrelines on the variations of permeability at meso-level (unit cell) textile. This virtual geometry is used as the basis for the calculation of local permeability values with the FlowTex software [25]. Through this work, permeability is characterised by a mean permeability value, a variance, which describes the range of permeability and correlations of the random permeability field; the statistics of permeability is compared with the statistics of the fabric geometrical parameters.

1.7.2   Measurement instruments

Alongside the uncertainty in permeability due to the internal variation, attention was also given to errors arising from the measurement instruments. Three main steps in this development involve (Figure 1-4, right panel).; (i) identification and quantification of sources of uncertainty in permeability measurements, (ii) a modelling method that includes uncertain contributing factors at different scales and is calibrated with experimental data (iii) statistical modelling of permeability.

A detailed discussion of the multiscale permeability analysis is proposed in the key publications that build the first part of this thesis.

1.8   Void formation

State of art equipment such as a semi-automated mixing machine and high injection pressure RTM allows fast resin injection into the mould cavity with a high throughput rate. As part of the development of HIPRTM, and in order to support this study, a relevant geometry demonstrator was selected, consisting of one spar, based on a design that was used for a wing of an Unmanned Air Vehicle (UAV). In this thesis the main experimental goal is to evaluate the effect of fast resin injection into the mould cavity on the void content of composite parts. Fast resin injection may pose problems of abrupt mould opening or fibre wash out. Hence, the effects of the process variants including mould gap, mould geometry and gate geometry of the mould were also investigated. Experimentally, a comparison of the quality RTM composite components with those of competing processes such as autoclave followed this work.

1.8.1   Experimental analysis of manufacturing process

In order to optimize the variables of the HIPRTM process in such a way as to improve the mechanical performance of the components produced by this process, an experimental framework was developed to examine the ways of eliminating or reducing voids as well as dry spots, aiming to obtain the autoclave-quality components.

All steps mentioned above are completed throughout the PhD framework that describes the possible strategies for the modifications of RTM, with the aforementioned carbon-expoxy 2/2 twill woven composite spar produced by the HIPRTM as a relevant geometry demonstrator.

1.9   Outline of the thesis

This thesis consists of two main parts. Part I explains the state of art multiscale analysis of permeability scatter and propose ways of quantifying the sources of uncertainty from a statistical point of view. Permeability analysis at each scale is indexed as key publications. Part II explains the state of art of HIPRTM and the need to design a mould to inject at high pressure in order to obtain high fibre volume fraction with autoclave-quality components.

Part I

Four papers were prepared in different international peer-reviewed journals.

(1)   At the meso scale: The effect of the internal geometry variations including yarn spacing, width and thickness and distortions of the yarn centerlines on the variations of permeability at meso-level (unit cell) textile are examined. The results were published in Composite Part A (2017), Volume 101, pages: 394-407 (Chapter https://doi.org/10.1016/j.compositesa.2017.05.030

(2) At the micro scale: the results of the analysis of permeability scatter as a function of random distribution of fibre is published in Composite Structures (2016), Volume 158, pages: 323-332 (Chapter 3).

http://dx.doi.org/10.1016/j.compstruct.2016.09.045

(3) At the tow scale: This study presents an experimental analysis of the relation between the variation of fibre volume fraction at tow level induced by the internal geometry variation of a 2/2 twill carbon fabric and permeability components, along and across the fibres. The results were published in Composite Part A (2017), Volume 101, pages: 444-458 (Chapter 4).

https://doi.org/10.1016/j.compositesa.2017.07.008

(4) At the mould scale: This study presents an evaluation of the uncertainties produced by measuring instruments and equipment in permeability determination for the RTM. Presented in 16th European conference on composite material (ECCM16), June 22nd-26th, Seville, Spain (Chapter 5).

http://www.escm.eu.org/eccm16/assets/0484.pdf

Part II

A study addressing a new variant of the RTM process, high injection pressure resin transfer moulding (HIPRTM) was published. In order to examine the potential of this new process, we carry out a set of experiments to compare HIPRTM with autoclave processing and vacuum bag processing(VBP) in terms of the resulting void content and void size distribution. The results of this study were published in Composite Part A (2016), Volume 83, pages: 88-99 (Chapter 6).

http://dx.doi.org/10.1016/j.compositesa.2015.11.042

Chapter 2

Inter-tow permeability

On the variability of mesoscale permeability of a 2/2 twill carbon fabric induced by variability of the internal geometry

Reinforcement variability can lead to large local scatter of permeability values. This paper introduces ways to incorporate the geometric variability in the determination of permeability, using distributions and spatial correlations of yarn spacing, width and thickness and distortions of the yarn centrelines. The approach is demonstrated for mesoscale flow in a 2/2 twill carbon fabric over a region of ten by ten unit cells. Variability of the fabric geometry is characterized using the earlier proposed methodology, based on representation of the yarn path deviations using Markov chains and the correlations between the deviations in the neighbouring yarns using Series Expansion approach. The Stokes equation is solved for the generated stochastic unit cells to predict inter-yarn permeability of each unit cell in principal directions; intra-yarn flow is neglected. There is a good agreement between the calculated mean permeability and the values obtained in the Permeability Benchmark II. The predictions show the following results permeability varies over the medium as a function of inter-yarn gaps, as larger gaps lead to larger permeabilities. Permeability variations show a correlation length of *circa*.20 mm, corresponding to the size of two unit cells of the textile reinforcement. Permeability values in *x* direction have no evident correlation with permeability values in *y* direction.

Keywords: Fabrics/textiles (A), Permeability (B), Anisotropy (B), Resin Transfer Moulding (RTM) (E), Statistical methods (C)

Introduction

Porosity (ϕ) and permeability (K) are material properties required to characterise flow behaviour through fibrous media based on the volume-averaging method [26], [27], described by the volume averaged continuity equation and momentum balance for creeping flow of a single fluid phase which is Darcy's equation (Eq. 2-1).

$$\frac{\delta(\phi\rho)}{\delta t} = -\nabla.(\rho v) \; ; \; v = \frac{K}{\mu}.\nabla p \qquad\qquad (\textbf{2-1})$$

where v is the (volume-averaged) superficial velocity, ρ is the density, μ is the viscosity and *p* is the (volume-averaged) pressure. Porosity and permeability vary continuously with the location within the mould [28][29][30]. Several researchers pointed out that spatial

variations in the local permeability originate in the spatial micro-level variations of the reinforcement geometry [31] [32] [33][34] [35]. Therefore, when establishing models for flow simulations, an understanding of the spatial distribution of local permeability and its effect on global permeability is necessary. Pan *et al.*[36] experimentally determined permeability values and concluded that global permeability is very well approximated by the arithmetic mean of the series of measurements on the global scale, assuming a normal distribution as the probability distribution function of such measurements. This was experimentally supported by Hoes *et al.*[15]. However, the statistics of global scale measurements does not represent directly the statistics of the local micro-scale variations. The distribution of local properties needs to be involved in determination of these local variations.

Spatial variations of permeability attracted attention of researchers in the last two decades. For a stochastic simulation of 1D non-isothermal mould filling, Padmanabhan and Pitchumani [16] assumed the random permeability as one of the uncertain input parameters. Unlike Pan *et al.*[36] and Hose *et al.*[15], they assumed a lognormal distribution for permeability and a normal distribution for porosity. They showed how uncertain material parameters, in fabric and resin alike, can combine in such a way as to reduce process output variabilities. Sozer [37] applied uncorrelated local random permeability in 2D flow simulation to observe the effect of textile reinforcement non-homogeneity on mould filling. In this case, permeability variations are not locally confined by a correlation function. He observed that uncorrelated local variations of permeability up to ±35% have insignificant effects on the mould filling but that if the variations happen in a correlated way, they have a more significant effect on the mould filling. To compare the effects of uncorrelated and correlated local permeability on global permeability, Desplentere *et al.*[38] divided a fibrous medium model into number of square zones (see Figure 2-7). They assigned the local permeability for each zone in the principal flow direction in two ways: (i) an uncorrelated normal distribution of permeability (ii) assigning the local permeability in a correlated way, limiting permeability variations between adjacent zones by a correlation function. They demonstrated that uncorrelated approach leads to a strong dependency of the scatter of the global permeability on the size of the discretised zones; hence the uncorrelated approach is not physical. The correlated approach was free from the discretisation size effect, and gave scatter predictions consistent with those found in [15] [39].

It is obvious that the local permeability variations are determined by the variations of the local textile geometry. Parseval *et al.*[39], modelling permeability variations introduced by the presence of dual-scale flow, proposed that the spatial harmonic mean of the local permeability values can properly represent the average global permeability. However, they accounted only for variations of intra-yarn permeability based on the aspect ratio of yarns cross sections, neglecting the effect of yarn spacing and distortions of the yarn centrelines. Lundstrom *et al.*[40] calculated inter-yarn permeability at meso-level (unit cell) textile from the dimensions of flow channels with variable gap size between fibre bundles. The results showed that with uncorrelated random distribution, global permeability decreased with the maximum gap size at mesoscale level. Meanwhile for a correlated distribution, global permeability could either increase or decrease depending on the type of deviations such as bundle dimension and bundle centroid distances as compared to an ideal unit cell.

The results of their study allowed them to include the local randomness in ordered fabrics such as non-crimp stitched fabrics. Wegh *et al.* [41] predicted permeability at mesoscale by employing unit-cell model associated with local variabilities due to shear angle, and compression and, subsequently, they carried out 3D flow simulations. However, the unit-cell model was simplified to a brick-model with a rectangular cross section, which does not adequately represent a real fabric. Loendersloot and Akkerman [42] employed internal geometry variations induced by the distortion of yarns in their analysis of the inter-yarn permeability variations of non-crimp fabrics. They found that both the amount of the variation and the spatial distribution of a fabric need to be taken into account for a proper representation of permeability variations. Both Vanaerschot *et al* [20]–[24] and Gommer *et al.* [43] studied the internal geometry variations of a 2/2 twill carbon fabric and identified a significant difference in warp and weft yarn gaps which will lead to spatially distributed permeability.

The experimental determination of spatial variations of permeability is a challenge. This property is inferred from a flow experiment in which fluid is injected into a fibrous medium [13] [14]. Determination of the average permeability thus involves the solution of an associated inverse problem using flow front position (*x*) data and Darcy's equation. These experiments, being made on a global scale, do not give access to local permeability values. Transient variations of the flow front speed, which are connected to the variations in local permeability, are not measured with the precision enough to clarify the differences of the permeability after the solution of the inverse problem.

Permeability can be estimated by empirical correlations with geometrical parameters of the porous media. Zhang *et al.*[44] used the Kozeny-Carman equation (Eq. 2-2) for the local permeability of a random fabric based on the continuum statistics.

$$K = \frac{r_f^2}{4k_c} \frac{\phi^3}{(1-\phi)^2}$$

$$k_c = C\tau^2, \tau = \frac{L_e}{L}$$

(2-2)

where k_c is the Kozeny constant, τ is tortuosity which is defined as the ratio of the effective average path length in a porous medium (L_e) to the shortest distance measured along the direction of the macroscopic pressure gradient (L) , C is a proportionality constant and r_f is the mean radius of circular solid fibres with the same specific surface area [45]. The constant k_c was experimentally determined by several authors for different fabrics, and there is an important discrepancy in results for different fabrics, fibre configurations, porosity values and the fluids used for impregnating [46] (Table 2-1).

Table 2-1: Kozeny constant k_c, experimental values

References	Fibrous media types	k_c	
		Transverse flow	Longitudinal flow
Lam and Kardos [47]	UD* Hercules AS-4 graphite	11	0.35-0.68
Gebart [48]	UD Ahlstrom R12-256	8	1.66-1.78
Gibson *et al.* [49]	UD Roving glass fibre (PPG Hybon 764)	8	1.06
Williams *et al.*[50]	Silane glass, Strach glass, carbon and nylon	0.1-0.8	
Lindsay[51]	Paper	3-7	
Muzzy *et al.*[52]	Random glass mat PPG	7.6	

* UD = unidirectional

Alternatively, as resin flow in RTM is a creeping and incompressible flow of a Newtonian fluid, permeability can be determined by a numerical solution of Stokes equation for flow through a unit cell of the textile reinforcement (inter-yarn flow). The first challenge for this method is that fibrous media need to be reconstructed in such a way as to mimic closely the real textile reinforcement in composites. Lundstrom [53] constructed a geometry model of non-crimp stitched fabrics at unit-cell scale. However, in his work, permeability, as predicted from the model, had a substantial deviation from experiments, because the cross-section area of yarns was assumed to be uniform and rectangular. Similarly, Yu and Lee [54] developed a unit cell with rectangular channel cross-section and aligned yarns. To describe the internal geometry of textile reinforcements at unit-cell scale, a number of tools are available. One of the most common tools is the WiseTex, developed at KU Leuven. To solve Stokes equations on the unit cell level, meso-scale simulation tools has been suggested [55][19]. This requires that the permeability prediction on unit cell level is sufficiently fast to be coupled with a macro-scale software tool for mould filling simulations. Verleye *et al.*[56], [57] developed FlowTex tool, which enables solution of the Stokes equation by a finite difference discretisation on unit cell level. Swery *et al.*[58] showed that FlowTex predicts similar permeability values as compared to a commercial Computational Fluid Dynamic (CFD) software, the Ansys CFX. This works demonstrated that, given an accurate geometrical model, a CFD solver can provide prediction of permeability values with a precision within the typical experimental scatter. Hence state-of-the-art numerical predictions of permeability can be a basis for simulating its variability, determined by the geometrical variability of the reinforcement.

This paper builds on the previous work of Vanaerschot *et al*. [20]–[24] in which a virtual geometry of a 2/2 twill carbon fabric was used to mathematically represent the internal geometry variations including yarn spacing, width and thickness and distortions of the yarn centrelines on the variations of permeability at meso-level (unit cell) textile. This virtual geometry is used as the basis for calculation of the local permeability values. The latter is done with the FlowTex software [25]. Permeability is characterised by the mean permeability value, the variance, which shows the range of variability for permeability data and correlations of the random permeability field; the statistics of the permeability values is compared with the statistics of the fabric geometrical parameters. The improvement we aim to bring to the field is the in-depth understanding of the statistics of the components that ultimately form the compound/emerging statistics of macro-scale permeability. We believe that this study, which is more fundamental, will ultimately lead to applications such as enabling better stochastic models of LCM, better understanding of the importance of fabric architecture or compaction on permeability variation (which can lead to different

fibre architectures, design guidelines, etc), as well as other applications and studies which we do not yet anticipateModelling of local variations of permeability: a road map

An approach to study local variations of permeability of a 2/2 twill carbon fabric is to define unit cells over the fibrous media and subsequently predict permeability of each unit cell. This creates a discrete random field of permeability values. The effect of internal geometry variations on permeability can be then examined. The major steps in this process are summarized in Figure 2-1: (1) building a virtual geometry of a fabric sheet with geometrical variations adequately representing the experimentally observed ones (this step for the studied fabric is done in [19]–[24], [59]); (2) extraction of the individual unit cells from the virtual sheet; (3) calculation of the unit cell permeability values and (4) evaluating the statistics of the created discrete random probability field (steps 2-3 are introduced in the present paper.
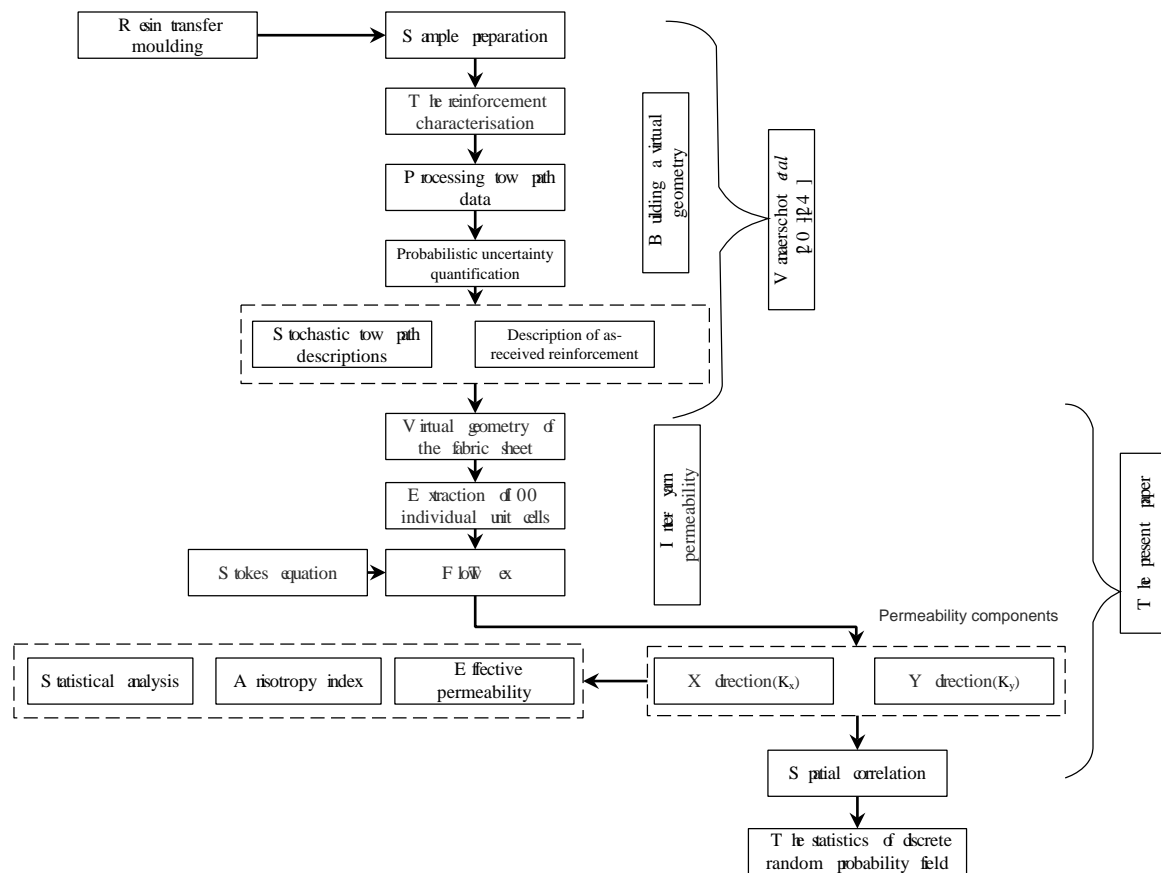

Figure 2-1: Framework of the uncertainty evaluation of permeability

2.1   Methods

2.1.1   Material

Table 2-2 shows the specifications of the fabric under analysis. One ply of the fabric was impregnated with a Biresin epoxy resin system.

Table 2-2: Specification of the textile in the experimental composite sample[20]–[24]

Fabric				Yarn	
Style	Weave pattern	Areal weight (gm^{-2})	ends /picks count, yarns/cm	Average fibre diameter (µm)	Number of fibres
280T	2×2 twill	280	3.5	7	6000

The impregnated fabric is shown in Figure 2-2a. The region of interest (115×115 mm^2) containing 10×10 repeats of the twill weave is shown as the red square zone in Figure 2-2a. The in-plane centroid of a yarn has a deviation from a straight line over the sample. The blue dots in the image (Figure2-2a) represent the in-plane yarn path, obviously deviating from the straight dashed line.

2.1.2   Generation of the virtual geometry

The detailed descriptions of fibrous media architecture, including geometric properties such as fibre diameter, fibre waviness, and yarn paths are required for reliable numerical simulation of fluid flow in fibrous media. Such a geometric model (Figure,2-2b Right), which closely mimics the woven 2×2 twill carbon fabric sheet, was developed by Vanaerschot *et al* [20]–[24] based on the spatial random fluctuations of the yarn paths. This virtual geometry contains one hundred unit cells. A unit cell (Figure2-2b, Left) is formed by four equally spaced warp yarns and four equally spaced weft yarns, yielding a unit cell size of $11.55 \times 11.48 \times 0.291$ mm^3. The virtual textile model (Figure2-2b, Right) was generated in a geometrical format, compatible for WiseTex [21]. Note that the virtual sheet geometry does not represent one-to-one the real fabric sheet geometry, but has the same statistical characteristics (mean and dispersion of the geometrical parameters and spatial correlation functions). The reader is referred to [21] for details of the virtual geometry creation. The virtual sheet geometry statistically represents a single ply within a laminate. As already pointed by [21], inter-ply influences have a limited contribution to the in-plane centroid path which allow one to apply the in-plane centroid data of single-ply to construct the in-plane position of a virtual sheet geometry for one ply within a laminate.
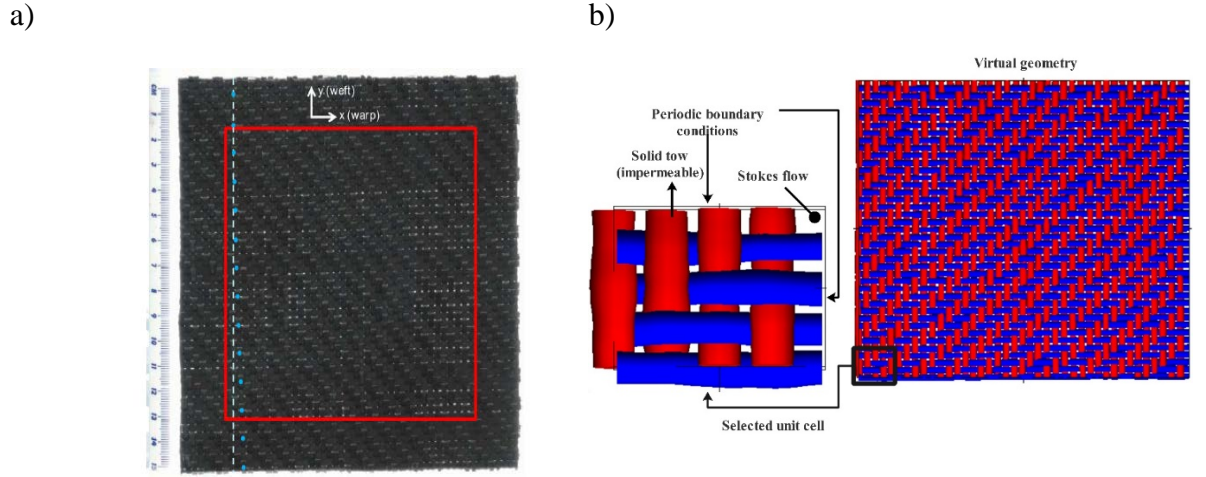
a)   b)

Figure 2-2: Impregnated twill 2x2 carbon fabric sheet [21] (a) Optical scan, (b)WiseTex representation of a virtual geometry (Right), spanning a region of 10×10 unit cells. Selected unit cell from the virtual geometry (Left).

2.1.3   Extraction of unit cells

One hundred unit cells are extracted from the virtual geometry, parameters of which are stored in an XML file; the structure of the file is described in [25]. This XML file (called "universal" below) contains 40 yarns in warp direction and 40 yarns in weft direction. Each yarn in the virtual geometry is divided into 320 segments, and 32 segments of each yarn cross section is the boundary of the segments. To extract the information of one unit cell, we read eight main items and 33 sub items of each main item from the universal XML file. The new ("local") XML file contains information of yarns of a unit cell, with the yarn path coordinates kept in the global coordinate system. The next step was to fit the box surrounding the extracted unit cell. To do so, first we transferred yarn path coordinates to the local coordinate system, centred in the centre of the unit cell and subsequently calculate the size of box to fit the unit cell. This results in a "local" XML description in a format readable by WiseTex. With a help of a Matlab script this procedure is applied to all 100 unit cells in the universal geometry, resulting in 100 WiseTex models of the local unit cells.

2.1.4   Local permeability calculation

The multiscale nature of the porous medium leads to both intra- and inter-yarn values for permeability. However, as was stated earlier, the goal of this paper is to provide a description of the statistics of permeability due to the inter-tow gap variations. This approach provides both a first insight into the statistics of the spatial distribution of permeability and a rough estimate of the overall permeability of the fabric. Models which consider impermeable tows can significantly underestimate global permeability particularly at high fibre volume fractions. However, the incorporation of the intra-yarn flow, where a tow contains 6K filaments for the current case study, in a prediction of the permeability components significantly increases computational time. Belov *et al.*[55],

Wang *et al.*[60], Nabovati *et al.*[61], Nedanov *et al.*[62] reported the difference in the computed global permeability of woven fabrics for the cases of permeable and impermeable tows to be lie in the range 10…30%. This difference justifies single-scale porosity (impermeable tows) is acceptable because standard deviations of 20-30% are usual for experimental results, where the difference of maximum and minimum values is one order of magnitude[15][63][13]. The current study takes into account the influence of mesoscale variability due to the gap variations among tows (inter-tow porosity, neglecting intra-tow porosity) on the statistics of permeability. Consequently, a prediction of the magnitude of mesoscale variability on the scatter of permeability allows a contribution to mould filling simulation and the optimisation of composite manufacturing process.It is noted that a spatially varying permeability field for a single layer of fabric will be observed in this paper. The next study will impose random fluctuations on the parameters that will define in this study, and the permeability field for a multi layer sample will be found through a numerical stacking process. The influence of nesting will be accounted by random variation in layer placement, this process being repeated several times to construct the statistics of the multilayer permeability response. The long term goal of this work is to more clearly establish the link between spatial variability in compaction response and permeability, and better understand their influence on processing.

For a given unit cell model (Figure 3b,the selected unit cell), the principal components of the permeability tensor in Cartesian coordinates, K_x and K_y, corresponding to the principal fabric axis are determined solving the Stokes equations with appropriate boundary conditions [57]. The boundary conditions in the thickness direction are periodic, hence the solution represents permeability of a thick laminate made of the fabric. In this solution the yarns are assumed solid and intra-yarn flow is neglected (Figure 3b,the selected unit cell). The calculated permeability corresponds to saturated flow conditions. After K_x and K_y are calculated, the average effective permeability, K_{eff}, is calculated as (Eq. 2-3) [54] [64].

$$K_{eff} = \sqrt{K_X K_Y} \hspace{4cm} \text{(2-3)}$$

To do permeability calculations, unit cells were loaded into WiseTex software [65] and then a geometric format, which is compatible for FlowTex [66], was generated. FlowTex was used to compute inter-yarn permeability of each virtual unit cell, neglecting intra-yarn permeability, in both x and y directions. Due to memory limitation, a voxel size of $0.04 \times 0.04 \times 0.03$ mm^3 was used, giving 743904 voxels in the unit cell. A finite difference Stokes solver of FlowTex is used to determine the inter-yarn permeability. The Stokes solver, which employs a Chorin projection method on a staggered grid, needs about 30 s for the simulation of one dimension, in a total of about 60 s for both dimensions for each unit cell.

2.1.5   Statistics

The sample size is important to make some statistical inferences from the sample. Therefore, it is necessary to find the minimum sample size (*n*) for the statistical analysis of permeability. The minimum sample size with unknown population is computed by Eq.4 [67]:

$$n = \frac{z^2 \sigma^2}{e^2} \tag{2-4}$$

where z is *z-score* at a 95% confidence interval, which is 1.96, σ is standard deviation, e is confidence interval. Although there is a significant difference between our case (permeability of one ply at unit cell level) and other reference experimental reports of permeability (the latest permeability exercise[13] (K_{bx}[2] and K_{by}) and Hoes *et al.*[15] (K_{hx}[3] and K_{hy})) we used their statistics to estimate the initial sample size (Table 3).

<p align="center">Table 2-3:The minimum sample size</p>

Sampling variables	K_{bx} [13]	K_{by} [13]	K_{hx} [15]	K_{hy} [15]
z	1.96	1.96	1.96	1.96
z^2	3.84	3.84	3.84	3.84
σ	17.7	28	40	30
σ^2	313.29	784	1600	900
e	25	30	80	77
e^2	625	900	6400	5929
n	48	100	77	45

From Table 3, it is observed that n is not same for the permeability components due to the higher scatter of the one direction compared to the other one. Essentially, the larger sample size more accurately reflects the statistics of permeability. Therefore, the minimum sample size of one hundred (100), would be distributed more closely to the mean value.

Permeability components, K_x and K_y, results from the analysis of 100 unit cells are subjected to statistical analysis. First, histograms of the data were generated to clarify whether they follow specific distributions. The Kolmogorov-Smirnov Statistic (KSS) was then used to test the data sets for normality based on P-values (Acknowledging that, if KSS test P <0.05, then there is significant probability of deviation from normality). It should be noted that KSS test is a nonparametric statistic, since it does not assume a specific type of a distribution. To graphically assess the goodness of fit of the potential distribution models determined from KSS test, Q-Q plots, Q stands for quantile, are generated. The anisotropy index (α) and the effective permeability (K_{eff}) are also subjected to statistical analysis. Histograms of α and K_{eff} which are calculated from the knowledge of K_x and K_y and normal, lognormal, and logistic statistical distribution models are fit to find the most appropriate distribution model.

For comparison, the data of the latest permeability exercise [13], which followed a jointly developed common experimental method [14] in order to foster data agreement is analysed.

Since permeability varies continuously because of the spatial geometrical fluctuations of a fabric, it can be regarded as a local variable [68]. Random field theory can be used to characterise the spatial variability [69].

---

[2] superscripts of bx and by represent the permeability components of benchmark II [13] in x and y directions, correspondingly.

[3] superscripts of hx and hy represent the permeability components of [15] in x and y directions, correspondingly.

A semivariogram function γ(h), as a function of lag distance ($h(x,y)$) (h is a vector which have both magnitude and direction), is used to characterise the spatial variability of the permeability field. This function (Eq. 2-5) allows the determination of the correlation between two observations K(z) and K(z+h) at two distinct locations z and z+h:

$$\gamma(h) = \frac{1}{2N(h)} \sum_{i=1}^{N(h)} (K(z_i) - K(z_i + h))^2$$

(2-5)

where z(x,y) represents the coordinates of a point in 2D space, N(h) is number of experimental pairs of points at the lag distance h. Based on the semivariogram plot, an exponential spatial correlation model (Eq. 2-6) is fitted:

$$\gamma(h) = c_0 \left[1 - \exp(-\frac{h}{a_0}) \right]$$

(2-6)

where c_0 is the maximum semivariogram value ($\lim_{h \to \infty} \gamma(h)$), a_0 is the maximum lag distance over which pairs of data points are no longer correlated.

2.2 Results and discussion

2.2.1 Permeability distribution

The descriptive statistics of permeability components, K_x and K_y, are shown by histograms with boxplots, as shown in Figure 2-3: Figure 2-3 shows the statistical graphics of permeability components, K_x and K_y: the permeability data obtained from 0×10 repeats of the twill weave, 100 observations for each direction.
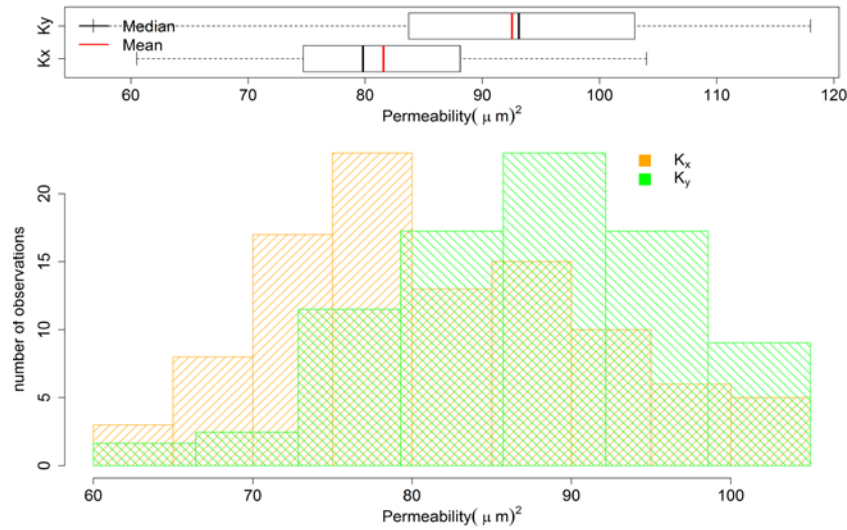
Figure 2-3: The descriptive statistics of permeability components. Below: Histograms of permeability. Kx in orange bins and Ky in green bins. Top: The boxplots of the permeability data with whiskers

The comparison of the two histograms shows that the mean value of K_y (92.5 μm^2, Figure 2-3, orange dashed line) is greater than that of K_x (81.5 μm^2, Figure 2-3, green dashed line) as shown in Figure 2-3 (below). The visual inspection of Figure 3 (below) also shows that the range of permeability variation in x direction is almost equal to that of y, ranging from *circa* 60 to 120 μm^2. However, the number of observations of permeability values quite frequently lie between 75and 80 μm^2 for x direction (Figure 2-3 (below), in orange bins), while between 90 and 100 μm^2 for y direction (Figure 2-3 (below), in green bins). From these statistical information, the minimum sample size using Eq.2-4 was estimated for the permeability components; n_{Kx} =20 and n_{Ky} =30. Hence, the selected sample size can adequately represent the statistics of permeability components.

The symmetry and the tail length of the two data sets are assessed by boxplot as shown in Figure 2-2 (top); K_y appears to have larger variability than K_x. The median (the black line in Figure 2-2 (top)) of K_x (79.8 μm^2) is slightly smaller than the mean of K_x, and hence the K_x data is skewed to the right. Meanwhile the median (the black line in Figure 2-2 (top)) of K_y (9.31 μm^2) is slightly larger than the mean value of K_y, and hence the K_y data is skewed to the left. From Figure 2-2 (top), it is observed that the boxplots of the two data sets show long tails (the dashed lines); the length of the whiskers far exceeds the length of the boxes.

For the skewed distributions, one common model is the lognormal distribution[44][16][70][29]. Despite this, others reported that the permeability of two-dimensional heterogeneous fibrous media is well approximated by the normal distribution [36][15][71][72] and they addressed the skewness in permeability due to local inhomogeneity resulted from nesting and the waviness of the fibre yarn paths. Although the distribution of permeability measurements might be described with these two distributions it is always important to choose the most appropriate.

These two data sets are subjected to Kolmogorov–Smirnov Statistic (KSS) test for normality in terms of both normal and log-normal distributions. The KSS analysis are listed

in Table 2-4. K_x in comparison with K_y gives higher P-values for the assumption of lognormal distribution compared to normal distribution assumption. Based on this information, shown in Table 2-4, it seems that both lognormal and normal are possible distributions.

Table 2-4: Results of Kolmogorov–Smirnov statistics (KSS) analysis

Permeability components	K_X, µm²		K_y, µm²	
Hypothesis	Normal	Log-normal	Normal	Log-normal
Mean	81.5	-1.09	92.5	-1.03
Standard deviation	10.1	0.053	13.9	0.068
P-value	0.44	0.77	0.94	0.59

While identifying data as normal or lognormal in KSS test may be less clear, one can help clarify the closeness to the expected bell shape by Q-Q plot of permeability predictions, and assessing their fit by comparing the original and logarithmic scale versions of these plots. Figure 2-4 shows Q-Q plot of the original and log-transformed data of K_x and K_y. In case of original data and transformed data of K_x, the plots closely fit the Gaussian model (points are inside the 95% interval dashed curves). Although in case of original data of K_y, the plots closely fit the Gaussian model, for transformed data of K_y, a few points are outside the 95% interval dashed curves. In summary, Table 2-4 and Figure 2-4 provide support for the hypothesis that the statistics of permeability presents a normal-type distribution.
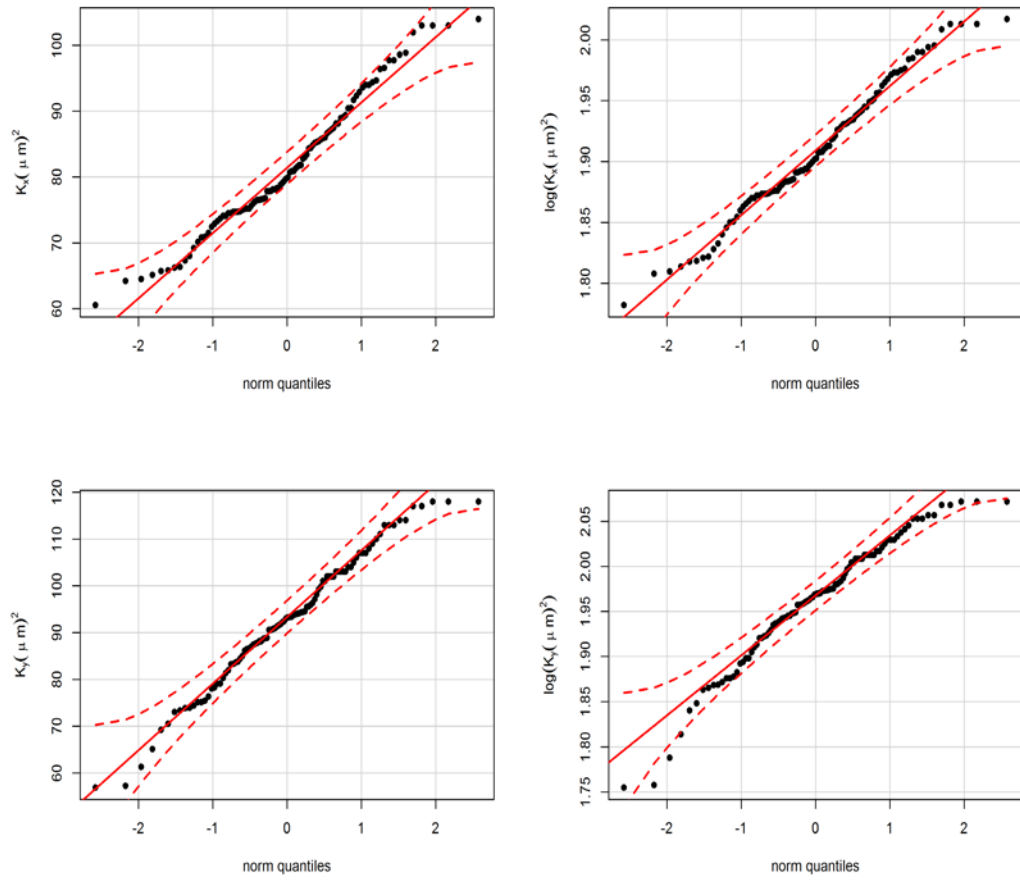
Figure 2-4: Q-Q plots of permeability data of Kx (top) and Ky (down) fit in a normal (left) and a lognormal (right) distribution. The broken lines for the plots indicate the 95% confidence interval for the Kolmogorov-Smirnov statistics.

To evaluate the distinguishability or the compatibility of the two data sets (K_x and K_y), two-dimension Kolmogorov–Smirnov method (KSS) test based on Empirical cumulative distribution function (ECDF) was applied.
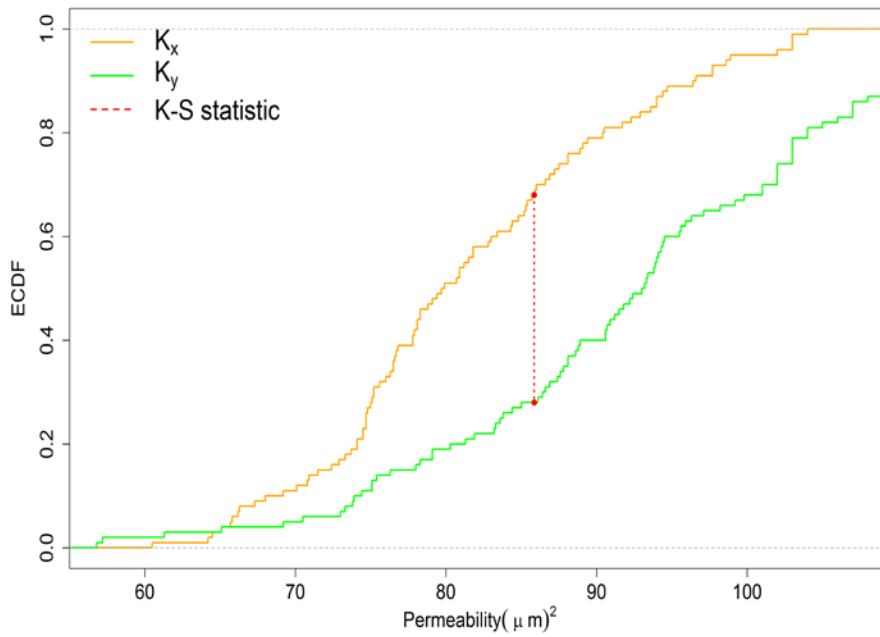
Figure 2-5: Two-sample Kolmogorov-Smirnov statistic. Orange (Kx) and green (Ky) lines each correspond to an empirical cumulative distribution function (ECDF)

Figure 2-5 shows the KS distance (red dashed line), which is based on the maximum distance between these two curves. It is observed that the two curves are not compatible and have a distance of 0.42. The KS test is associated with a p-value of 4.3×10^{-8} suggesting that the distributions are significantly different from each other. This is also confirmed by Figure 6 in which K_x and K_y are not same for a specific unit-cell inter-yarn porosity fractions (ϕ). Figure 2-6 also shows the variations of the inter-yarn permeability values in both x and y directions as a function of unit-cell inter-yarn porosity fractions (ϕ). From Figure 2-6, the positive correlation coefficient between inter-yarn porosities and permeability components is evident, albeit weak. Note that 4% change of the inter-yarn porosity leads to1.5 times change of permeability, and hence the correlations $R^2=0.145$ and 0.03 for x and y directions, respectively, considered weak may be actually significant.

For a better understanding of the correlation between permeability components and inter-yarn porosity, the binning technique was used. This technique smooths an arranged data value by consulting the values around it. The arranged values are grouped into a number of bins. Therefore, the porosities values and the corresponding permeabilities was grouped into equal-frequency bins of size 10 (i.e., each bin contains 10 porosity values). Then, each porosity value and the corresponding permeability in a bin was replaced by the mean value of the bin. Figure 2-6 shows the white-triangle symbols and black-square symbols for x and y directions, respectively, which were generated by the binning technique. Comparing the means of each bin in x direction with the means of each bin in y direction shows the higher correlation for x direction due to additional variance from tow spacing in the weft direction.
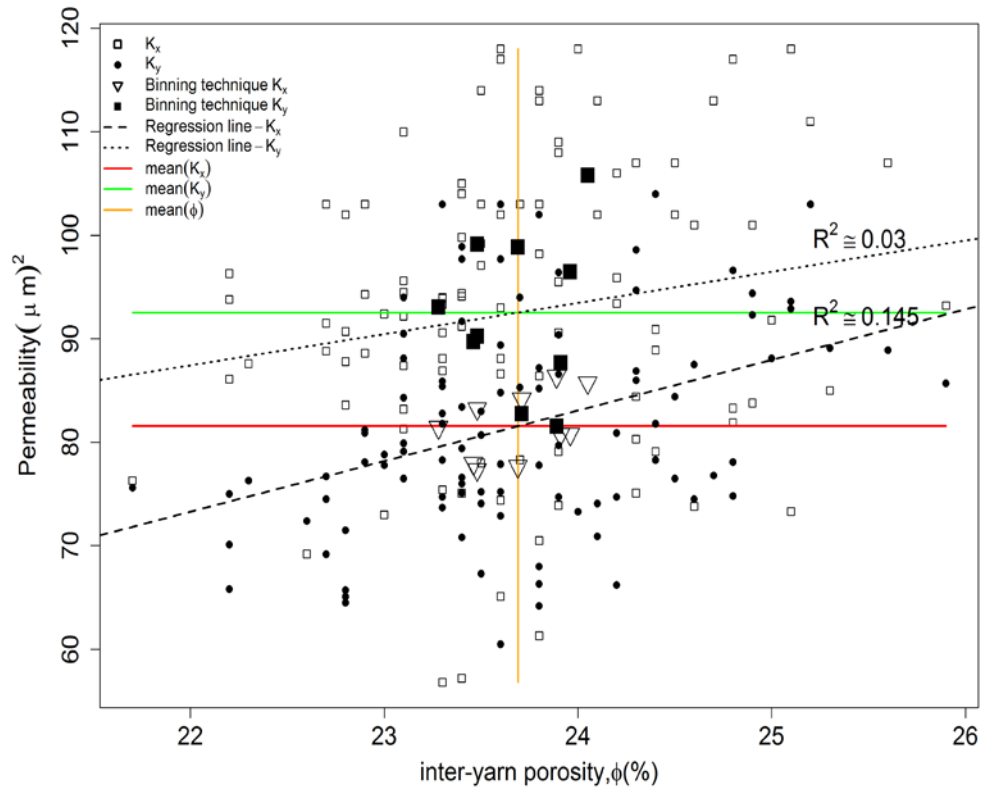
Figure 2-6: Correlation between the permeability values and inter-yarn porosity

In order to visualize such a variation as moving from a unit cell to the neighbouring one, it is helpful to represent the spatial distribution of permeability.

100 permeability values (K_x and K_y components) of individual unit cells are plotted in a "heat plot" in Figure 2-7, where the value of each colour is corresponding to the permeability of one specific unit cell in a given direction. From Figure 2-7, it is observed that K_x and K_y values for each unit cell are not the same; for example, for the unit cell located in the lower left corner, the K_x and K_y were 94 and 78 μm^2, respectively, and continuously varies over the considered area. In this sense, the fibrous medium shows permeability anisotropy, meaning permeability in x direction is not the same as that of y direction. Each direction has a different response to a fluid flow, leading to different flow velocities.
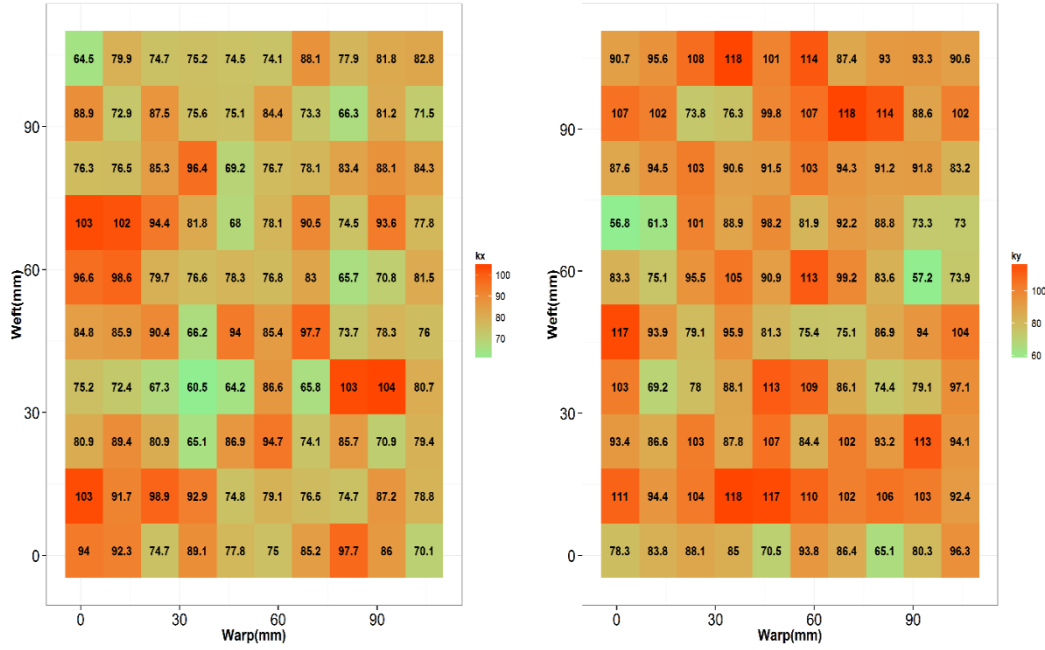
Figure 2-7: The spatial distribution of permeability components, *Kx* (left) and *Ky* (µm)2 (right).

To find whether or not there exists correlation between permeability values for the two directions over the fabric sheet, K_x is plotted against K_y as shown in Figure 2-8, left. The visual inspection of Figure 2-8, left, shows the majority of the data (68 out of 100 pairs of K_x and K_y) is populated in the regions of 1 and 2 where K_x and K_y have negative correlation. However, there is no clear correlation between K_x and K_y. This may be explained by alterations to the fabric geometry along the gaps formed between the fibre yarns. The plot of the gaps components (width w_{gap} in warp direction or x and height h_{gap} in weft direction or y) are shown in Figure 2-8, right. The width of the gaps w_{gap} 2-2.5 times larger than the height of the gaps. Therefore, the width and the height fluctuations respectively in x and y-directions result in an unequal distribution of permeability in y and x-directions, causing anisotropic permeability.
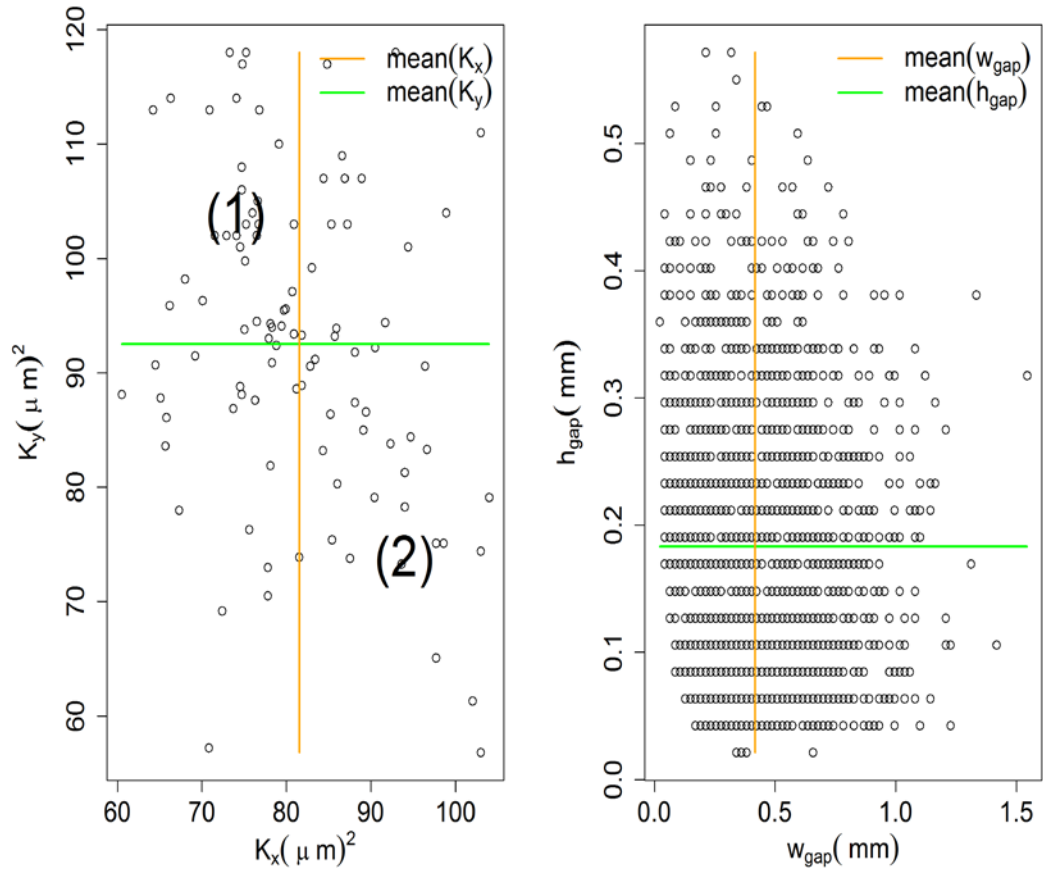
Figure 2-8: Correlation between *Kx* and *Ky* (left) and wgap and hgap (right)

The histogram of the anisotropy index $\alpha = K_y/K_x$ [15] is shown in Figure 2-9. Figure 2-9 shows the normal density overlie the histogram (Figure 2-9 left), and the Q-Q plots (Figure 2-9 right) closely fit the Gaussian model (points are inside the 95% interval dashed curves). Hence, the anisotropy index follows the normal distribution and ranges between 0.4 and 1.8. The anisotropy index is quite frequently lies between 1and 1.2. The standard deviation of anisotropy index is 20% of the mean anisotropy index, which is close to the value of 25% reported by Hoes *et al.*[15] for a balanced glass woven fabric. This similarity is not trivial, as our calculations represent variability of local values in one fabric sheet, but measurements [12] give variability of the global permeability between different laminates.
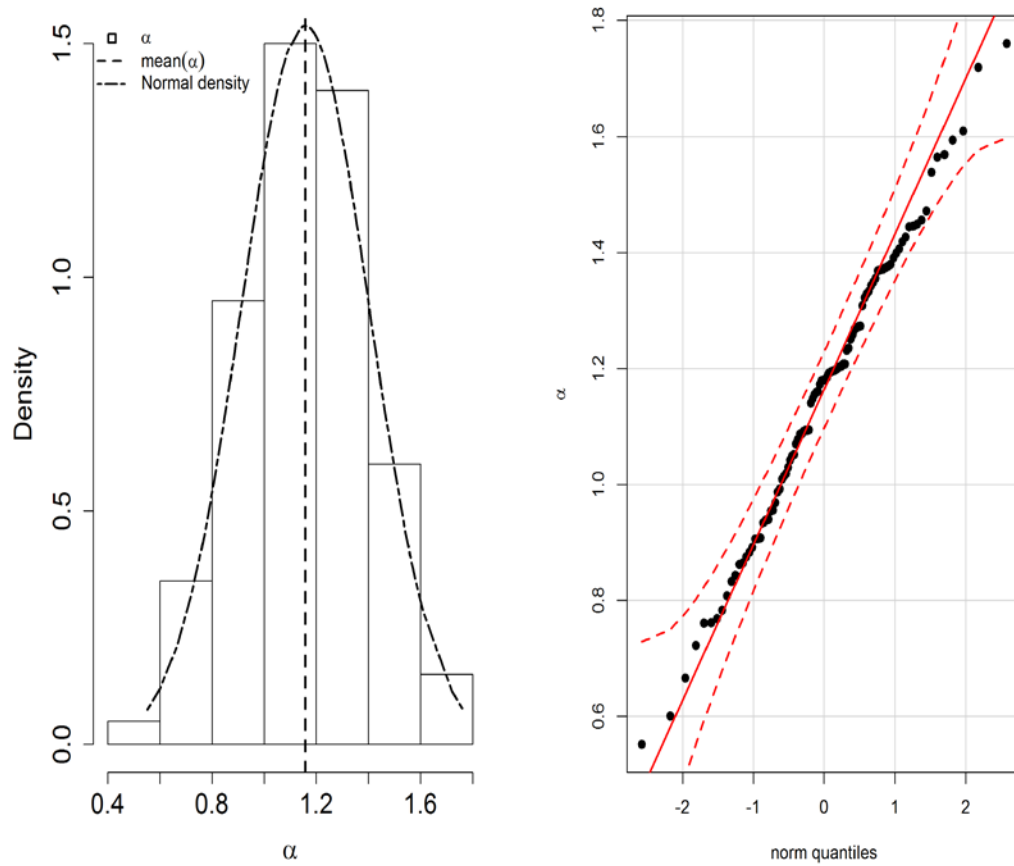
Figure 2-9: Distribution of the anisotropy index. Histogram (right) and Q-Q plot(left)

K_x and K_y in an anisotropic medium can be converted to an average effective permeability (Eq. 2-3). An appropriate distribution for K_{eff} is assessed by plotting data histograms of the effective permeability, and assessing their fit by comparing the original and logarithmic scales versions of these plots. Figure 2-10, shows both original (left) and log-transferred (right) histograms of this data.
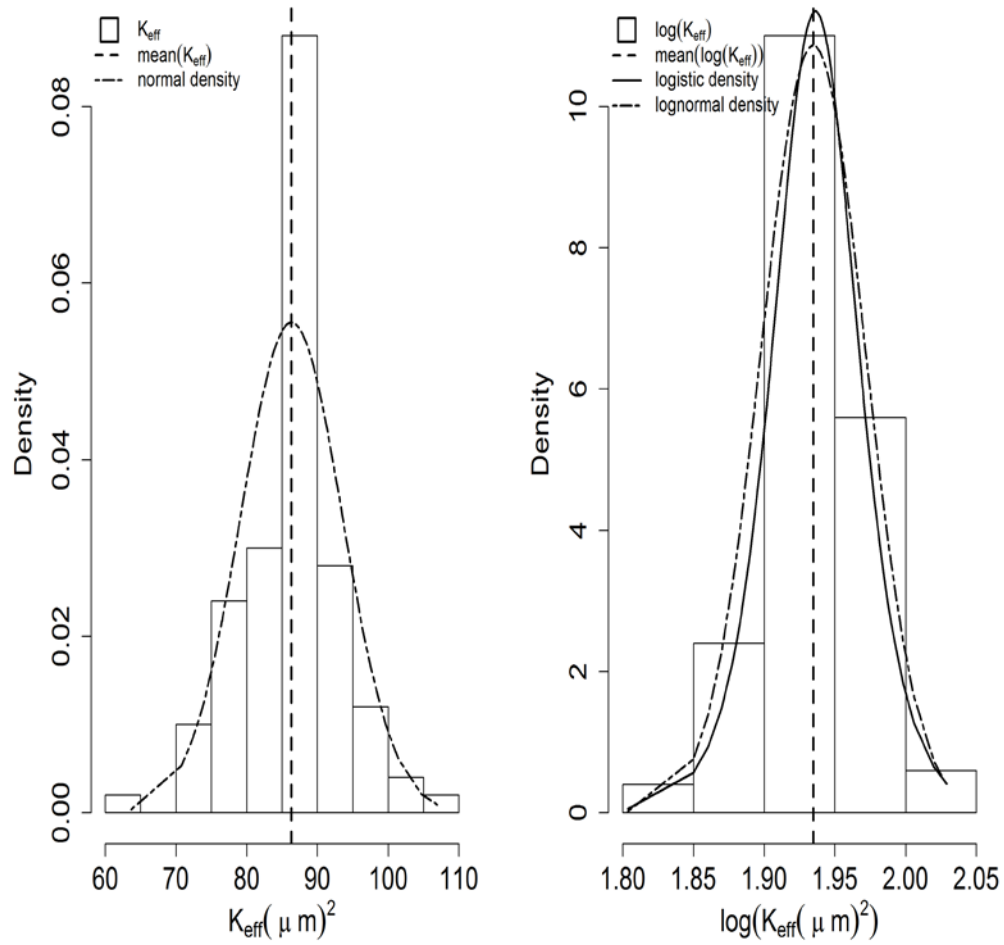
Figure 2-10: Histogram of the effective permeability: Original data (left), transformed data(right)

One can observe that the Gaussian model fails to fit in original scales (Figure 2-10 left), while in the transformed scale the lognormal and logistic model yield good fits (Figure 2-10 right). To find which of these distributions gives better fit to the data, the data is subjected to KSS test. The D_{KSS} computations are listed in Table 2-5. The logistic takes the highest P-values and the smallest D_{KSS}. Based on this information, shown in Table 2-5, we conclude that the logistic distribution provides the best fit.

Table 2-5: Kolmogorov–Smirnov statistics (KSS) and corresponding p values of K_{eff}

Effective permeability	K_{eff}		
Hypothesis	Normal	Log-normal	Logistic
Mean	86.3	1.93	81.5
Standard deviation	7.18	0.036	13
D_{KSS}	0.08	0.066	0.05
P-value	0.44	0.77	0.94

2.2.2   Spatial correlation

The semivariograms, characterization of spatial correlation, from the permeability data are shown in Figure 2-11 as discrete points using Eq. 2-5. The scatter plots (Figure 2-11) show fairly typical semivariograms. An exponential spatial correlation model was fitted to the scatter plots by a nonlinear-mixed effects methods, incorporating fixed and random effects [73]. Table 2-6 gives the exponential model parameters for both K_x and K_y.

Table 2-6: Exponential semivariogram model parameters

Variables	a_0(mm)	c_0
K_x	17.8	0.0153
K_y	19.4	0.0253

The semivariograms of K_x and K_y increase with lag distance, which refers to the discretisation step of 11 mm, (e.g. decreasing correlation) and despite considerable scatter, γ, describing the degree of spatial correlation of a spatial random field, levels off at a distance lag of *circa* 20 mm, corresponding to two unit cells. (Figure 2-11), which is called sill. Comparing the sill in x direction with the sill in y direction shows the higher sill for y direction: indicating an additional variance from yarn spacing in the weft direction (Table 2-6). This suggests larger permeability variability in y direction over shorter distances compared to x direction. This is confirmed by the high coefficient of variation obtained for K_y (Table 2-4). The semivarograms estimated for both K_x and K_y corroborate spatial correlation.
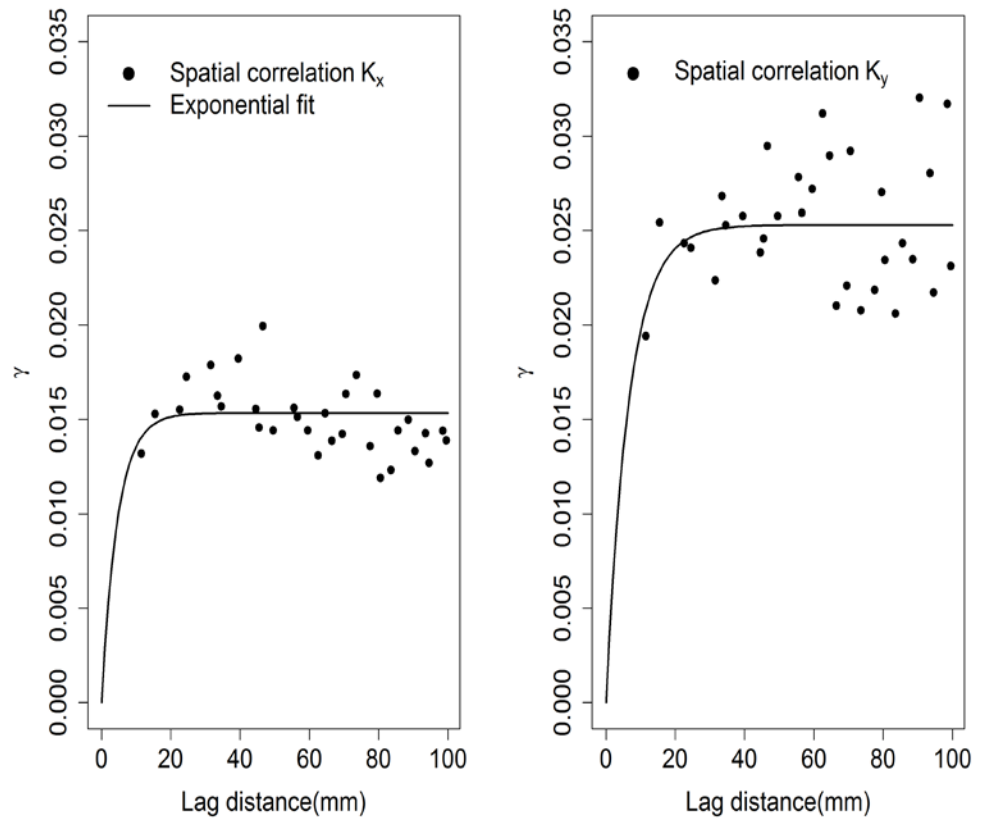
Figure 2-11: Semivariogram function for permeability components

Since the correlation length depends on the dimension of yarn spacing, there might be a link between this dimension and the permeability of fabric. Using Eq. 2-6, the correlation function was plotted for the gap area (Figure 2-12). Through the gap area data an exponential spatial correlation model (Table 2-6) was fitted resulting in a distance lag of *circa* 21 mm. This corresponds to seven yarn-space centerlines (*circa* 3 mm) or two unit cells. These results are consistent with the observations by Desplentere *et al.*[74].
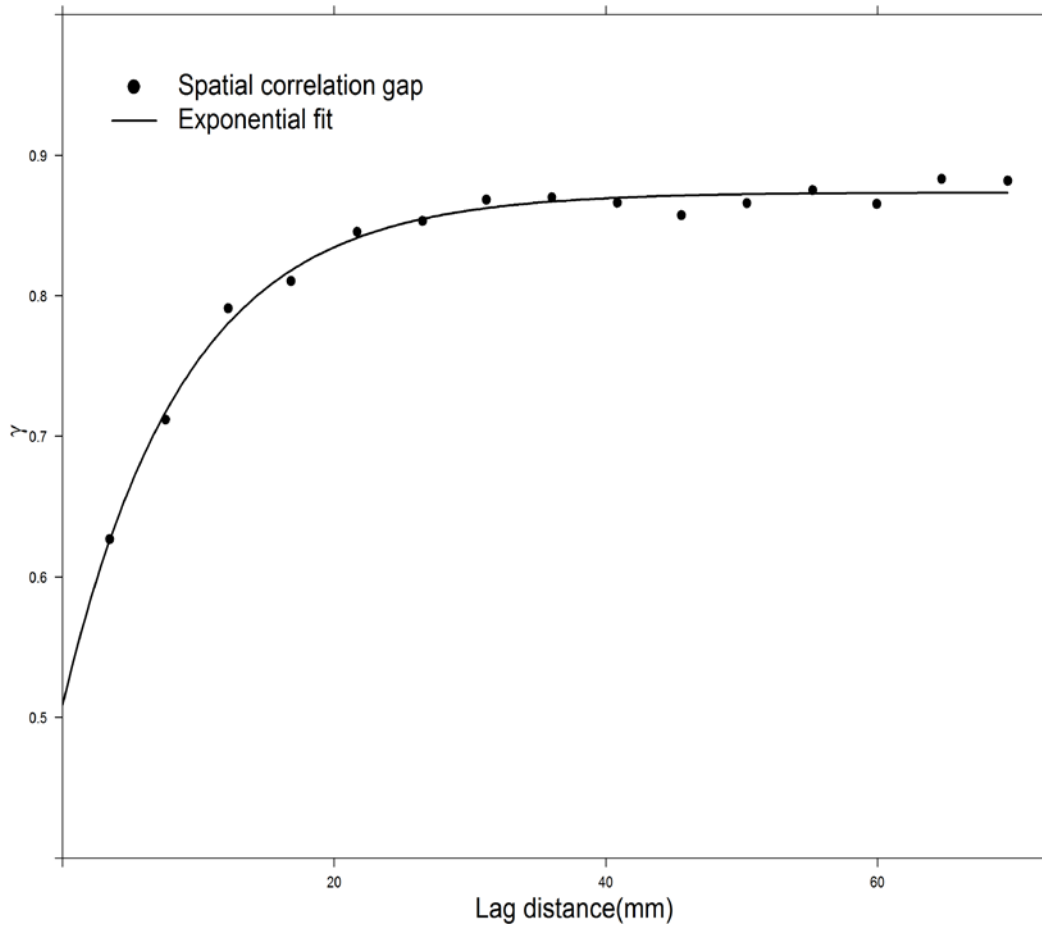
Figure 2-12: Semivariogram function for gap area

2.2.3   Comparison with permeability benchmark II

Permeability results predicted for the virtual geometry were compared with the results from the benchmark II exercise [13]. In this permeability benchmark, twelve participants followed a guideline document [14] to minimize experimental uncertainties (injection pressure, viscosity, fibre volume fraction, etc.), in order to introduce better control on the experiment conditions, observed in the permeability benchmark I [12]. This exercise showed a much smaller variation in permeability data compared to the first data set, supporting the concepts contained in the guideline document in this second case. The resulting variability contained in permeability was attributed to differences between experimental procedures (which were normalised, but performed in different labs) and the intrinsic variability of the textile material (global variability). Our calculations provide local variability, which is only one of the sources of variability seen in the measurements.

Figure 2-12 shows the histograms of permeability components, K_{bx} (orange bins) and K_{by}(green bins) from the benchmark II exercise [13].The comparison of the two histograms shows that the mean value of K_{by} (131 μm^2, Figure 2-13, orange dashed line) is greater than that of K_{bx} (81 μm^2, Figure 2-13, green dashed line) as shown in Figure 2-13. The higher average permeability in weft direction is consistent with that of the virtual geometry. In

addition, permeability shows higher variability in the weft direction (28) compared to the warp direction (17) which is same as what is observed in the permeability data of the virtual geometry.
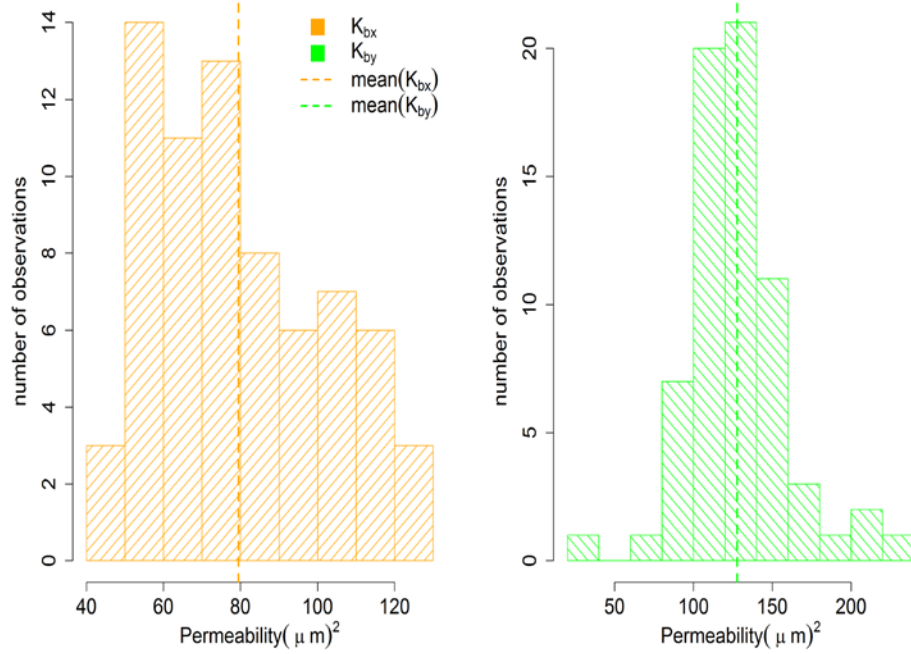

Figure 2-13: histograms of permeability data from benchmark II[13]: warp direction, Kbx, (left) and weft direction, Kby, (right). To differentiate data of benchmark II from the permeability data of the virtual geometry, a superscript bx and by

Table 2-7 summarises statistical characterisations of K_x and K_y from the virtual geometry compared to those of K_{bx} and K_{by} from the benchmark II exercise [13]. The means of the both data set are close, and validate the calculations performed in the present paper. Generally speaking, an average value of permeability components is necessary to represent the flow characteristics of a heterogeneous fibrous medium at larger scale. Extending from micro-/mesoscale to macroscale poses the problem of how to calculate the permeability components at macroscale on the basis of the geometry model. Table 2-7 shows two common averaging methods, including arithmetic and harmonic for permeability components from the virtual geometry. The correct method for averaging of the permeability components would be harmonic along the rows, and then arithmetic of the results.

It can be expected that the local variation would show higher variability than the variability between fabric sheets, which are averages of local permeabilities. However, the standard deviations of K_{bx} and K_{by} are approximately twice larger than K_x and K_y, leading to higher coefficient variations as shown in Table 2-7.

There a few possible explanations for this difference, which involve additional factors causing variability in the measurement aside from the local variability.

First, the number of observations may affect the magnitude of the standard deviation; K_{by} from the benchmark II exercise shows the highest standard deviation because of the

least number of observations (see Table 2-7). The previous studies by Hoes *et al.* [15] and Lu and Parnas [75] support 75-100 experiments are required to obtain a relatively narrow symmetric distribution. From Table 2-7, it is observed that the skewness with estimates of higher standard deviation is large. The skewness of K_x and K_y for the virtual geometry were 0.33 and -0.25, respectively, and those were 0.48 and 0.41 for benchmark II. The skewnesses of the permeability data lies between -0.5 and 0.5, resembling a normal distribution, similar to that reported by Pan et al.[36] for woven fabrics. In their study, they obtained a coefficient of variation of 13.1% which is close to the value of 12-15% in this study.

Second, the larger standard deviation may be caused by nesting [15], which adds variability to the laminate geometry in comparison with the variability of single plies and reduces permeability. We agree that permeability through thickness (K_z) is of utmost importance, and it can be assessed using FlowTex calculations. However, we do not address this aspect in the present paper, concentrating on the in-plane permeability components, as K_z calculations need representation of nesting of laminates and statistics related to it, which is a heavy subject, not fitting in the size of this paper. LamTex module of WiseTex package would allow, after certain modifications, modelling of nesting of statistically variable layers, and we plan to address this problem in future work. Increase in nesting reduces permeability [76] by progressively varying space between the yarns. Therefore, the broad permeability distributions can be caused by the different variations of nesting of yarns between adjacent layers. Third possible cause for the higher variability scatter is difference between experimental procedures in different labs.

Table 2-7: Estimated permeability vs. Benchmark II[13].

Statistics		Virtual geometry		Benchmark II	
		K_x(Warp)	K_y(Weft)	K_x(Warp)	K_y(Weft)
Number of observations		100	100	72	69
μ= mean $(\mu m)^2$	Arithmetic	81.5	92.5	80.7	131
	Harmonic	80.4	90.9	-------	-------
σ=Standard Deviation$(\mu m)^2$		10.1	13.9	17.7	28
COV(%)=σ/μ		12	15	21.9	21.3
Median$(\mu m)^2$		79.8	93.1	75.5	123
Minimum$(\mu m)^2$		60.5	56.8	43.6	23.1
Maximum$(\mu m)^2$		10.4	11.8	12.8	22.6
Skewness		0.33	-0.25	0.48	0.41

2.3 Conclusion

The heterogeneity of the microstructure of fibrous media plays an important role in the accurate prediction of local permeability and subsequently the mould-filling pattern in liquid composite moulding. A methodology for evaluation of the statistical characteristics of the local permeability distribution for woven fabric was developed and applied to the case of 2×2 twill woven carbon fabric, based on its virtual representation. The calculations consist of the following steps:

(1) building a virtual geometry of a fabric sheet with geometrical variations adequately representing the experimentally observed ones with the algorithms described in[20]–[24], [59];

(2) extraction of individual unit cells from the virtual sheet and building WiseTex geometrical models for them;

(3) calculation of the unit cells permeability values using FlowTex software, creation of the instance of the permeability discrete random field and

(4) Evaluation of statistics of the random field.

For a particular 2/2 twill balanced carbon fabric the following features of the field were observed:

(1) A difference in K_x and K_y of one specific unit cell was observed which is attributed to the difference in warp and weft yarn width, confirming that a wider inter-yarn gap leads to higher permeability in that direction.

(2) It was, however, not possible to establish a clear correlation between K_x and K_y. The channel width can vary unequally in both weft and warp directions, causing anisotropic permeability.

(3) It was shown that K_x and K_y as well as anisotropic index follows a normal distribution while the effective permeability follows a logistic distribution.

(4) Spatial correlations of the permeability values were calculated and found that the permeability variations showed a correlation length of *circa* 20 mm, corresponding to two unit cells.

These observations are consistent with measurements of permeability of the same fabric in benchmark II exercise [13].

Chapter 3

Micro-scale permeability

On the statistics of transverse permeability of randomly distributed fibre

An RVE-based stochastic numerical model is used to calculate the permeability of randomly generated porous media at different values of the fiber volume fraction for the case of transverse flow in a unidirectional ply. Analysis of the numerical results shows that the permeability is not normally distributed. With the aim of proposing a new understanding on this particular topic, permeability data are fitted using both a mixture model and a unimodal distribution. Our findings suggest that permeability can be fitted well using a mixture model based on the lognormal and power law distributions. In case of a unimodal distribution, it is found, using the maximum--likelihood estimation method (MLE), that the generalized extreme value (GEV) distribution represents the best fit. Finally, an expression of the permeability as a function of the fiber volume fraction based on the GEV distribution is discussed in light of the previous results.

Keywords: Transport properties, Statistics, Finite element analysis (FEA), Tortuosity, Permeability

Introduction

The flow of a fluid through porous media is a central problem in many engineering applications such as composite manufacturing, rheology, geophysics, oil engineering, etc. An excellent review of the relevant contributions in the field is reported in [77]

In liquid composite molding (LCM), the porous medium consists of dry fibres, while the fluid is a polymer resin. The knowledge of the transport properties is crucial when setting the manufacturing process parameters, and their determination has been investigated using experimental techniques [48] [78] [79] [80] [81] [54] [82] [83] numerical simulations such as the lattice Boltzmann method (LBM) [55] or the Finite Element Method (FEM) [84], and analytical solutions [54] [82] [83].

The determination of the transport properties of a fluid through a porous medium is a complicated task and depends on parameters such as pressure gradient, velocity, viscosity and compressibility of the fluid. However, in composites manufacturing several simplifications apply. First of all, the viscosity of the resin is high: in the region of 100-1000 mPa.s for resin transfer moulding (RTM), and the velocity of the fluid is very small, therefore creeping flow (known also as Stokes). Resin can also be considered incompressible so that viscosity, μ, is the only material parameter that plays a role in the determination of the transport properties.

When considering the porous material as homogeneous, and under the hypothesis of creeping flow, Darcy's law applies, i.e. the flow is proportional to the pressure drop and inversely proportional to the fluid viscosity. In the described conditions, fluid motion is described in terms of the permeability, K, that depends only on the geometry of the porous medium. On the other hand, at very low Reynolds number (creeping flow), the Carman--Kozeny (CK) equation applies [85] [86], and permeability is expressed as a function of the geometry of the particles that form the porous bed[4]. Strictly speaking, Carman-Kozeny (CK) equation applies to porous beds of spherical particles, but it has been applied also to the case of fibrous media. If a random distribution of fibers is considered, a modification of CK equation is required [84].

The study of the flow of the resin at a micro-scale level, and the effects of the micro-structure, have already been investigated in previous studies [48] [84]. In those studies, the fibers are considered regularly arranged and the effect of random distribution of the fiber is not taken into account. The uncertainties associated with permeability originated from fiber size distribution, porosity and compaction, will cause significant errors [87] when simulating the transport properties of fluid in porous media. Although previous studies have assumed permeability as a random variable in porous media modeling, the complexity involved in establishing a mutual relationship between micro- and macro-scale uncertainties is not common, with only one paper [88] so far proposing a probability density function for permeability.

Nevertheless it is undeniable that the random distribution of the fibers has an effect on the permeability [89] [90]–[92]. The aim of this paper is therefore to quantify this effect and point at ways to propose a method to calculate the saturated permeability of the fibrous porous medium.

Here, only the transverse permeability is investigated (permeability in the transverse direction of the fiber), the two-dimensional case is considered, and two--dimensional Representative Volume Elements (RVEs) are generated to model the fibers as impermeable circles (the capillarity effects and permeability of the fiber is neglected). The RVEs are generated by using the algorithm previously developed by the authors [93] and it is applied to a range of fibre volume fractions. Finally, a method for the estimation of the permeability at each fiber volume fraction is proposed.

It should be noted that several micro--structural effects influence permeability, including: i) the shape of the fiber, ii) the size of the fiber and its statistical variation, iii) the volume fraction of the composite and its statistical variation, and iv) the fiber distribution. In this paper we focus on the effects of the random distribution of the fibers alone.

---

[4] At the micro--scale, the porous medium consists of several cylindrical fibers, all nearly parallel between them, and randomly distributed.

3.1 Methodology

In the case of a stationary creeping flow of a Newtonian incompressible fluid such as resin system in RTM in the absence of body forces, the Stokes equations can be written as Eqs. 3-1 and 3-2:

$$\nabla.\left[-pI + \mu(\nabla u + (\nabla u)^T)\right] = 0 \tag{3-1}$$

$$\rho\nabla.u = 0 \tag{3-2}$$

where p is the pressure, u is the velocity, I the identity matrix, ρ and μ the density and the dynamic viscosity of the fluid, respectively.

Assuming no voids, superficial velocity U is obtained from the local velocity of the fluid as given in Eq. 3-3:

$$U = \frac{1}{V}\int_{v_f} udv = \phi\overline{u} = (1-V_f)\overline{u} \tag{3-3}$$

where V is the total volume, v_f is the volume of the fluid, u is the local velocity of the fluid, $\overline{u}$ is the average velocity, ϕ is the porosity, and V_f is the fibre volume fraction. Darcy's law relates the superficial velocity within the RVE to the pressure gradient across the characteristic size of the RVE, L (Eq. 3-4):

$$U = -\frac{K}{\mu}\nabla p \tag{3-4}$$

where K is the permeability of the porous bed and ∇p is the pressure gradient. Permeability depends only on the geometry of the RVE, and is independent from the superficial velocity and from the pressure. Therefore it can be written as Eq. 3-5.

$$K = K(d, L, V_f) \tag{3-5}$$

where d is the diameter of the fiber, and L is the characteristic length of the RVE. As dimensionally, permeability can be normalised to $\tilde{K} = K/d^2$. Then equation 3-4 can be rewritten as Eq. 3-6:

$$\tilde{K} = \tilde{K}(N_f, V_f) \tag{3-6}$$

where $N_f = L/r$, being r the radius of the fiber. The normalized permeability in Eq. 3-6 is a function of the fiber volume fraction, V_f, and of the size of the RVE, N_f.

The dependence on the size of the RVE can be eliminated if sufficiently big RVEs are used. A preliminary study on the minimum size of the RVE is required to the dependence on N_f, and hence Eq. 3-6 is only a function V_f ; $\tilde{K} = \tilde{K}(V_f)$.

3.2   Numerical model

3.2.1   Detail of the FE model

Computational Fluid Dynamics (CFD) models were created using the commercial software COMSOL Multiphysics 4.4 [94]. Matlab R2013b [95] was used to generate the random distribution of fibers [93] and to run CFD simulations in a FOR loop. 2000 simulations were run at every volume fraction, $V_f = 0.3, 0.35, 0.4, .., 0.8$. A total of 22000 simulations were run to obtain the statistical distribution of the normalized permeability.

RVEs were meshed using triangular mesh elements. In a preliminary phase simulations were run with the aim of choosing the appropriate element dimension. In order to insure convergence, this work verified that the size of the chosen element represented a good compromise between computational cost and accuracy of results. The mesh independence of the results was also verified. Periodic boundary conditions were applied to the exterior edges of the RVE (in yellow in Figure 3-1) meanwhile wall boundary conditions were imposed at the interior edges. To impose a periodic boundary condition, the source and sink edges need to be defined. If the flow goes from West (W) to East (E), the boundary conditions are written as Eqs. 3-7 and 3-8 (please refer to Figure 3-1):

$$p_E - p_W = \nabla p \neq 0 \qquad\qquad\qquad\qquad\qquad\qquad \textbf{(3-7)}$$

$$p_N - p_S = 0 \qquad\qquad\qquad\qquad\qquad\qquad\qquad \textbf{(3-8)}$$

where ∇p is the applied arbitrary pressure drop. Under this assumption, in fact, permeability is independent from the applied pressure drop.
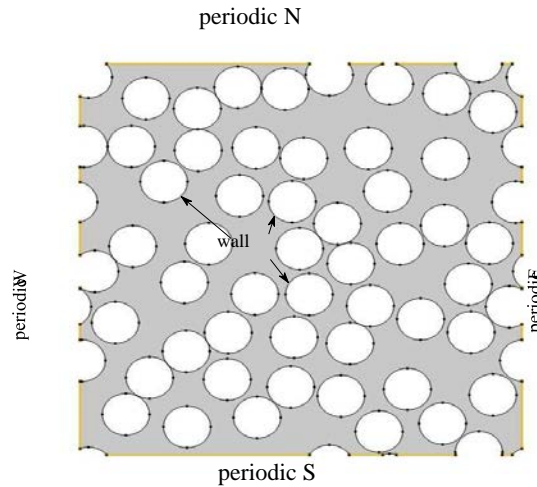

Figure 3-1: Applied boundary conditions.

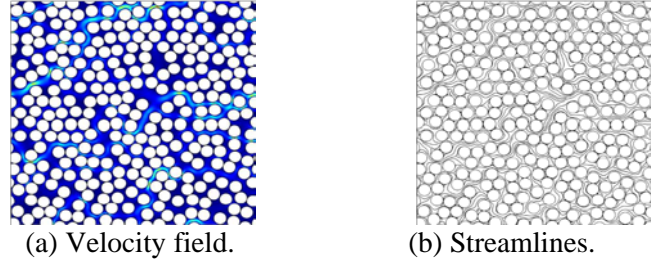(a) Velocity field.   (b) Streamlines.

Figure 3-2: Results of the numerical model.

After running the simulation, velocity fields and streamlines are obtained as reported in Figure 3-2 (a) and 3-2 (b), respectively. The velocity fields can be integrated by Eq. 3-3 to calculate the superficial velocity U. At this point, by knowing the applied pressure drop ∇p, the size of the RVE, and the viscosity of the fluid, the permeability is calculated as shown in Eq.3-4. Streamlines are used to infer the tortuosity, which is defined as the ratio between the length of the streamline and the length of the porous bed. In the present case it is proposed to calculate the tortuosity as Eq. 3-9:

$$\tau = \frac{\sum l_e^i}{\sum l_p^i} \qquad\qquad\qquad (\textbf{3-9})$$

where l_e^i is the effective length of the i–th streamline, and l_p^i is the length of the streamline projected along the flow direction.

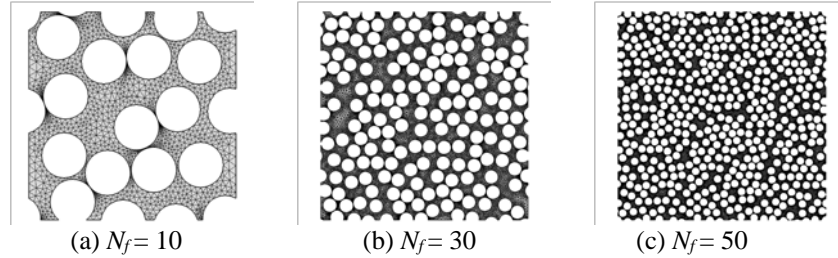(a) $N_f = 10$ (b) $N_f = 30$ (c) $N_f = 50$

Figure 3-3: RVEs' dimensions (not in scale).

3.2.2   Size of RVE

If the size of the RVE is sufficiently large, or under the assumption of ergodicity, the expected value associated with the permeability distribution, and its standard deviation converge. This has been shown in [89] and it is confirmed by our calculations. Examples of the generated RVEs are reported in Figure 3-3. Figures 3-4(a) and 3-4 (b) show the probability density function (pdf) of the normalized permeability as a function of the dimension of the RVE. The pdf is calculated using the kernel smoothing estimation based on Gaussian distribution. It is observed that small RVEs may lead to an error in the estimation of the expected value and to big standard deviations. Figures 3-4 (a) and 3-3 (b) show that when the size of the RVE is 30 times larger than the radius of the fiber ($N_f \geq 30$), both the expected value and the standard deviation of the statistical distribution converge. In this study, $N_f = 40$ is used.
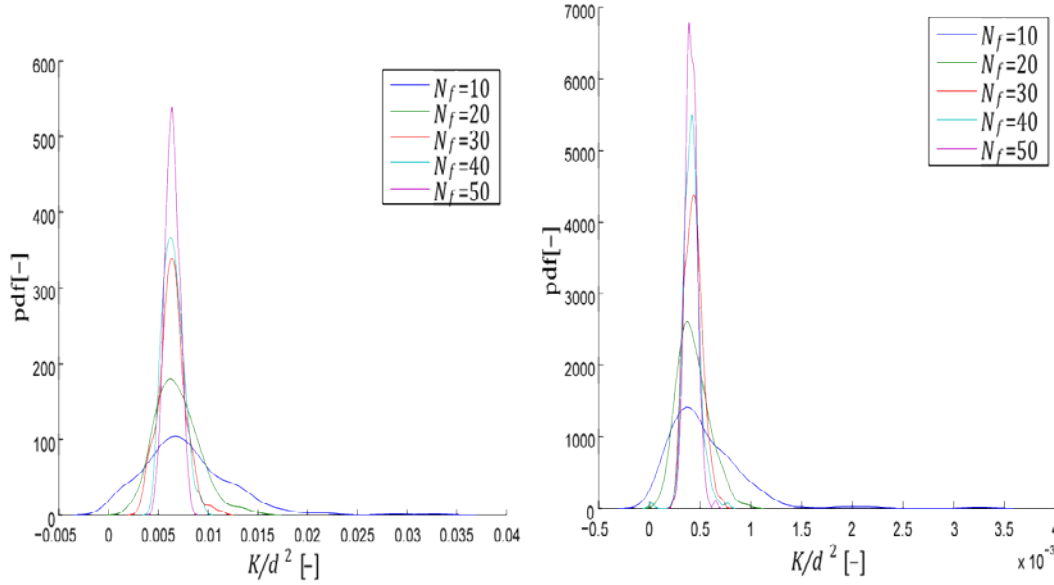
Figure 3-4: pdfs of the normalized permeability as a function of the size of RVE

3.3   Results and discussion

3.3.1   The normality test

Matlab Statistical Toolbox [95] and R Statistical Software [96] are used for the statistical analyses performed in the following.

Figure 3-5 shows the histogram and Q–Q plot obtained for $V_f = 0.5$. It is evident that the normal distribution cannot be an appropriate estimation for the permeability distribution. The same considerations apply to the permeability distributions obtained for different values of the volume fraction. However, for the sake of conciseness, Q–Q plots concerning these distributions are not reported here. From Figure 3-5 it can be observed that permeability distributions show fatter tails and thinner body than the normal distribution (Figure 3-5 (left)), and that it is approximately symmetric (Figure 3-5 (right)). It should be noticed that the true and normal density (Figure 3-5 (right)) cross each other twice on each side of the mean value, satisfying Finuncan's condition [97] which states that fatter tails are often associated to more peaked distributions.
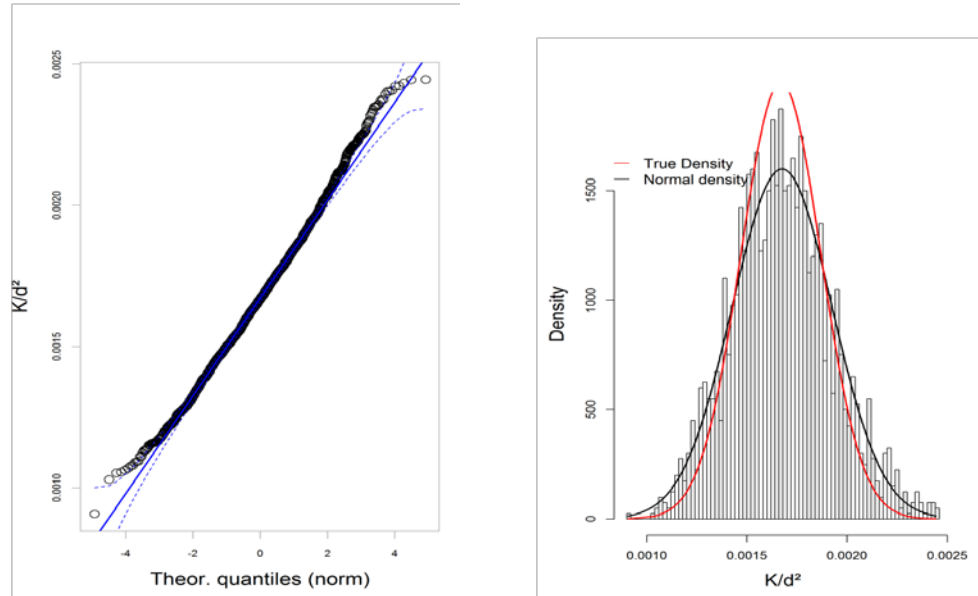
Figure 3-5: Q–Q plots and pdf of permeability data ($V_f = 0.5$). (left) Normal distribution fit (dashed lines indicate the 95% confidence interval using the KS test (right) Histogram, normal fit (black) and true density (red)

Moreover, with reference to [98] , the difference in the appearance of the distributions is due to the difference in variances and not in kurtosis. This is shown in Table 3-1, where skewness and kurtosis of the permeability data are reported.

Table 3-1: Skewness and kurtosis of the numerical distributions

V_f	0.3	0.35	0.4	0.45	0.5	0.55	0.6	0.65	0.7	*0.75*	*0.8*
skewness	0.21	0.21	0.048	0.19	0.23	0.21	0.16	0.20	0.31	*0.38*	*0.15*
kurtosis	3.0	2.8	2.8	2.8	3.0	2.9	2.9	2.9	2.9	*2.5*	*2.9*

Table 3-1 shows that the skewnesses of the permeability data lies between 0 and 0.5, implying that the permeability distribution is approximately symmetric. In addition, the kurtosis values are around 3 which is consistent with a normal distribution. As expected, there is no significant difference between the calculated kurtosis and that of the normal distribution and hence this method does not allow one to detect the large variation in the tails [97].

3.3.2   Permeability statistics

Statistical characterizations of the derived permeability for different values of V_f are summarized in Table 3-2 Table 3-2 shows that permeability coefficients of variation (COVs) for different values of V_f lie between 0.12 and 0.16, which is approximately 10 times larger than the tortuosity COVs. These observations suggest that uncertainty associated with permeability is one order of magnitude greater than that associated with tortuosity. Thus, although tortuosity influences the mean value of permeability, it does not explain the uncertainty of permeability. It is thought that, in the present case, the larger uncertainty of permeability is caused by the porosity distribution. In addition, the

coefficient of variation for permeabilities is approximately in the same range as reported in [63][99] for smaller sample sizes.

Table 3-2: Statistical characterizations of permeability data derived from RVEs

V_f	τ (mean)	COV (τ)	K/d^2(mean)	COV (K/d^2)	Chi-square test	
					Normal	Lognormal
0.3	1.34	0.0074	0.024	0.131	0.0779	0.0029
0.4	1.42	0.007	0.0064	0.145	0.00013	1.89E-10
0.5	1.47	0.108	0.0016	0.148	0.042	0.027
0.6	1.51	0.08	0.00047	0.157	0.2438	0.003262
0.7	1.54	0.008	0.00012	0.161	0.3	2.10E-09
0.8	1.53	0.006	1.83E-05	0.125	0.1558	0.05813

The chi-square test, with a significance of 5%, was also applied to permeability data in terms of normal and lognormal distributions. The p values reported in Table 3-2 suggest the appropriateness of using a lognormal distribution, over a normal distribution, to represent permeability data. However, a close observation of Figure 3-6 allows one to conclude that although the true density and lognormal fit are virtually the same (as shown in Figure 3-6 (b)), the lognormal distribution cannot represent the whole set of data. In fact, even after logarithmic transformation, the distribution shows a substantial skewness, as reported in Figure 3-6 (a). Moreover, from the Q–Q plot of Figure 3-6 (a), it can be concluded that both upper and lower tails fail to represent the permeability at very low probability.
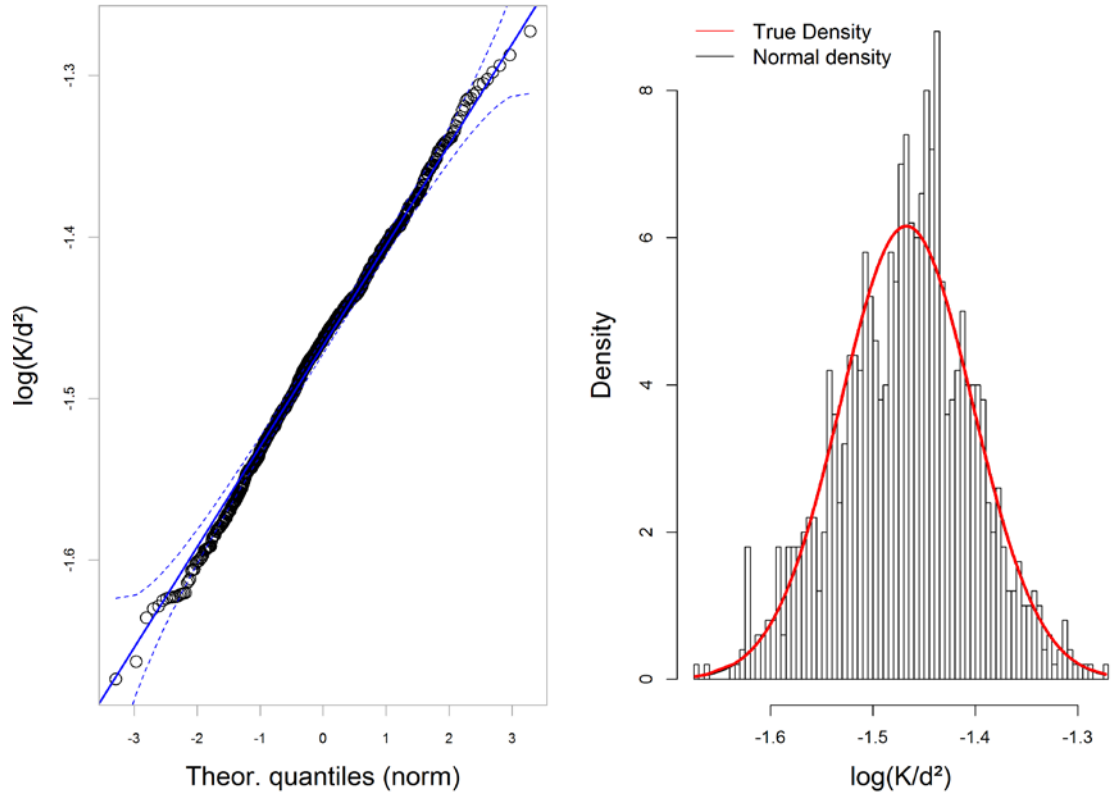
Figure 3-6: Q–Q plots and pdf of permeability data ($V_f = 0.5$) after log transformation. (left) Normal distribution fit (dashed lines indicate the 95% confidence interval using the KS test (right) Histogram, normal fit (black) and true density (red)

In summary, the lognormal distribution can be used to fit the data of the body of the empirical distribution, but fails at low probability (i.e. in the tails). To take into account the tails, extreme value theory is used. In the following, two approaches are proposed to fit the permeability data: i) the use of a mixture of two or more distributions [100], ii) the use of heavy-tailed distribution models.

Mixture modeling and threshold estimation

This section proposes two different distributions for the body and the tails of the empirical distribution. In the previous section it was concluded that the lognormal distribution fits well the empirical data in the body of the distribution; therefore, for the body the lognormal distribution is used. For the tails, a power distribution is used. The reason is that, in the framework of extreme values theory [101], it has already been shown that power distribution is the best choice for fat tails. Figure 3-7 shows the mixture model of the permeability data for $V_f = 0.5$. The estimation of the threshold (represented as vertical dashed lines in Figure 3-7) where the transition from one model to another occurs, is critical. This transition exists in both the left and right tails of the empirical distribution, but in Figure 3-7 only the upper threshold is represented for clarity.
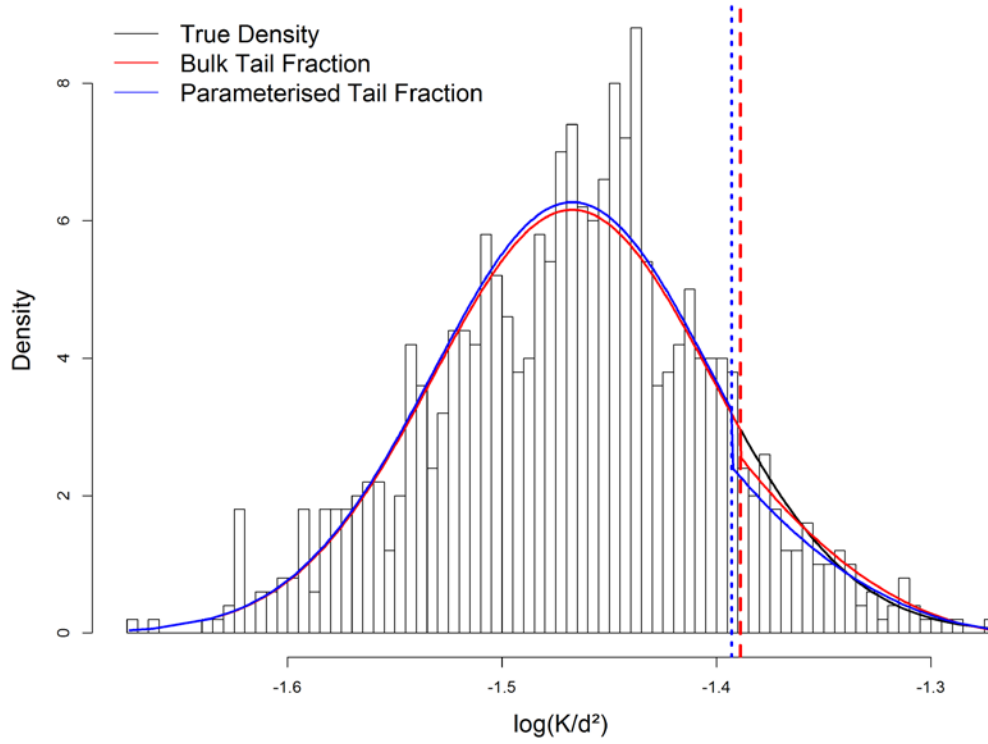
Figure 3-7: Histogram of permeability data at $V_f = 0.5$ with parametric estimation of tail: the bulk tail fraction in red fitted with normal and parameterised tail fraction in blue fitted with Generalized Pareto distribution. The vertical dashed lines indicated the threshold.

Mathematically, a probability distribution of the permeability data following a power law model can be expressed as Eq.3-10.

$$P_p(K) = \beta \, \tilde{K}_{min}^{\beta} \, \tilde{K}^{-(\beta+1)}$$ (3-10)

where β and $\tilde{K}_{min}^{\beta}$ are experimental positive constants.

The lognormal distribution model is given in Eq.3-11.

$$P_{ln}(K) = \frac{1}{\sigma\sqrt{2\pi}} \frac{1}{\tilde{K}} \exp(-\frac{(\ln \tilde{K} - \mu(\tilde{K}))^2}{2\sigma^2})$$ (3-11)

where σ is the variance of the average normalized permeability.

Taking the logarithm of Eqs. 3-10 and 3-11 yields:

$$\ln(P_p(K)) = \ln(\beta) + \beta \ln(\tilde{K}_{\min}) - (\beta + 1)\ln(\tilde{K}) \qquad (3\text{-}12)$$

$$\ln(P_{\ln}(K)) = -\ln(\sigma\sqrt{2\pi}) - \ln(\tilde{K}) - \frac{(\ln \tilde{K} - \mu(\tilde{K}))^2}{2\sigma^2} \qquad (3\text{-}13)$$

In case of large σ, Eq. 3-13 would show near-linear log-density behaviour. Hence, both the power and lognormal distributions would have near–linear log Complementary Cumulative Distribution Functions (LCCDF). The LCCDF of the permeability data is plotted for $V_f = 0.5$ in Figure 3-8. As expected, the body of the empirical distribution can be fitted using a lognormal model while the tails are fitted using a power law model in [102] (blue and red lines in Figure 3-8, respectively).
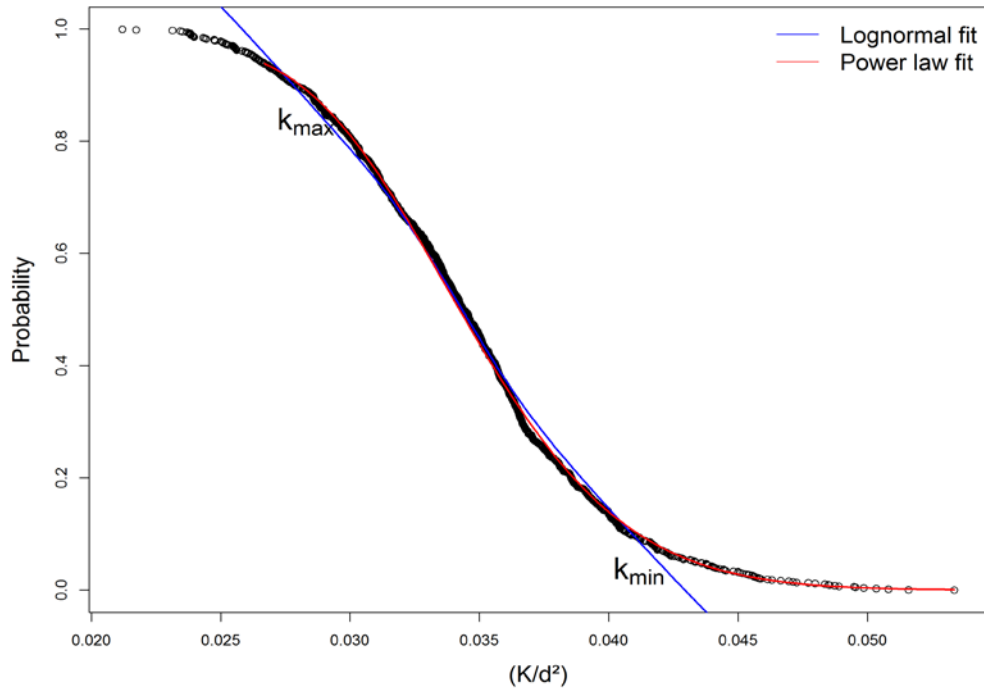

Figure 3-8: LCCDF of the permeability data at V_f=0.5

Therefore, the permeability data can be fitted using a linear combination of the lognormal and power law models: in the range $\tilde{K}_{\min} \leq \tilde{K} \leq \tilde{K}_{\max}$ the permeability data can be fitted using a lognormal model, while outside this range ($\tilde{K} < \tilde{K}_{\min}$ and $\tilde{K} > \tilde{K}_{\max}$) the permeability data is fitted using a power law model. This behaviour was already observed by [103] who showed that a mixture of lognormal distributions in terms of a geometric distribution would behave lognormally in the body and have a power law model in the tails. More recently, the above model was corrected by a double Pareto distribution [100] who showed that the mixture distribution specifically have Pareto (power law) behaviour in the tails. Hence, one could conclude that an appropriate permeability

distribution model closely fits the body of a lognormal distribution and the tails of the double Pareto distribution. It is not clear what could cause the fat tails. Strictly speaking, fiber distribution is not completely random. It is clear that Complete Spatial Randomness (CSR) cannot be achieved, as found already in [93]: due to the finite size of fibers, their distribution cannot be completely random because the space occupied is limited by others (it should be noticed that for the generation of the RVE a hard–core model is used, therefore interpenetration between fibers cannot occur).

Fitting extreme value distribution

Statistical tests allow one to reject the null hypothesis that a sample comes from a given statistical distribution but do not determine from which distribution a given sample comes from. Of course this is not a simple task and even if several statistical methods (as the methods of moments) can be applied to this purpose, the determination of the distribution cannot be rigorous. Nonetheless, this paper proposes to obtain the candidate statistical distribution as the distribution that best fit the numerical data. Several distributions were used to fit the data. In particular: beta, birnbaumsaunders, exponential, extreme value, gamma, generalized extreme value, generalized pareto, inverse gaussian, logistic, loglogistic, nakagami, normal, rayleigh, rician, tlocationscale, and weibull were studied. The best fit was obtained using the maximum-likelihood estimation (MLE) method and minimizing the negative logarithm of the likelihood. Figure 3-9 shows the empirical pdf and the best fits (among the distributions aforementioned). The distributions are listed in the legend in order of best fit. It is possible to observe that the generalized extreme value (GEV) represents the best fit the data for all the volume fractions considered.
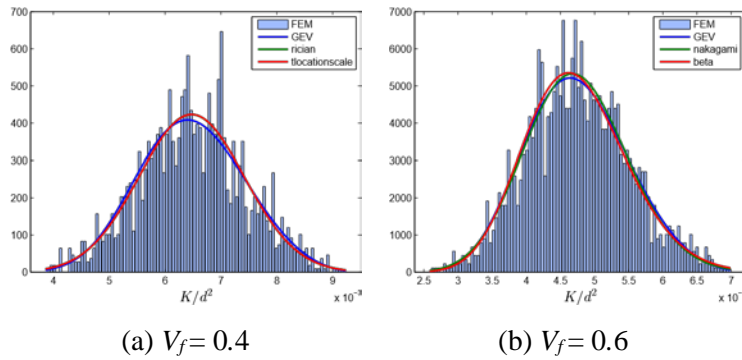

(a) $V_f = 0.4$ (b) $V_f = 0.6$

Figure 3-9:pdfs of the normalized permeability distributions (for the sake of conciseness the distributions are reported only for $V_f = 0.4, 0.6$).

3.4 Correlation

In the previous sections, it was shown that a mixture model (consisting of a lognormal distribution for the body and a power law model (or pareto [102]) for the tails) or a GEV provide better fit over normal distributions for permeability of macroscopic samples with randomly arranged fibers. These families of distributions (GEV, power law, pareto, lognormal) have been found to be useful for stochastic modelling [104][88][105][106][107] when inputs such as permeability follow heavy–tailed distributions. However, the use of mixture model is more complex than GEV. Thus, for the

sake of convenience, the GEV model is used in the following because it i) provides a closed-form expression, ii) yields a permeability model with two parameters, iii) encompasses a range of classes of tail behaviour. The pdf of the GEV distribution is formulated as Eq. 3-14.

$$f = \frac{1}{\sigma}\left[1+k(\frac{x-\mu(\text{x})}{\sigma})\right]^{-1-\frac{1}{k}} \exp\left\{-\left[1+k(\frac{x-\mu(\text{x})}{\sigma})\right]^{-\frac{1}{k}}\right\} \qquad (\textbf{3-14})$$

where μ, σ, and κ are the location parameter, the scale parameter, and the shape parameter for the GEV distribution, respectively. Figure 3-10 shows the variation of μ and σ as a function of the volume fraction.
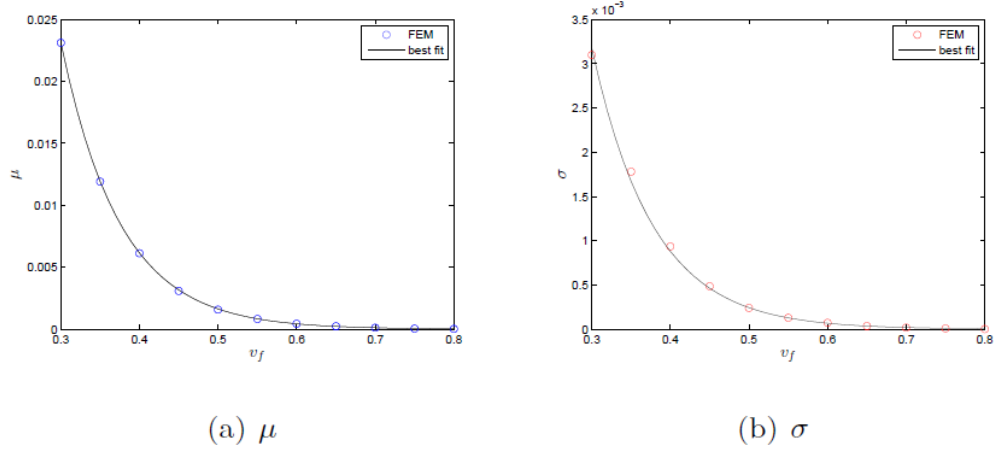

(a) μ (b) σ

Figure 3-10: Location and scale parameters as a function of fibre volume fraction

The location, the scale, and the shape parameter can be fitted as:

$$\mu(V_f) = 1.232\exp(-13.25V_f) \qquad (\textbf{3-15})$$

$$\sigma(V_f) = 0.149\exp(-12.48V_f) \qquad (\textbf{3-16})$$

$$k = -0.215 \qquad (\textbf{3-17})$$

as the shape parameter is approximately constant when varying the fiber volume fraction. Eqs. 3-15, 3-16, and 3-17 allow the calculation of permeability as a function of the fiber volume fraction. The normalized permeability is obtained as the expected value of the GEV distribution(Eq. 3-18).

$$\frac{K}{d^2} = E(\text{x};V_f) = \mu - \frac{\sigma}{k} + \frac{\sigma}{k}\Gamma(1-\text{k}) \qquad (\textbf{3-18})$$

where $\Gamma(\bullet)$ is the gamma function of $(\bullet)$. Figure 3-11 shows the normalized permeability as a function of the volume fraction and the confidence interval at 95%. Permeability can also be obtained by the Carman–Kozeny equation [86] as Eq. 3-19.

$$K = \frac{\phi \mu u}{\nabla p} = \frac{\phi D_h^2}{\psi_{CK}} \qquad\qquad\qquad (\ 3\text{-}19)$$

where $D_h = 4/d$ [84] is the hydraulic diameter and ψ_{CK} is the Kozeny factor. Substituting the expression of the hydraulic diameter in Eq. 3-19 and rearranging yields Eq. 3-20.

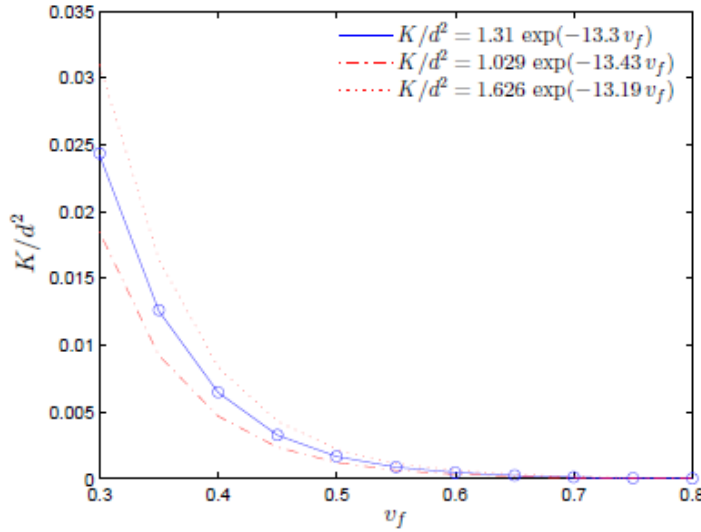$$\psi_{CK} = \frac{d^2 (1 - V_f)^3}{K V_f^2} = \frac{d^2 \phi^3}{K(1 - \phi)^2} \qquad\qquad (\ 3\text{-}20)$$

Figure 3-11: normalized permeability as a function of the volume fraction.

The Kozeny factor is a dimensionless parameter usually obtained experimentally. Substituting Eq. 3-18 in Eq. 3-20 allows the calculation of the Kozeny factor as a function of V_f as shown in Figure 3-12. The Kozeny factor can be fitted as Eq. 3-21:

$$\psi_{CK} = (0.01374 \frac{V_f}{1 - V_f} + 0.05038 - 0.004641 \frac{1 - V_f}{V_f})^{-2} \qquad (\ 3\text{-}21)$$

At this point, it is worth comparing the Kozeny factor, ψ_{CK}, calculated using Eq. 3-21, with both experiments and models found in the literature. Figure 3-12 shows this comparison considering models and experiments reported by other authors [48][84][89][108][109][110][111][112][113]. It is noted that the proposed model correlates well with the original ψ_{CK} and Gebart's model [48] only for large values of porosity. On the contrary, for small values of the porosity, the results of our model do not match the prevision of Gebart's model [48] but they correlate better with the experiments.
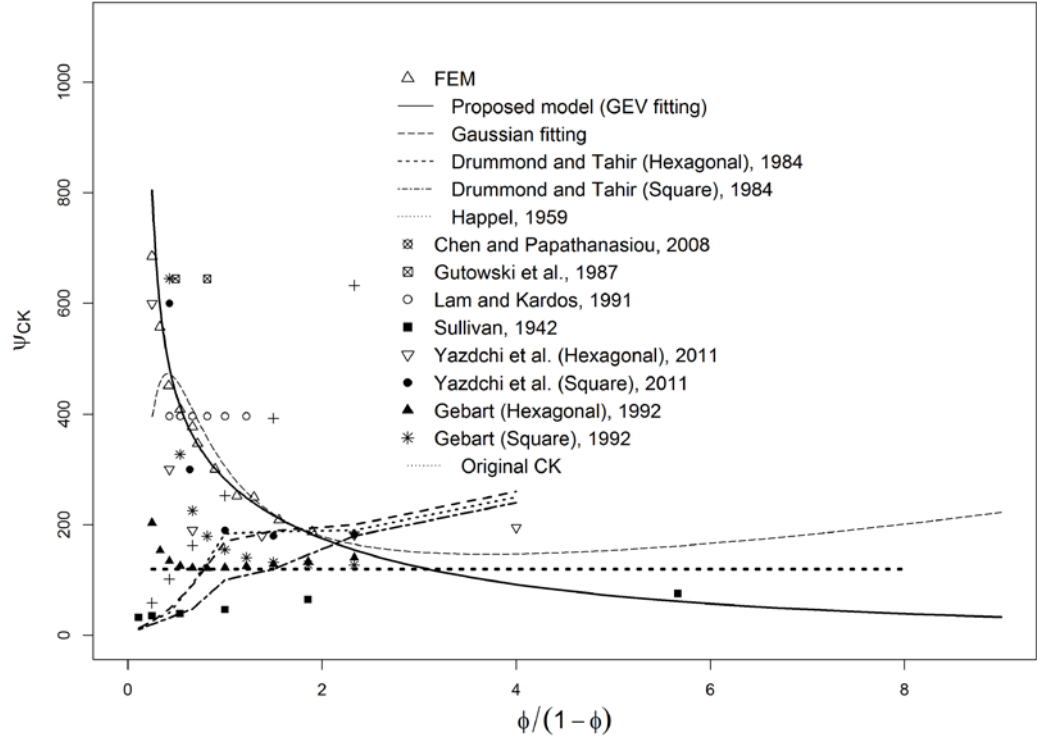
Figure 3-12: Comparison of the proposed model with experiments and models found in literature.

As proposed by Carman [86] the Kozeny factor can also be written as Eq.3-22.

$$\psi_{CK} = \varphi\tau^2 \qquad\qquad (\textbf{3-22})$$

where τ is the tortuosity and φ is a parameter taking into account the shape of the particles (or the fibers). The tortuosity was estimated by Carman [86] to be constant and equal to *circa* 1.4 for a porous bed composed by spherical particles. The tortuosity calculated using Eq. 3-9 is reported in Figure 3-13 as a function of V_f. Please, notice that the value proposed by Carman does not substantially differs from the value calculated here for the case of cylindrical fibers. The tortuosity calculated can be fitted as Eq.3-23:

$$\tau = 1.552\exp\left\{-\left[(V_f - 0.7787)/1.221\right]^2\right\} \qquad\qquad (\textbf{3-23})$$

Finally, the shape parameter φ as a function of V_f is derived from the combination of Eqs. 3-24 and 3-25 as given as Eq. 3-26.

$$\varphi = 81.33(\frac{1-V_f}{V_f})^{-0.7508} + 48.67 \qquad\qquad\qquad (\textbf{3-27})$$
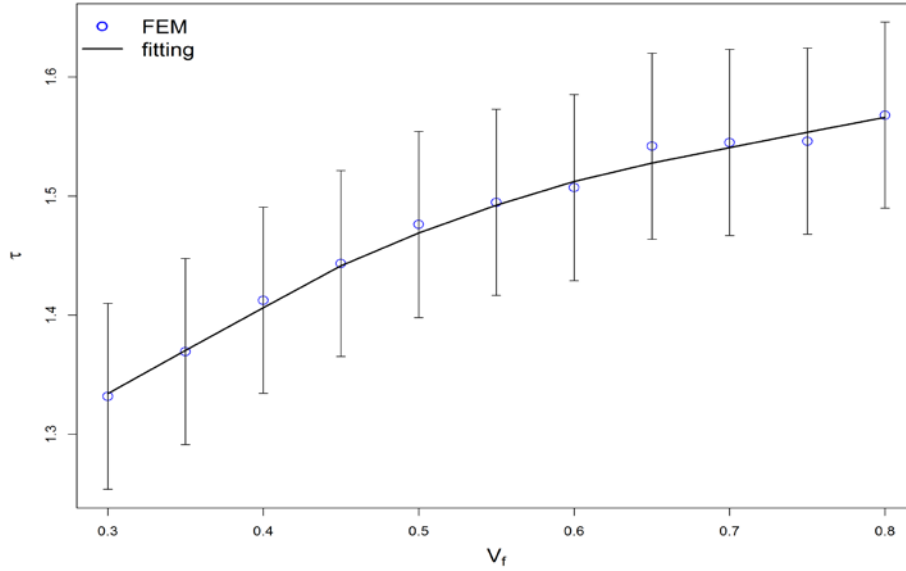

Figure 3-13: Tortuosity as a function of the volume fraction. Error bars represent the standard deviation.

3.5   Conclusion

The main conclusions of this work may be summarized in the following points.

• It was demonstrated that using CFD simulations and applying appropriate boundary conditions is possible to obtain the statistical distribution of the saturated permeability of a fibrous porous medium. Only the saturated transverse permeability was considered in this paper. The uncertainty in the calculation of permeability depends on several parameters: 1) the uncertainty in the measure of the volume fraction, 2) the uncertainty in the dimension of the fibers (fiber diameter is not constant but varies); 3) the effect of the random distribution of the fiber. Only the last effect was considered here.

• The normalized permeability distribution appears not to be normal. Q–Q plots showed that the permeability distribution has fatter tails than the normal distribution. The fact that the normalized permeability is not normally distributed may be surprising but it may be explained with the fact that the position occupied by the fibers is not completely random. Complete Spatial Randomness (CSR) exists only for points generated in a region using a Poisson distribution. Circles, which have finite dimensions, do not allow CSR because of the fact that the space occupied by a given circle is unavailable to other circles [93].

• It is common practice to ignore the extreme values, as done in the second worldwide permeability benchmark [99]. The results, however, showed that extreme values in permeability data cannot be considered outliers with negligible probability and that a normal distribution cannot be the characteristic model for permeability.

• It was also showed how to identify both the lower and upper tails in the data. It was postulated that the reasons for this non–normal behaviour could be, i) a combination of micro– and macro–scale flows, ii) undetectable patterns of permeability because of heterogeneous distributions of fibers, iii) random distribution of fibers.

• This article proposed that a mixture model (consisting of a lognormal distribution for the body and a power law model (or pareto[102]) for the tails) or a GEV provide better fit for the description of the statistics of permeability.

• An expression of the permeability and of other relevant parameters used in Carman–Kozeny equation, was obtained as a function of the volume fraction V_f.

Chapter 4

Intra-tow permeability

On the stochastic variations of intra-tow permeability of a 2/2 twill carbon fabric induced by internal geometry

This study investigates the stochastic variation of tow cross sections in a 2/2 twill carbon fabric and intra-tow permeability. A large sampling of tow cross sections (720 per layer) done by X-ray Micro-Computed-Tomography of a 7-layer composite plate is used to validate the use of the following statistical distributions of the random geometrical parameters: tow thickness (normal), tow width (log-logistic), intra-tow fibre volume fraction (log-normal) – and intra-tow permeability (gamma). The intra-tow fibre volume fraction and permeability variables are auto-correlated with a correlation length of *ca*. 3 mm, which corresponds to a correlation length of the out-of-plane tow centroid coordinates and is close to the spacing of the warp and weft yarns. The findings can serve as guidelines in doing Monte Carlo modelling of woven preforms variability and continue previously published work on inter-tow geometry and permeability.

Keywords: A. Tow; B. Permeability; C. Statistical methods; A. Fabrics

Introduction

In Liquid Composite Moulding (LCM) processes, a liquid thermosetting resin is injected into a dry fibre preform, filling the empty spaces within the fibrous medium. Porosity (ϕ) and permeability (K) are preform properties required to characterise flow behaviour through the fibrous media [26] [27]. Porosity is the total fraction of empty spaces in a preform. These spaces are filled with resin during impregnation process. This porosity is formed by channels between the tows and channels among fibres within a tow. It should be noticed that the definition of porosity is for unblocked pores. At higher fibre volume fraction (over 50%), binder materials are applied on the individual fabric mat to prevent fibre displacement [114] [115]. Excessive amount of binder materials could block porosity between the tows, leading to a small amount of blocked porosities [114].

In this study the preform is constituted by the seven ply 2/2 twill carbon woven fabric plies. Channels between tows have typical size width of 80 to 250 μm; the tows are in the order of 1000 μm (Figure 4-1i) and channels between fibres have approximately 1 μm and together they form a tow (containing intra-tow porosity) ; 10 μm is a scale of fibres themselves (Figure 4-1ii) [19]. Such media have a dual porosity scale (Figure 4-1):

channels between fibres form the microscale porosity (intra-tow porosity) and channels between tows form the mesoscale porosity (inter-tow porosity).The intra-tow porosity, which is the purpose of this study, is defined as the ratio of the channels volume within a tow to the total volume of the tow. To determine the inter-tow porosity, tows are assumed to be impermeable, and the ratio of the channels volume among the tows to the total laminate volume is taken.
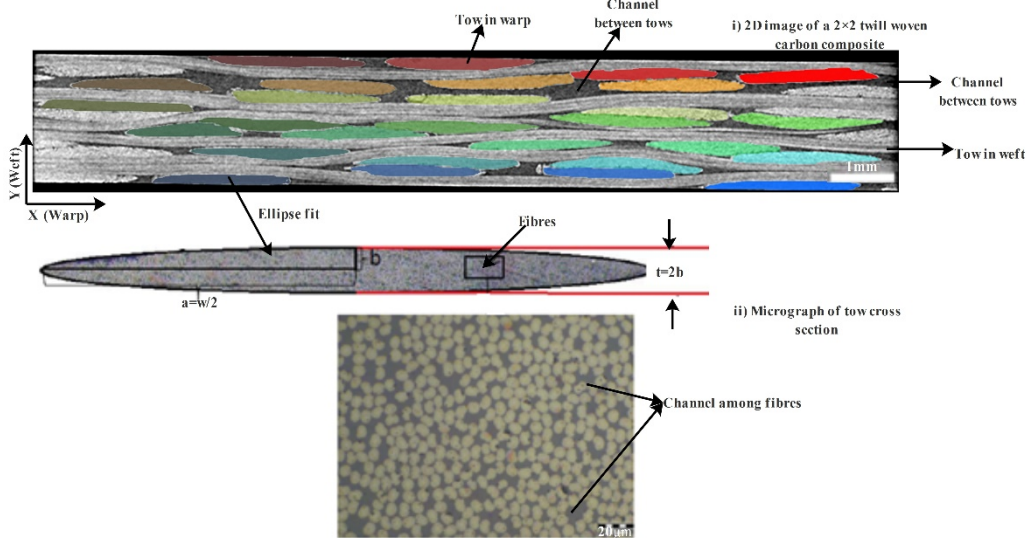

Figure 4-1: The 2D image slice, perpendicular to the warp tows; the schematic of the dual porosity characteristics: (i) a 2/2 twill woven carbon composite cross section (channels between tows making inter-two porosity), (ii) Fibres inside a tow (channels between the fibres making intra-tow porosity)

Such heterogeneous microstructure forms high permeability (inter-tow) and low permeability (intra-tow) zones within fibrous media[116] [117]. Therefore, preform heterogeneity results in an imbalanced flow rate between intra- and inter-tow regions during the impregnation process, forming fingering, or saturation lead-lag flow, induces common defects such as void formations and dry spots.[115] [118] [119]. Pillai and Advani [117] suggested that there is a certain value (0.1 at V_f=50%) for the ratio of low to high permeability zones beyond which the flow in intra-tow porosity region cannot be neglected for the calculation of the global permeability. Senoguz *et al.* [120] observed that intra-tow flow is the dominant phenomenon in the differences in saturated and unsaturated permeabilities. Dungan and Sastry [121] included the physics of intra-tow flow in the flow model to obtain reasonable results for unsaturated flow in woven fabrics. Huber and Maier [122]developed a model to account the ratio of saturated permeability to unsaturated permeability by the combination of the inter-tow and intra-tow permeability. These two papers and similar works by Parnas and Phelan [123] show the characteristics of flow exchange in inter-tow porosity need to involve tow-level effects.

The intra-tow permeability becomes more critical in composite parts with high fibre volume fractions. The effect of local fabric deformation on intra-tow permeability along and perpendicular to the fibre tows is studied. Lundstrom and Gebart [124], Loendersloot and Akkerman [125], Huber and Maier [122] and Bechtold and Ye [126] studied the effect of the fibre packing bundle and observed a significant influence for the intra-tow

permeability components. An increase in the longitudinal permeability is found for irregular packed fibres [124] [125], whereas a decrease is found for the transverse permeability for an increasing disorder in the packing [122] [124] [126].

The concept of a dual-scale model for a textile composite was first presented by Phelan and Wise [127]. Their results showed the increasing influence of intra-tow permeability on global permeability with increase of the overall fibre volume fraction; the ratio of "solid-tows" and "permeable-tows" permeability can reach one to two decimal orders of magnitude at high fibre volume fraction (70 to 75%). Sadiq *et al.*[128] ran experiments to study transverse flow for a Newtonian fluid through a fibrous medium array which was constructed in two forms, one consisting of regular arrays of circular, solid cylinders (homogeneous) with 40 % $< V_f <$ 60 % and the other consisting of regular arrays of circular, permeable cylinders (heterogeneous, with certain distribution of local fibre volume fractions: for example, fibre volume fraction inside a fibre tow is larger than fibre volume fraction outside a fibre tow) with 62 % $<$intra-tow fibre volume (V_f^{tow}) $<$ 75 %. They have shown that the predictions of permeability based on global fibre volume fraction only will not be correct for heterogeneous fibrous media. A similar conclusion was reached by Ranganathan *et al.*[129] and Papathanasiou [130] [131], Tung *et al.*[132], Song *et al.*[133], using different methods for permeability calculation. In [18] Wang *et al* even suggested that intra-tow permeability can be neglected only when global fibre volume fraction is as low as 30%; in [133] this limit is set at 50%. Belov *et al.*[55], Wang *et al.*[60], Nabovati *et al.*[61], Nedanov *et al.*[62] reported the difference in the computed global permeability of woven fabrics for the cases of permeable and impermeable tows to be lie in the of 10% to 30%. Tahir *et al.* [134] showed that the intra-tow porosity less than 50% has a significant effect on the computed global permeability. It follows from the discussion above that models which consider impermeable tows can significantly underestimate global permeability particularly at high fibre volume fractions. This knowledge of intra-tow permeability is relevant to the new variants of RTM where high pressure injection (>10 bars) combined with dynamic fibre compaction using state-of-the-art presses, has opened a possible window for jumps of the current 50-55% to over 65% fibre volume in RTM [115].

Intra-tow permeability for the regular arrangements of long cylindrical fibres inside tows has been widely studied and various models such as Happel[135], Sangani and Acrivos[136], Gebart[48], Bruschke and Advani[137], Lee and Yang[138], and Sharaoui and Kaviany[139] for correlations between transverse permeability and porosity have been derived. One of the most extensively used model is proposed by Gebart[48]. He estimated principal permeability along the fibres (K_L) based on Kozeny-Carman equation and perpendicular to the fibres (K_T) at a fibre volume fraction V_f^{tow}:

$$K_L = \frac{d_f^2}{16c_1}\frac{(1-V_f^{tow})^3}{(V_f^{tow})^2} \qquad\qquad (4\text{-}1)$$

and

$$K_T = \frac{c_2 d_f^2}{4} \left(\sqrt{\frac{V_f^{\max}}{V_f^{tow}}} - 1 \right)^{\frac{5}{2}}$$ (4-2)

where d_f is the radius of the fibre and parameters c_1, c_2, V_f^{max} depend on fibre arrangement, fibre diameter and fibre volume fraction. Endruweit et al.[35] calculated c_1 and c_2 based on the numerically generated data for intra-tow permeability with random fibre arrangement [140], giving the following values for coefficients in (Eqs 4-1 and 4-2) for the case of carbon fibre tows:

$V_f^{max} = 0.91$, $d_f^2/16c_1 = 5.69$ μm^2, $d_f^2 c_2/4 = 27.49$ μm^2.

Tung et al.[132] showed that the construction of the dual-scale porosity has a significant influence on flow pattern. Previous studies [59] [71] [141] revealed that the tow paths in textile composites are stochastic rather than deterministic, and fluctuate around their mean; other parameters of fabric internal structure, as tow spacing and dimensions [28] [53] and in-plane tow waviness [142] are also variable. Effects of geometric variability on permeability was studied by Endruweit et al.[31] and Loendersloot [143]. It was shown that there is a strong correlation between tow architecture variability and the broad scatter of the fabric permeability [75] [144]. However, these studies did not consider intra-tow permeability, which is the subject of the present work.

The object chosen as an example here is a 2/2 twill carbon fabric, which was used in the permeability Benchmarks I and II [12][13]. The variability of the 2/2 twill carbon fabric geometry has been extensively studied by Olave et al.[145] , Vanaerschot et al [20]–[24] and Gommer et al.[43]; in the latter two papers the fabric is the same as in the present work. In the previous paper [146] the present authors incorporated the geometric variability, measured and mathematically described by Vanaerschot et al. [20]–[24] in the determination of inter-tow permeability, using distributions and spatial correlations of yarn spacing, width and thickness and distortions of the yarn centrelines. This paper adds to this study the link between the geometrical variability and statistics of intra-tow permeability. The model of Vanaerschot et al. [20]–[24] and their experimental data allows one to describe the internal geometry variations of textile reinforcements. Using Gebart-Endruweit's model[35] for prediction of intra-tow permeability we transform the statistical parameters of tow geometry (a sampling of 4320 tow cross sections) into statistics of permeability variation, including correlation characterisation.

4.1 Methodology

4.1.1 The material

A textile-based polymer composite with a 2×2 twill woven carbon architecture from Hexcel (G0986 injecttex) was selected for this study. Table 4-1 summarizes the nominal values of the fabric specifications.

Table 4-1:Specification of the textile in the experimental composite sample[20]–[24]

	Fabric			Tow	
Style	Weave pattern	Areal weight (gm^{-2})	ends /picks count(1/cm)	Average Fibre diameter (µm)	Number of fibres
280T	2×2 twill	280	3.5	7	6000

The composite plate was produced in multiple stages. First, seven layers of the fabric were stacked into a mould cavity to build a fibrous preform. The mould was subsequently closed, compacting the preform to *ca.* 2 mm thickness, a global fibre volume fraction of *ca.*55.3 %. Then, a Biresin epoxy resin system is injected into the mould under pressure (one bar) to impregnate the seven-layer dry preform.

The fabric we have studied is a well-known material of aeronautic grade, and has stable parameters of its textile structure. This is discussed in detail in our previous publication [146] and also supported by other studies with this fabric, including Permeability Benchmark II [13]. Therefore the study of statistics of the fabric internal structure parameters, based on investigation of certain location in the laminate, can be considered representative for the studied fabric.

4.1.2   Image processing

X-ray Micro-Computed-Tomography (micro-CT) device GE Nanotom was used to acquire 3D images. Based on the difference in absorption of X-rays between the resin and the fibres, the parameters of X-ray source (voltage and current of the beam) are set to 33 KV and 295 µA, respectively, to obtain high resolution images with voxel size of (6.75 µm)^3. To evaluate the fibre distribution, additional micro-CT scans require to be done with a voxel size of at least the fibre radius (3.5 micron). These small scale variations are expected to be almost negligible for the intra-tow measurement, but necessary to simulate damage initiation and progression [147], [148]. Sample cross section dimensions were 12.5 mm ×12.5 mm.

The scan yields a 3D volumetric representation of the composite sample that can be converted into a number of equally spaced 2D slices in the warp and weft direction. The cross-section of tows in the warp direction are characterised from slices parallel to the weft direction and vice versa. The 2D image slices were analysed to capture the spatial variability of each tow in the composite sample (see Figure 4-1i). Nineteen slices, spaced by 0.65 mm, were analysed for the both warp and weft tows.

4.1.3   Characterisation of tow cross-section

To characterise the geometry of the tows, ellipses are fit to the imaged tow cross-section by the freeware ImageJ, as shown in Figure in Figure 1i. Due to the nature of RTM process, the preform continuously undergoes deformation, the shape of tow cross-sections can differ from the most often assumed elliptical contour, as discussed for example in [140] [149] [150]. Nevertheless, The ellipse-shaped cross-section is an acceptable approximation to determine tow geometry [145] and is used here to define the tow dimensions in an

unambiguous way (main axis of the approximating ellipse with the same area as the actual cross section).

Under this approximation, tow thickness t and width w were estimated. The tow thickness is equivalent to twice the length of the minor radius, *2b* and the tow width is equivalent to twice the length of the major radius, *2a* (see Figure 4-1ii).

4.1.4   Local permeability calculation

To determine the V_f^{tow} value of each tow, the number of fibres per tow n_t and the radius of fibre were considered as specified in Table 4-1. With knowledge of a pair (t, w), the V_f^{tow} of each tow was computed from the following equation (Eq. 4-3):

$$V_f^{tow} = \frac{n_t \pi r^2}{\pi \dfrac{wt}{4}}$$

$$(\text{4-3})$$

For the given V_f^{tow}, the local permeability along the fibre tow (K_L) and perpendicular to the fibre tow (K_T) were determined by Gebart's equations, Eqs 4-1 and 4-2, with parameters from Endruweit *et al.* [140].

Statistics

The measured tow dimensions, fibre volume fraction within the tows and the calculated permeability were statistically processed as follows:

Pairs of t, w are subjected to statistical analysis and subsequently a statistical distribution model is fit to the scatter plot of w against t. Knowledge of t, w for each tow segment allows the direct calculation of the mean and variance of each property and their covariance for each tow segment.

Histograms of the V_f^{tow} data and permeability components, K_L and K_T, are generated to find out whether they follow certain distribution. The Kolmogorov-Smirnov Statistic (KSS) is used to test the data sets for normality based on P-values. If in the KSS test P <0.05, there is significant probability of deviation from normality. It should be noted that KSS test is a nonparametric statistic, since it does not assume a specific type of a distribution. To graphically assess the goodness of fit of the potential distribution models determined from KSS test, Q-Q plots, Q stands for quantile, are generated.

Since permeability varies continuously because of the spatial geometrical fluctuations of a tow, it can be regarded as a local variable [68]. Random field theory can then be used to characterise the spatial variability of permeability [69].

A semivariogram function *γ(h)*, as a function of lag distance (*h*), is used to characterise the spatial variability of the permeability field. This function (Eq. 4-4) allows one to determine the correlation between two observations(K(z) and K(z+h)) at two distinct locations (z and z+h):

$$\gamma(h) = \frac{1}{2N(h)} \sum_{i=1}^{N(h)} (K(z_i) - K(z_i + h))^2 \qquad\qquad \textbf{(4-4)}$$

where the vector z(x,y) holds coordinates of a point in 2D, N(h) is number of experimental pairs of points separated by a lag distance h. Based on the semivariogram plot, an exponential spatial correlation model(Eq. 4-5) is fitted:

$$\gamma(h) = c_0 \left[1 - \exp(-\frac{h}{a_0}) \right] \qquad\qquad (4\text{-}5)$$

where c_0 is the maximum semivariogram value ($\lim_{h \to \infty} \gamma(h)$), a_0 is the maximum lag distance over which pairs of data points are no longer correlated.

4.2   Results and discussion

4.2.1   Tow cross section and intra-tow fibre volume fraction

Thickness and width of tow

Table 4-2 shows the geometric characteristics of the seven layers. Tow thickness is 0.2±0.02 mm and tow width is 2.50 mm ±0.15 mm (number of measured tow cross-sections per layer is 144). Coefficient of variation, *COV*, of tow thickness is higher than *COV* of tow width. When the preform is compacted to the desired thickness, tow can be deformed more easily in thickness direction rather than the width direction due to the constraint to the tow width at constant tow spacing (3 mm). The measured difference of 11% between maximum and minimum of the tow width and 19% for the tow thickness is in agreement with the data for the similar fabric in Olave *et al.*[145]. The *COV* values are comparable with those reported by Saunders *et al.* [151] for a plain weave glass fabric.

Table 4-2: Tow width and thickness

Statistics	Layer 1		Layer 2		Layer 3		Layer 4		Layer 5		Layer 6		Layer 7	
	t	w	t	w	t	w	t	w	t	w	t	w	t	w
Number of observation per tow path	144	144	144	144	144	144	144	144	144	144	144	144	144	144
μ=Arithmetic mean (mm)	0.20	2.50	0.205	2.35	0.19	2.65	0.20	2.40	0.19	2.45	0.20	2.40	0.185	2.65
σ=Standard Deviation mm	0.02	0.07	0.02	0.14	0.02	0.25	0.02	0.1	0.02	0.13	0.02	0.15	0.02	0.25
COV(%) = σ/μ	10	2.9	11.7	6	11.8	9	10	4.8	11.3	5.4	12	6	13.2	10
Median mm	0.2	2.5	0.2	2.4	0.2	2.5	0.2	2.4	0.2	2.5	0.2	2.4	0.19	2.5
Minimum mm	0.13	2.3	0.15	2	0.12	2	0.15	2	0.15	2.1	0.16	2	0.12	2.1
Maximum mm	0.25	2.7	0.24	2.7	2.6	3	0.2	2.7	0.22	3.3	0.3	2.27	0.2	3.2

The means of *t* and *w* do not vary significantly from one layer to another and their means are *ca* 0.20 mm and 2.5 mm [22] [23] [24] [42]. It could be expected that the compaction of the preform results in more deflection in the tows of the surface layers compared to those of the inner layers (because of more freedom to deform for the tows less constrained on the surface than in the middle of the laminate), but this difference has not been observed. There is also no significant through-the-thickness variation of tow width and thickness (hence also fibre volume fraction in the tows). The sum of the average thickness of all layers (2.74 mm), where the nominal thickness of a layer is taken equal to the doubled tow thickness, is higher than the actual global thickness (2.17 mm). This difference is because of the shift of the layers in relation to their neighbours, leading to nesting [152]. To quantify this nesting, the sum of the average thickness of all layers was divided to the global thickness, resulting in a nesting value of 1.26 which is close to the nesting value of 1.24 reported by Olave *et al.* [145] for a 2/2 twill carbon fabric geometry.

Figure 2 shows the normal distribution (dashed lines) overlying the histogram of the tow thickness t (Figure 4-2 left). The Q-Q plots (Figure 4-2 right) closely fit the Gaussian model (points are inside the 95% interval – dashed curves (the dashed red line), indicating the 95% confidence interval for the Kolmogorov-Smirnov statistics). Hence, tow thickness follows a normal distribution (bar graph) and ranges two standard deviations (2σ) of mean (μ) ; 0.20 mm $\pm2\times0.02$ mm ($\mu\pm2\sigma$) = (0.16 … 0.24) mm. One should note that the limit of $\mu \pm2\sigma$ states that for normally distributed tow thickness 95% range extend from 0.16 mm to 0.24 mm.
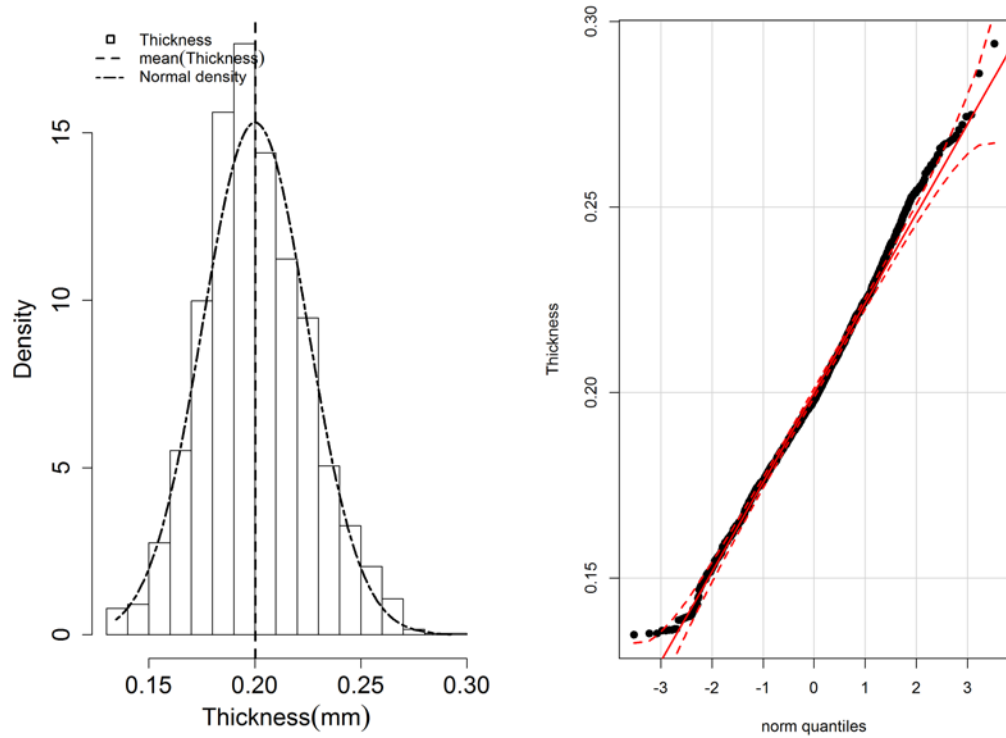
Figure 4-2: Distribution of the tow thickness t. Histogram (left) and Q-Q plot(right). The broken lines (the dashed red line) for the plots indicate the 95% confidence interval for the Kolmogorov-Smirnov statistics.

On the other hand, the tow width *w* does not follow the normal distribution as shown in Figure 4-3, which plots both original (left) and log-transferred (right) histograms of this data. One can observe that the Gaussian model fails to fit in original scales (Figure 4-3 left), while in the transformed scale the normal and log-logistic model yield good fits (Figure 4-3 right). Hence, both the lognormal and log-logistic models can be chosen to characterise the statistics of the tow width. The log-logistic distribution is the probability distribution of a random variables whose logarithm has a logistic distribution. It is similar in shape to the log-normal distribution but has heavier tail.
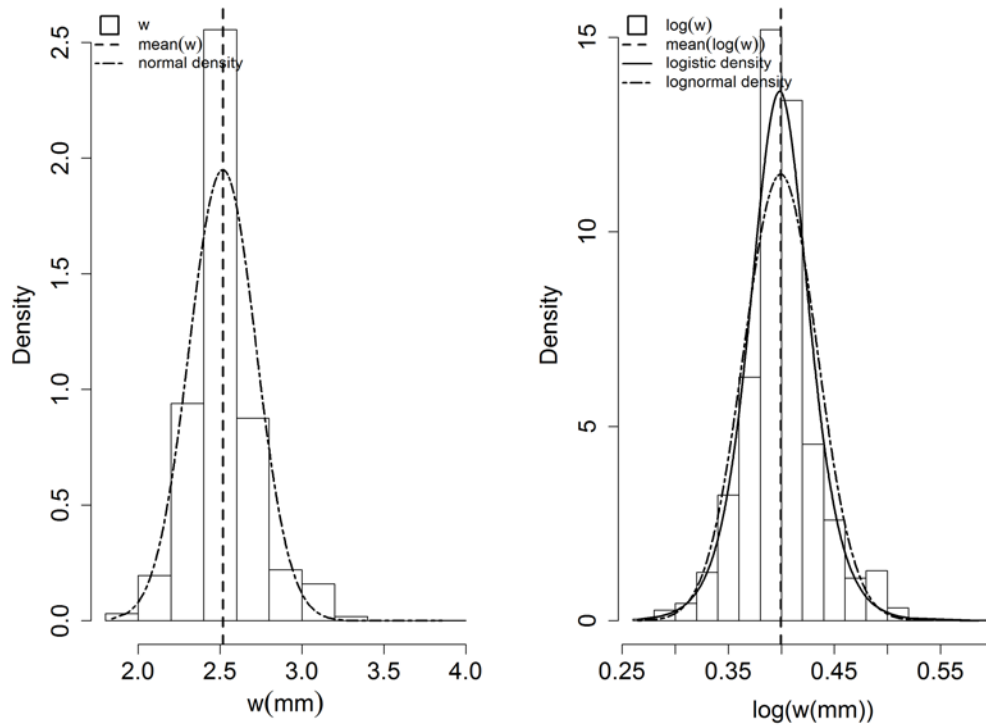
Figure 4-3: Histogram of the tow width w: Original data (left), transformed data (right)

In order to further compare the fitted distributions, the data is subjected to KSS test. The KS distances, which is the distance between the fitted parametric distribution and the kernel density, are listed in Table 3. The log-logistic distribution shows the highest P-value and the smallest KS-distance among the given distributions for the width data. Hence, Table 4-3 suggests that the log-logistic distribution provides the best fit for the width data.

Table 4-3: Kolmogorov-Smirnov statistics(KSS) and corresponding P-values of w

Tow width	W		
Hypothesis	Normal	Log-normal	Logistic
D_{KSS}	0.092	0.078	0.042
P-value	0.46	0.73	0.95

Thus, from our observations, the distribution of the tow thickness, approximated with Gaussian fit, is in agreement with the observation of Olave et al.[145] while the distribution of the tow width, approximated with either log-logistic or lognormal fit, is not. The disagreement in the distribution of the tow width may be due to the difference in the number of measurements; Olave et al.[145] measured a total of 22 tow cross-sections which have 12000 fibres per tow (12K material) and 72 tow cross-sections which have 3000 fibres per tow (3K material) with similar fabric structures while the current study involves 720 measurements per layer.

To find whether or not there is a correlation between the tow width and the thickness (one can expect the negative correlation between t and w because of Poisson effect during compaction of the tow), t is plotted against w as shown in Figure 4, approximated using a linear regression (Figure 4-4, red line) with the coefficient of determination (R^2) of 0.64.

The low R^2 value means that the linear regression is not adequate to represent the correlation between t and w. Then a covariance error ellipse fit was used. The covariance error ellipse (Figure 4 blue ellipse) fit to the data is a measure of strength of the correlation between t and w. In Figure 4-4, a 95% confidence ellipse indicates the region in which the majority of the data resides. The angle of ellipse major axis inclination is determined by the covariance of the data COV (t,w), estimated to be ca -0.12, indicating a negative correlation between t and w. Magnitudes of ellipse's axes are defined by the standard deviations of t (σ_t) and w (σ_w).
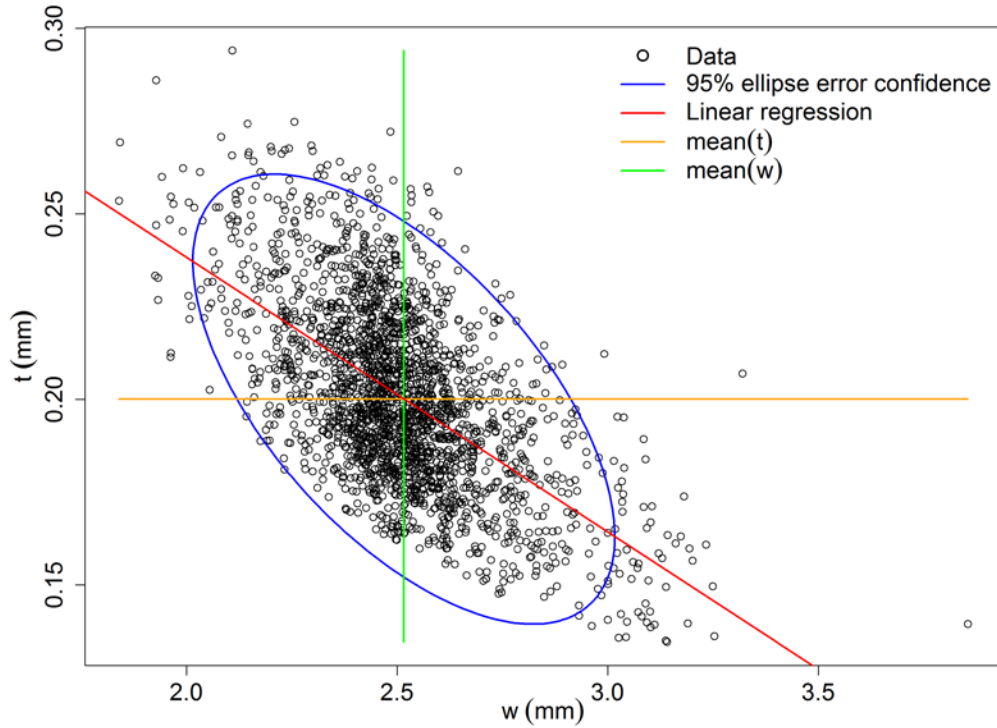
Figure 4-4: Distributions of thickness t and width w and their correlation

In order to further compare the variation of the tow width and the thickness, t and w are plotted versus tow cross section area ($A= \pi \times t \times w/4$) as given in Figure 4-5. The purpose of the comparison is to show their contributions to the variation of A. Figure 4-5 shows that the variability of tow cross-section area ($A= \pi \times t \times w/4$) is dominated by the variability of t. The thickness data (t) show an uphill pattern as moving from left to right in the section area (A) values. On the other hand, the section area (A) is less variable with the variation of tow width (t): 0.15 mm change in thickness and 1 mm change in width lead to 0.2 mm^2 change in the section area. Hence, the correlation between variance of t and w is not as strong as it could be expected. This may be another result of constraining of the tow widening by its neighbouring tows, which affect the Poisson behaviour.
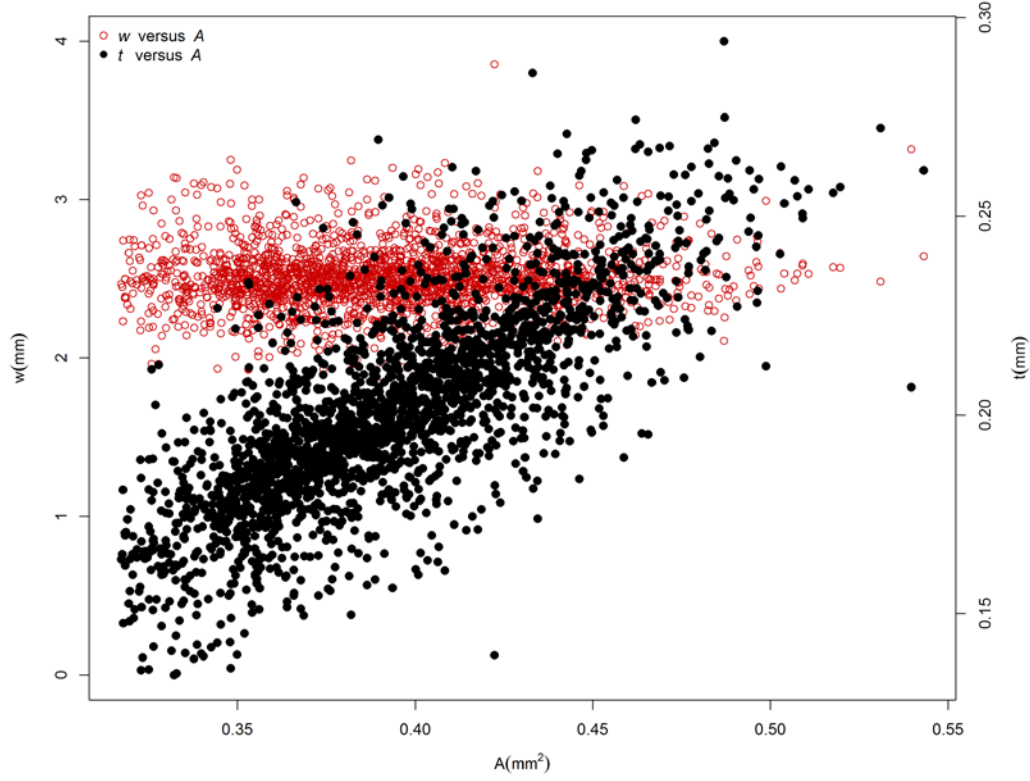
Figure 4-5: Scatter plot of *w* and *t* versus tow section area (*A*)

4.2.2   Statistics of V_f^{tow}

The distribution of V_f^{tow}

Figure 4-6 shows the kernel density estimation of 144 V_f^{tow} segments with a smoothing bandwidth of 5 along warp tows (35 warp towsfor the whole seven layers). The visual inspection of Figure 4-6 shows that the local average values of V_f^{tow} for the warp tows are not much different for all tow paths, ranging from *ca* 57% to 61% (see Table 4-3). Table 4-4 shows that all tow paths have approximately equivalent *CV*s, *ca* 10%. Hence, all tow paths are statistically equivalent, and then the sampling V_f^{tow}, which is obtained from the combination of the 5040 tow segments from seven layers, can be used to characterise the statistics of V_f^{tow}.
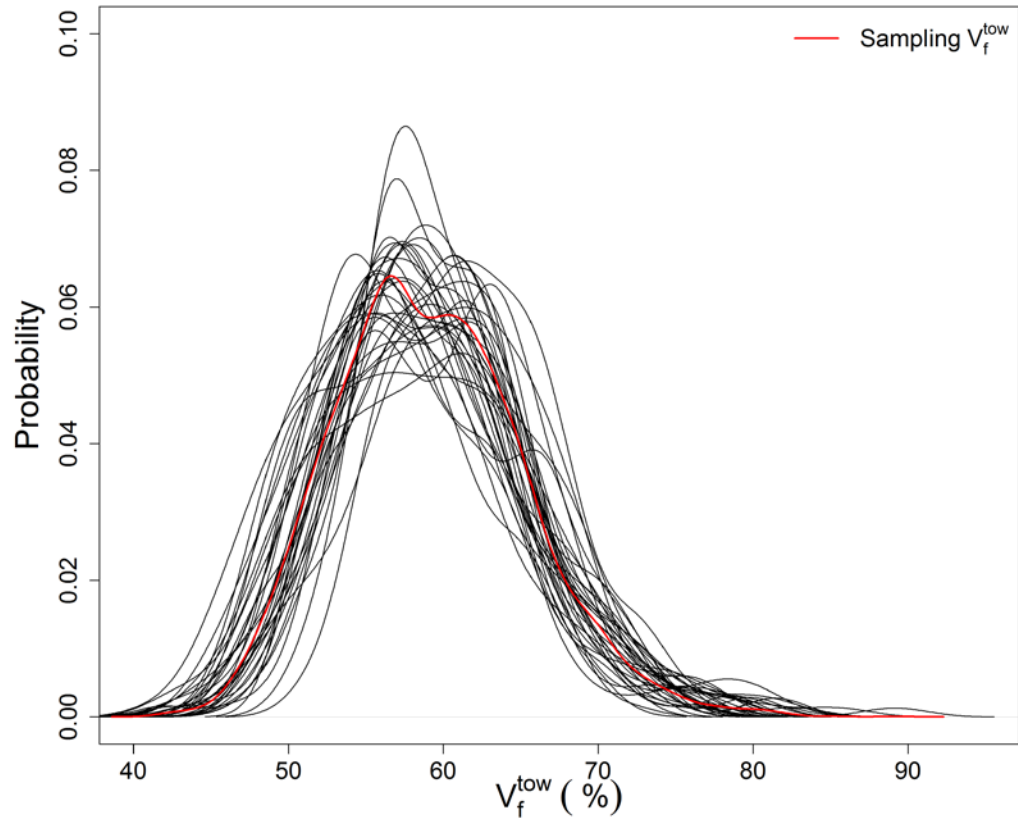
Figure 4-6: The distributions of V_f^{tow} for the different layers. The combined sampling of 4320 tow cross sections resulting in a sampling V_f^{tow} distribution shown in red line

The average of sampling V_f^{tow} is 58.9% (Figure 4-6 in red line). The average of sampling V_f^{tow} is close to that of 12K (58.1%) and is less than that of 3K (62%) observed by Olave *et al.*[145]. The *CV* of sampling V_f^{tow} (10%) is close to what was observed in 12K (12.7%) [145]. A scale effect, mentioned in [145], may have effect on differences in CV.

Table 4-4: Statistics of V_f^{tow} for each layer

Statistics	Layer 1	Layer 2	Layer 3	Layer 4	Layer 5	Layer 6	Layer 7
Number of observation per tow path	144	144	144	144	144	144	144
μ=Arithmetic mean (%)	59.02	57.67	58.57	58.85	60.47	58.45	60.38
σ=Standard Deviation (%)	6.29	5.81	5.95	6.15	5.66	6.08	6.56
COV(%) = σ/μ	10.66	10.08	10.01	10.04	9.36	10.40	10.91
Minimum (%)	43.6	41.71	44.52	44.03	41.98	42.41	43.77
Maximum (%)	81.37	77.36	78.62	78.45	78.45	82.13	81.16

Figure 4-6 shows that the distribution of V_f^{tow} is skewed to the right (Skewness=0.40) while a normal distribution has a zero skewness. The skewed distribution can be described by the truncated normal distribution [140]. However, the observed skewness in [140] was negative and also Endruweit *et al.*[140] did not examine the appropriateness of the suggested distribution model. Hence, the V_f^{tow} data was subjected to the statistical analysis to find which kind of the statistical distribution model can properly describe the variation of the sampling V_f^{tow}

An appropriate distribution for the sampling V_f^{tow} is assessed by plotting data histograms of the sampling intra-tow fibre volume fraction data, and assessing their fit by comparing

the original and logarithmic scales versions of these plots. Figure 4-7, shows both original (left) and log-transferred (right) histograms of this data.
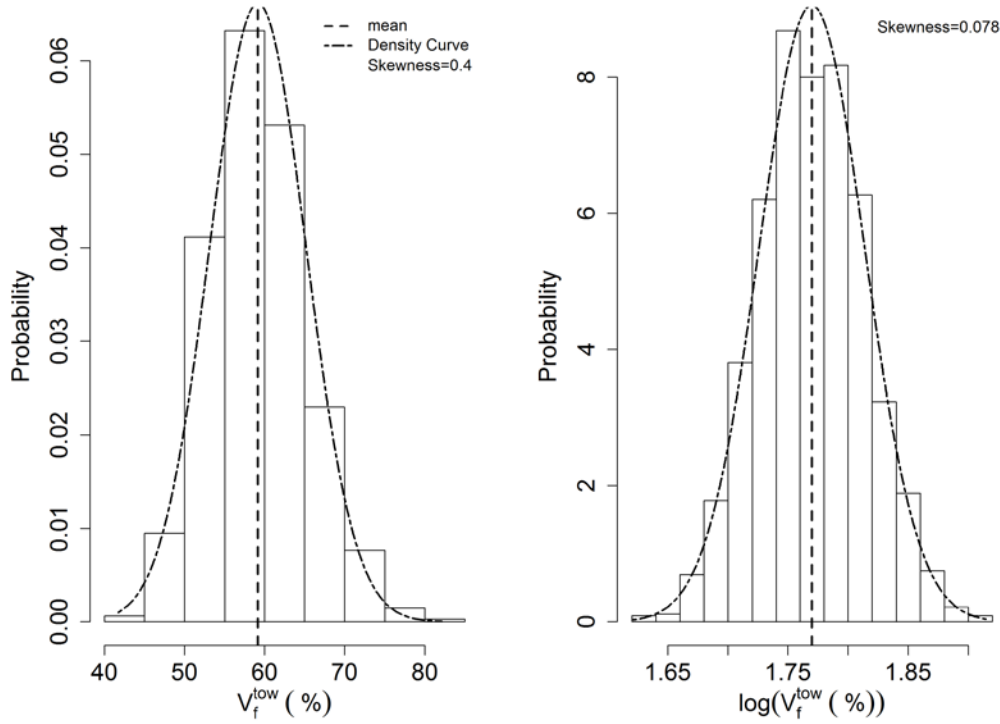

Figure 4-7: Histogram of the sampling V_f^{tow}: Original data (left), transformed data (right)

Although the normal density curve goes almost through the centres of histogram columns (Figure 4-7 left), the curve cannot capture the skewness of the distribution. On the other hand, in the transformed scale (Figure 4-7 right), the normal density curve not only goes through the centres of histogram columns but also captures the tails. This observation is further confirmed by the values of skewness and kurtosis; the log-transformed data has a skewness value of 0.073 and a kurtosis of 2.99, which ranges between the -3 and 3 accepted [153], while those values are 0.4 and 3.34 for the case of original data. In that sense, although the Gaussian model may to some extend describe the statistics of V_f^{tow} in original scales (Figure 4-7 left), in the transformed scale the lognormal model seems more appropriate (Figure 4-7 right).

In order to further compare the fitted distributions, the data is subjected to KSS test. The KS distances, which is the distance between the fitted parametric distribution and the kernel density, are listed in Table 4-5. The log-normal distribution shows the higher P-value and the smaller KS-distance compared to the normal distributions for the V_f^{tow} data. Hence, Table 4-5 suggests that the log-normal distribution provides the best fit for the V_f^{tow} data.

Table 4-5: Kolmogorov-Smirnov statistics(KSS) and corresponding P-values of w

intra tow fibre volume	V_f^{tow}	
Hypothesis	Normal	Log-normal
D_{KSS}	0.035	0.017
P-value	0.62	0.98

As t and w have a negative correlation and, especially w, have limitation in variation due to the weave structure (Figure 4-5), the distribution of V_f^{tow}, which depends on w and t (Eq.3), is not necessarily symmetric and normal [154][155], which is what is observed.

4.2.3   Statistics of permeability

The distribution of permeability

For each V_f^{tow} obtained from the cross section of each tow, the local permeability values along the tow path (K_L, longitudinal permeability) and perpendicular to the tow path (K_T, transverse permeability) were determined by Gebart-Endruweit's model [35], using the same fibre geometry-related parameters, as were identified for permeability of carbon tows with random fire distribution in [35]. The improvement of Gebart-Endruweit's model [35] compared to the models reported in Happel [135], Gutowski *et al.* [156], , Sharaoui and Kaviany [139], Bruschke and Advani (1993) [137] and Lee and Yang [138], which developed semi-empirical equation for the regular arrangement of fibres, either hexagonal or square arrangement, is that the values of the constants in Gebart-Endruweit's model [35], which depend on fibre packing arrangement, were computed the distance from each fibre to its number of the nearest neighbouring fibres with approximately identical distance based on the Voronoi cell tessellation.

The kernel density estimation of K_L and K_T are plotted in Figure 4-8. The visual inspection of Figure 4-8 shows a broad scatter of permeability in both directions for all tow paths, ranging from *ca* 0.10 μm^2 to 7.00 μm^2 for K_L and *ca* 1.00×10^{-4} μm^2 to 5.50×10^{-2} μm^2 for K_T. The comparison of the probability distributions of permeability each layer shows that there is not significant difference between the layers in permeability.
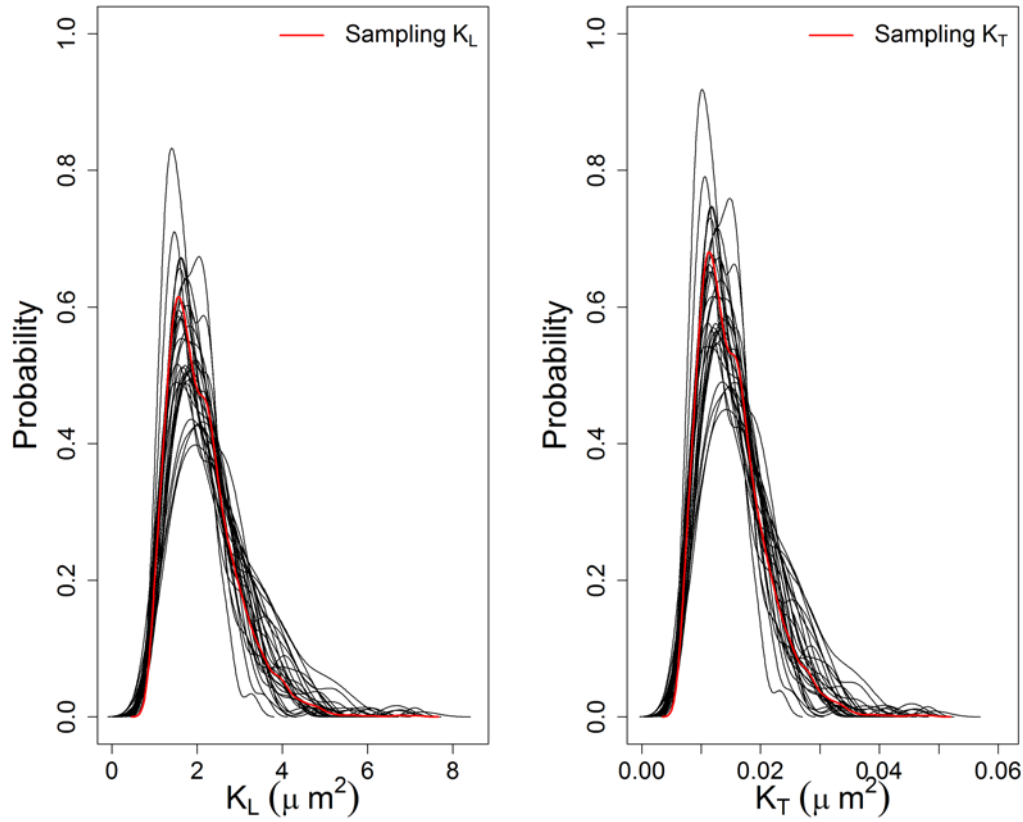
Figure 4-8: The probability distributions of permeability along tow paths for all seven layers: K_L (left) and K_T (right). The combined sampling of 4320 tow cross sections resulting in sampling K_L (left) and K_T (right) distributions shown in red line

Similar to the equivalent statistics of V_f^{tow}, the equivalent statistics of permeability components for all tow paths are presented by Figure 4-8 and Table 4-6. Hence, the variation of permeability along warp tows is due to the existences of regions with high packing density of tows, where V_f^{tow} is high and vice versa.

Table 4-6: Statistics of permeability components

Statistics	Layer 1		Layer 2		Layer 3		Layer 4		Layer 5		Layer 6		Layer 7	
	K_L	K_T	K_L	K_T	K_L	K_T	K_L	K_T	K_L	K_T	K_L	K_T	K_L	K_T
Number of observation per tow path	144	144	144	144	144	144	144	144	144	144	144	144	144	144
μ=Arithmetic mean (μm²)	1.35	0.009	1.52	0.01	1.36	0.009	1.32	0.008	1.3	0.0089	1.41	0.009	1.35	0.009
σ=Standard Deviation (μm²)	0.85	0.006	0.91	0.0063	0.81	0.005	0.83	0.005	0.92	0.006	0.8	0.006	0.8	0.006
COV(%) = σ/μ	63	66	59	63	59	55	63	62	66	67	60	66	63	66

The sampling K_L and K_T, which are obtained from the combination of the 5040 tow segments from seven layers, can be used to characterise the statistics of permeability components (Figure 4-8 red line). The detailed statistical characterizations of the sampling permeability components are summarised in Table 4-7. The difference between maximum and minimum values of permeability is two order of magnitude as shown in Table 4-7. The

mean values of K_L and K_T are 1.31 μm^2 and 0.92× 10^{-2} μm^2 as shown in Table 4-7. The standard deviations are 61% of the mean values of K_L and K_T.

Table 4-7: Statistical characterization of the permeability values along and across the fibre predicted by Gebart-Endruweit's model[35] (Eq.s 4-1 and 4-2)

Permeability	K_L	K_T
Number of observations	4320	4320
μ=Arithmetic mean (μm^2)	1.31	0.92× 10^{-2}
σ=Standard Deviation(μm^2)	0.813	5.6× 10^{-3}
COV(%)=σ/μ	61	61
Median(μm^2)	1.15	0.81× 10^{-2}
Minimum(μm^2)	0.0481	1.74 × 10^{-4}
Maximum(μm^2)	6.42	0.043
Skewness	1.3	1.2

The values of skewness reported in Table 4-7, which is out of the normality range (-0.5<skewness<0.5), suggest that the Gaussian model is not appropriate for statistical characterisations of intra-tow permeability components. In fact, the normal distribution does not fit all the values; the expression of the data by $\mu\pm\sigma$ does not imply the assumption of a normal distribution. For example, subtracting 2σ from μ leads to negative values while permeability data must be positive, by definition. Furthermore, simulation results showed that permeability values at microscale cannot physically follow a normal distribution [72]. Figure 4-9 shows the histograms of the permeability components, K_L (Figure 4-9 left) and K_T (Figure 4-9 right).
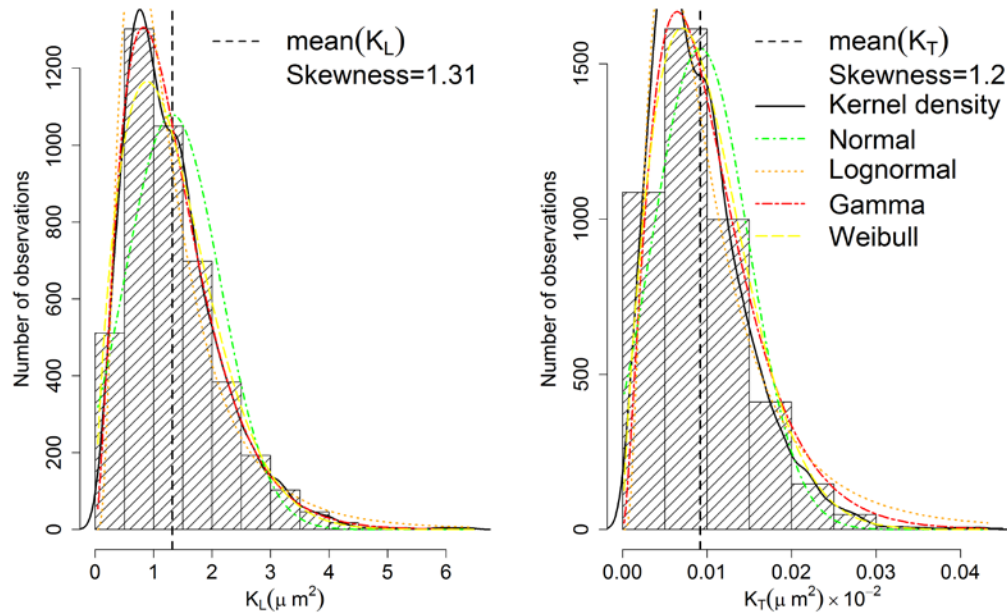
Figure 4-9: Histograms of the overall permeability along the fibre (left) and across the fibre (right)

Figure 4-9 illustrates how well the different distributions including normal, lognormal, Gamma, and Weibull fit to the kernel density. It is clear that the normal distribution fails to represent the distribution of permeability values. Figure 4-9 also shows the Gamma provide better fit to the Kernel density than both the Weibull and the lognormal

distributions. The previous studies [29][15][44] suggested the lognormal distribution for the right-skewed permeability distributions.

To assess which of these distributions better fits to the data, two data transformation methods are applied to the permeability components: log transformation and the cube root of the data [157]. If the data looks symmetric after log transformation, the lognormal distribution would work better to represent the variation of the permeability. If the data looks symmetric after the cube root transformation, the gamma distribution would work better for the permeability variation[157].

According to Figure 4-10 (left), although the log transformation seems to fit well in the body of the permeability components, the data is left-skewed on the log scale. The left skewness on log scale was also observed in the work of Zhang *et al.*[44]. On the other hand, Figure 4-10 (right) shows that the histogram of the cube root of the intra-tow permeability components looks symmetric, supporting the appropriateness of the gamma distribution.
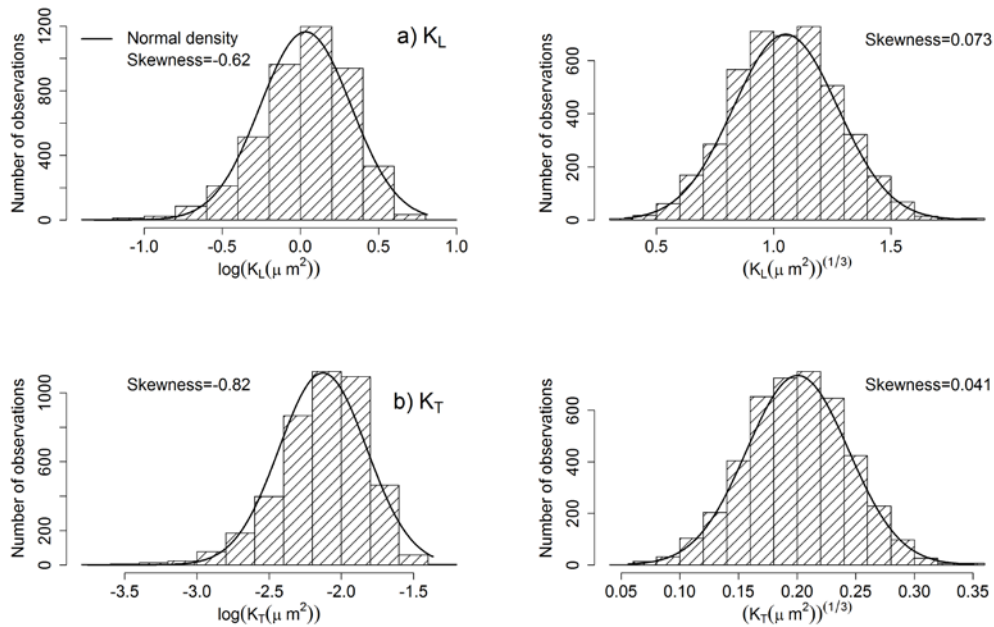
Figure 4-10: The histograms of permeability components, K_L(a) and K_T (b) after log transformation(left) and the cube root transformation(right).

4.2.4   Applicability of the gamma distribution

In order to examine the applicability of gamma distributions to other empirical permeability equations [158] [135] [156] [48] [139] [138], these equations were first applied to calculate the sampling $K(V_f^{tow})$. Then the sampling $K(V_f^{tow})$ are subjected to the Kolmogorov-Smirnov Statistics(KSS) for goodness of fit test in terms of normal, lognormal, Gamma, Weibull and Beta distribution models. As shown in Table 4-6, most of studies related to the circular array of solid fibre with a square or hexagonal configuration. The Darcy or Navier-Stokes equations were used to find correlation between permeability and fibre volume fraction within the given geometries. In Figure 4-11, the Kernel densities of various correlations between intra-tow permeability and intra-tow fibre volume fraction

are plotted. It is observed that the graphs of the correlations by Happel [135], Gutowski *et al.* [156], Gebart- Endruweit [35] , Sharaoui and Kaviany [139], Bruschke and Advani (1993) [137] and Lee and Yang [138] follow the same asymptotic nature as the Kozeny-Carman equation[158]. Despite different geometric structure from granular beds in Kozeny-equation [158] to fibre packing tows in Gebart- Endruweit [35], the Kernel densities of the various correlations are almost identical with long-right tails. Hence, one can conclude that the quality of the correlations are not truly different from each other. Different equations, in spite of different assumptions used for their derivation and different ranges of applicability (fibre arrangements, fibre volume fractions etc) describe the same variability behaviour of a fibrous medium.
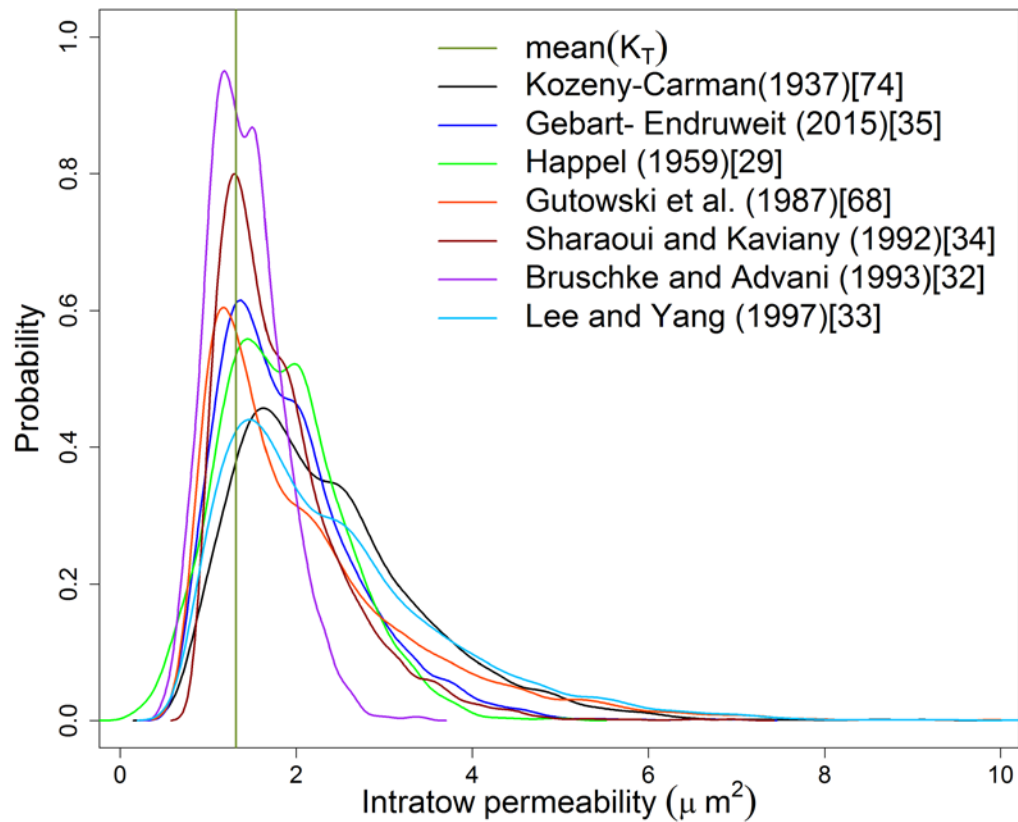
Figure 4-11: The comparison of various correlations between intra-tow permeability and intra-tow fibre volume fraction

The P-value computations are listed in Table 4-7. Gamma distribution shows the largest P-values among the given distributions for the different empirical permeability equations. Hence, based on the information in Table 4-7, it is suggested that the gamma distribution provides the best fit for the all models. *CV*s of the intra-tow permeability obtained from all empirical equations range between 44 and 74%. Note that, the relations by Happel [135], Gutowski *et al.* [156], Gebart- Endruweit [35] , Sharaoui and Kaviany [139], Bruschke and Advani (1993) [137] and Lee and Yang [138] follow the same asymptotic nature as the Kozeny-Carman equation[158]. Hence, these different models, which principally follow the same correlation structure, can produce the same distribution model (the gamma distribution).

However, the previous studies suggested [44] [16] that lognormal distribution can be used for the statistics of permeability for different types of fabrics. Meanwhile, the calculations (Table 4-7) show that the lognormal model is as poor as normal distribution. Although permeability is continuous over the warp tows, permeability components in this study were calculated from discretised regions (at 0.75 mm intervals). Then, one could propose a mathematical interpolation characterising the predicted permeability data to fill the gap in the observations. However, the permeability variation over a warp tow is a probabilistic process rather than a deterministic process and hence that it follows the gamma distribution for which the permeability of the inter-interval gap between any two sequence tow cross sections is a gamma random variable.

Table 4-8: Applicability of gamma distribution for different intra-tow permeability models

Intra-tow models	COV (%)	Distribution model				
		Normal	Lognormal	Gamma	Weibull	Beta
Kozeny-Carman(1937) [158]	47.5	4.6e-13	4.4e-5	0.346	2.9e-06	1.0e-09
Happel (1959) [135]	44	2.1e-8	1.3e-5	0.1697	3.3e-4	4.7e-4
Gutowski et al. (1987) [156]	73	2.2e-16	2.2e-9	0.2948	7.6e-4	4.8e-3
Gebart K_a (1992) [48]	61	6.1e-15	1.2e-8	0.5244	3.8e-4	2.2e-16
Gebart K_p (1992) [48]	61	4.9e-11	4.9e-6	0.3171	1.5e-05	4.8e-3
Sharaoui and Kaviany (1992) [139]	54	2.2e-16	2.2e-16	0.2336	1.8e-3	2.3e-4
Bruschke and Advani (1993) [137]	52	4.6e-14	1.1e-4	0.2883	1.3e-6	1.5e-8
Lee and Yang (1997) [138]	53	7.8e-12	1.6e-7	0.1209	3.1e-3	4.3e-4

4.2.5   K variation along the tow

The spatial distribution of the warp out-of-plane centroid path of single layer (Z), the tow aspect ratio (AR), tow area (A), V_f^{tow}, and K_L along the tow path are plotted in Figure 4-12. Because of the similar variation patterns of K_L and K_T, the distribution of K_L along the tow path is only reported here. The visual observation of graphs (Figure 4-12) for the tow geometry suggests that the geometric variability of the tow follows periodic patterns that correlate with the tow shape defined by the weave architecture (particularly the positions of the tow crossover points) (Vanaerschot et al. [22]). The AR, A and V_f^{tow} and K_L are correlated with the location of the crossover points. The K_L is minimum at crossover point and V_f^{tow} is maximum, where the area (A) is minimum [22], as shown in Figure 4-12. This means that the tow crossover points constrain the movement of tows, which are long and tortuous, and hence randomly moving from one point to another cannot change too much V_f^{tow} and permeability components at the crossover points, leading to non-normal behaviour of permeability components and V_f^{tow}.
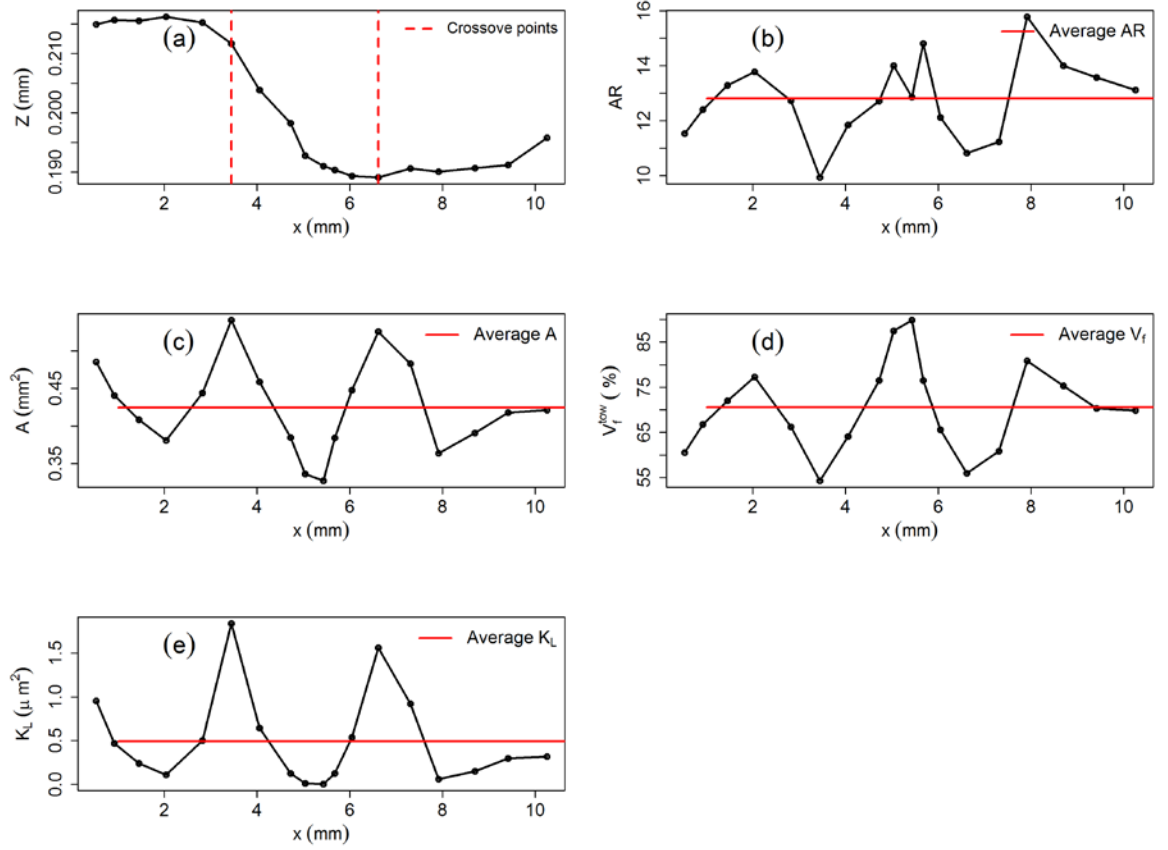
Figure 4-12:The variation of tow geometry parameters and theirs correlation with V_f^{tow} and K_L along a tow path: (a) Z, (b) AR, (c) A (d) V_f^{tow} (e) K_L

The *CV* of the *A* is *ca* 4%, while the *CVs* of *AR* and V_f^{tow} are *ca* 12 and 10%. K_L is more sensitive than *AR* and V_f^{tow}, where its *CV* is *ca* 61%. In fact, the higher variation of the intra-tow permeability (*ca* 61%) compared to V_f^{tow} (*ca* 10%) is due to the structure of the Eqs.4-1 and 4-2 (the Gebart- Endruweit equation [35]). Consider the second order Taylor expansion, around ($\mu_{V_f^{tow}}$) for K_L (V_f^{tow}):

$$K_L := K_L(V_f^{tow}) = K_L(\mu_{V_f^{tow}})$$

$$+ \frac{dK_L(\mu_{V_f^{tow}})}{dV_f^{tow}}(V_f^{tow} - \mu_{V_f^{tow}}) + \frac{d^2 K_L(\mu_{V_f^{tow}})}{d^2 V_f^{tow}}\frac{(V_f^{tow} - \mu_{V_f^{tow}})}{2}$$

$$\frac{dK_L(\mu_{V_f^{tow}})}{dV_f^{tow}} = -569\frac{(\mu_{V_f^{tow}} - 1)^2(\mu_{V_f^{tow}} + 2)}{100(\mu_{V_f^{tow}})^3} = -1.315 \qquad (4\text{-}6)$$

$$\frac{d^2 K_L(\mu_{V_f^{tow}})}{d^2 V_f^{tow}} = -1707\frac{(\mu_{V_f^{tow}} - 1)}{50(\mu_{V_f^{tow}})^4} = -37.545$$

where $\dfrac{dK_L}{dV_f^{tow}}$ and $\dfrac{d^2K_L}{d^2V_f^{tow}}$ are the 1st and 2nd derivatives of K_L with respect to V_f^{tow}, respectively, and and $\mu_{V_f^{tow}}$ is the average value of V_f^{tow}. Then the equation (Eq.4-6) for the variance (σ^2) becomes:

$$\sigma^2(K_L(V_f^{tow})) = \left[\frac{dK_L(\mu_{V_f^{tow}})}{dV_f^{tow}}\right]^2 \sigma(V_f^{tow}) - \frac{\left[\dfrac{d^2K_L(\mu_{V_f^{tow}})}{d^2V_f^{tow}}\right]^2}{4}\sigma^2(V_f^{tow}) \ (\textbf{4-7})$$

From Eq.4-7, the approximation of CV (K_L (V_f^{tow})) is 62 %, corresponding to CV (V_f^{tow}) =10 %.

The K_L was normalized to zero mean (K_L-μ(K_L)). The graphical summary of autocorrelation function (ACF) is shown in Figure 4-13. The dashed lines on the both sides of the zero mean are two standard deviations from zero. The autocorrelation plot of the normalized data (Figure 4-13) shows periodicity around the zero mean and decays towards zero.
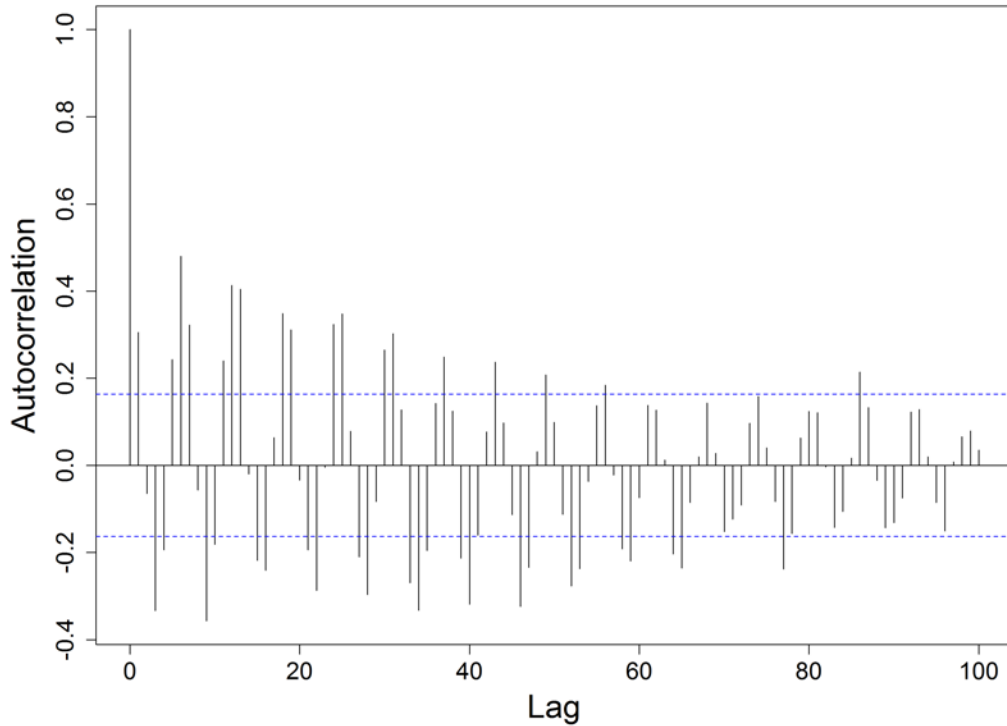
Figure 4-13: The autocorrelation of permeability variations parallel to fibre along the tow path concealing a sine function.

The sine structure of the autocorrelation is observable. There is a dependency between the intra-tow permeability components and fibre tow waviness, which agreed with the observation of Endruweit and Long [28] who assumed the local variation of permeability

is primarily occurred by the stochastic variation of tow path. The stochastic cycle pattern can be a sine wave with a period of T_K in Eq.4-8:

$$K_L(x) = K_0 + A\sin(2\pi\frac{x}{T_k}))\tag{4-8}$$

where x is the pitch distance between two points on the tow centreline, A is the amplitude of the sine wave (*ca* 2 μm^2), and K_0 is average K_L. Eq.4-8 defines the spatial variation of the permeability along a tow path, T_K is the distance for one cycle. The periodic variation of the tow centroid positions also takes the sin function with period, T_p. By fitting Eq. 4-8 to Figure 4-12 (e), the period of K_L variation was estimated T_k=3.3mm, corresponding to the tow spacing (3 mm). The period of tow centroid position was estimated T_p=6 mm, corresponding to the length of a tow float (5.7 mm), which is two times larger than T_k. This was also confirmed by the correlation length of 3.2 mm by linking semivariogram and the variations of K_L.

As shown by Vanaerschot *et al.* [22],the continuity of tow paths leads to the spatially correlated random field of the V_f^{tow} and permeability components. The semivariogram, characterization of spatial correlation, for V_f^{tow} and K_L is shown in Figure 4-14 as discrete points using Eq. 4-4. The scatter plots (Figure 4-14) show fairly typical semivariograms.
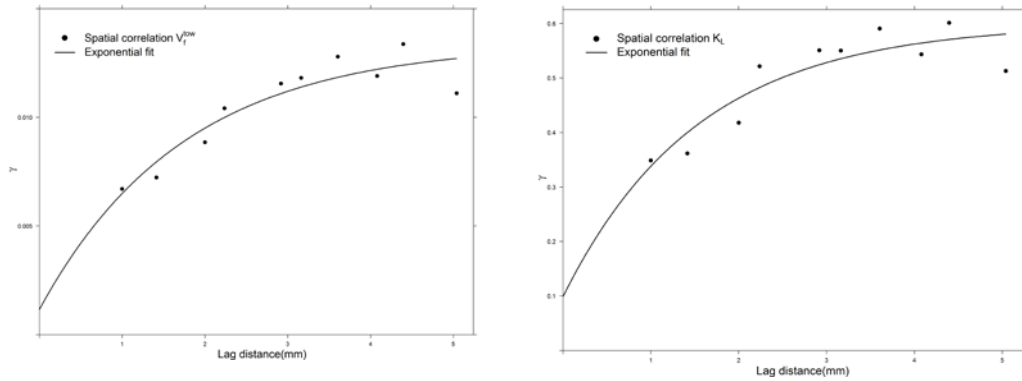
Figure 4-14: Semivariogram function: V_f^{tow} (left), K_L(right)

An exponential spatial correlation model was fitted to the scatter plot by a nonlinear-mixed effects methods, incorporating fixed and random effects [73]. Table 4-8 gives the exponential model parameters for V_f^{tow} and K_L. The results for K_T was the same as those reported for K_L.

Table 4-9: Exponential semivariogram model parameters

Variables	a_0(mm)	c_0
V_f^{tow}	3.2	0.012
K_L	3.1	0.47

The semivariograms of V_f^{tow} and K_L increase with lag distance, which refers to the discretisation step of 1 mm, (e.g. decreasing correlation) and γ, describing the degree of spatial correlation of a spatial random field, levels off at a distance lag of *ca* 3.1 mm, corresponding to a tow space centreline, (Figure 4-14), which is called sill. This correlation length is the same as the reported weft tow correlation length of 2-4 mm in [22]. Comparing the sill (c_0) for V_f^{tow} (Figure 4-14, left) with the sill for K_L (Figure 4-14, right) shows the higher c_0 for K_L: indicating higher variance of permeability (Table 4-8). This suggests larger permeability variability over shorter distances compared to the V_f^{tow} variability. Therefore, the variations of K_L correspond to the tow spacing rather than the twill structure. In that sense, the through thickness interaction of tows due to compression and nesting is more influential rather than their crimp.

Note that our calculations, based on the average V_f in tow cross sections, allow only evaluate variations of longitudinal (K_L) and transvers (K_T) permeability, based on an abstraction of the tow local structure as a unidirectional array of fibres randomly (and uniformly) distributed over the cross section. The fact that K_L and K_T correspond to the principle directions is inherent to this abstraction. One can suspect that in vertically compacted tows the permeability tensor is not transversely isotropic. This question was never addressed in the literature and is definitely worth investigating in the future.

Another possible direction of the future work related to the change of cross section of tows after draping of the fabric. There are studies of this process, some of them use the same fabric as studied in the present paper[159]. These studies contain information of change of the tow geometrical parameters after the fabric deformation. An interesting direction of the future work can be an attempt to calculate change of the statistical distributions, investigated by us in the present paper, after tow transformations because of the deformations in draping.

4.2.6   Comparison with permeability benchmark II

Intra-tow permeability results predicted for the seven-layer 2×2 twill woven carbon can be analysed taking into account the results from the benchmark II exercise, where the same fabric was studied [13]. In this permeability benchmark, twelve participants followed a guideline document [14] to minimize experimental uncertainties (injection pressure, viscosity, fibre volume fraction, etc.), in order to introduce better control on the experiment conditions, observed in the permeability benchmark I [12]. This exercise showed a much smaller variation in permeability data compared to the first data set, supporting the concepts contained in the guideline document in this second case. The resulting variability contained in permeability was attributed to differences between experimental procedures (which were normalised, but performed in different labs) and the intrinsic variability of the textile material (global variability).

Our calculations provide local variability, which is only one of the sources of variability seen in the measurements. Although this study looks into the same material that was considered in the benchmark II exercise [13], a direct comparison between permeability results obtained in the proposed methodology and those are published in Vernet *et al.* [13] is not entirely possible. In fact, our results ignore the intrer-tow flow, whereas the benchmark II exercise results [13] are macro-experiments, integrate inter-yarn flow.

Table 4-9 summarises statistical characterisations of intra-tow permeability (microscale), K_L and K_T, compared to those of K_{bx} and K_{by}[5] (macroscale) from the benchmark II exercise [13] and K_x and K_y from the virtual geometry (mesoscal) [146]. It can be expected that the local variation would show higher variability than the variability between fabric sheets, which are averages of local permeabilities. The coefficient of variation of K_{bx} and K_{by} are approximately three times smaller than K_L and K_T, as shown in Table 4-9. This is of no surprise, as the overall permeability is a result of averaging of the flow velocity, hence the large variations of the local permeability results in smaller variation of the average.

Table 4-10: Intra-tow permeability vs. overall permeability(benchmark II [13])

Statistics	Intra-tow permeability (microscale)		Inter-tow permeability (mesoscale)[146]		Benchmark II (macroscale) [13]	
	K_L	K_T	K_x(Warp)	K_y(Weft)	K_{bx}(Warp)	K_{by}(Weft)
Number of observations	5040	5040	100	100	72	69
μ= mean $(\mu m)^2$ Arithmetic	1.31	5.6×10^{-2}	81.5	92.5	80.7	131
σ=Standard Deviation$(\mu m)^2$	0.813	5.6×10^{-3}	10.1	13.9	17.7	28
CV(%)=σ/μ	61	61	12	15	21.9	21.3
Statistical distribution model	Gamma	Gamma	Normal	Normal	Normal	Normal

4.3   Conclusion

The influences of the tow geometry variability along tow paths on intra-tow permeability components (K_L and K_T) for the case of a 2×2 twill woven carbon fabric were studied. K_L and K_T were predicted from V_f^{tow} by applying Gebart-Endruweit's model[35]. V_f^{tow} was computed from the ellipse-fit tow cross-section area. The tow geometry was characterised by the width (w) and the thickness (t). The statistical parameters of tow geometry, a sampling of 5040 tow cross-sections, were transferred into statistics of permeability variation, including correlation characterisation, and the following features were observed:

(1) Constraint of the tow widening under compression in the weave structure leads to a difference in the statistical behaviour of the tow width and thickness: the tow thickness follows a normal distribution while the tow width follows either a lognormal or a log-logistic distribution. The tow width and thickness are correlated and a negative correlation was evident, albite weak.

---

[5] superscripts of bx and by represent the permeability components of benchmark II in x and y directions, correspondingly.

(4) The statistical analysis suggested that the statistical variation of V_f^{tow} and the permeability components over the fabric at tow level follow a log-normal distribution and a gamma distribution models, respectively.

(5) The statistical analysis also shows that intra-tow crossover points and inter-layer nesting are the major contributors to the permeability variations.

(6) Spatial correlations of V_f^{tow} and the permeability values were calculated and found that the V_f^{tow} and permeability variations showed a correlation length of *ca* 3 mm, corresponding to the tow spacing in the fabric.

These features provide guidelines for the Monte-Carlo modelling of the intra-tow variability in woven laminated in the unit cell level studies of the stochastic characteristive of the spatial variability of the homogenised permeability.

Chapter 5

Experiment errors

Accounting experiment errors in uncertainty propagation of permeability measurements of a 2/2 twill carbon fabric

Experimental statistics is an important part of the interpretation of permeability data. This study presents an evaluation of the uncertainties produced by measuring instruments and equipment in in-plane permeability determination for a preform consisting of seven-layer 2/2 twill carbon reinforcement. The uncertainty measurements were quantified in terms of device accuracy and performance limitations. Preliminary results reveal that viscosity, pressure and porosity parameters have significant influence on permeability measurements. The statistical distribution models are obtained by applying Monte-Carlo simulation based on the experimental uncertainty propagation. The predictions show that both porosity and permeability components follow the Gaussian normal distribution. The results also indicate that the variation in permeability is mainly due to the internal geometry variations of fabric rather than the measuring system.

Keywords: Permeability; Uncertainty; Resin Transfer Moulding (RTM); Monte-Carlo method

Introduction

The reliability of mathematical models to predict flow fronts inside fibrous media is strongly dependent upon the accuracy of input variables; one of the most elusive of which is the permeability of the fibrous medium, in part because permeability is not directly determined but calculated via several other measured values. However, a common problem is the observed high standard deviations in permeability data; Hoes *et al.* [15], Pan *et al.*[36], and Vernet *et al.*[13] reported the coefficient of variations lie in the range 13-22%. This large standard deviation is caused with various sources of uncertainty, some come from experimental procedure and set ups (macroscale 5 mm-0.5 m)and some come from not only the heterogeneous nature of fabrics (dual scale nature; microscale 10-500 μm, and mesoscale 500 μm -20 mm) but also nesting.

As with other properties, so too has the uncertainty of permeability been characterized by using probability density functions to describe its variability, in which, an appropriate statistical distribution model to permeability data is a key part of data analysis. Recent efforts reveal a shift towards propagating the uncertainties in statistical model predictions.

Research has been done in the past to fit suitable statistical models to permeability data. Pan *et al.* [36] conducted a series of experiments for two types of fibrous preform, and

proposed that a normal distribution would be a suitable model for macroscopic permeability. Hoes *et al.* [15] suggested that macroscopic permeability values at a specific fibre volume fraction exhibit a broad distribution which would be approximated by a normal distribution model and attributed the large scatter in permeability values to the nesting. Li *et al.* [70] suggested the normal and the Weibull distributions for macroscopic permeability without and with race-tracking. Endruweit *et al.*[71] showed the scatter of macroscopic permeability values as a result of fibre shear could be modelled by a normal distribution . Wong and Long [72] attributed a large skewness in mseo-scale permeability data to internal geometry variations of the fabric architecture and showed this variation would tend to a normal distribution in large domain.

Despite this, Padmanabhan and Pitchumani [16]assumed a normal distribution for porosity and a lognormal distribution for permeability in order to avoid negative results in cases with high standard deviations and to exhibit a narrow distribution of permeability values. Zhang *et al.*[44] showed a normal distribution for fibre volume fraction and a lognormal distribution for the micro-scale permeability for a random fibre fabric. Furthermore, simulation results of [105] showed that permeability values at microscale could not follow a normal distribution due to tow orientation and nesting.

One major limitation of the proposed statistical models is that they attributed the statistics of permeability to the heterogeneous nature of fabric and did not include the possible errors from experimental measurement. Additionally, the simulations for proposing an appropriate statistical model might lead to wrong conclusions without consideration of the possible errors resulted from the experiment measurements. It implies that the validation of a statistical model should encompass all possible sources of uncertainties.

The state of the art, explained above, reveals a need for the uncertainty propagation for an appropriate statistical distribution model of permeability. Identifying where errors propagate in a measurement system is important for development of a robust permeability measurement. Uncertainty propagation helps reveal the significant parameters in a measurement system, and to establish how different input variables associated with errors affect the magnitude of permeability. Additionally, this uncertainty propagation also provides insight into how to improve the measurement system to reduce or eliminate these errors.

Quantifying the different sources of uncertainty (from macro to microscale) in one-step computation will be a complex task. In addition, separating these steps would help one to identify the significance of various uncertainty contributors to the statistics of the permeability. In the previous papers [146] [160] we incorporated the geometric variability in the determination of intra-tow and inter-tow permeability, using distributions and spatial correlations of yarn spacing, width and thickness and distortions of the yarn centrelines as well as random distribution of filaments inside a tow. The focus of the current study is the influence of macroscale variability due to the device accuracy and performance limitations on the statistics of permeability.

This study aims at establishing an uncertainty analysis for 2D permeability as a result of device accuracy and performance limitations. The first objective is to identify sources of uncertainty that cause variations in composite quality. The second objective is to quantify the performance of measuring tools to see the contributing factors of uncertainties in permeability measurement system. The final objective is to carry out a multiple statistical simulation from the input distributions by Monte Carlo simulation. An appropriate distribution function is then fit to simulation outputs.

5.1 Methodology

5.1.1 Material

Table 5-1 shows the specifications of the fabric under analysis. Seven plies of the aligned circular fabric were impregnated with epoxy resin system (Norsodyne I 16333).

Table 5-1: Specification of the textile in the experimental permeability.

Fabric				Yarn	
Style	Weave pattern	Areal weight(gm^{-2})	ends /picks count, yarns/cm	Average fibre diameter (μm)	Number of fibres
280T	2×2 twill	280	3.5	7	6000

To place the preform so that it fits the mould cavity, the region of 320 mm diameter was cut from the fabric. A hole of 8 mm in diameter was created in the centre of each ply for the purpose of central resin injection, allowing to track the injection pressure by pressure sensor.

5.1.2 Experiment set up

Based on the work of Hoes et al.[144], an experimental setup was developed. The reinforcement is placed in the circular cavity (Figure 5-1a), whose height is controlled by eight spacer discs. Four pressure transducers Keller PR-21S are placed on the back of the bottom plate: one in the middle and the other three 95mm from the centre, at 90º, 45º and 0º, identified as sensors 1, 2, 3 and 4, respectively (Figure 5-1b). The spacer discs (Figure 5-1c) are inserted in the surface that surrounds the cavity in the bottom plate of the aluminium rig. The thickness of each disc determines the height of the cavity where the fabric layers are placed.
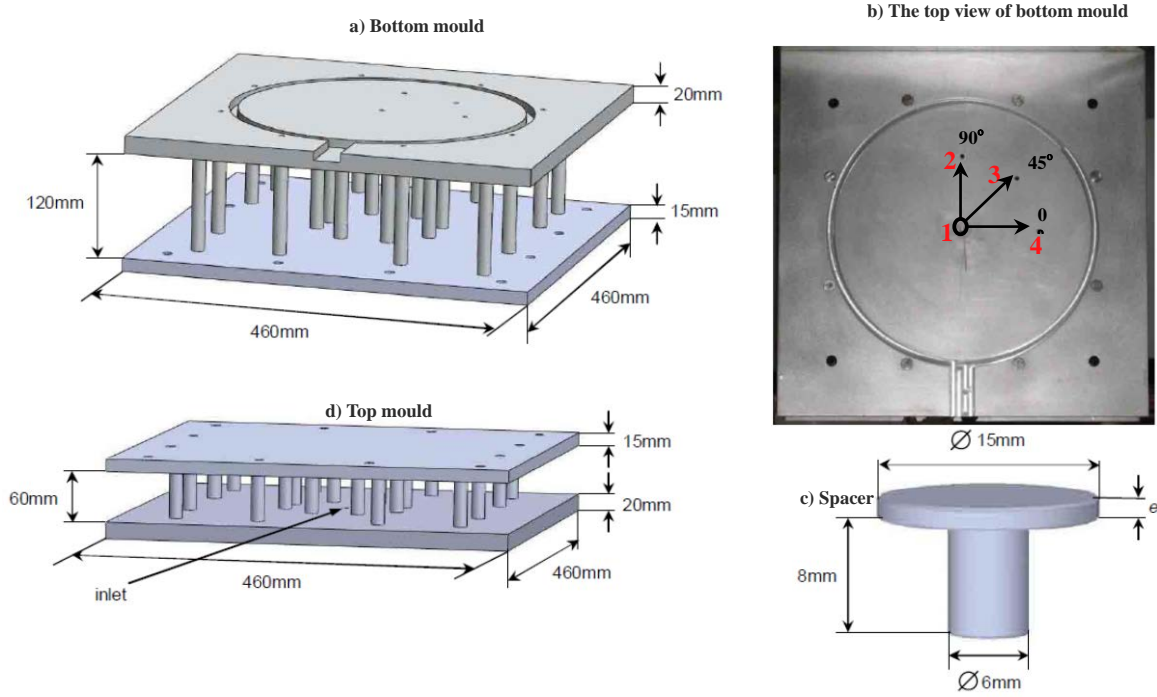
Figure 5-1: The moulding set ups for the in-plane measurements of permeability

The thicknesses of discs are 2.01mm, 1.71mm and 1.45mm. Together, the seven layers had a thickness of 2.4mm. Hence, even with the 2.01mm spacer discs the possible draining of the flow between the surface of the upper layer and the upper plate of the rig is prevented. After placing the preform in the mould cavity and the mould is closed by a press. Subsequently, epoxy resin was injected into the mould cavity through the inlet located in the centre of the top mould (Figure 5-1d), using a pressure pot. The pressure values tracked by each sensor were acquired by means of a data acquisition system[161]. Then the permeability of the reinforcement was calculated by Eq. 5-1 and the experiment was repeated four times for each spacer disc.

$$K = \frac{r^2 \left(2. \ln \dfrac{r}{r_{inj}} - 1 \right) + r_{inj}^2}{4.t.P_{inj}} \mu\phi \qquad \qquad \textbf{(5-1)}$$

where r is flow front position at each instance of time t, r_{inj} is radius of injection tube, and P_{inj} injection pressure[162]

5.1.3 Uncertainty propagation

Experimental uncertainty is a combination of systematic uncertainty and random uncertainty. Systematic uncertainty is due to measuring instruments that are reproducible errors throughout the experiments. On the other hand, random uncertainty is a result of statistical fluctuations arising from limitations of the device accuracy. Accuracy of permeability measurement is affected by systematic and random errors. Uncertainty measurement of permeability can result only in random errors if the same experimental set-

up and calibration procedure of measuring instruments are used. The magnitude of random error can be estimated by error analysis of permeability measurement technique.

To characterize the uncertainty of a measurand, F, that is a function of independent variables $X_1,\ldots, X_n$ Eq. 5-2 [163]:

$$F(X_1,\ldots, X_n) \tag{5-2}$$

It is combined with a standard uncertainty, $U(F)$, is used, and expressed as Eq. 5-3:

$$U^2(F) = \sum_{i=1}^{n}\left[\left(\frac{\partial F}{\partial X_i}\right)^2 u^2(X_i)\right] \tag{5-3}$$

where $u(X_i)$ is the standard uncertainty of variable X_i Eq. 5-4:

$$u^2(X_i) = \frac{\sigma^2(X_i)}{N} + u_e^2(X_i) \tag{5-4}$$

where $\sigma^2(X_i)$ is variance (square of standard deviation) of X_i , N is number of measurements of X_i and $u_e(X_i)$ is standard uncertainty of X_i due to measurement system. Variance, σ^2, itself is expressed as Eq. 5-5:

$$\sigma^2(X_i) = \frac{1}{N-1}\sum_{j=1}^{n}\left(X_{ij} - \overline{X_i}\right)^2 \tag{5-5}$$

where X_i is value of each of the N measurements and $\overline{X_i}$ is mean value of the N measurements.

According to Eq. 5-6, the combined standard uncertainty of permeability for each instant of time can be written as:

$$U^2(K) = \left(\frac{\partial K}{\partial t}\right)^2 u^2(t) + \left(\frac{\partial K}{\partial r}\right)^2 u^2(r) + \left(\frac{\partial K}{\partial r_{inj}}\right)^2 u^2(r_{inj})$$
$$+ \left(\frac{\partial K}{\partial P_{inj}}\right)^2 u^2(P_{inj}) + \left(\frac{\partial K}{\partial \mu}\right)^2 u^2(\mu) + \left(\frac{\partial K}{\partial \varepsilon}\right)^2 u^2(\varepsilon) \tag{5-6}$$

Since all of the variables except porosity are obtained by single measurements, their variances are non-existent. The standard uncertainty of these variables is therefore determined only by the uncertainty due to the measuring system used. Thus Eq. 5-7can be recast as:

$$u^2(X_i) = u_e^2(X_i) \tag{5-7}$$

Considering the uncertainty propagation discussed above one can study the different contributions to this scatter from its constituents. To determine which of the parameters have significant influence on accuracy of permeability measurements, the relative standard deviations of variables are calculated by recasting Eq. 5-8:

$$U_K^2 = (r\frac{\partial K}{\partial r})\left(\frac{U_r}{r}\right)^2 + (r_{inj}\frac{\partial K}{\partial r})\left(\frac{U_{r_{inj}}}{r_{inj}}\right)^2 + (\mu\frac{\partial K}{\partial r})\left(\frac{U_\mu}{\mu}\right)^2$$

$$+ (P_{inj}\frac{\partial K}{\partial r})\left(\frac{U_{P_{inj}}}{P_{inj}}\right)^2 + (\phi\frac{\partial K}{\partial r})\left(\frac{U_\varepsilon}{\varepsilon}\right)^2 + (t\frac{\partial K}{\partial r})\left(\frac{U_t}{t}\right)^2$$

(5-8)

5.1.4   Simulation study

In order to reflect the uncertainties associated with permeability, the Monte-Carlo method (MCM) was used: the statistical distribution of the permeability components was obtained from the mathematical combination of the input distributions reflecting the variability of permeability during the experimental measurements (Eq. 5-10).

$$K = f(F)$$

(5-9)

The MCM superimposed the uncertainty in permeability calculation resulted from uncertainties of the input variables. The MCM was performed as follows:

1- The number of iterations was selected: N=10000

2- N vectors were generated by random sampling of the probability density functions (PDFs) for each of the input variables. The number of input variables (M) considered in this study was six, including: time instant (t), the position of flow front (r), the radius of injection point r_{inj}, injection pressure P_{inj}, resin viscosity μ, porosity ϕ.

3- For each vector, Eq. 5-9 was evaluated to yield the corresponding permeability.

4- Permeability values resulting from MCM where statistically characterised, including the mean and standard deviation.

5- Histograms of the simulated permeability data and proposing appropriated distribution models for permeability components.

5.1.5   Statistics

Porosity and Permeability components, $K_x(0°)$ and $K_y(90°)$, which resulted from MCM were subjected to statistical analysis. Histograms of the data were generated in order to find whether they follow specific distributions. The Kolmogorov-Smirnov Statistic (KSS) was used to test the data sets for normality based on P-values. If in the KSS test P <0.05, there is significant probability of deviation from normality. It should be noted that KSS test is a nonparametric statistic, since it does not assume a specific type of a distribution. To graphically assess the goodness of fit of the potential distribution models determined from KSS test, Q-Q plots, where Q stands for quantile, were generated. The anisotropy index (α) (Eq. 5-11) [15] and the effective permeability (K_{eff}) (Eq. 5-12) [54], [64] were also subjected to statistical analysis.

$$\alpha = \frac{K_y}{K_x}$$

(5-10)

$$K_{eff} = \sqrt{K_x K_y}$$

(5-11)

Histograms of α and K_{eff} which are calculated from the knowledge of K_x and K_y is plotted and Normal, Lognormal, and logistic statistical distribution models are fit to find the most appropriate distribution model.

For comparison, the data of the latest permeability exercise [13], which followed a jointly developed common experimental method [14] in order to foster data agreement is analysed.

5.2   Results and discussion

5.2.1   Statistical characterisations of permeability components

Table 5-2 shows the statistical characterisations of permeability components, K_x and K_y: permeability data was obtained from the twill weave, where four observations were done for each spacer thickness.

Table 5-2: Statistical characterization of measured permeability components

Statistics	K_y (μm)^2			K_x (μm)^2		
	Spacer thickness (mm)			Spacer thickness (mm)		
	2.01	1.71	1.45	2.01	1.71	1.45
Number of observations	4	4	4	4	4	4
μ=Arithmetic mean (μm)^2	12.49	5.92	4.81	7.49	3.18	1.76
σ=Standard Deviation(μm)^2	4.58	2.26	0.65	5.25	1.94	1.16
COV(%)=σ/μ	36	38	24	70	60	37

From Table 5-2, it is observed that K_x and K_y values for each spacer thickness are not the same; for example, for the spacer thickness 2.01mm, the average K_x and K_y were 7.49 and 12.49 (μm)^2, respectively, and continuously varies over the considered area. In this sense, the fibrous medium shows permeability anisotropy (permeability in x direction is not the same as that of y direction). Each direction has a different response to a fluid flow, leading to different flow velocities. Additionally, the higher average permeability in 90º direction is observed compared to the average permeability in 0º direction. In addition, permeability shows higher variability in 90º direction compared to 0º direction which is same as what is observed in the permeability exercise II [13]. However, coefficient variation (COV) of K_x and K_y are much larger than the permeability exercise II. There are a few possible explanations for this difference, which involve additional factors causing higher variability in the measurement apart from the preform heterogeneity.

First, the number of observations may affect the magnitude of the coefficient of variation; the permeability components from the current study were obtained from four observations meanwhile the permeability data from exercise II were obtained from 70 observations. The previous study by Hoes et al. [15] also shows that 75-100 experiments are required to obtain a relatively narrow symmetric distribution. However, due to the

limitations of the material availability, it was impractical to repeat the experiments. Second possible cause for the higher COV is difference between experimental procedures used in this study (2D permeability experiment) and the permeability exercise II (1D permeability experiment) [13]. Nevertheless, the different experimental approaches for the same fabric should lead to close error bound. Third, the higher COV may be caused by the imperfection of the measurement tools. This cannot be confirmed without uncertainty analysis. Uncertainty analysis helps reveal the significant sources of input uncertainties. Hence the next section presents the uncertainty propagation to recognise the most contributing input parameters.

5.2.2   Uncertainty analysis

Considering the uncertainty propagation discussed in the methodology section one can study the different contributions to the scatter of permeability from its constituents. Table 5-3 lists the error bound of the measurements tools of input variables other than porosity ϕ. Porosity is not measured, but calculated from measured values.

Table 5-3: uncertainty values of measurement tools

Measurement tools (measurand)	Uncertainties ($u(measurand)$)
Spider 8-30 multichannel system (t)	$\pm 0.05\%$
Ruler (r)	± 0.5(mm)
Caliper (r_{inj})	± 0.02 (mm)
sensor Keller PR-21S and Spider 8-30 multichannel system (P_{inj})	$\pm 4.4 \times 10^3$ (Pa)
Viscometer μ	$\pm 5 \times 10^{-4}$ mPa.s

ϕ can be formulated as Eq. 5-12

$$\phi = 1 - V_f = 1 - \frac{M_f / \rho_f}{V_{cav}} = 1 - \frac{M_f}{\pi \left(r_{cav}^2 - r_{inj}^2 \right) h_{esp} \rho_f} \qquad (5\text{-}12)$$

where M_f is the reinforcement mass, ρ_f the fibre density, r_{cav} is radius of mould cavity and h_{esp} is height of the spacers.

From the propagation of uncertainty principal, the squared combined standard uncertainty of ϕ can be expressed as Eq. 5-13:

$$u^2(\phi) = \left(\frac{\partial \phi}{\partial M_f} \right)^2 u^2(M_f) + \left(\frac{\partial \phi}{\partial \rho_f} \right)^2 u^2(\rho_f) + \left(\frac{\partial \phi}{\partial r_{cav}} \right)^2 u^2(r_{cav})$$

$$+ \left(\frac{\partial \phi}{\partial r_{inj}} \right)^2 u^2(r_{inj}) + \left(\frac{\partial \phi}{\partial h_{esp}} \right)^2 u^2(h_{esp})$$

$$(5\text{-}13)$$

the partial derivatives on the right side of Eq. 5-13 are as Eqs. 5-14 to 5-18:

$$\frac{\partial \phi}{\partial M_f} = -\frac{1}{\pi \left(r_{cav}^2 - r_{inj}^2 \right) h_{esp} \rho_f} \tag{5-14}$$

$$\frac{\partial \phi}{\partial \rho_f} = \frac{M_f}{\pi \left(r_{cav}^2 - r_{inj}^2 \right) h_{esp} \rho_f^2} \tag{5-15}$$

$$\frac{\partial \phi}{\partial r_{cav}} = \frac{2 r_{cav} M_f}{\pi \left(r_{cav}^2 - r_{inj}^2 \right)^2 h_{esp} \rho_f} \tag{5-16}$$

$$\frac{\partial \phi}{\partial r_{inj}} = -\frac{2 r_{inj} M_f}{\pi \left(r_{cav}^2 - r_{inj}^2 \right)^2 h_{esp} \rho_f} \tag{5-17}$$

$$\frac{\partial \phi}{\partial h_{esp}} = \frac{M_f}{\pi \left(r_{cav}^2 - r_{inj}^2 \right) h_{esp}^2 \rho_f} \tag{5-18}$$

Table 5-4 lists the error bound of the measurements tools of input variables for the calculation of standard uncertainty of ϕ.

Table 5-4: uncertainty values of measurement tools. ρ_f=1.890×10-3 g/mm^3, r_{cav}=160 mm and r_{inj}=3.4mm

Measurement tools (measurand)	Uncertainties (u(measurand))
Balance (M_f)	±5×10^{-6} (Kg)
Ruler (r_{cav})	±0.5 (mm)
Micrometer (h_{es})	±5×10^{-4} (mm)
Provided by supplier (ρ_f)	-----------
Viscometer μ	±5 × 10^{-4} mPa.s

Substituting Eqs. 5-14 to 5-18 as well as the uncertainty values from Table 5-4 into Eq. 5-13, the uncertainty of porosity was calculated and summarised in Table 5-5. From Table 5-5 it is observed that the magnitude of uncertainty of porosity varies as a function of the spacer thickness. This observation led us to the conclusion that as the size of spacer decreases, fibre volume fraction increases. Hence there is less free space for the same number of fabric layers for the tow mobility, leading to less variability.

Table 5-5: uncertainty values of porosity at different spacer thickness

Spacer (mm)	u^2(ϕ)
2.01	5.1
1.71	4.8
1.45	2.7

Knowing the uncertainties of measurement tools as well as porosity, the standard uncertainty of permeability components, K_x and K_y for each spacer was calculated and summarised in Table 5-6. The magnitude of uncertainty for permeability consistently

decreases with a decrease in the spacer thickness: a higher thickness in spacer tends to possess a higher probability of obtaining larger uncertainty associated with porosity and permeability components. This may originate from the effect of nesting. Increasing nesting increases the scatter in permeability [76] by progressively varying the space between the yarns. Therefore, higher permeability uncertainty at higher spacer height, corresponding to lower fibre volume fraction (V_f), can be caused by the nesting of yarns in the adjacent layers. Additionally, in our case, K_y was subject to more uncertainty compared to K_x. This may be explained by alterations to the fabric geometry along the channels formed between the fibre yarns. As higher fluctuations of the inter-yarn gap areas lead to higher scatter is the permeability.

Table 5-6: uncertainty values of permeability components, K_x and K_y, at different spacer thickness

Spacer (mm)	$u^2(K_x)$	$u^2(K_y)$	$V_f(\%)$
2.01	36.82	47.34	52
1.71	12.01	22.22	62
1.45	8.36	16.07	72

In order to identify the significant parameters affecting uncertainty in permeability measurements the relative uncertainty contribution was calculated (5-19 and 5-20)

$$(r\frac{\partial K}{\partial r}) + (r_{inj}\frac{\partial K}{\partial r}) = (\mu\frac{\partial K}{\partial r}) = (P_{inj}\frac{\partial K}{\partial r}) = (\varepsilon\frac{\partial K}{\partial r}) = (t\frac{\partial K}{\partial r}) = K \qquad (5\text{-}19)$$

$$U_K^{*2} = U_r^{*2} + U_{r_{inj}}^{*2} + U_\mu^{*2} + U_{P_{inj}}^{*2} + U_\varepsilon^{*2} + U_t^{*2} \qquad (5\text{-}20)$$

From the relative uncertainty contribution of the variables (Figure 5-2a), it is revealed that viscosity, pressure and porosity measurement errors account for 96% of the relative uncertainty contribution. The uncertainties of viscosity, pressure and porosity measurement therefore require attention so that the 2D permeability results are improved. In that sense, the uncertainty in permeability results may, to a great extent, result from the uncertainties of pressure and porosity measurements. As pressure and viscosity are directly measured by a pressure meter and a viscometer, uncertainty will be reduced by using measuring tools with higher accuracy.
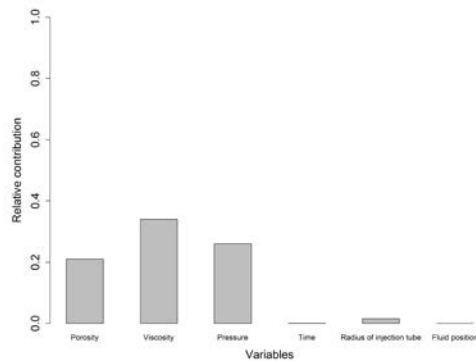
a)   b)
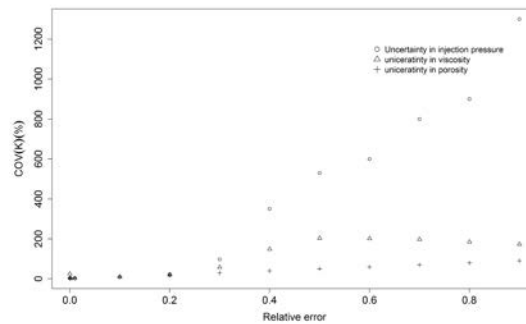
Figure 5-2: (a) Relative uncertainty contribution of the variables, (b) COV of K versus relative error

Figure 5-2b shows the increasing effect of pressure on the statistics of permeability compared to viscosity and porosity as the relative error increases. On the other hand, the increase of the injection pressure will reduce the effect of the other uncertainty on the scatter of permeability. Hence, the uncertainty contribution of viscosity and porosity will become insignificant by increasing injection pressure with known uncertainty. This observation requires to be examined by series of experiment to study the effects of pressure level on the statistics of permeability.

Regarding porosity, by evaluating relative standard uncertainty, it was found out that radius of mould cavity (r_{cav}) is a significant parameter in porosity calculation. Therefore, the dimension of the mould must be adequately large compared to the dimension of r_{cav} to reduce the effect of the dimension of the injection gate on permeability scatter. Another reason for this significant contribution of r_{cav} may be due to the imperfections between layers where the hole of top layer does not fit perfectly to the hole of below layer.

5.2.3   Simulation study

Statistics of ϕ

Monte Carlo simulations were used to estimate uncertainties of porosity and permeability by using the values of variables and the estimated variable uncertainties. Figure 5-3 graphs the statistics of porosity, ϕ: the porosity data obtained from 10000 repeats of MCM for each spacer.

a)   b)

(c)
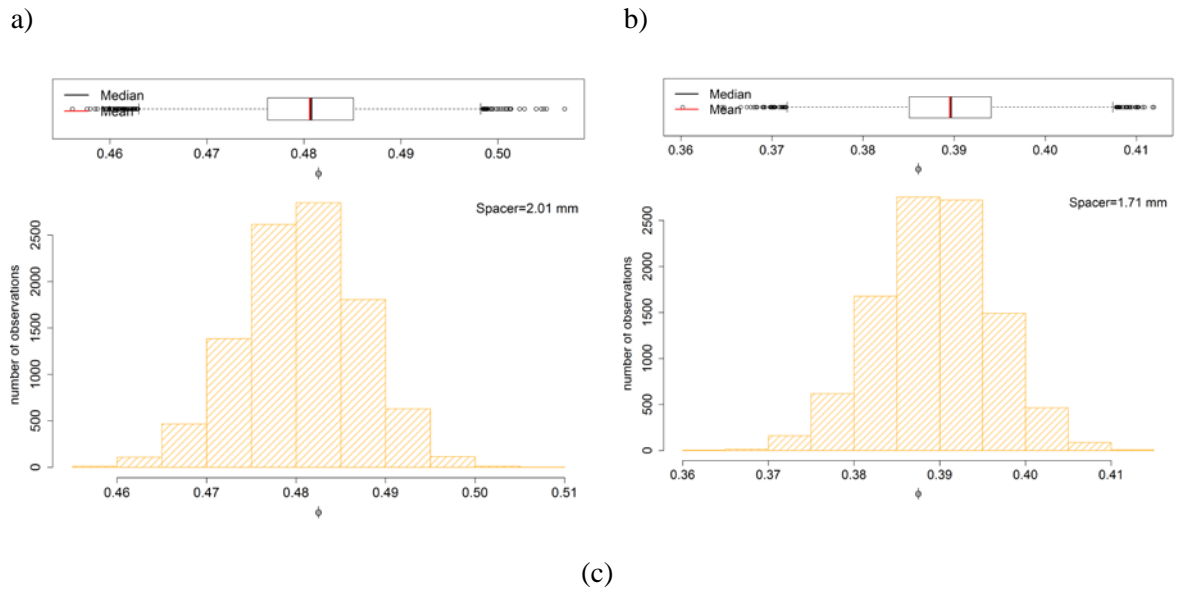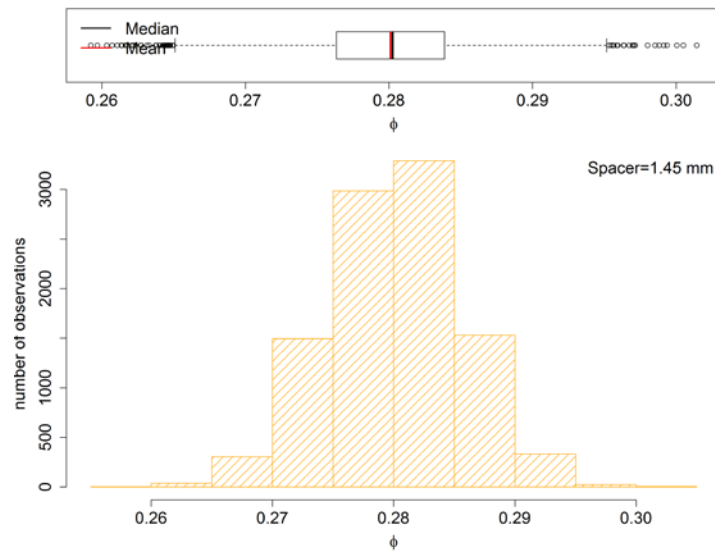
Figure 5-3: Below: Histograms of porosity at different spacer thicknesses. Top: The boxplots of the porosity data with whiskers

The number of observations of porosity values quite frequently lie between 48 and 48.5 % for spacer 2.01mm, between 38.5 and 39 % for spacer 1.71 mm, and between 28 and 28.2 % for spacer 1.45 mm (Figure 5-3 (below)).

The detailed statistical characterizations of the sampling permeability distribution are summarised for ϕ in Table 5. The difference between maximum and minimum values of permeability is two order of magnitude as shown in Table 5.

Table: Statistics of permeability components

Statistics	Spacer 2.01 ϕ	Space 1.71 ϕ	Spacer 1.45 ϕ
Number of observation			
μ=Arithmetic mean (μm^2)	0.48	0.39	0.28
σ=Standard Deviation (μm^2)	0.006	0.006	0.005
COV(%) = σ/μ	1.2	1.5	1.7
Median(μm^2)	0.48	0.39	0.28
Minimum(μm^2)	0.45	0.36	0.26
Maximum(μm^2)	0.5	0.41	0.3
Skewness	-0.08	-0.07	0.006

The symmetry and the tail length of the three data sets are assessed by boxplot as shown in Figure 5-3 (top). The medians and the means (the black line in Figure 5-3 (top)) of the porosity data sets at different spacer thicknesses are approximately the same, and hence the data is not skewed. From Figure 5-3 (top), it is observed that the boxplots of the three data sets show long tails (the dashed lines); the length of the whiskers far exceeds the length of the boxes. For zero skewness, one common model is the normal distribution[44].

Statistics of permeability components

   Using the same approach, a Monte Carlo simulation was applied to estimate uncertainties of the permeability by using the values of variables and the estimated variable uncertainties. Figure 5-4 shows the statistical graphics of permeability components, K_x and K_y: the permeability data obtained from 10000 repeats of MCM for each spacer.

a)

b)

c)
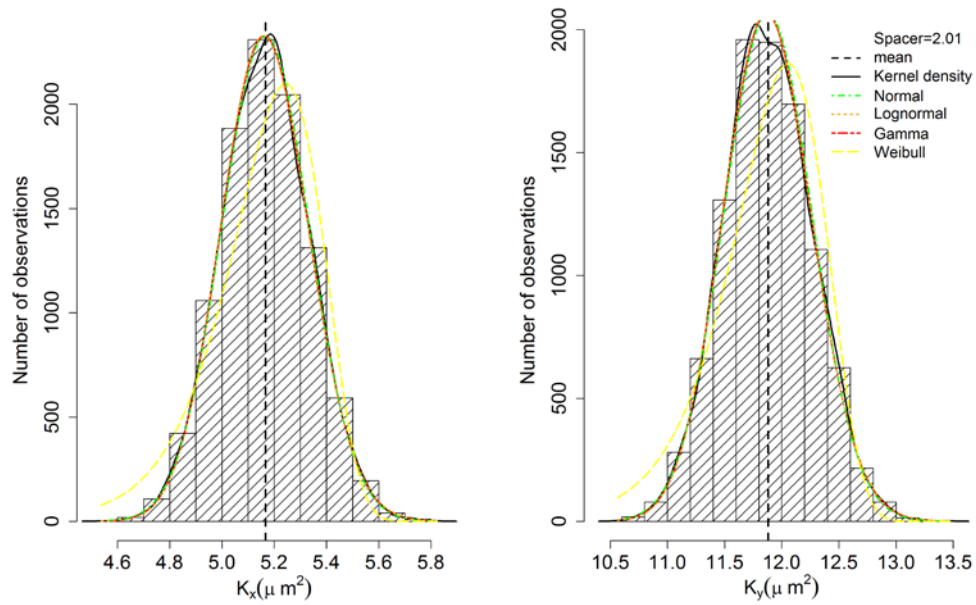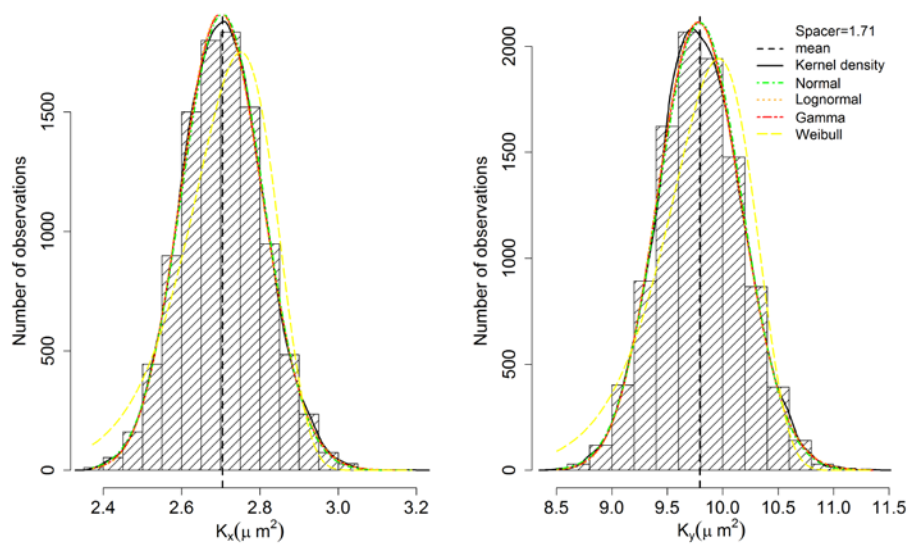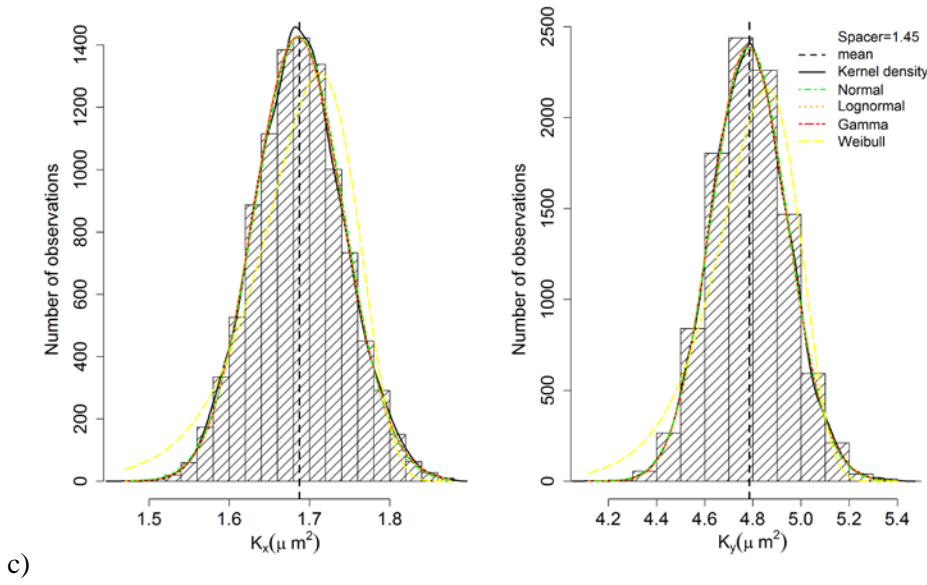
Figure 5-4: histograms of permeability data from MCM simulations for different spacer height: 0º direction, Kx, (left) and 90º direction, Ky, (right). (a) 2.01 mm (b) 1.71 mm (c) 1.45 mm

The detailed statistical characterizations of the permeability components for each spacer are summarised in Table 5.

Table 5-7: Statistics of permeability components

Statistics	Spacer 2.01		Space 1.71		Spacer 1.45	
	K_x	K_y	K_x	K_y	K_x	K_y
Number of observation	10000	10000	10000	10000	10000	10000
μ=Arithmetic mean (μm²)	5.16	11.87	2.7	9.8	1.68	4.7
σ=Standard Deviation (μm²)	0.16	0.38	0.10	0.37	0.05	0.15
COV(%) = σ/μ	3.1	3.2	3.7	3.7	2.9	3.2
Median(μm²)	5.16	11.87	2.7	9.8	1.68	4.7
Minimum(μm²)	4.57	10.42	2.31	8.34	1.48	4.22
Maximum(μm²)	6	13.31	3.09	11.3	1.89	5.5
Skewness	0.12	0.07	0.09	0.1	0.08	0.09

The values of skewness reported in Table 5-7, which is in the normality range (-0.5<skewness<0.5), suggest that the Gaussian model is appropriate for statistical characterisations of the permeability components. This observation is in agreement with [36][15][71][72] and they addressed the skewness in permeability due to local inhomogeneity resulted from nesting and the waviness of the fibre yarn paths. Despite this, others reported that the permeability of two-dimensional heterogeneous fibrous media is well approximated by the lognormal distribution[44][16][70][29].

The appropriateness of Gaussian model is further confirmed by Figure 5-4 in which the different distributions including normal, lognormal, Gamma, and Weibull fit to the Kernel density. It is clear that the Weibull model fails to represent the distribution of permeability values. Figure 5-4 also shows the lognormal and Gamma provide better fit to the Kernel density than the Weibull.

To find whether a correlation exists between permeability values for the two directions over the fabric sheet, K_x is plotted against K_y for spacer height 2.01 mm as shown in Figure 5-5. The visual inspection of Figure 5-5 shows there is no clear correlation between K_x and K_y. This may be explained by alterations to the fabric geometry along the channels formed between the fibre yarns[164].
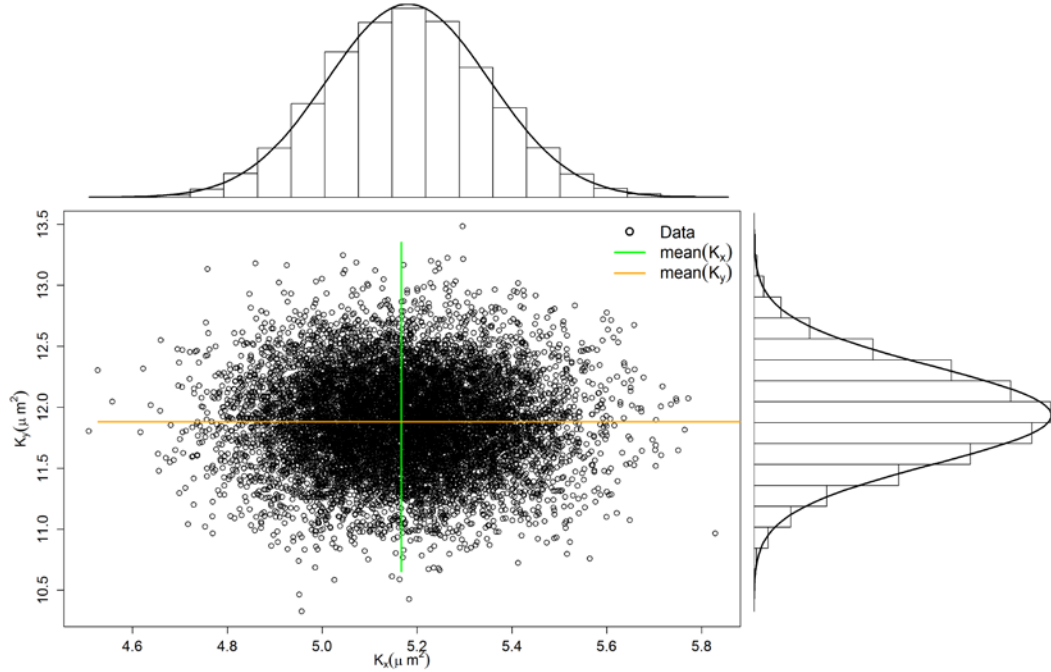
Figure 5-5: Correlation between Kx and Ky for spacer height 2.01 mm

The histogram of the anisotropy index $\alpha = K_y/K_x$ [15] is shown in Figure 5-6. Because of the similar variation patterns of the anisotropy index, the distribution of α for the spacer height of 2.01 mm is only reported here. Figure 5-6 shows the normal density overlie the histogram. Hence, the anisotropy index follows the normal distribution and ranges between 1.9 and 2.8. The anisotropy index is quite frequently lies between 2.25 and 2.3. The standard deviation of anisotropy index is 5% of the mean anisotropy index, which is 5 times less than the value of 25% reported by Hoes *et al.*[15] for a balanced glass woven fabric. This difference is not trivial, as our calculations exclude the uncertainties caused by the measurement tools, but measurements [12] give the variability of the global permeability between different laminates without excluding the uncertainties associated with the measurement tools.
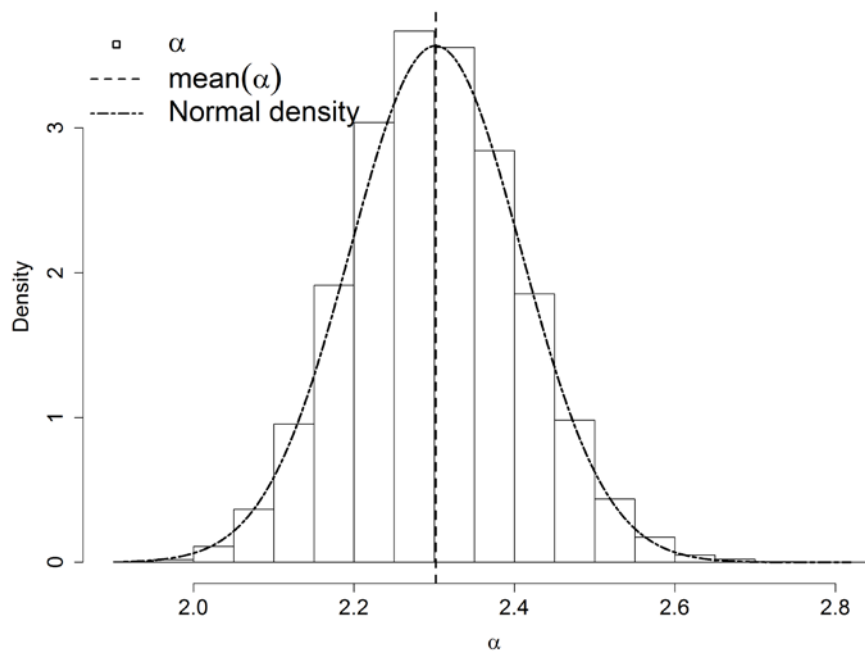
Figure 5-6: Histogram of the anisotropy index for spacer height 2.01 mm.

K_x and K_y in an anisotropic medium can be converted to an average effective permeability (Eq.5-10). Figure 5-7, shows histogram of K_{eff} for spacer height 2.01 mm. Figure 5-9: Histogram of the effective permeability. One can observe that the Gaussian model yields good fits (Figure 5-7). Based on this, we conclude that the Gaussian distribution provides the best fit.
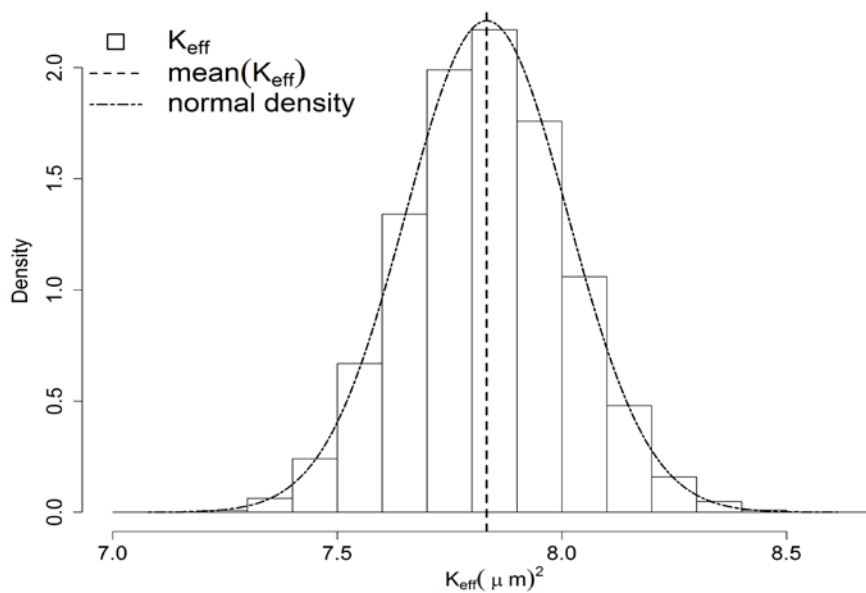
Figure 5-7: Histogram of the effective permeability for spacer height 2.01 mm.

5.3　Conclusion

This study presented an uncertainty analysis for 2D flow permeability measurement. The sources of uncertainty were discussed and individual parameter uncertainties were estimated versus device accuracy and performance limitations. Their influence on the permeability uncertainty was analysed by uncertainty propagation. The relative uncertainty was also calculated to identify the significant parameters. In order to reflect the uncertainties associated with permeability, a Monte-Carlo simulation was used: the statistical distribution of the permeability components was obtained from the mathematical combination of the input distributions reflecting the variability of permeability during the experimental measurements.

For a particular 2/2 twill balanced carbon fabric the following features of the field were observed:

(1) By evaluating uncertainty of 2D permeability results, the measurements at viscosity, pressure and porosity were identified to have the biggest influence on uncertainty of permeability.

(2) It should be noted that porosity is a function of some variables, radius of mould cavity among which introduced the highest degree of uncertainty. In this sense, the dimension of mould must be high enough compared to the dimension of the hole located in the middle of the fabric for the central injection. Additionally, it is suggested that the holes of seven layers must perfectly fit to each other and any imperfection would result an error in porosity determination.

(3) A difference in K_x and K_y of individual experiment was observed which is attributed to the difference in warp and weft yarn width.

(4) It was, however, not possible to establish a clear correlation between K_x and K_y. The channel width can vary unequally in both weft and warp directions, causing anisotropic permeability.

(5) It was shown that a normal distribution can properly describe the scatter in porosity, K_x and K_y, as well as anisotropic index, and the effective permeability.

In summary, this uncertainty evaluation approach can be applied to the determination of the quality of permeability measurements obtained by different experimental setups. Furthermore, the proposed method can be utilized in many aspects of composite manufacturing processes, such as providing inputs (e.g. edge effects or race tracking, mould deformation, air entrapment, curing and fibre compaction) for stochastic simulation.

Chapter 6

Void formation

Experimental characterization of voids in high fibre volume fraction composites processed by high injection pressure RTM

Replacing autoclave processes is a well-known industry drive in the composites community. One of the most recognized candidates for this replacement is high injection pressure resin transfer moulding (HIPRTM), because it is both an out of autoclave process and because the high processing pressures can, hypothetically, reduce the size of voids, thereby reducing void content. In order to clarify this issue, this paper presents our results on the size distribution and total void fraction of composites containing high fibre volume fractions (>60%) composites produced by HIPRTM. To substantiate this work we present a comparative study considering both autoclave and RTM at lower pressure / fibre volume fractions. Results show that HIPRTM is able to produce high fibre volume fraction parts at very low void content (<0.05%) and is comparable to autoclave results. Future work should study the mechanical properties of these laminates in order to clarify further the limits of HIPRTM.

Keywords: A.Polymer-matrix composites (PMCs); D. Optical microscopy D. Physical methods of analysis; E.RTM; B.Defects

Introduction

A shift in technology towards injection at high pressures (above 15 bar) has the potential to significantly reduce the RTM mould filling time without compromising part quality. This therefore helps materialize an increase in the use of composites [165]. As the use of fibre reinforced thermoset composites is rising, due to increasing production rates and cost competitiveness, composite manufacturing processes, like resin transfer moulding (RTM), have become high priority research fields for high volume production [166]. RTM provides fast cycle time, low capital cost and the capability of consolidating complex shapes compared to the hand-layup prepreg/autoclave. However, in its present form, RTM is still limited by long filling time, low production rate and relatively high void content for high performance composites, in part we argue because of the low injection pressures (<10 bar) used, but also by resin cure kinetics and viscosity [167]. Therefore, RTM needs modifications in such a way as to produce composites with void contents as low as the hand-layup prepreg/autoclave and faster than the current production methods.

HIPRTM continues the net shape and surface quality of RTM with a high pressure resin injection and, thus, shorter filling time. This is still an RTM variant, the process starts by placing a fibrous preform into a mould cavity. The mould is subsequently closed, compacting the preform to the desired thickness, and, optionally, air is evacuated from the cavity. Subsequently, a pre-mixed resin is injected into the mould cavity under high pressure ($\geq$20 bars) allowing a significant reduction in the filling time. Finally, the cured part is de-moulded to complete the production cycle [168][7]. One important aspect of the study of this new fast process is the understanding of the possibility of inadequate wet-out due to high-speed resin flow inside a fibrous preform, undermining mechanical properties of the composite by void formation or dry spots [169]. Voids are the major cause of strength reduction leading to early failure of thermoset-based polymer composites [170]. Research has shown how the mechanical properties of composites are drastically degraded as a direct function of void content [171][172][173][174][175][176][177]. In the other words, determining whether or not HIPRTM is able to produce composite parts with void content as low as Autoclave processing. To address this, a thorough study of effects of the HIPRTM variables on void behaviour is required.

To our knowledge, very few experiments have been reported that present part quality results of these processing conditions. Existing studies do not cover the questions of moulding conditions and chemorheology of the resin, which also affect final void content of composite parts. Barraza *et al.* [6] looked at void content as a function of postfill cure pressure levels and reported an average reduction of *circa* 1% in the void content. However, in their work, curing pressures are both low (0 to 0.8 MPa). Similarly, Hamidi *et al.* [178] [17] applied a postfill pressure by which they forced further resin into the mould cavity and compared the void content with the case without postfill i.e. a void content of *circa* 2.2% and *circa* 0.2% without and with postfill pressures, respectively. However, the packing pressure (0.6 MPa) used was lower than one expects to use in HIPRTM. Recently, Khoun *et al.* [7] studied the experimental effect of process parameters, such as the injection flow rate, the vacuum assistance sequence, mould gap control and binder concentration, on mechanical performance. Their results reinforced the understanding that vacuum assisted impregnation improves the quality of composite parts produced by HIPRTM. However, the authors did not specify the void sizes obtained or their distribution.

It is useful to compare the quality of composite parts produced by HIPRTM with those of competing processes: a comparative approach provides a framework within which this understanding contemplates the substitution of prepeg parts for HIRTM parts. However, a limited number of studies have reported direct comparisons of autoclave and RTM. Hayward *et al.*[180] who compared quality of laminate properties produced by vacuum assisted RTM with alternative processes, used different resin systems for each manufacturing method. Abraham *et al.*[181] compared laminate properties arising from an RTM and a wet lay-up with autoclave consolidation and S. Laurenzi *et al.*[182] reported 47% cycle time reduction in RTM technique as compared to the prepreg-based technique. However, no comparison has been made between HIPRTM and other processes and it is unclear what improvements it is possible to obtain compared to autoclave processing.

This work aims to study the quality of an aerospace related manufacturing case study, where we assess HIPRTM against their stablished autoclave process. For this purpose, we

manufactured five demonstrator U-shaped CFRP parts in different processes: 1) autoclave curing pressure (two samples); 2) vacuum bag processing (VBP) (one sample); and 3) HIPRTM (two samples). The sequence of the production of U-shaped CFRP parts for comparative studies is summarized in the flow chart of Figure 6-1. The left side of Figure 1 illustrates two manufacturing processes, prepreg/autoclave and prepreg/vacuum bag processing (VBP). As shown in the right side of Figure 6-1, in HIPRTM, in contrast to the prepregs, dry fabrics are used in the composite processing. Once these U-shaped parts are produced void characterization is carried out by optical microscopy for the comparative study. For the purpose of this paper, we only include the analysis of macrovoids due to limitations of our optical microscope.
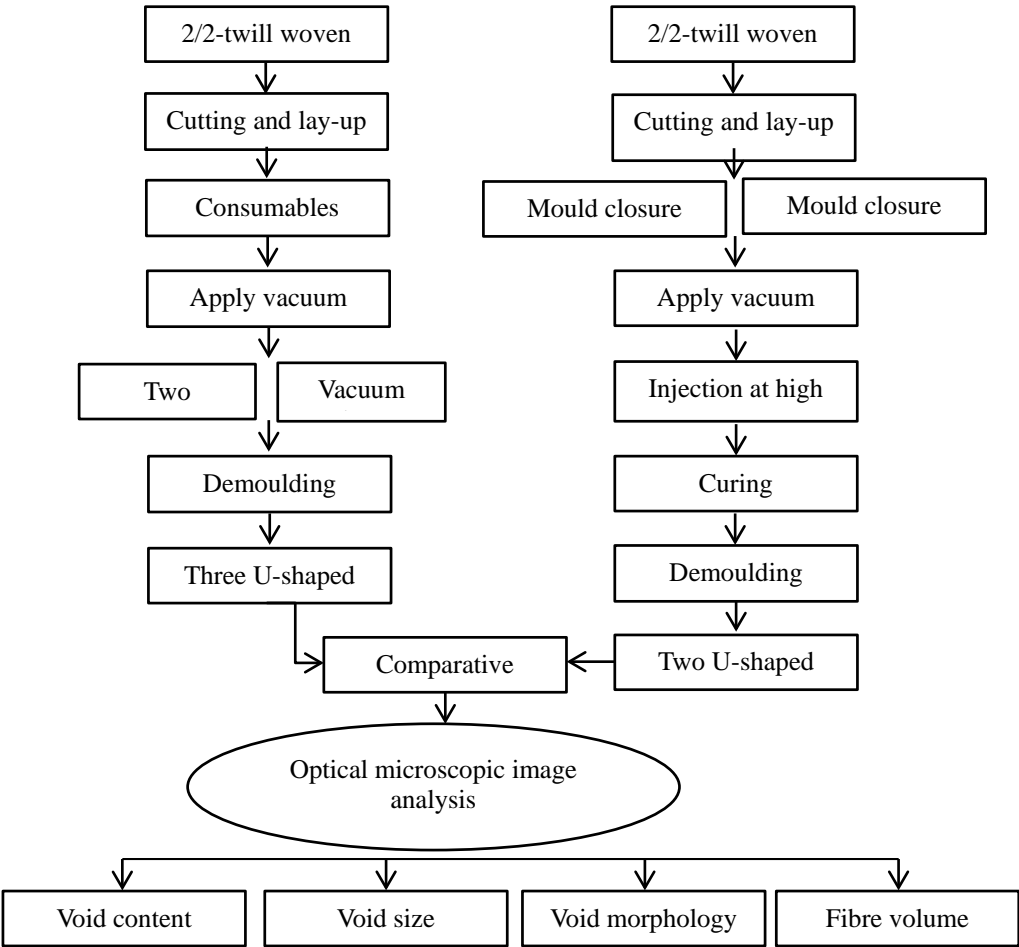
Figure 6-1: Flow diagram for manufacturing processes of U-shaped CFRP parts

Table 6-1 summarizes process variables for the comparative study. We compare the first reference U-shaped part fabricated by autoclave curing at 600 kPa to parts fabricated by autoclave curing at 400 kPa, VBP and HIPRTM. We evaluate void formation by microscopic image analysis of the cross section of U-shaped parts, and present effects of the process variables on void content and void size for these samples.

Table 6-1: Processes and their variables selected for the comparative study

Variables Process	Fibre orientation	Injection pressure (kPa)	Compaction pressure (kPa)	Hydraulic cylinder pressure (kPa)	Mould gap (mm)
Autoclave (Reference)	[0°]	---	700	---	---
Autoclave	[0°]	---	500	---	---
VBP	[0°]	---	---	---	---
HIPRTM	[0°]	200	---	6000	0.2
HIPRTM	[0°]	200	---	6000	---

6.1 Experimental details

As part of the development of HIPRTM and in order to make a comparison study, a relevant geometry demonstrator was selected, consisting of one spar, based on a design that was used for a wing of an unmanned aerial vehicle (UAV) [183]. The UAV, a 3m wingspan, "flying wing" design, is predominantly composed of fiber glass sandwich in the airframe and a carbon fiber spar to adequately distribute the high loads from the wings into the fuselage during flight [183]. The selected a U-shaped UAV spar with variable width in the longitudinal direction because this geometry provides a real application with a degree of complexity when compared to typical considered plate-shaped samples and allows this exploratory study of the effect of geometry or void formation. The design of the U-shaped part shown in Figure 6-2 considers 2 mm uniform thickness and 900 mm length and 100 mm width.
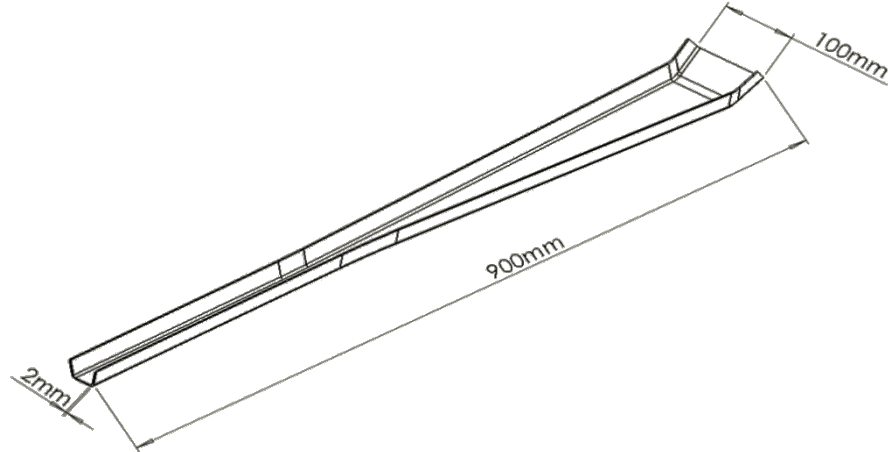
Figure 6-2: representation of the case study: a wing spar

6.1.1   Autoclave and vacuum bag processing

The material used in this study was a carbon fiber/epoxy prepreg(CC284/ ET445) manufactured by SAATI, featuring a woven 2 × 2 twill fabric(Figure 6-3).

Figure 6-3: A carbon fiber/epoxy prepreg(CC284/ ET445) manufactured, featuring a woven 2×2 twill fabric

Compaction pressures (P_c) were computed by the total pressure difference between the pressure within the vacuum bag (P_{in}) and the pressure in the surrounding environment(P_{out}) (see Eq. 6-1):

$$P_c = P_{out} - P_{in}$$

(**6-1**)

6.1.2   Autoclave

Two of the samples were cured in an autoclave under two pressure levels with the same temperature profile shown in Figure 6-4. The compaction pressures for those samples in an autoclave were 500 kPa and 700 kPa.
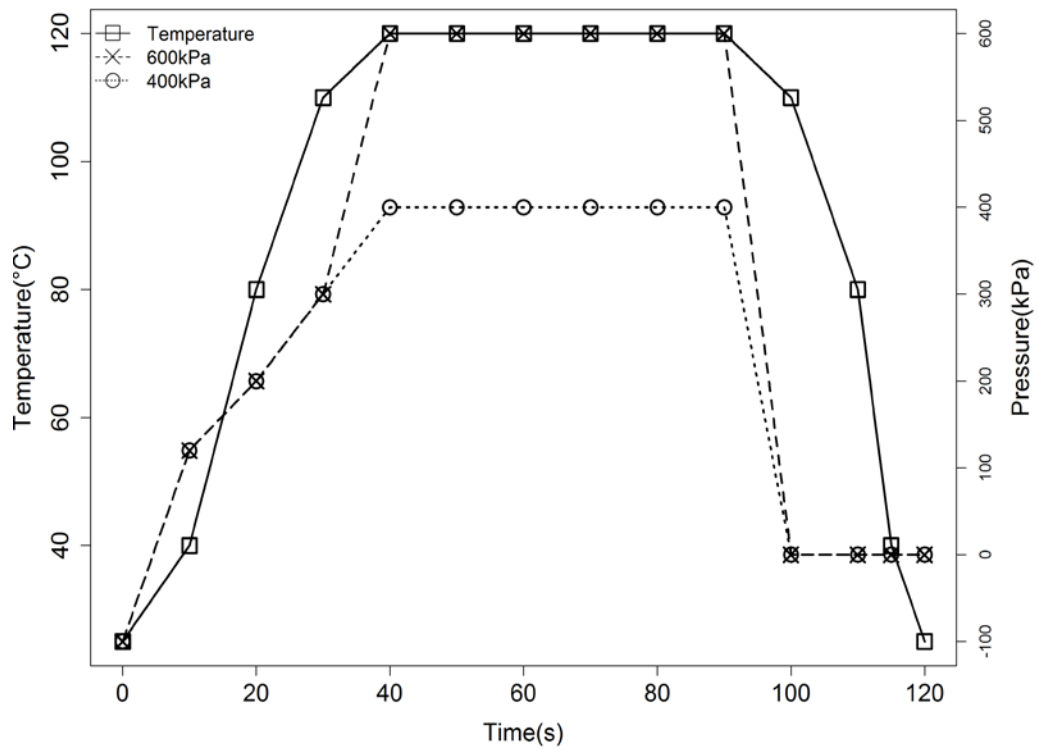
Figure 6-4: Prepreg cure cycle in Autoclave

6.1.3   Vacuum bag processing

For the vacuum bag processing (VBP) case, the laminate was cured under vacuum with the same temperature profile as the one used for the autoclave sample (See Figure 6-5). The compaction pressure was 1bar.
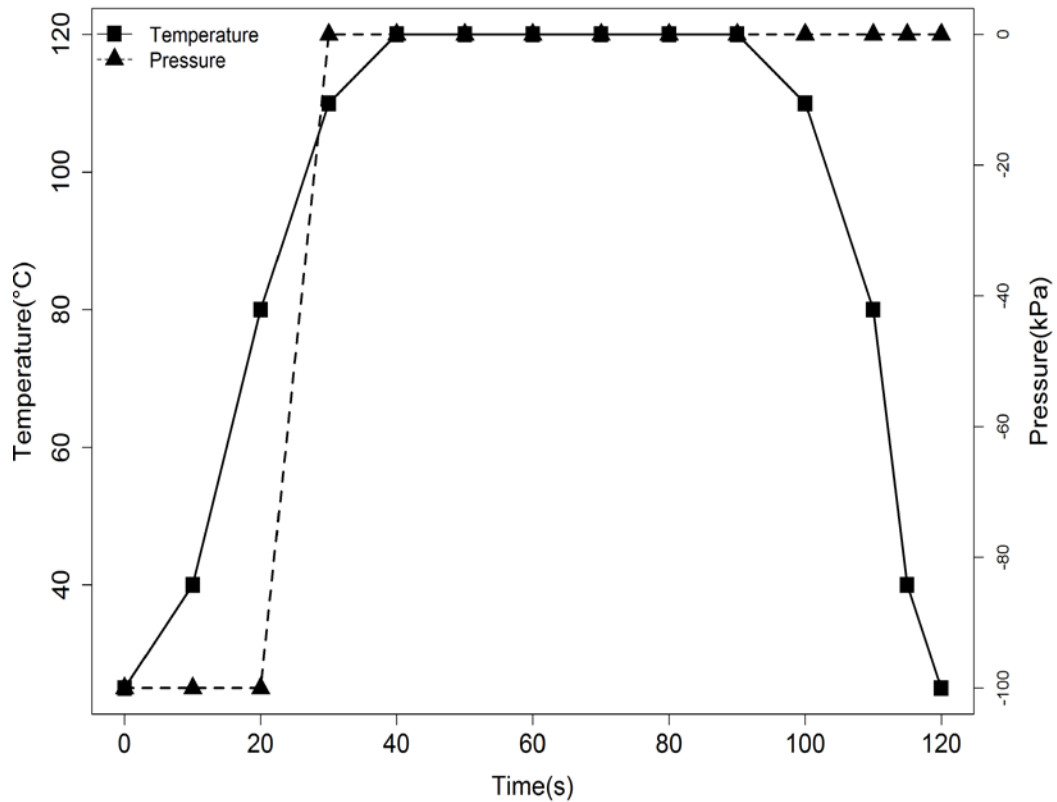
Figure 6-5: Prepreg cure cycle in VBP

6.1.4   High injection pressure resin transfer moulding

A Biresin epoxy resin system (resin: Biresin CR120 from Sika, hardener: Biresin CH120-3) and a woven 2×2 twill fabric (Figure 6-6.A) from Hexcel were used for the study of the HIPRTM process. The areal weight of the carbon fibre used is 280 g/m^2. In order to reduce fibre displacement effects, an epoxy-based binder(AIRTECH) was applied to the carbon fibre mat.

A semi-automated injection machine was used to mix the chosen epoxy resin and the hardener at a 100:30 weight ratio. The mixing was done at a pressure of 20 bar and ambient temperature, and the high pressure injection filled the mould within 5 min. Such high injection pressure may cause preform deformation, and as a result of that the mould filling gets difficult with increasing fibre volume fraction. In order to overcome preform deformation or fibre washout, two inlet gates on a single path (a distribution manifold) were considered instead of single point injection (Figure 6-6.B). The distribution manifold accommodates even distribution of the resin and minimizes abrupt changes in the pressure of the resin additionally. The pressure difference between inlet and outlet was kept constant at 15 bar to eliminate causes of void formation from the flow velocity variations. For RTM mould manipulation and control compression force, a hydraulic compression press, 1600 kN press force, was used (Figure 6-6.C). This also prevented fibre movement. The mould clamping force was set to high enough to prevent resin leakage; the clamping force (Fc) was 476.6 kN while the opening force was 323 kN, which includes injection force as well

as fabric compaction. Finally, the cured part was de-moulded to complete the production cycle (Figure 6-6.D).
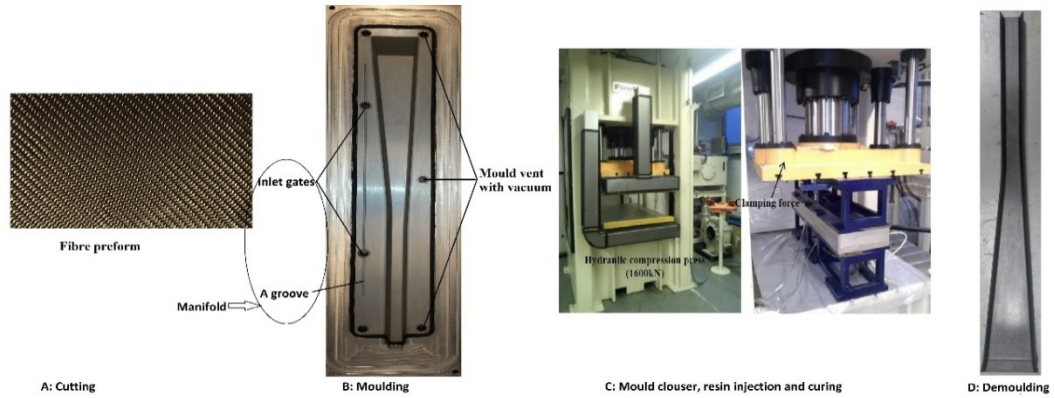
Figure 6-6: A schematic of the process sequence of HIPRTM

In order to study the HIPRTM process variants, two scenarios were considered: (i) a stack of six fabric layers leaving a 0.2mm gap between the stack and the top platen once the mould was closed, (ii) a stack of eight fabric layers with no gap between the stack and the top platen, providing the external clamping force on the stack.

6.1.5 Image analysis

Optical microscopy and image analysis are the most common approach for the determination of void size, shape, content and its distribution[16] [17] [184][185]. In this study, an Olimpus PNG3 optical microscope equipped with a CCD camera was used. The samples were cut perpendicular to the fibre direction, the samples were polished manually in four steps (sandpaper grits 320, 400, 800, and 1000), and subsequently photographed at various magnifications. In the experimental plan, we considered the possibility that void content and distribution are determined by flow velocity for the HIPRTM case, the sample analysis was divided into three zones (injection side, top and outlet side) and were equally cut along the injection direction (from left to right) which created 10 regions, as shown in Figure 6-7.
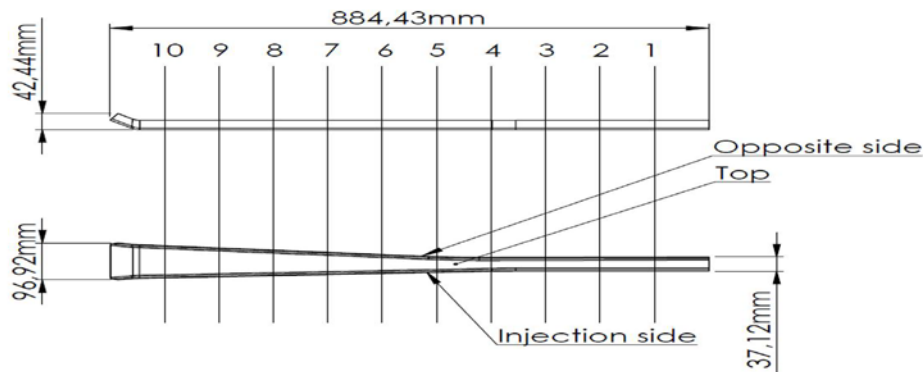
Figure 6-7: Composite part divided into 10 equal regions for void analysis by optical microscopy

6.1.6 Void characterization

Due to void size variation, it was necessary to categorize voids based on their size. It should be noted that although voids generated in composite parts produced by different manufacturing processes possess different and irregular shapes, for the sake of convenience, their dimensions were characterized by an equivalent diameter d_{eq} ,which is determined by the ratio of the area A of a regular polygon in terms of the radius r of its inscribed circle to its perimeter p, rather than by the area, Eq.6-2 [186]:

$$d_{eq} = \frac{A}{p} = \frac{\frac{1}{2} \cdot p \cdot \frac{d}{2}}{p} = \frac{d}{4}$$

(6-2)

In order to determine void size through the thickness, each section is scanned at 75 times magnification by using an optical microscope. This magnification exposes a surface area of about 0.5×0.2 mm^2, providing a total of 30 frames containing voids. Then, the equivalent void diameters were calculated by a Matlab code and ranged from <50 µm to 400 µm. The equivalent diameters are categorized into 9 classes or intervals. Finally, the distributions of void size in each the class interval were determined for the samples.

The void content was determined from the obtained micrography considering that volumetric void content (V_v) in a given area of the image is the ratio of total void area (A_v) to the area of the image (A) (Eq.6-3):

$$V_v = \frac{A_v}{A}$$

(6-3)

In our experiments V_v was determined by image processing Matlab™. The image processing toolbox provides a comprehensive set of functions for image analysis such as finding shapes, eliminating noise, counting objects, and extracting statistical data analysis.

However, the issue of applying a correct range of grayscale levels to return a binary image (black (i.e., voids) and white image (i.e., fibre and resin)) is the main step in automated analysis of microscope images. Figure 6-8 shows the graph of a grayscale sample level for the line scan over the image (Figure 6-8, top). The results of the scan confirm there is a range of grayscale levels for the voids.
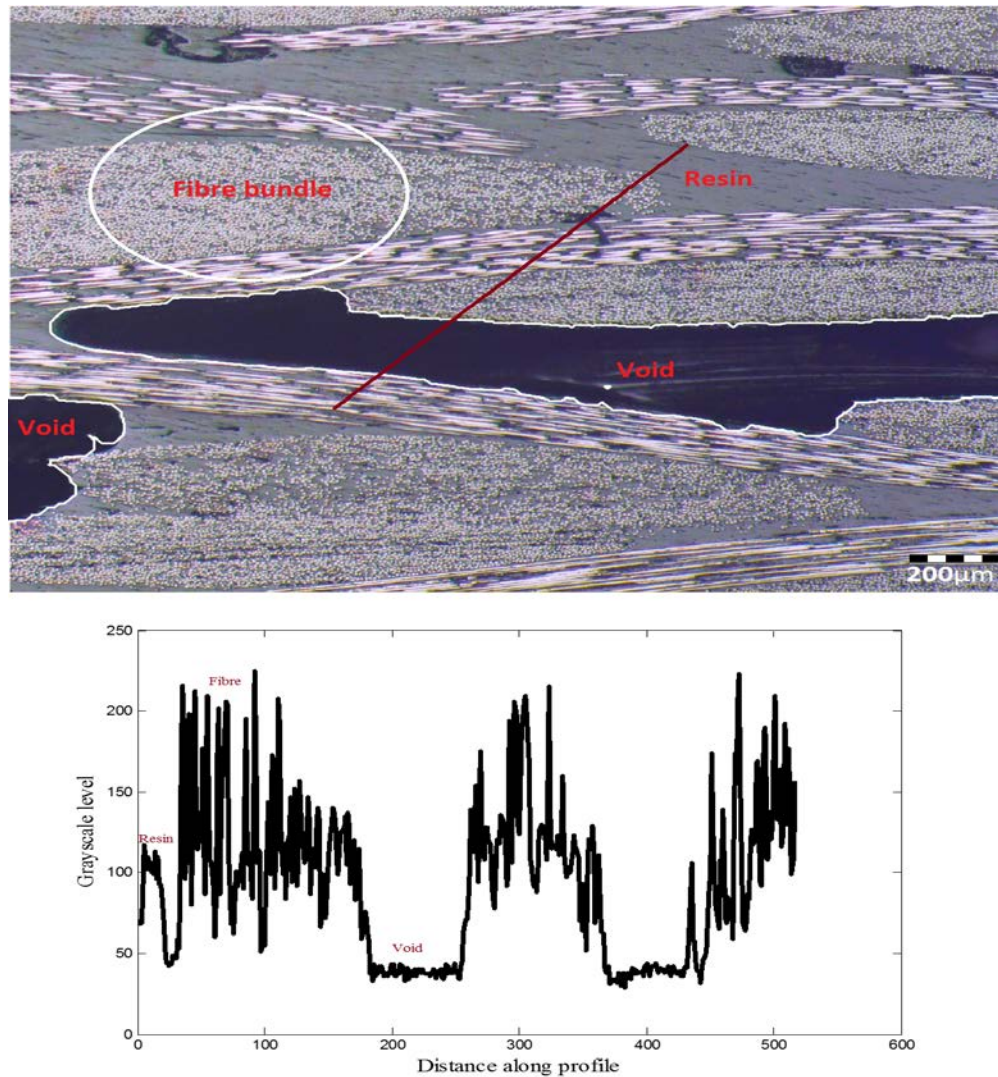
Figure 6-8: The grayscale values along the profile line (red line)

To minimize that uncertainty, it is necessary to repeat the graph of grayscale levels for each void in an image to obtain a representative range. The samples were therefore systematically analysed and a grayscale level was determined to be the optimum value (in our case 40). However some areas with similar gray scale value were also included. Therefore, there needs to be a threshold that is chosen from grayscale images to avoid misclassification of the areas as voids.   Figure 6-9 shows a schematic of the image analysis procedure.

1.Micrograph	2.Convert colourmap to grayscale image	3.Gaussian filter	4.Threshold
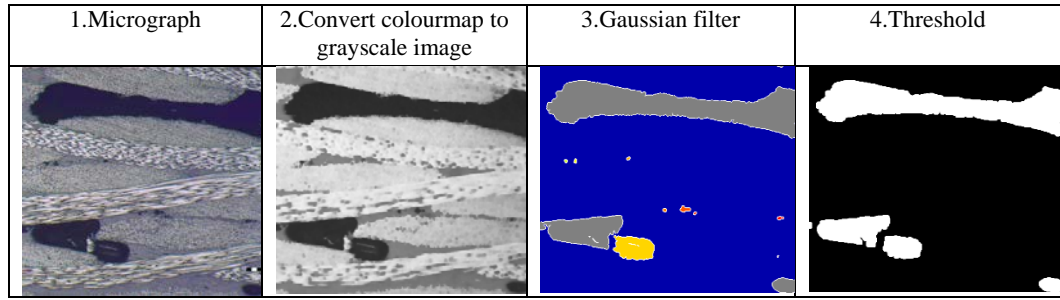
Figure 6-9: The image analysis procedure used for the composite samples

6.1.7 Uncertainty

The more images analysed, the better estimate of average void content in the composite part. However, the relationship between number of images for void content error is non-linear. To estimate the number of images for minimizing uncertainty (error), the error was calculated by the true void content(V_c) which is the average void content of the entire cross section and the estimated void content(V_c^*) which is the average void content of the number of analysed images was computed (Eq.6-4) [187].

$$Error = \frac{\left|V_c^* - V_c\right|}{V_c}$$

(6-4)

Figure 6-10 shows how the size of this error varied with the number of images in our samples. The statistical analysis of the void content revealed that 20 to 25 images provide representative data that can be used to determine void content with Error less than 0.2 [187].
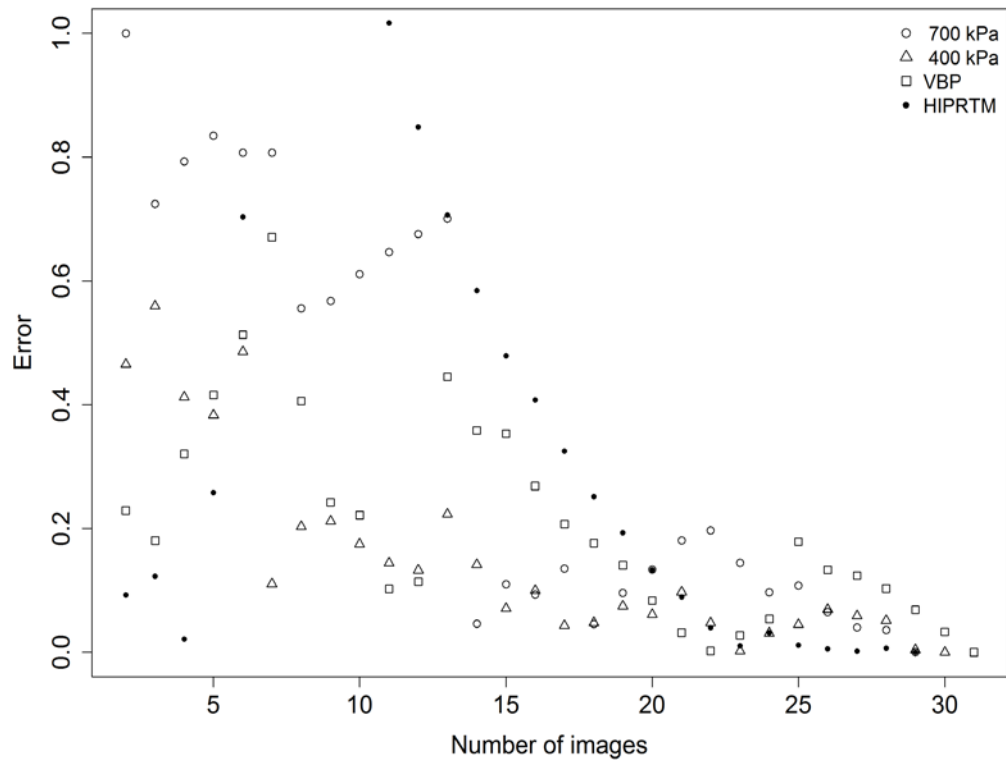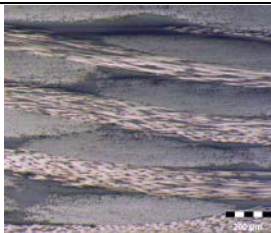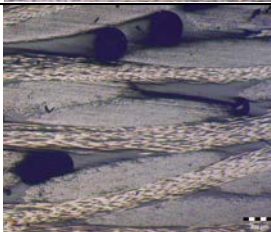
Figure 6-10: The magnitude of void content error as a function of number of images.

6.2   Results and discussion

6.2.1   Comparison of autoclave and Vacuum bag processing

Table 6-2 shows cross-section images of the samples, along with their void content and thickness. The micrographs show that voids are nearly circles. The table also shows that the volume of void varies considerably, and is reduced by increasing the curing pressure.

Table 6-2: Cross-section images of the samples cured at different pressure. The data of void content, thickness and void size are tabulated.

Curing pressure (kPa)	Cross-section image	Void content (%Vol)	Thickness (mm)	Void size (µm)	Fibre content (%Vol)
Reference(600)		<0.2	2.02±0.021	<50-150	49.5±.47
400		2.3±0.04	2.14±0.024	<50-150	46.72±.47
0		3±0.031	2.18±0.023	<50-450	45.81±.44

For the composites cured in the autoclave and the oven, unimodal distributions of void size are observed (Figure 6-11). Their distributions are bell-shaped distribution, implying that the voids are randomly formed along the composite part. Thus, for these cases, void size distribution is characterized by the mean value and standard deviation.

The composite component that has been cured in autoclave at 5 bar (Figure 6-11, left) presented an average equivalent diameter of 67.36µm; and voids with equivalent diameter between 50 µm and 100 µm show the highest frequency (of *circa* 26%). The composite component cured at atmospheric pressure presented an average void size of 136.34µm, and voids with an equivalent diameter between 100 µm and 150 µm show the highest frequency of occurrence (*circa* 34%).
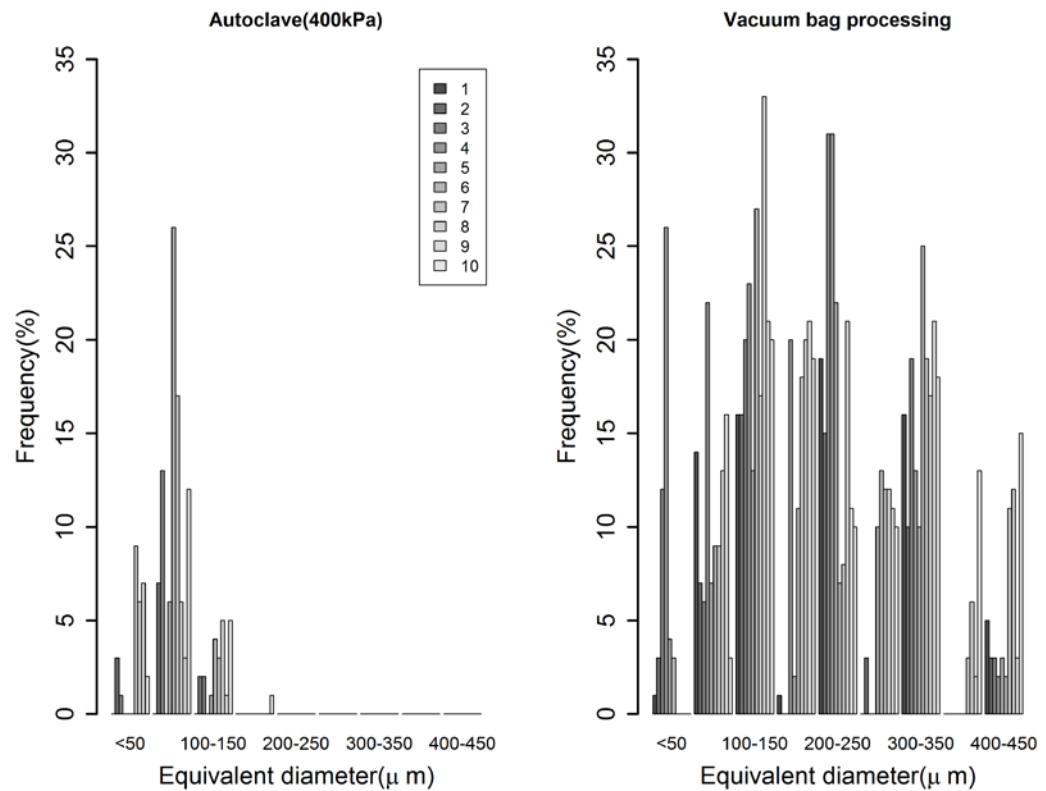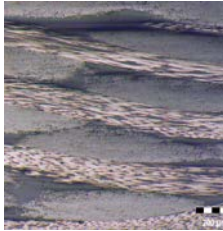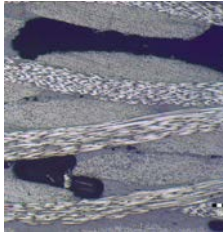
Figure 6-11: Distribution of void size in pre-impregnated carbon parts cured in autoclave (left) and oven (right). The numbers ranged from one to ten in the legend correspond to the composite parts divided into 10 regions.

One can therefore summarize the following: (i) as expected, the relatively high pressure in an autoclave is effective in suppressing void in the sense that vacuum bagging involves actual removal of bubbles within the resin. The effect of the vacuum is decreased when the viscosity of resin increases, especially during gelation [188]. When vacuum is maintained, and subsequently the autoclave pressure is applied to the parts a further decrease of the void content from 3 to 0.2% was observed (going from vacuum bag to autoclave), (ii) the compaction pressure levels significantly affect the mean diameter; the void size distribution was broader for the vacuum bag-cured laminate, while, as the cure pressure levels were increased above the atmospheric pressures, the void size distributions became narrower.

6.2.2 High injection pressure resin transfer moulding

Table 6-5 and Figures 6-12 – 6-14 compare the composites produced by the two different scenarios of the HIPRTM process.

Table 6-3: shows cross-section images of the samples, along with their void content and thickness. The micrographs show the pancake-shaped voids.

HIPRTM	Cross-section image	Void content (%Vol)			Thickness (mm)	Void size (μm)	Fibre content (%Vol)
		Injection side	Top surface	Opposite side			
Without gap		<0.05	<0.05	<0.02	2±0.03	<50-450	61.6±.95
With gap		3.4±0.058	1.26±0.015	1.2±0.037	2.01±0.07	<50-450	49.7±.15

The key difference between the Figures is that they show the void content and void size distribution and fibre volume fractions with and without a gap closure between the top plate and the stack. When there is no the mould gap, as shown in Table 6-5, compared to the mould gap case, a significant reduction in void volume is observed as the void content is reduced from *circa* 3.4% to less than 0.05%. Figure 6-12 describes the effect of the flow distance from the inlet on the void size.
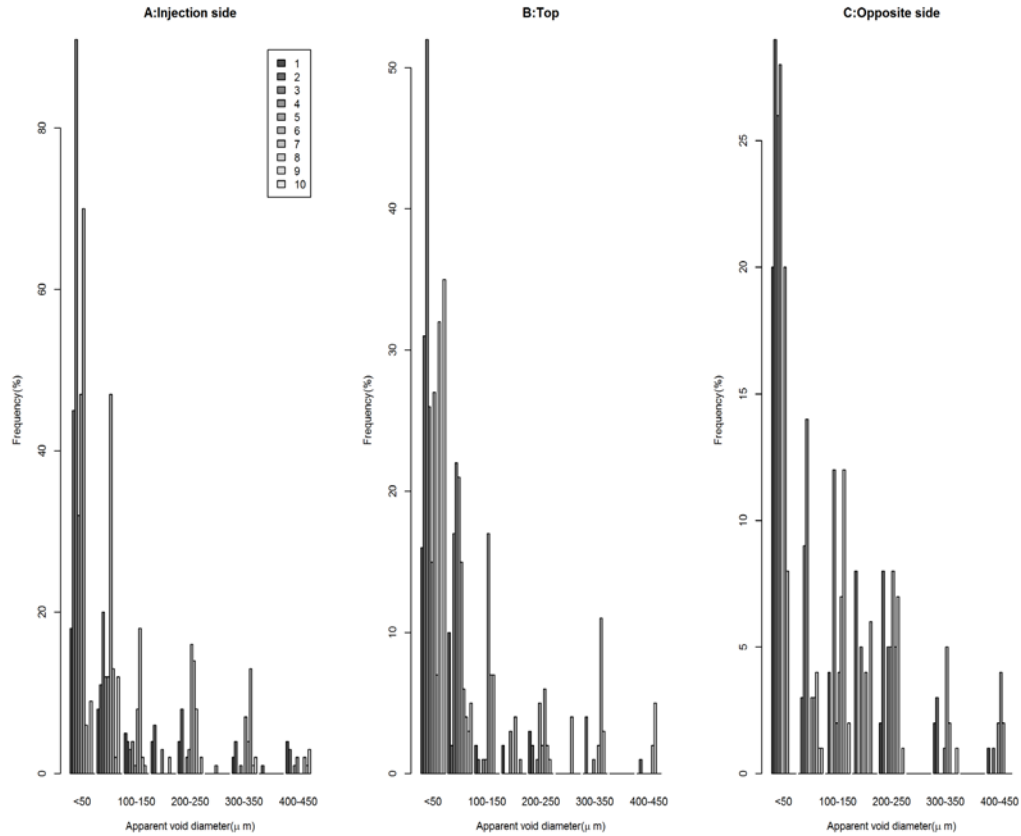
Figure 6-12: Distribution of void size for the 6-layered composite part. The numbers ranged from one to ten in the legend correspond to the composite parts divided into 10 regions.

As an overall trend, it can be seen that the number of voids decreases as the size of voids increases. In addition, this is an overall reduction in void content is also observed as the flow progresses through the mould (less voids further away from the gate). Similar results were reported by Patel *et al.* [189] who observed the zones with high micro-void content localized close to the injection point. The resin flow inside the fibrous reinforcement is highly influenced by the fibres' spatial variability and heterogeneity. Such meso-scale variability from ideal fibre paths forms fingering or saturation lead-lag flow as a result of imbalance between capillary and viscous pressures during the impregnation process[189]. This lead-lag in flow front is highly affected by the flow rates. Then, in our case studies, as the injection was carried at a constant inlet pressure, the flow rates decreased with time, leading to a variable flow front saturation lead-lag as the flow progresses. Therefore, the void content is a function of the flow front distance from the inlet. To our knowledge there have been no reports of this variation in void content in the conditions of HIPRTM with gap. However, work on porosity reduction [190] and in the characterization of voids in different velocity conditions [169] lead us to postulate that the observed effect may be caused by the following: in the beginning of the injection, the gap on the top of the stack creates a high lead-lag with high velocities both in the gap and through thickness. This, in a similar way to what is described by Ruiz *et al.* [169] in the situations of high inter-tow flow speeds creating intra-tow voids, originates a situation where gap flow overtakes the impregnation of the laminate which, in turn, generates voids. (the left side of Figure 6-13). As the flow progresses, there is an overall reduction in flow velocity in the gap because of a reduction in pressure differential at the flow front, allowing

for more time for laminate impregnation. As a consequence, voids become smaller (the right side of Figure 6-13).
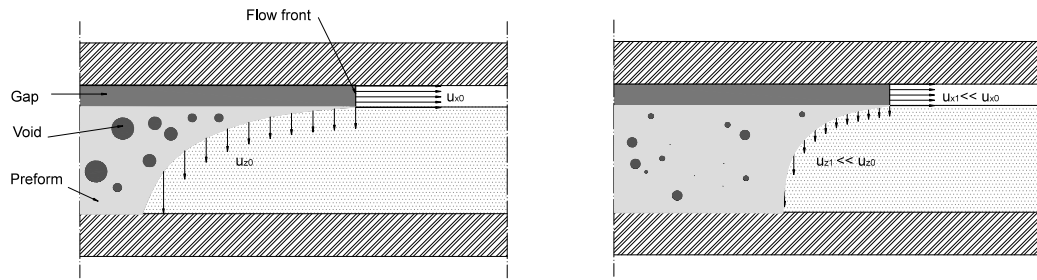

Figure 6-13: Schematic of gap effect

In the injection side, the void size distribution is sharply skewed right (Figure 6-12A), indicating a high small void content at the beginning of the injection process. With increasing resin flow distance from the gate, in the top surface sample (Figure 6-12B), the void distribution is still skewed right. However, the maximum frequency for voids less than 50μm is smaller than at the injection side (c.40% reduction in void frequency). As the resin flow reaches the outlet, a further decrease in voids is observed, as the maximum frequency of voids is reduced from *circa* 90% void frequency in the injection side to *circa* 30% void frequency in the opposite side (Figure 6-12C).

It can therefore be observed that, in agreement with other works [178] [179] [191], the monotonous reduction in void size is dependent on speed and distance to the gate. In addition, we were unable to see a pattern in the size of voids, at micro and macro- scales, along the length of mould when resin injection is performed at a constant pressure and the volume of macro-voids appear to remain fairly constant as the flow-front moves away from the inlet. In contrast, the micro-scale void content shows a clear drop as a function of the flow-front distance from the inlet. These results suggest that (i) despite great care taken in the reduction of air bubbles in the resin by the on-line resin mixing, some micro bubbles, which are the primary cause of microvoids [192] [193] [194], remain; (ii) the mould gap led to a higher permeability in flow direction than the transverse permeability, resulting in high concentration of voids through the thickness.

Figure 6-14 shows that the maximum void occurrence frequency for voids with equivalent diameter less than 50μm is reduced from *circa* 90% to *circa* 7% for the composite produced without the mould gap. Therefore the results demonstrate the effectiveness of the post-fill pressure procedure (e.g. without gap), which makes easy to squeeze resin from the stack and favours complete fibre wetting through thickness in the sense that the clamping force increased the through thickness permeability. Having this basic information, we postulate that the significant decrease in void content from the without gap case is a result of compression of the bubbles close to flow front. The observations reveal that the main cause of void formation in RTM is mechanical entrapment rather than void growth during curing [178].
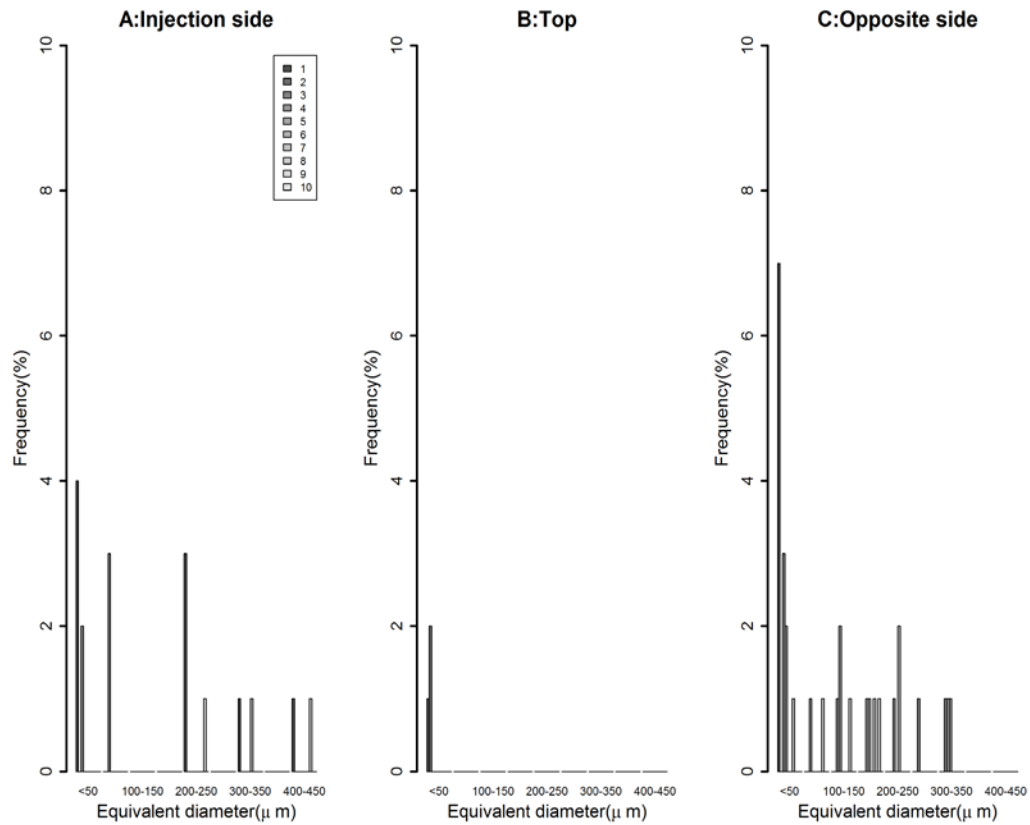
Figure 6-14: Distribution of void size for the 8-layered composite part

The overall results of this study are shown in Figures 6-15 and 6-16. Figure 6-15 shows the total void content (%) per U-shaped CFRP part for each manufacturing method. The void content with the autoclave curing at 600 kPa as the reference process was less than 0.2%. The HIPRTM without the mould gap resulted in the lowest void content (*circa* 0.05%). The HIPRTM with the mould gap and VBP resulted in the highest void content (*circa* 3%). The autoclave curing at 400 kPa followed with *circa* 2.3%. For composite parts produced by autoclave, the measured void content dependence on cure pressure levels, as shown in Figure 6-15 in the sense that autoclave pressures suppress void development. This finding is consistent with previous study by Grunenfelder and Nutt [195] showing that the autoclave pressures prevent the formation and development of voids by forcing moisture to remain in solution. However, in VBP, compaction and curing occurs under atmospheric pressure, making the laminates more susceptible to void growth from uptake moisture. On the other hand, due to replacement of air in the mold cavity by the resin, the mechanism of void formation in HIPRTM is different from that in the autoclave and VBP. The origin of voids in the parts produced by HIPRTM may occur by mechanical entrapment of air during mold filing, and air bubble, volatile substances such as moisture in the resin [177][6][178][179].A fundamental question is about the origin of voids in the composite parts produced by HIPRTM with and without gap. Evidence from the literature [177][6][178][179] suggests that the mechanical entrapment of air and nucleation and growth of void are possible void formation mechanisms and findings indicate that the packing pressure in HIPRTM on the one hand disrupts the nucleation and growth kinetics of voids, and on the other hand increases pressure in the surrounding resin and thereafter compresses void.
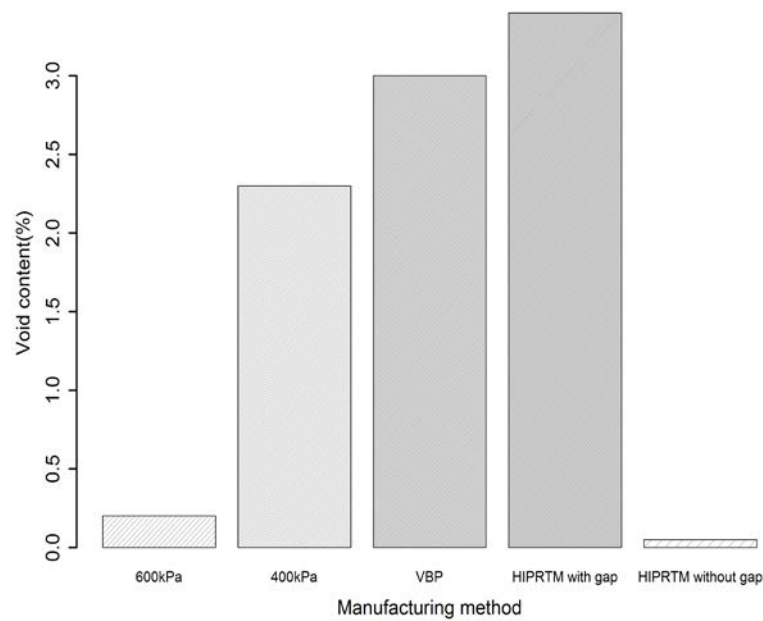
Figure 6-15: Total void content (%) for each manufacturing method. The autoclave curing at 600 kPa is considered the reference which the alternative manufacturing processes are compared to.

Figure 16 shows the frequency of the void size for autoclave processing (600kPa) and the HIPRTM without the mould gap. Autoclave processing (600kPa) as the reference process is presented on the left of the Figure 6-16. The HIPRTM without the mould gap shows a reduction in the frequency of the void size over the autoclave process. On average, the frequency of the void size with an equivalent diameter less than 50 µm was reduced by *circa* 4% for the HIPRTM compared to the autoclave process. As a consequence this suggests that HIPRTM without the mould gap is comparable to autoclave processing in terms of void content and frequency of void size.
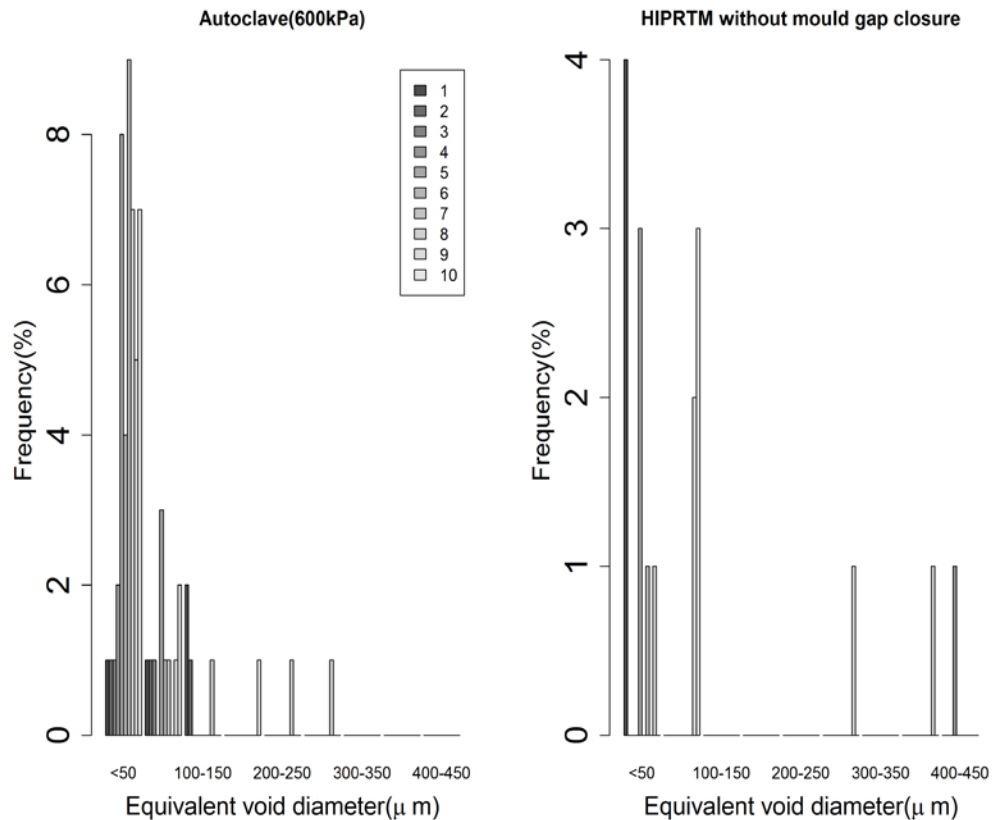
Figure 6-16: Total void content (%) for each manufacturing method

6.3   Conclusion

This study addressed a new variant of the RTM process, high injection pressure resin transfer moulding (HIPRTM). In order to examine the potential of this new process, we carried out a set of experiments to compare HIPRTM with autoclave processing and vacuum bag processing(VBP) in terms of the resulting void content and void size distribution. In addition, we investigated effects of the mould gap and subsequent compression on frequency of occurrence of classes of void size. In order to make a comparison study, a relevant geometry demonstrator was selected, consisting of one spar, based on a design that was used for a wing of an UAV.

Results showed that: (1) the void size distribution of Autoclave and VBP composite parts followed a bell shape distribution while we observed a right-skewed distribution for HIPRTM due to the dependence of void sizes on fluid flow speed and distance to the gate. (2) One very important result from the study was that the HIPRTM composite quality produced without the gap closure (continuously compacted) was comparable with the autoclave results. In both fibre volume fraction and void content, HIPRTM assisted with external compaction pressures yielded a composite part with the lowest void content of all studied processes providing a better quality component than it is possible to obtain from autoclave processing. In this study we have used normal resin systems and one type of fabric and presented experiments that describe how the void content is reduced by HIPRTM. However, role of other processing parameters such as the effect of fast curing

resin, fibre architectures and fibre orientation remain unclear. Consistently addressing additional parameters affecting void formation will result in a better understanding of why the voids are formed in composite parts, elucidate the limits of HIPRTM for composites manufacturing.

Chapter 7

Conclusion

7.1   Concluding remarks

Some of the major goals facing RTM today are autoclave-part quality, which can be understood as enabling over 60% fibre volume fraction and sub-1% void content parts. To allow jump from the current 50-55% to over 65% fibre volume fraction and from 2-3% to sub-1% void content, a new variant of RTM, high injection pressure resin transfer moulding (HIPRTM) has emerged in recent years. As the resin has to be injected at high pressure while preform undergoes deformation in this complex process, the quality of composite parts is dominated by preform deformation. For the given preform, the local geometric variation in tow and fibre arrangement occurs. One knows that permeability varies locally as a function of the micro and meso arrangement of fibres and tows due to natural intra-tow variability, material handling, textile architecture, nesting etc. The spatial variation of permeability leads to the variable flow patterns, which in turn may result in void formation. Additionally, high pressure resin injection may pose the problem of fibre roving, fibre wash out as well as inadequate preform wetting. One must include not only the local variation of permeability due to complex compaction and natural variability in preform but also the injection strategy to better understand the process in terms of its emergent defects which are manifest in such as fibre wash-out, void formation and others. Hence, a large scale and efficient use of HIPRTM will require a better understanding of the variability of permeability within the preform which can be achieved through an adaptation of existing simulation software packages to include these phenomena. It is a critical stage to help improve the reliability of current mould filling simulation softwares towards the quality level of hand lay-up/autoclave. In this thesis, the accurate simulation of flow within this complex manufacturing process is the basis for the need for an accurate description of the statistics of permeability in order to feed downstream stochastic simulation models. As such models can quantify the robustness of this manufacturing process, which is a significant help towards high volume production such as in the automotive industry.

The goal of addressing out-of-autoclave quality with HIPRTM was also directly addressed. As it is will remain impossible, for the time being, to control all process variables in HIPRTM. Further optimization of the process needs to be implemented to eliminate or reduce voids as well as dry spots, aiming at real the autoclave quality.

In this thesis, the author addressed the issue of scatter in measured permeability values as a result of various sources of uncertainty; some come from the internal geometry variation of fabrics and some come from experimental procedure and set ups. The relation between the internal variation of the preform and the statistics of its permeability was

studied. A roadmap was described to incorporate this variability into the permeability prediction. Due to the hierarchical structure of preform, different length scales were taken into account for the statistics of permeability (micro and meso scales). Quality concerns, including void content and void size, due to HIPRTM process variables were also addressed. Image analysis was used to evaluate and compare void content and the size distribution of a wing spar composite part by three processing techniques. The techniques were vacuum bag processing, hand lay-up/autoclave processing (using two different compaction pressure), and High Injection pressure Resin Transfer Moulding (HIPRTM).

The two main topics, presented in this thesis, is meant to address the challenges to the industrial application of HIPRTM process for polymer-based composites manufacturing:

1- Multiscale permeability variations as a result of internal geometry variation of a 2/2 twill woven carbon fabric, including the effects of preform deformation on the statistics of permeability.

2- Experimental study to quantify the void content of 2/2 twill woven carbon-epoxy composite wing spars in this new family of LCM. Two configurations of the HIPRTM process were used: with and without a 0.2 mm gap between the upper mould face and the preform after clamping the mould.

Thus, the first part of this thesis addressed permeability scatter cuased by the internal geometric variation of tows by studying a specific 2 by 2 twill woven carbon fabric was analyzed. This variation was analysed in detail for three main sources of fabric heterogeneity, including: (i) the distortions, induced by the tow undulations through the fabrics, forming mesoscale channels, (ii) random arrangement of fibres inside a tows, forming microscale channels, and (iii) the stochastic variation of tows cross sections geometry, forming microscale channels as well as misalignment. From this work, permeability variations were correlated to the geometric variation in the fibre preform.

It is observed that the variations of permeability not only are largely dominated by the internal geometric variation of the 2 by 2 twill woven carbon fabric but also correlated across the spatial domain of the fabric, disproving the assumption of a spatially uncorrelated medium. In addition, the sampling scale can influence the statistics of permeability. For the data from the meso-scale, permeability components are statistically characterised by a normal distribution. On the other hand, the normal distribution is not necessarily suitable for micro-scale permeability. These results indicate that the variations of tow cross sections as well as the tow paths (misalignment) lead to higher scatter in the permeability (*ca* 61%) compared to the mesoscopic variability (*ca* 18%) and random arrangement of fibre inside a tow (*ca* 18%). Therefore, for such a heterogeneous medium (2 by 2 twill woven fabric), not only are there two main modes in the statistical distributions of permeability but also microscopic internal variations (tow geometry) of fabric introduce significant uncertainty to the statistics of the global permeability.

The above observations are relevant to HIPRTM where tow cross-section shape is an important variable: as the global fibre volume fraction increases as the tow shape become more elliptical, the impact of the intra-tow permeability on the global permeability increases. This dependency also implies that the variations of macroscopic permeability, which is determined in macroscopic flow experiments, can never completely replicate the

actual local inhomogeneity. In that sense, to predict flow and its variability within a fibrous media, local permeability is significant and the models should be linked to the preform microstructure.

The second part of thesis formed a basis for understanding of the relevance of HIPRTM variables such as mould gap as well as compaction towards the achievement of high performance composite parts within a relatively short cycle time. In comparison to normal RTM, the impregnation of the fibrous media was conducted at high injection pressure (20 bar) thanks to the state of art press and semi-automated mixing resin system. This allowed this thesis to explore novel topics, such as looking at the benefit of a short impregnation time independent of the part geometry and size.

Results showed that the mould gap and the compaction pressure influence fibre volume fraction and void contents of the final composite part. It was also shown that it is possible to produce autoclave-part quality (a void content of less than 1%) and a fibre volume fraction of 61% within a relatively short cycle time (less than 2 minute) in a highly compacted preform during the high pressure resin injection (without gap). On the other hand, the HIPRTM process with the gap led to the highest void content of all the techniques studied. This showed that it is possible to achieve the autoclave-part quality to produce with HIPRTM and this understanding allows this thesis to propose how one can expect to produce high quality, low cycle time parts, from RTM, in the future.

However, the higher amount of microvoids compared to the amount of macrovoids is not completely described by the process variables (mould gap and subsequent compaction pressure). These results indicated unsteady local flow velocity due to the increasing influence of local permeability on global permeability. Therefore, when establishing stochastic models for flow simulations in HIPRTM, one has to account the statistics as well as the spatial distributions of local permeability (as shown in the first of this thesis), which are linked to the geometric characteristics of the deformed heterogeneous medium, in simulation models. Furthermore, these results reveal that considered as a stochastic flow simulation within fibrous media, the scale at which flow modelling is done can be largely influenced by voids locations and the characterisations of voids at the micro- and mesoscale become important.

7.2   Future works / Recommendations

Still, this research conducted in HIPRTM makes only a small contribution in the continual progression towards high fibre volume fraction composites with autoclave quality. A number of recommendations arose from the above conclusions and the more detailed discussion in each chapter. The recommendations for future work are:

7.2.1   Linking internal variations of the fibrous medium with stochastic flow simulation

The relevance of flow models for liquid composite moulding depends on the scientific community's ability to provide statistically relevant, estimates of fill times and filling problems. The barrier to this is the understanding of how material properties at different

scales are combined in statistically representative permeabilities at the flow modelling scale. There are basically two methods to represent statistics of permeability across a fibrous preform: (1) a simple random value with knowledge of a specific probability density function (such as normal distribution) of permeability, (2) random fields. Clearly, the first approach, as shown in this thesis, cannot properly represent the properties of the heterogeneous fibrous medium. On the other hand, in the random fields, the value of permeability across the fibrous medium is not constant, as shown in this thesis, and follows some correlation pattern. Therefore, the random field approach allows one to include more detailed information about uncertainties of permeability in flow simulation process than the use of a simple random value of permeability. This thesis addressed the information required for the spatial variation of the permeability across the fabric. However, the modelling strategy to generate corresponding random field and produce the samples required for flow simulations is required.

This random field representation of permeability is more relevant for HIPRTM where preform undergoes high compaction pressure, and subsequently subjects to significant internal variations. Additionally, this issue will be further important for fibre volume fraction more than 60-65%. A rise up to 60-65% in V_f means that the compaction of preform leads to shorter distance and denser packing of tows. In this sense, tows in the woven fabric cannot freely move closer to the adjacent tow and hence they have a limited range of tow shape variation. Consequently, the inclusion of variations of the intra-tow and inter-tow flows are important for flow simulation at macro and mesoscale. In this sense, the linking of spatial randomness of fibrous media with the multiscale permeability is expected to improve the advancement of fluids, and therefore would impose significant influence over the final part quality.

7.2.2   Variability of resin viscosity

HIPRTM allows the use of fast-curing resins for speeding up RTM manufacturing process, reducing the cycle time to less than 5 min. The flow behviour in textile reinforcements becomes more complex as the resin viscosity is changing during impregnation stage. In addition, resin injection at high flow rate will pose the problem of fibre roving and misalignment, leading to local variations of textile permeability. Therefore, the inclusion of the permeability variability as well as a rheo-kinetic model, describing the spatial variation of the viscosity are the essential inputs for the stochastic flow simulation of HIPRTM process. In this thesis, the ways to define the variabilities in permeability were proposed. However, this thesis did not address the ways to define the changing of viscosity during impregnation processes. Next to permeability, it is important to take into account the variability in viscosity for stochastic flow simulations.

The definitions of the variabilities in permeability and rheo-kinetic models as inputs for a stochastic mould filling simulation at high injection pressures would allow one to obtain further results as compared to a deterministic mould filling simulation.

7.2.3   Laminate geometry

It was proven within the framework of this thesis that it is possible to produce composite parts with high degree of complexities. In this thesis, permeability measurements and predictions were carried out for constant thickness which is relevant for the flat geometries. However, most aerospace and automotive components have complex geometries with high degree of complexity such as the spar wing which was produced by HIPRTM in this thesis. Unlike the flat laminates, the thickness of complex geometry may not be constant: such as corners and curvatures in localized regions of the preform compared to other regions. Hence, it is expected that there would be uneven flow pattern among these regions, increasing the possibility of the formation of fibre roving and inadequate wetting zones at high injection pressure which is relevant to HIPRTM. Therefore, as this process introduces some additional variabilities compared to conventional RTM process, it would be interesting to take into account variable thickness for fluid flow and permeability evaluations.

7.2.4   Sample size

At the mesoscale, the permeability evaluation was carried out on the generated virtual geometry in the size of 110×110 mm^2. The random variations in the internal geometry of preform establish a direct correlation between the variation in the macroscopic permeability and the geometrical variability at the lower scale. The size of sample can influence the degree of randomness in the geometrical variabilities, and subsequently the variation of permeability. Increasing the size of sample helps reveal the reproducibility of permeability data, having more reliable explanation of permeability scatter. In other words, increasing the sample size can effectively boost the statistics of the estimated permeability. Hence, the issues of estimate permeability distribution versus sample size to underlie probability density function (PDF) needs to be recognised. Because permeability is statistically a random variable, and the estimated permeability values in this thesis was only from one hundred sample unit cells extracted from a virtual geometric model.

Intuitively, the author would expect that as the number of data increases, the estimated permeability value approaches the expected value. Therefore, it should be useful to know how many data are required to achieve sufficiently accurate statistics of permeability.

7.2.5   Through thickness permeability

One potential problem associated with HIPRTM process is the possibility of fibre roving during high pressure in-plane fluid injection. This thesis dealt with this problem by considering two inlet gates on a single path. However, it may not work for the use of fast curing resin, where the resin needs to impregnate preform less than one minute. One possible strategy is to inject resin into a gap between the preform and the upper mould, where the tooling is not completely clamped and hence the preform is not compacted. The impregnation is carried out using the mould clamping force. This external compaction pressure forces resin to impregnate the preform through thickness. In this sense, the contribution of through thickness permeability is as important as in-plane permeability for the impregnation of preform. As the through thickness permeability becomes important, 3D flow modelling is necessary. Hence, in addition to in-plane permeability as an input for

flow simulation, an accurate characterisation of through thickness is required for the flow simulation.

The proposed uncertainty evaluation is developed for in-pane permeability of woven textile, but this methodology can be applicable for the characterization of through-thickness permeability. There is still a substantial lack of incorporating the internal geometry variations into through-thickness permeability measurements.

7.2.6   On-line mixing

Considering equipment, HIPRTM injection process was conducted at a constant pressure. In order to inject resin at relatively high injection pressure, an on-line mixing machine was designed. Although useful from an automation viewpoint, problems arising from an inhomogeneous curing of the final composite parts are plausible. If hardener and resin are mixed in constant ratio during the injection stage, the resin that impregnates textile reinforcements at the early stages of the impregnation will have a higher degree of curing than the resin that impregnates at a later time. Hence, the final composite part will not polymerize homogenously and demoulding the composite part is not possible until the last-resin arrivals has cured. Therefore, adjustments to high-pressure on-line mixing can be considered to improve the applicability of HIPRTM for high-volume production. Currently, few studies developed strategies for the control of degree of polymerization during injection stages in case of on-line mixing. However, these studies are limited to low pressures (one bar) which were lower than one expects to use in HIPRTM.

The on-line mixing injection machine can be further extended by considering the effect of injection pressure on the dynamics of resin-hardener proportions, degree of mix of the components, and consequently the degree of cure of the mix for the first few seconds (while the dynamic effects are felt).

References

[1]   K. Jacques, L. Bax, H. Vasiliadis, I. Magallon, and K. Ong, "Polymer composites for automotive sustainability," p. 56, 2015.

[2]   A. Maffezzoli and A. Grieco, "Optimization of parts placement in autoclave processing of composites," *Appl. Compos. Mater.*, vol. 20, no. 3, pp. 233–248, 2013.

[3]   J. Ramaswamy Setty, A. R. Upadhya, G. N. Dayananda, G. M. Kamalakannan, and J. Christopher Daniel, "Autoclaves for aerospace applications: Issues and challenges," *Int. J. Aerosp. Eng.*, vol. 2011, 2011.

[4]   P. Rosenberg *et al.*, "Effect of process parameters on cavity pressure and component performance in high pressure RTM process variants."

[5]   M. Pérez, "Table of of contents," p. 2004, 2003.

[6]   H. J. Barraza, Y. K. Hamidib, L. Aktasb, E. a. O'Rear, and M. C. Altan, "Porosity Reduction in the High-Speed Processing of Glass-Fiber Composites by Resin Transfer Molding (RTM)," *J. Compos. Mater.*, vol. 38, no. 3, pp. 195–226, 2004.

[7]   L. Khoun, D. Maillard, and M. Bureau, "Effect of process variables on the performance of glass fibre reinforced composites made by high pressure resin transfer moulding," in *12 th Automotive Composites Conference*, 2012.

[8]   A. Siddiqui, "High Pressure RTM Process modeling of Carbon Fibre Composites with Ultra-Fast-Cure resins," 2010.

[9]   P. Harrison, W. R. Yu, and A. C. Long, "Rate dependent modelling of the forming behaviour of viscous textile composites," *Compos. Part A Appl. Sci. Manuf.*, vol. 42, no. 11, pp. 1719–1726, 2011.

[10]   M. V. B. and R. P. Advani S. G., "Resin Transfer Molding," in *Flow and Rheology in Polymeric Composites Manufacturing*, Suresh G. Advani, Ed. Amsterdam, 1994, pp. 465–516.

[11]   D. C. Charmpis, G. I. Schuëller, and M. F. Pellissetti, "The need for linking micromechanics of materials with stochastic finite elements: A challenge for materials science," *Comput. Mater. Sci.*, vol. 41, no. 1, pp. 27–37, 2007.

[12]   R. Arbter *et al.*, "Experimental determination of the permeability of textiles: A benchmark exercise," *Compos. Part A Appl. Sci. Manuf.*, vol. 42, no. 9, pp. 1157–1168, 2011.

[13]   N. Vernet *et al.*, "Experimental determination of the permeability of engineering textiles: Benchmark II," *Compos. Part A Appl. Sci. Manuf.*, vol. 61, pp. 172–184, 2014.

[14]   J. B. Alms, N. Correia, S. G. Advani, and E. Ruiz, "Experimental Procedures to Run Longitudinal Injections to Measure Unsaturated Permeability of LCM Reinforcements," *FPCM Collab.*, 2010.

[15]   K. Hoes *et al.*, "New set-up for measurement of permeability properties of fibrous reinforcements for RTM," *Compos. - Part A Appl. Sci. Manuf.*, vol. 33, no. 7, pp. 959–969, 2002.

[16]   S. K. Padmanabhan and R. Pitchumani, "Stochastic modeling of nonisothermal flow during resin transfer molding," *Int. J. Heat Mass Transf.*, vol. 42, pp. 3057–3070, 1999.

[17]   E. Fauster and R. Schledjewski, "Uncertainty analysis for optical permeability ," in *ICCM19*, 2013, no. 28 July-3 August.

[18]   E. Fauster, H. Grössing, and R. Schledjewsk, "2D Anisotropic Permeability Calculation in Terms of Uncertainty Propagation," in *ECCM16*, 2014, no. June, pp. 22–26.

[19]   S. V. Lomov *et al.*, "Textile composites: Modelling strategies," *Compos. - Part A Appl. Sci. Manuf.*, vol. 32, no. 10, pp. 1379–1394, 2001.

[20] A. Vanaerschot, B. N. Cox, S. V. Lomov, and D. Vandepitte, "Stochastic multi-scale modelling of textile composites based on internal geometry variability," *Comput. Struct.*, vol. 122, pp. 55–64, 2013.

[21] A. Vanaerschot, B. N. Cox, S. V. Lomov, and D. Vandepitte, "Simulation of the cross-correlated positions of in-plane tow centroids in textile composites based on experimental data," *Compos. Struct.*, vol. 116, no. 1, pp. 75–83, 2014.

[22] A. Vanaerschot, B. N. Cox, S. V. Lomov, and D. Vandepitte, "Stochastic framework for quantifying the geometrical variability of laminated textile composites using micro-computed tomography," *Compos. Part A Appl. Sci. Manuf.*, vol. 44, no. 1, pp. 122–131, 2013.

[23] A. Vanaerschot, B. N. Cox, S. V Lomov, and D. Vandepitte, "Multiscale Modeling and Uncertainty Quantificationof Materials and Structures," *Multiscale Model. Uncertain. Quantif. Mater. Struct.*, pp. 1–303, 2014.

[24] A. Vanaerschot, B. N. Cox, S. V. Lomov, and D. Vandepitte, "Experimentally validated stochastic geometry description for textile composite reinforcements," *Compos. Sci. Technol.*, vol. 122, pp. 122–129, 2016.

[25] S. V. Lomov, I. Verpoest, J. Cichosz, C. Hahn, D. S. Ivanov, and B. Verleye, "Meso-level textile composites simulations: Open data exchange and scripting," *J. Compos. Mater.*, vol. 48, no. 5, pp. 621–637, 2013.

[26] J. Bear, *Dynamics of Fluids in Porous Media*, Dover. New York: The American Elsevier Company, 1972.

[27] S. Whitaker, *The Method of Volume Averaging*. Kluwer Academic Publishers, 1998.

[28] A. Endruweit and A. C. Long, "Influence of stochastic variations in the fibre spacing on the permeability of bi-directional textile fabrics," *Compos. Part A Appl. Sci. Manuf.*, vol. 37, no. 5, pp. 679–694, 2006.

[29] F. Desplentere, I. Verpoest, and S. V Lomov, "Multiscale modelling of stochastic effects in mould filling simulations for thermoplastic composites," in *The 9th International Conference on Flow Processes in Composite Materials, FPCM-9*, 2008, vol. 9, no. July.

[30] J. M. Berg and V. R. Voller, "An identification and control strategy for a liquid composite molding process," *Appl. Math. Model.*, vol. 22, no. 4–5 /5, pp. 207–218, 1998.

[31] A. Endruweit, A. C. Long, F. Robitaille, and C. D. Rudd, "Influence of stochastic fibre angle variations on the permeability of bi-directional textile fabrics," *Compos. Part A Appl. Sci. Manuf.*, vol. 37, no. 1, pp. 122–132, 2006.

[32] X. S. Zeng, a C. Long, F. Gommer, A. Endruweit, and M. Clifford, "3D Carbon Reinforcements," in *18th International Conference on Composite Materials*.

[33] L. Fang, J. Jiang, J. Wang, and C. Deng, "Effect of Nesting on the Out-of-Plane Permeability of Unidirectional Fabrics in Resin Transfer Molding," *Appl. Compos. Mater.*, vol. 22, no. 3, pp. 231–249, 2015.

[34] S. Bickerton, P. Šimáček, S. E. Guglielmi, and S. G. Advani, "Investigation of draping and its effects on the mold filling process during manufacturing of a compound curved composite part," *Compos. Part A Appl. Sci. Manuf.*, vol. 28, no. 9–10, pp. 801–816, 1997.

[35] A. Endruweit, X. Zeng, and A. C. Long, "Multiscale modeling of combined deterministic and stochastic fabric non-uniformity for realistic resin injection simulation," *Adv. Manuf. Polym. Compos. Sci.*, vol. 1, no. 1, pp. 3–15, 2015.

[36] R. Pan, Z. Liang, C. Zhang, and B. Wang, "Statistical characterization of fiber permeability for composite manufacturing," *Polym. Compos.*, vol. 21, no. 6, pp. 996–1006, Dec. 2000.

[37] E.M.Sozer, "Effect of preform non-uniformity on mold filling in RTM process," in *nt. SAMPE Tech. Conf. Ser.*, 2001, pp. 176–189.

[38] V. I. Desplentere F, Lomov S, "EA405.pdf," in *25th SAMPE Eur.*, 2004, pp. 331–336.

[39] Y. DE Parseval, K. M. Pillai, and S. G. Advani, "A Simple Model for the Variation

of Permeability due to Partial Saturation in Dual Scale Porous Media," *Transp. Porous Media*, vol. 27, no. 3, pp. 243–264, 1997.

[40] T. S. Lundstrom, V. Frishfelds, and a. Jakovics, "A Statistical Approach to Permeability of Clustered Fibre Reinforcements," *J. Compos. Mater.*, vol. 38, no. 13, pp. 1137–1149, 2004.

[41] N. Wegh, S. Bachschuster, D. Gaudlitz, and M. Klein, "Three-dimensional simulation of the impregnation stage of the RTM process considering the local structure of the fiber layup," *WIT Trans. Eng. Sci.*, vol. 89, pp. 487–499, 2015.

[42] R. Loendersloot and R. Akkerman, "A permeability prediction for non-crimp fabrics," in *Flow process in composite materials*, 2006, no. July.

[43] F. Gommer, L. P. Brown, and R. Brooks, "Quantification of mesoscale variability and geometrical reconstruction of a textile," *J. Compos. Mater.*, 2015.

[44] F. Zhang, S. Comas-Cardona, and C. Binetruy, "Statistical modeling of in-plane permeability of non-woven random fibrous reinforcement," *Compos. Sci. Technol.*, vol. 72, no. 12, pp. 1368–1379, Jul. 2012.

[45] P. Xu and B. Yu, "Developing a new form of permeability and Kozeny-Carman constant for homogeneous porous media by means of fractal geometry," *Adv. Water Resour.*, vol. 31, no. 1, pp. 74–81, 2008.

[46] S. Amico and C. Lekakou, "An experimental study of the permeability and capillary pressure in resin-transfer moulding," *Compos. Sci. Technol.*, vol. 61, no. 13, pp. 1945–1959, 2001.

[47] R. C. Lam and J. L. Kardos, "The permeability and compressibility of aligned and cross-plied carbon fiber beds during processing of composites," *Polym. Eng. Sci.*, vol. 31, no. 14, pp. 1064–1070, 1991.

[48] B. R. Gebart, "Permeability of Unidirectional Reinforcements for RTM," *J. Compos. Mater.*, vol. 26, no. 8, pp. 1100–1133, 1992.

[49] C. W. M. Gibson L. Batch, Yung-Tin Chen, "Capillary Impregnation of Aligned Fibrous Beds: Experiments and Model," *J. Reinf. Plast. Compos.*, vol. 15, pp. 1027–1051, 1996.

[50] J. G. Williams, C. E. M. Morris, and B. C. Ennis, "Liquid Flow Through Aligned Fiber Beds," *Polym. Eng. Sci.*, vol. 14, no. 6, pp. 413–419, 1974.

[51] I. N. Gîlcă, E. Ungureanu, T. Măluţan, and I. Valentin, "Institute of Paper Science and Technology," *Sci. Technol.*, no. 902, p. 2012, 2012.

[52] J. Muzzy, John D. and Zhang, Yi and Bradley, "Flow of thermoplastics through fibre assemblies." .

[53] T. S. Lundström, "Permeability of non-crimp stitched fabrics," *Compos. Part A Appl. Sci. Manuf.*, vol. 31, no. 12, pp. 1345–1353, 2000.

[54] B. Yu and L. James Lee, "A simplified in-plane permeability model for textile fabrics," *Polym. Compos.*, vol. 21, no. 5, pp. 660–685, 2000.

[55] E. B. Belov *et al.*, "Modelling of permeability of textile reinforcements: Lattice Boltzmann method," *Compos. Sci. Technol.*, vol. 64, no. 7–8, pp. 1069–1080, 2004.

[56] B. Verleye, S. V. Lomov, A. Long, I. Verpoest, and D. Roose, "Permeability prediction for the meso-macro coupling in the simulation of the impregnation stage of Resin Transfer Moulding," *Compos. Part A Appl. Sci. Manuf.*, vol. 41, no. 1, pp. 29–35, 2010.

[57] B. Verleye *et al.*, "Predicting the permeability of textile reinforcements via a hybrid navier- stokes/brinkman solver," *8th Int. Conf. Flow Process. Compos. Mater.*, no. July, 2006.

[58] E. E. Swery, R. Meier, S. V. Lomov, K. Drechsler, and P. A. Kelly, "Predicting permeability based on flow simulations and textile modelling techniques: Comparison with experimental values and verification of FlowTex solver using Ansys CFX," *J. Compos. Mater.*, 2015.

[59] A. Vanaerschot, B. N. Cox, S. V Lomov, and D. Vandepitte, "Stochastic characterisation of the in-plane tow centroid in textile composites to quantify the multi-scale variation in geometry," *Int. Union Theor. Appl. Mech.*, 2014.

[60] Q. Wang, B. Mazé, H. V. Tafreshi, and B. Pourdeyhimi, "A note on permeability simulation of multifilament woven fabrics," *Chem. Eng. Sci.*, vol. 61, no. 24, pp. 8085–8088, 2006.

[61] A. Nabovati, E. W. Llewellin, and A. C. M. Sousa, "Through-thickness permeability prediction of three-dimensional multifilament woven fabrics," *Compos. Part A Appl. Sci. Manuf.*, vol. 41, no. 4, pp. 453–463, 2010.

[62] P. B. Nedanov and S. G. Advani, "Numerical computation of the fiber preform permeability tensor by the homogenization method," *Polym. Compos.*, vol. 23, no. 5, pp. 758–770, 2002.

[63] R. Arbter *et al.*, "Experimental determination of the permeability of textiles: A benchmark exercise," *Compos. Part A Appl. Sci. Manuf.*, vol. 42, no. 9, pp. 1157–1168, 2011.

[64] T. J. Wang, C. H. Wu, and L. J. Lee, "In-Plane Permeability Measurement and Analysis in Liquid Composite Molding," *Polym. Compos.*, vol. 15, no. 4, pp. 278–288, 1994.

[65] S. V Lomov *et al.*, "Virtual Textile Composites Software Wisetex : Integration With Micro- Mechanical , Permeability and Structural," pp. 2–3.

[66] B. Verleye *et al.*, "Permeability of textile reinforcements: Simulation, influence of shear and validation," *Compos. Sci. Technol.*, vol. 68, no. 13, pp. 2804–2810, Oct. 2008.

[67] D. Montgomery, *Introduction to statistical quality control*, 6th ed. John Wiley and Sons, 2009.

[68] M. Murata, R. Matsuzaki, A. Todoroki, Y. Mizutani, and Y. Suzuki, "Three-dimensional reconstruction of resin flow using capacitance sensor data assimilation during a liquid composite molding process: A numerical study," *Compos. Part A Appl. Sci. Manuf.*, vol. 73, pp. 1–10, 2015.

[69] E. Vanmarcke, *Random fields: analysis and synthesis*. 1983.

[70] J. Li, C. Zhang, R. Liang, and B. Wang, "Statistical characterization and robust design of RTM processes," *Compos. Part A Appl. Sci. Manuf.*, vol. 36, no. 5, pp. 564–580, 2005.

[71] A. Endruweit, P. McGregor, A. C. Long, and M. S. Johnson, "Influence of the fabric architecture on the variations in experimentally determined in-plane permeability values," *Compos. Sci. Technol.*, vol. 66, no. 11–12, pp. 1778–1792, 2006.

[72] C. C. Wong and A. C. Long, "Modelling variation of textile fabric permeability at mesoscopic scale," *Plast. Rubber Compos.*, vol. 35, no. 3, pp. 101–111, 2006.

[73] M. Davidian and D. Giltinan, "Nonlinear models for repeated measurement data: An overview and update," *J. Agric. Biol. Environ. Stat.*, vol. 8, no. 4, pp. 387–419, 2003.

[74] F. Desplentere, S. V Lomov, and I. Verpoest, "Correlated Permeability Distribution : Mould Filling Simulations Versus Experimental Results," no. July, pp. 427–434, 2006.

[75] Q. Liu, R. S. Parnas, and H. S. Giffard, "New set-up for in-plane permeability measurement," *Compos. Part A Appl. Sci. Manuf.*, vol. 38, no. 3, pp. 954–962, 2007.

[76] L. Fang, J. Jiang, J. Wang, and C. Deng, "Effect of Nesting on the Out-of-Plane Permeability of Unidirectional Fabrics in Resin Transfer Molding," *Appl. Compos. Mater.*, vol. 22, no. 3, pp. 231–249, 2014.

[77] T. a K. Sadiq, S. G. Advani, and R. S. Parnas, "Experimental Investigation of Transverse Flow-through Aligned Cylinders," *Int. J. Multiph. Flow*, vol. 21, no. 5, pp. 755–774, 1995.

[78] R. S. Parnas and A. J. Salem, "A comparison of the unidirectional and radial in-plane flow of fluids through woven composite reinforcements," *Polym. Compos.*, vol. 14, no. 5, pp. 383–394, 1993.

[79] C.-H. Wu, T. James Wang, and L. James Lee, "Trans-plane fluid permeability measurement and its applications in liquid composite molding," *Polym. Compos.*,

vol. 15, no. 4, pp. 289–298, 1994.

[80] B. R. Gebart and P. Lidstrom, "Measurement of in-plane permeability of anisotropic fiber reinforcements," *Polym. Compos.*, vol. 17, no. 1, pp. 43–51, 1996.

[81] C.-H. Shih and L. J. Lee, "Effect of fiber architecture on permeability in liquid composite molding," *Polym. Compos.*, vol. 19, no. 5, pp. 626–639, 1998.

[82] B. Yu, H.-T. Chiu, Z. Ding, and L. James Lee, "Analysis of Heat Tranfer and Flow in Liquid Composite Molding," *Polym. Process.*, vol. 15, no. 53, pp. 273–283, 2002.

[83] B. Yu, L. J. Lee, and H. Cao, "A fractal in-plane permeability model for fabrics," *Polym. Compos.*, vol. 23, no. 2, pp. 201–221, 2002.

[84] K. Yazdchi, S. Srivastava, and S. Luding, "Microstructural effects on the permeability of periodic fibrous porous media," *Int. J. Multiph. Flow*, vol. 37, no. 8, pp. 956–966, 2011.

[85] P. C. Carman, *Flow of gases through porous media*. Butterworths, London, 1956.

[86] P. C. Carman, "Fluid Flow Through Granular Beds," *Trans. Instn Chem. Engrs*, vol. 15, pp. 32–48, 1937.

[87] M. Bodaghi, C. T. Gonçalves, and N. C. Correia, "A quantitative evaluation of the uncertainty of permeability measurements in constant thickness bre reinforcement," in *Proceedings of ECCM--16 Conference*, 2014.

[88] F. Zhang, S. Comas-Cardona, and C. Binetruy, "Statistical modeling of in-plane permeability of non-woven random fibrous reinforcement," *Compos. Sci. Technol.*, vol. 72, no. 12, pp. 1368–1379, 2012.

[89] X. Chen and T. D. Papathanasiou, "The transverse permeability of disordered fiber arrays: A statistical correlation in terms of the mean nearest interfiber spacing," *Transp. Porous Media*, vol. 71, no. 2, pp. 233–251, 2008.

[90] Y. Matsumura and T. L. Jackson, "Numerical simulation of fluid flow through random packs of cylinders using immersed boundary method," *Phys. Fluids*, vol. 26, no. 4, p. , 2014.

[91] Y. Matsumura and T. L. Jackson, "Numerical simulation of fluid flow through random packs of polydisperse cylinders," *Phys. Fluids*, vol. 26, no. 12, p. , 2014.

[92] Y. Matsumura, D. Jenne, and T. L. Jackson, "Numerical simulation of fluid flow through random packs of ellipses," *Phys. Fluids*, vol. 27, no. 2, p. , 2015.

[93] G. Catalanotti, "On the generation of RVE-based models of composites reinforced with long fibres or spherical particles.," *Compos. Struct.*, 2015.

[94] COMSOL, "COMSOL Documentation." 2015.

[95] MATLAB, "MATLAB R2013b." Natick, Massachusetts, United States., 2013.

[96] R Core Team, "R: A Language and Environment for Statistical Computing." Vienna, Austria, 2013.

[97] K. P. Balandaa and H. L. Macgillivray, "Kurtosis: A Critical Review," *Am. Stat.*, vol. 42, no. 2, pp. 111–119, 1987.

[98] H. L. T. DeCarlo, "On the meaning and use of kurtosis," *Psychol. Methods*, vol. 2, no. 3, pp. 292–307, 1997.

[99] N. Vernet *et al.*, "Experimental determination of the permeability of engineering textiles: Benchmark II," *Compos. Part A Appl. Sci. Manuf.*, vol. 61, no. 0, pp. 172–184, 2014.

[100] W. J. Reed, "The Pareto law of incomes: an explanation and an extension," *Phys. A Stat. Mech. its Appl.*, vol. 319, pp. 469–486, 2003.

[101] H. Fofack and J. P. Nolan, "Tail Behavior, Modes and other Characteristics of Stable Distributions," *Extremes*, vol. 2, no. 2, pp. 39–58, 1999.

[102] M. E. J. Newman, "Power laws, Pareto distributions and Zipf's law," *Contemp. Phys.*, vol. 46, no. 2, pp. 323–351, 2005.

[103] E. W. Montroll and M. F. Shlesinger, "Maximum Entropy Formalism, Fractals, Scaling Phenomena, and 1/f Noise: A Tale of Tails," *J. Stat. Phys.*, vol. 32, no. 2, pp. 209–230, 1983.

[104] A. C. L. F.Gommer A.Endruweit, "Analysis of filament arrangements and

generation of statistically equivalent composite micro-structures," *Contemp. Phys.*, vol. 99, pp. 45–51, 2014.

[105] F. Zhang, B. Cosson, S. Comas-Cardona, and C. Binetruy, "Efficient stochastic simulation approach for {RTM} process with random fibrous permeability," *Compos. Sci. Technol.*, vol. 71, no. 12, pp. 1478–1485, 2011.

[106] S. K. Padmanabhan and R. Pitchumani, "Stochastic modeling of nonisothermal flow during resin transfer molding," *Int. J. Heat Mass Transf.*, vol. 42, no. 16, pp. 3057–3070, 1999.

[107] T. S. Mesogitis, A. A. Skordos, and A. C. Long, "Uncertainty in the manufacturing of fibrous thermosetting composites: A review," *Compos. Part A Appl. Sci. Manuf.*, vol. 57, no. 0, pp. 67–75, 2014.

[108] R. R. Sullivan, "Specific Surface Measurements on Compact Bundles of Parallel Fibers," *J. Appl. Phys.*, vol. 13, no. 11, pp. 725–730, 1942.

[109] J. Happel, "Viscous flow relative to arrays of cylinders," *AIChE J.*, vol. 5, no. 2, pp. 174–177, 1959.

[110] J. E. Drummond and M. I. Tahir, "Laminar Viscous Flow Through Regular Arrays of Parallel Solid Cylinders," *Int. J. Multiph. Flow*, pp. 515–540, 1984.

[111] T. G. Gutowski, Z. Cai, S. Bauer, D. Boucher, J. Kingery, and S. Wineman, "Consolidation Experiments for Laminate Composites," *J. Compos. Mater.*, vol. 21, no. 7, pp. 650–669, 1987.

[112] R. C. Lam and J. L. Kardos, "The permeability and compressibility of aligned and cross-plied carbon fiber beds during processing of composites," *Polym. Eng. Sci.*, vol. 31, no. 14, pp. 1064–1070, 1991.

[113] P. Xu and B. Yu, "Developing a new form of permeability and Kozeny-Carman constant for homogeneous porous media by means of fractal geometry," *Adv. Water Resour.*, vol. 31, no. 1, pp. 74–81, 2008.

[114] G. Estrada and S. G. Advani, "Experimental characterization of the influence of tackifier Material on preform permeability," *J. Compos. Mater.*, vol. 36, no. 19, pp. 2297–2310, 2002.

[115] M. Bodaghi, C. Cristóvão, R. Gomes, and N. C. Correia, "Experimental characterization of voids in high fibre volume fraction composites processed by high injection pressure RTM," *Compos. Part A Appl. Sci. Manuf.*, vol. 82, pp. 88–99, 2016.

[116] J. Breard, Y. Henzel, F. Trochu, and R. Gauvin, "Analysis of dynamic flows through porous media. Part II: Deformation of a double-scale fibrous reinforcement," *Polym. Compos.*, vol. 24, no. 3, pp. 409–421, 2003.

[117] K. M. Pillai and S. G. Advani, "A model for unsaturated flow in woven fiber preforms during mold filling in resin transfer molding," *J. Compos. Mater.*, vol. 32, no. 19, pp. 1753–1783, 1998.

[118] N. Kuentzer, P. Simacek, S. G. Advani, and S. Walsh, "Permeability characterization of dual scale fibrous porous media," *Compos. Part A Appl. Sci. Manuf.*, vol. 37, no. 11, pp. 2057–2068, 2006.

[119] F. Zhou, N. Kuentzer, P. Simacek, S. G. Advani, and S. Walsh, "Analytic characterization of the permeability of dual-scale fibrous porous media," *Compos. Sci. Technol.*, vol. 66, no. 15, pp. 2795–2803, 2006.

[120] M. T. SENOGUZ, F. D. DUNGAN, A. M. SASTRY, and J. T. KLAMO, "Simulations and Experiments onLow-Pressure Permeation of Fabrics:Part II-The Variable Gap Model andPrediction of Permeability," *J. Compos. Mater.*, vol. 35, no. 14, pp. 1285–1322, 2001.

[121] A. . Dungan, F.D. , Sastry, "Saturated and unsaturated polymer flows:micropheomena and modeling," *Compos. Mater.*, vol. 36, pp. 1581–1603, 2002.

[122] M. Huber, Ulrich and Maier, "Flow behaviour in saturated and unsaturated unidirectional fibres beds-a flow model," in *The 6th International Conference on flow processes in Composite Materials, ICCM 17*, 2002.

[123] R. Parnas and F. Phelan, "The effect of heterogeneous porous media on mold filling in resin transfer molding," *Sampe Q.*, vol. 22, no. 2, pp. 53–60, 1991.

[124] T. S. Lundstrom and B. R. Gebart, "Effect of Perturbation of Fibre Architecture on Permeability Inside Fibre Tows," *J. Compos. Mater.*, vol. 29, no. 4, pp. 424–443, 1995.

[125] R. Loendersloot, R. Akkerman, and C. Group, "a Least Squares Approximation of Annular Flow," *Composites*, no. May 2017.

[126] G. Bechtold and L. Ye, "Influence of fibre distribution on the transverse flow permeability in fibre bundles," *Compos. Sci. Technol.*, vol. 63, no. 14, pp. 2069–2079, 2003.

[127] F. R. Phelan and G. Wise, "Analysis of transverse flow in aligned fibrous porous media," *Compos. Part A Appl. Sci. Manuf.*, vol. 27, no. 1, pp. 25–34, 1996.

[128] T. a K. Sadiq, S. G. Advani, and R. S. Parnas, "Experimental Investigation of Transverse Flow-through Aligned Cylinders," *Int. J. Multiph. Flow*, vol. 21, no. 5, pp. 755–774, 1995.

[129] S. Ranganathan, F. R. Phelan, and S. G. Advani, "A generalized model for the transverse fluid permeability in unidirectional fibrous media," *Polym. Compos.*, vol. 17, no. 2, pp. 222–230, 1996.

[130] T. D. Papathanasiou, "On the effective permeability of square arrays of permeable fiber tows," *Int. J. Multiph. Flow*, vol. 23, no. 1, pp. 81–92, 1997.

[131] T. D. Papathanasiou, "Flow across structured fiber bundles: A dimensionless correlation," *Int. J. Multiph. Flow*, vol. 27, no. 8, pp. 1451–1461, 2001.

[132] K.-L. Tung, J.-S. Shiau, C.-J. Chuang, Y.-L. Li, and W.-M. Lu, "CFD analysis on fluid flow through multifilament woven filter cloths," *Sep. Sci. Technol.*, vol. 37, no. 4, pp. 799–821, 2002.

[133] Y. S. Song, K. Chung, T. J. Kang, and J. R. Youn, "Prediction of permeability tensor for three dimensional circular braided preform by applying a finite volume method to a unit cell," *Compos. Sci. Technol.*, vol. 64, no. 10–11, pp. 1629–1636, 2004.

[134] M. W. Tahir, S. Hallström, and M. Åkermo, "Effect of dual scale porosity on the overall permeability of fibrous structures," *Compos. Sci. Technol.*, vol. 103, pp. 56–62, 2014.

[135] J. Happel, "Viscous flow relative to arrays of cylinders," *AIChE J.*, vol. 5, no. 2, pp. 174–177, 1959.

[136] A. S. Sangani and A. Acrivos, "Slow flow past periodic arrays of cylinders with application to heat transfer," *Int. J. Multiph. Flow*, vol. 8, no. 3, pp. 193–206, 1982.

[137] M. V. Bruschke and S. G. Advani, "Flow of generalized Newtonian fluids across a periodic array of cylinders," *J. Rheol.*, vol. 37, no. 3, pp. 479–498, 1993.

[138] S. L. Lee and J. H. Yang, "Modeling of Darcy-Forcheimer Drag for Fluid Flow across a Bank of Circular Cylinders," *Int. J. Heat Mass Transf.*, vol. 40, no. 13, pp. 3149–3155, 1997.

[139] M. Sahraoui, M. Kaviany, A. Mechanics, and A. Arbor, "Slip and no-slip velocity boundary conditions interface of porbus, plain -media," *Mech. Eng.*, vol. 35, no. 4, pp. 927–943, 1992.

[140] A. Endruweit, F. Gommer, and A. C. Long, "Stochastic analysis of fibre volume fraction and permeability in fibre bundles with random filament arrangement," *Compos. Part A Appl. Sci. Manuf.*, vol. 49, pp. 109–118, 2013.

[141] F. Desplentere, S. V. Lomov, D. L. Woerdeman, I. Verpoest, M. Wevers, and A. Bogdanovich, "Micro-CT characterization of variability in 3D textile architecture," *Compos. Sci. Technol.*, vol. 65, no. 13, pp. 1920–1930, 2005.

[142] C. C. Wong, A. C. Long, M. Sherburn, F. Robitaille, P. Harrison, and C. D. Rudd, "Comparisons of novel and efficient approaches for permeability prediction based on the fabric architecture," *Compos. Part A Appl. Sci. Manuf.*, vol. 37, no. 6 SPEC. ISS., pp. 847–857, 2006.

[143] R. Loendersloot, "The Structure - Permeability Relation of Textile Reinforcements," 2006.

[144] K. Hoes, D. Dinescu, H. Sol, R. S. Parnas, and S. Lomov, "Study of nesting induced scatter of permeability values in layered reinforcement fabrics," *Compos. Part A Appl. Sci. Manuf.*, vol. 35, no. 12, pp. 1407–1418, Dec. 2004.

[145] M. Olave, A. Vanaerschot, S. V. Lomov, and D. Vandepitte, "Internal Geometry Variability of Two Woven Composites and Related Variability of the Stiffness," *Polym. Compos.*, vol. 33, no. 8, pp. 1335–1350, 2012.

[146] N. C. C. M. Bodaghi, A. Vanaerschot, S.V. Lomov, "On the variability of mesoscale permeability of a 2/2 twill carbon fabric induced by variability of the internal geometry," *Compos. - Part A Appl. Sci. Manuf.*, vol. in press, 2016.

[147] B. N. Cox *et al.*, "Stochastic Virtual Tests for High-Temperature Ceramic Matrix Composites," *Annu. Rev. Mater. Res.*, vol. 44, no. 1, pp. 479–529, 2014.

[148] B. Cox and Q. Yang, "In Quest of Virtual Tests for Structural Composites," *Science (80-.).*, vol. 314, no. 5802, pp. 1102–1107, 2006.

[149] G. Hivet and P. Boisse, "Consistent mesoscopic mechanical behaviour model for woven composite reinforcements in biaxial tension," *Compos. Part B Eng.*, vol. 39, no. 2, pp. 345–361, 2008.

[150] M. Karahan, S. V. Lomov, A. E. Bogdanovich, D. Mungalov, and I. Verpoest, "Internal geometry evaluation of non-crimp 3D orthogonal woven carbon fabric composite," *Compos. Part A Appl. Sci. Manuf.*, vol. 41, no. 9, pp. 1301–1311, 2010.

[151] R. a. Saunders, C. Lekakou, and M. G. Bader, "Compression and microstructure of fibre plain woven cloths in the processing of polymer composites," *Compos. Part A Appl. Sci. Manuf.*, vol. 29, no. 4, pp. 443–454, 1998.

[152] S. V. Lomov, I. Verpoest, T. Peeters, D. Roose, and M. Zako, "Nesting in textile laminates: geometrical modelling of the laminate," *Compos. Sci. Technol.*, vol. 63, no. 7, pp. 993–1007, May 2003.

[153] H.-Y. Kim, "Statistical notes for clinical researchers: assessing normal distribution (2) using skewness and kurtosis.," *Restor. Dent. Endod.*, vol. 38, no. 1, pp. 52–4, 2013.

[154] D. V. Hinkley, "Biometrika Trust," *Biometrika*, vol. 56, no. 3, pp. 635–639, 1969.

[155] A. Cedilnik, K. Kosmelj, and A. Blejec, "Ratio of two random variables: a note on the existence of its moments," *Metod. Zv.*, vol. 3, no. 1, pp. 1–7, 2006.

[156] T. G. Gutowski, Z. Cai, S. Bauer, D. Boucher, J. Kingery, and S. Wineman, "Consolidation Experiments for Laminate Composites," *J. Compos. Mater.*, vol. 21, no. July, pp. 650–669, 1987.

[157] E. B. Wilson and M. M. Hilferty, "The Distribution of Chi-Square," *Proc. Natl. Acad. Sci.*, vol. 17, no. 12, pp. 684–688, 1931.

[158] P. C. Carman, "Fluid flow through granular beds," *Chem. Eng. Res. Des.*, vol. 15, pp. 150–167, 1937.

[159] M. Barburski, I. Straumit, X. Zhang, M. Wevers, and S. V. Lomov, "Micro-CT analysis of internal structure of sheared textile composite reinforcement," *Compos. Part A Appl. Sci. Manuf.*, vol. 73, pp. 45–54, 2015.

[160] G. Bodaghi, M. Catalanotti and N. Correia, "On the statistics of transverse permeability of randomly distributed fibres," *Compos. Struct.*, vol. 158, pp. 323–332, 2015.

[161] N. C. Correia, I. Management, and R. R. Frias, "A study on the determination of stochastic reinforcement premeability in constant injection pressure conditions," *17th Int. Conf. Compos. Mater. ICCM 17*, vol. i, 2009.

[162] A. W. Chan, D. E. Larive, and R. J. Morgan, "Anisotropic Permeability of Fiber Preforms: Constant Flow Rate Measurement," *J. Compos. Mater.*, vol. 27, no. 10, pp. 996–1008, Jan. 1993.

[163] Joint Committee for Guides in Metrology (JCGM), "Evaluation of measurement data: Guide to the expression of uncertainty in measurement," no. September, p. 120, 2008.

[164] N. C. C. M. Bodaghi, A. Vanaerschot, S.V. Lomov, "On the variability of mesoscale permeability of a 2/2 twill carbon fabric induced by variability of the internal

geometry," *Compos. - Part A Appl. Sci. Manuf.*, vol. In press, 2016.

[165]   G. Gardiner, "The what and when of HP-RTM," *CompositesWorld*, pp. 1–7, 2015.

[166]   G. Gardiner, "Out-of-autoclave prepregs: Hype or revolution? : CompositesWorld," *High-Performance Compos.*, 2011.

[167]   R. A. Witik, F. Gaille, R. Teuscher, H. Ringwald, V. Michaud, and J. A. E. Månson, "Economic and environmental assessment of alternative production methods for composite aircraft components," *J. Clean. Prod.*, vol. 29–30, no. 3–4, pp. 91–102, 2012.

[168]   O. Geiger and D. Schmidt, "Compression RTM - A new process for manufacturing high volume continuous fiber reinforced composites," *5th Int. CFK-Valley Stade Conv.*, 2011.

[169]   E. Ruiz, V. Achim, S. Soukane, F. Trochu, and J. Bréard, "Optimization of injection flow rate to minimize micro/macro-voids formation in resin transfer molded composites," *Compos. Sci. Technol.*, vol. 66, no. 3–4, pp. 475–486, 2006.

[170]   S.W.Beckwith, "Manufacturing defects in composite structures," *SAMPE J.*, vol. 48, pp. 52–53, 2012.

[171]   X. Zhang, Y. Duan, X. Zhao, and D. Li, "Effects of quasi-3D stacking architecture on interlaminar shear strength and void content of FRP," *J. Appl. Polym. Sci.*, vol. 41076, pp. 1–9, 2014.

[172]   C.-H. Shih and L. J. Lee, "Tackification of Textile Fiber Preforms in Resin Transfer Molding," *J. Compos. Mater.*, vol. 35, no. 21, pp. 1954–1981, 2001.

[173]   M. De Almeida, M. Cerqueira, and M. Leali, "The influence of porosity on the interlaminar shear strength of carbon / epoxy and carbon / bismaleimide fabric laminates," *Compos. Sci. Technol.*, vol. 61, pp. 2101–2108, 2001.

[174]   C. Lee and U. K. Wei, "Resin Transfer Molding (RTM) Process of a High Performance Epoxy Resin. II: Effects of Process Variables on the Physical, Static and Dynamic Mechanical Behavior," vol. 4, no. 4, pp. 935–943, 2000.

[175]   C. L. Lee and K. H. Wei, "Effect of material and process variables on the performance of resin-transfer-molded epoxy fabric composites," *J. Appl. Polym. Sci.*, vol. 77, no. 10, pp. 2149–2155, 2000.

[176]   A. Zhang, D. Li, H. Lu, and D. Zhang, "Qualitative separation of the effect of voids on the bending fatigue performance of hygrothermal conditioned carbon/epoxy composites," *Mater. Des.*, vol. 32, no. 10, pp. 4803–4809, 2011.

[177]   D. W. L.Liu, B.Zhang, Z.Wu, "Effects of cure pressure induced voids on the mechanical strength of carbon/epoxy laminates.," *J. Mater. Sci. Technol.*, vol. 21, pp. 87–91, 2005.

[178]   Y. K. Hamidi, L. Aktas, and M. C. Altan, "Effect of packing on void morphology in resin transfer molded E-glass/ epoxy composites," *Polym. Compos.*, vol. 26, no. 5, pp. 614–627, 2005.

[179]   Y. K. Hamidi, L. Aktas, and M. C. Altan, "Composite Materials Effect of Nanoclay Content on Void Morphology in Resin Transfer," vol. 131, no. April 2009, pp. 1–11, 2008.

[180]   B. H. J.S.Hayward, "Effect of process variables on the quality of RTM mouldings.," *SAMPE J.*, vol. 26, no. 3, p. 39–46., 1990.

[181]   D. Abraham, S. Matthews, and R. McIlhagger, "A comparison of physical properties of glass fibre epoxy composites produced by wet lay-up with autoclave consolidation and resin transfer moulding," *Compos. Part A Appl. Sci. Manuf.*, vol. 29, no. 7, pp. 795–801, 1998.

[182]   S. Laurenzi, A. Casini, and D. Pocci, "Design and fabrication of a helicopter unitized structure using resin transfer moulding," *Compos. Part A Appl. Sci. Manuf.*, vol. 67, pp. 221–232, 2014.

[183]   M. S. Prabhu, J. N. Raj, and G. Vignesh, "Optimization of Unmanned Aerial Vehicle Wing," *Int. J. Innov. Sci. Eng. Technol.*, vol. 2, no. 3, pp. 28–34, 2015.

[184]   K. a Olivero, H. J. Barraza, E. a O. Rear, and M. C. Altan, "Effect of Injection Rate and Post-Fill Cure," *J. Compos. Mater.*, vol. 36, no. 16, pp. 2010–2028, 2011.

[185] S. R. Ghiorse, "A comparison of void measurement methods for carbon/epoxy composites," 1991.

[186] W. W. Sampson, "Spatial variability of void structure in thin stochastic fibrous materials," *Model. Simul. Mater. Sci. Eng.*, vol. 20, no. 1, 2011.

[187] R. Garcia-Gil, "SCHOOL OF MECHANICAL , MATERIALS , Forming and Consolidation of Textile Composites by Rafael Garcia Gil Thesis submitted to the University of Nottingham for the degree of Doctor of Philosophy," Nottingham., 2003.

[188] F. Y. C. Boey and S. W. Lye, "Void reduction in autoclave processing of thermoset composites. Part 1: High pressure effects on void reduction," *Composites*, vol. 23, no. 4, pp. 261–265, 1992.

[189] N. Patel and L. J. Lee, "Modeling of void formation and removal in liquid composite molding. Part II: Model development and implementation," *Polym. Compos.*, vol. 17, no. 1, pp. 104–114, 1996.

[190] J. S. Leclerc and E. Ruiz, "Porosity reduction using optimized flow velocity in Resin Transfer Molding," *Compos. Part A Appl. Sci. Manuf.*, vol. 39, no. 12, pp. 1859–1868, 2008.

[191] Y. Ledru, G. Bernhart, R. Piquet, F. Schmidt, and L. Michel, "Coupled visco-mechanical and diffusion void growth modelling during composite curing," *Compos. Sci. Technol.*, vol. 70, no. 15, pp. 2139–2145, 2010.

[192] T. Lundström and B. Gebart, "Influence from process parameters on void formation in resin transfer molding," *Polym. Compos.*, vol. 15, no. 1, pp. 25–33, 1994.

[193] T. S. Lundstrom, B. R. Gebart, and C. Y. Lundemo, "Void Formation in RTM," *J. Reinf. Plast. Compos.*, vol. 12, no. 12, pp. 1339–1349, 1993.

[194] T. S. Lundstrom, "Bubble transport through constricted capillary tubes with application to Resin Transfer Molding," *Polym. Compos.*, vol. 17, no. 6, pp. 770–779, 1996.

[195] L. K. Grunenfelder and S. R. Nutt, "Void formation in composite prepregs - Effect of dissolved moisture," *Compos. Sci. Technol.*, vol. 70, no. 16, pp. 2304–2309, 2010.

[196] S. A. Alan Stuart, Keith Ord, *Kendall's advanced theory of statistics*, 6th ed. London: Arnold, 1998.

[197] R. C. Elandt-Johnson and N. L. Johnson, *Survival Models and Data Analysis*. John Wiley and Sons, 1980.

Appendix A

A.1   Making unit cells from the virtual geometry

As received virtual geometry file in XML format which is compatible with WiseTex software, one has to convert this file to a Matlab structure. Then the following script is applied to break down the global XML file to number of sub-XML file.   This script converts a universal geometry to a number of divided geometries.

```matlab
%clear all xml2struct convert xml file to Matlab structure.
 [ s ] = xml2struct( 'twill_woven_variable_sample_field_1.fabx' );
%clear all
%load('s.mat');
clear new
%
a=str2double(s.WiseTex_dash_XML.Fibres.Fibre_dash_2.General.Color
.Text)

clc

enum=1:32;
enum=enum-17;
enum(end+1)=enum(end)+1;

for i=1:4:40
    for j=1:4:40
        major_element=strcat('major_element_',    num2str((i+3)/4),
'_', num2str((j+3)/4));
        elem_cnt_i=1;
        elem_cnt_j=1;
        for k=0:3
            %          fprintf('i=%d j=%d k=%d\n',i,j,k);
            Item_das_taar=strcat('Item_dash_', num2str(i+k));
            Item_das_pood=strcat('Item_dash_', num2str(j+k+40));

            Item_das_taar_new=strcat('Item_dash_', num2str(k+1));

            Item_das_pood_new=strcat('Item_dash_', num2str(k+1+4));

            elem_cnt_i=elem_cnt_i+1;
            elem_cnt_j=elem_cnt_j+1;

            sub_element_cnt=1;
            e_counter=1;
            for m=((j+3)/4-1)*32+1:(j+3)/4*32
                data_addr_taar=strcat('Item_dash_', num2str(m));
                data_addr_taar_new=strcat('Item_dash_',
num2str(sub_element_cnt));


new.(major_element).(Item_das_taar_new).AveD1=s.WiseTex_dash_XML.
Fabric.Yarns.YarnInFabric.(Item_das_taar).AveD1;

new.(major_element).(Item_das_taar_new).AveD2=s.WiseTex_dash_XML.
Fabric.Yarns.YarnInFabric.(Item_das_taar).AveD2;
```

```matlab
new.(major_element).(Item_das_taar_new).AveVf=s.WiseTex_dash_XML.
Fabric.Yarns.YarnInFabric.(Item_das_taar).AveVf;


new.(major_element).(Item_das_taar_new).YarnSectionData.(data_add
r_taar_new)=s.WiseTex_dash_XML.Fabric.Yarns.YarnInFabric.(Item_da
s_taar).YarnSectionData.(data_addr_taar);


new.(major_element).(Item_das_taar_new).StructurePosition=s.WiseT
ex_dash_XML.Fabric.Yarns.YarnInFabric.(Item_das_taar).StructurePo
sition;

new.(major_element).(Item_das_taar_new).Yarn=s.WiseTex_dash_XML.F
abric.Yarns.YarnInFabric.(Item_das_taar).Yarn;



            % Now modify the values of x and y
            %
new.(major_element).(Item_das_taar_new).YarnSectionData.(data_add
r_taar_new).x.Text=num2str
(str2double(new.(major_element).(Item_das_taar_new).YarnSectionDa
ta.(data_addr_taar_new).x.Text)+ enum_i*11.375);
            %
new.(major_element).(Item_das_taar_new).YarnSectionData.(data_add
r_taar_new).y.Text=num2str
(str2double(new.(major_element).(Item_das_taar_new).YarnSectionDa
ta.(data_addr_taar_new).y.Text)+ enum_j*11.375);

new.(major_element).(Item_das_taar_new).YarnSectionData.(data_add
r_taar_new).x.Text=num2str     (enum(e_counter)*11.558/32);     %-
5.5*11.19 + (j+3)/4*11.19

new.(major_element).(Item_das_taar_new).YarnSectionData.(data_add
r_taar_new).y.Text=num2str  ((k-2)*2.886  );  %-  5.5*11.19  +
(i+3)/4*11.19
            %
new.(major_element).(Item_das_taar_new).YarnSectionData.(data_add
r_taar_new).z.Text=num2str (0);
            e_counter=e_counter+1;

            sub_element_cnt=sub_element_cnt+1;

            % add the last one
            if (m==(j+3)/4*32)
                data_addr_taar_new=strcat('Item_dash_',
num2str(sub_element_cnt));


new.(major_element).(Item_das_taar_new).AveD1=s.WiseTex_dash_XML.
Fabric.Yarns.YarnInFabric.(Item_das_taar).AveD1;

new.(major_element).(Item_das_taar_new).AveD2=s.WiseTex_dash_XML.
Fabric.Yarns.YarnInFabric.(Item_das_taar).AveD2;

new.(major_element).(Item_das_taar_new).AveVf=s.WiseTex_dash_XML.
Fabric.Yarns.YarnInFabric.(Item_das_taar).AveVf;
```

```matlab
new.(major_element).(Item_das_taar_new).YarnSectionData.(data_add
r_taar_new)=s.WiseTex_dash_XML.Fabric.Yarns.YarnInFabric.(Item_da
s_taar).YarnSectionData.(data_addr_taar);


new.(major_element).(Item_das_taar_new).StructurePosition=s.WiseT
ex_dash_XML.Fabric.Yarns.YarnInFabric.(Item_das_taar).StructurePo
sition;

new.(major_element).(Item_das_taar_new).Yarn=s.WiseTex_dash_XML.F
abric.Yarns.YarnInFabric.(Item_das_taar).Yarn;



                % Now modify the values of x and y
                %
new.(major_element).(Item_das_taar_new).YarnSectionData.(data_add
r_taar_new).x.Text=num2str
(str2double(new.(major_element).(Item_das_taar_new).YarnSectionDa
ta.(data_addr_taar_new).x.Text)+ enum_i*11.375);
                %
new.(major_element).(Item_das_taar_new).YarnSectionData.(data_add
r_taar_new).y.Text=num2str
(str2double(new.(major_element).(Item_das_taar_new).YarnSectionDa
ta.(data_addr_taar_new).y.Text)+ enum_j*11.375);

new.(major_element).(Item_das_taar_new).YarnSectionData.(data_add
r_taar_new).x.Text=num2str (enum(33)*11.498/32); %- 5.5*11.19 +
(j+3)/4*11.19

new.(major_element).(Item_das_taar_new).YarnSectionData.(data_add
r_taar_new).y.Text=num2str  ((k-2)*2.886  );  %-   5.5*11.19  +
(i+3)/4*11.19
            end


        end

        sub_element_cnt=1;
        e_counter=1;
        for n=((i+3)/4-1)*32+1:(i+3)/4*32
            data_addr_pood=strcat('Item_dash_', num2str(n));
            data_addr_pood_new=strcat('Item_dash_',
num2str(sub_element_cnt));



new.(major_element).(Item_das_pood_new).AveD1=s.WiseTex_dash_XML.
Fabric.Yarns.YarnInFabric.(Item_das_pood).AveD1;

new.(major_element).(Item_das_pood_new).AveD2=s.WiseTex_dash_XML.
Fabric.Yarns.YarnInFabric.(Item_das_pood).AveD2;

new.(major_element).(Item_das_pood_new).AveVf=s.WiseTex_dash_XML.
Fabric.Yarns.YarnInFabric.(Item_das_pood).AveVf;


new.(major_element).(Item_das_pood_new).YarnSectionData.(data_add
```

```matlab
r_pood_new)=s.WiseTex_dash_XML.Fabric.Yarns.YarnInFabric.(Item_da
s_pood).YarnSectionData.(data_addr_pood);


new.(major_element).(Item_das_pood_new).StructurePosition=s.WiseT
ex_dash_XML.Fabric.Yarns.YarnInFabric.(Item_das_pood).StructurePo
sition;

new.(major_element).(Item_das_pood_new).Yarn=s.WiseTex_dash_XML.F
abric.Yarns.YarnInFabric.(Item_das_pood).Yarn;



            % modify the x and y and z
            %
new.(major_element).(Item_das_pood_new).YarnSectionData.(data_add
r_pood_new).x.Text=num2str                                      (
str2double(new.(major_element).(Item_das_pood_new).YarnSectionDat
a.(data_addr_pood_new).x.Text) + enum_i*11.375);
            %
new.(major_element).(Item_das_pood_new).YarnSectionData.(data_add
r_pood_new).y.Text=num2str                                      (
str2double(new.(major_element).(Item_das_pood_new).YarnSectionDat
a.(data_addr_pood_new).y.Text) + enum_j*11.375);

new.(major_element).(Item_das_pood_new).YarnSectionData.(data_add
r_pood_new).x.Text=num2str   ((k-2)*2.886   );   %-   5.5*11.19   +
(j+3)/4*11.19

new.(major_element).(Item_das_pood_new).YarnSectionData.(data_add
r_pood_new).y.Text=num2str    (enum(e_counter)*11.19/32    );    %-
5.5*11.19 + (i+3)/4*11.19
            %
new.(major_element).(Item_das_pood_new).YarnSectionData.(data_add
r_pood_new).z.Text=num2str(0);
            e_counter=e_counter+1;

            sub_element_cnt=sub_element_cnt+1;


%               Add the last one
            if (n==(i+3)/4*32)
                data_addr_pood_new=strcat('Item_dash_',
num2str(sub_element_cnt));



new.(major_element).(Item_das_pood_new).AveD1=s.WiseTex_dash_XML.
Fabric.Yarns.YarnInFabric.(Item_das_pood).AveD1;

new.(major_element).(Item_das_pood_new).AveD2=s.WiseTex_dash_XML.
Fabric.Yarns.YarnInFabric.(Item_das_pood).AveD2;

new.(major_element).(Item_das_pood_new).AveVf=s.WiseTex_dash_XML.
Fabric.Yarns.YarnInFabric.(Item_das_pood).AveVf;


new.(major_element).(Item_das_pood_new).YarnSectionData.(data_add
r_pood_new)=s.WiseTex_dash_XML.Fabric.Yarns.YarnInFabric.(Item_da
s_pood).YarnSectionData.(data_addr_pood);
```

```matlab
new.(major_element).(Item_das_pood_new).StructurePosition=s.WiseT
ex_dash_XML.Fabric.Yarns.YarnInFabric.(Item_das_pood).StructurePo
sition;

new.(major_element).(Item_das_pood_new).Yarn=s.WiseTex_dash_XML.F
abric.Yarns.YarnInFabric.(Item_das_pood).Yarn;


                % modify the x and y and z
                %
new.(major_element).(Item_das_pood_new).YarnSectionData.(data_add
r_pood_new).x.Text=num2str                                       (
str2double(new.(major_element).(Item_das_pood_new).YarnSectionDat
a.(data_addr_pood_new).x.Text) + enum_i*11.375);
                %
new.(major_element).(Item_das_pood_new).YarnSectionData.(data_add
r_pood_new).y.Text=num2str                                       (
str2double(new.(major_element).(Item_das_pood_new).YarnSectionDat
a.(data_addr_pood_new).y.Text) + enum_j*11.375);

new.(major_element).(Item_das_pood_new).YarnSectionData.(data_add
r_pood_new).x.Text=num2str  ((k-2)*2.886   );    %-   5.5*11.19   +
(j+3)/4*11.19

new.(major_element).(Item_das_pood_new).YarnSectionData.(data_add
r_pood_new).y.Text=num2str  (enum(33)*11.19/32  );  %-  5.5*11.19  +
(i+3)/4*11.19


            end

        end



        data_addr_pood=strcat('Item_dash_', num2str(m));

        fprintf('Sq(%i,%i)          %s.%s          ||          %s.%s
\n',(i+3)/4,(j+3)/4,Item_das_taar,Item_das_pood,data_addr_taar,da
ta_addr_pood);


        %               counter=counter+1;
      end
   end
end



for i=1:10
   for j=1:10
      major_element=strcat('major_element_',   num2str(i),   '_',
num2str(j));

      output.Masoud.Fabric.Data=s.WiseTex_dash_XML.Fabric.Data;
      output.Masoud.Yarns.Fabric.Fibres=new.(major_element);
```

```matlab
        struct2xml(  output,   strcat('output\output_',num2str(i),
'_', num2str(j),'.xml') );

        movefile(strcat('output\output_',num2str(i),          '_',
num2str(j),'.xml'),     strcat('output\output_',num2str(i),    '_',
num2str(j),'.fabx'));

        fprintf('Output (%i,%i) saved \n',i,j);

    end
end
```

Appendix B

B.1. Statistics of the permeability data

As permeability is an uncertain parameter, it is necessary to characterise this property from a statistical point of view. Hence, an appropriated distribution model is first necessary to represent the uncertainty of permeability. This appendix introduces a number of distribution model that were applied to analyse the permeability data at different scale.

In statistics, there are two methods for the estimation of the probability density function: Non-parametric model and parametric models

B.2. Kernel density

Kernel density is a not-parametric method. Let data=$(x_1, x_2,…,x_n)$ be an independently and identically distributed sample taken from some distribution with an unknown density function f. To estimate the shape of this function, the Kernel density is applied:

$$f = mean(phi((x - data)/h)/h)$$
$$phi = \exp(-0.5x^{0.2})/\sqrt{2\pi}$$
$$h = \sigma(data)(\frac{4}{3n})^{0.2}$$
$$n = length(data)$$

(B-1)

B.3. Parametric model

There is a number of parametric models. Some of these models, which were used in this thesis, are introduced.

The normal distribution fit to random variables can be described by the arithmetic mean μ and the standard deviation σ in the form $\mu \pm \sigma$. x is said to follow Gaussian distribution with parameter μ and σ in Eq.B-2 as [16]:

$$F(x;\mu,\sigma) = \frac{1}{\sqrt{2\pi\sigma^2}}\exp(-\frac{(x-\mu)^2}{2\sigma^2})$$

(B-2)

If the random number, x, shows a skewed distribution and log(x) becomes normally distributed, x is said to be log-normally distributed (Eq.B-3):

$$F(\ln x;\mu,\sigma) = \frac{1}{\sqrt{2\pi\sigma^2}}\exp(-\frac{(\ln x-\mu)^2}{2\sigma^2})$$

(B-3)

To characterize x, for which a log-normal distribution yields a good fit, the mean value (μ^*) and standard deviation (σ^*) are calculated by Eqs.B-4 and 5, respectively.

$$\mu^* = \frac{\sum_{i=1}^{n} \ln x_i}{n} \tag{B-4}$$

$$\sigma^* = \left[\frac{\sum_{i=1}^{n} \left[\ln \frac{x_i}{\mu^*} \right]^2}{n-1} \right]^{1/2} \tag{B-5}$$

μ^* and σ^* are calculated and then back-transformed into $\overline{\mu}^*$ and $\overline{\sigma}^*$,which denote geometric mean and multiplicative standard deviation, respectively, by Eqs.B-6 and 7, respectively:

$$\overline{\mu}^* = \exp\left(\frac{\sum_{i=1}^{n} \ln x_i}{n}\right) = \left(\sum_{i=1}^{n} \ln x_i\right)^{1/n} \tag{B-6}$$

$$\overline{\sigma}^* = \exp\left(\left[\frac{\sum_{i=1}^{n} \left[\ln \frac{x_i}{\mu^*} \right]^2}{n-1} \right]^{1/2} \right) = \left(\sum_{i=1}^{n} \left[\ln \frac{x_i}{\mu^*} \right]^2 \right)^{1/[2(n-1)]} \tag{B-7}$$

These parameters determine an interval which contains 66% of the data, and are an equivalent to μ±σ for the normal distribution (additive). If the original data is not available, $\overline{\mu}^*$ and $\overline{\sigma}^*$ can be calculated from μ and σ according to Eqs.B-8 and 9, correspondingly:

$$\overline{\mu}^* = \frac{\mu}{\sqrt{1 + \left(\frac{\sigma}{\mu}\right)^2}} \tag{B-8}$$

$$\overline{\sigma}^* = \exp\left(\sqrt{\ln\left(1 + \left(\frac{\sigma}{\mu}\right)^2\right)}\right) \tag{B-9}$$

If the random number, x, shows a left skewed distribution after log transformation and $x^{1/3}$ becomes normally distributed, x is said to follow Gamma distribution with parameters α and θ (Eq.B-10).

$$F(x;\alpha,\theta) = \frac{X}{\Gamma(\alpha)\theta^\alpha} \exp\left(-\frac{(x-\mu)^2}{2\sigma^2}\right) \tag{B-10}$$

$$\mu = \alpha\theta, \sigma = \alpha\theta^2$$

A common observed phenomenon at different scales was the existence of tails after making the histograms of permeability data. At macro and meso-scale, the tails were not fat and normal distribution can properly represent their distribution. However, at

microscale, the observed tails were fat and normal distribution cannot describe this property. The observed tail showed can be well fit Generalised Extreme Values (GEV) with the tails shape parameter, ξ (Eq.B-11).

$$f(x;\xi,\mu,\sigma) = \frac{1}{\sigma}(1+\xi\frac{x-\mu}{\sigma})^{-1-\frac{1}{\xi}}\exp(-(1+\xi\frac{x-\mu}{\sigma})^{-\frac{1}{\xi}})$$ (B-11)

When $\xi=0$, the GEV distribution follows the Gumbel class, including gamma, normal, lognormal and exponential distribution.

B.4. Kurtosis and Skewness

Kurtosis and Skewness (Eqs.B-12 and 13) are frequently used to evaluate the normality of the random number, x, based on its shape.

$$Skweness = \frac{n\sum_{i=0}^{n}(x-\mu)^3}{(n-1)(n-2)\left[\sum_{i=0}^{n}\frac{(x-\mu)^2}{n-1}\right]^{3/2}}$$ (B-12)

$$Kurtosis = \frac{n(n+1)\sum_{i=0}^{n}(x-\mu)^4}{(n-1)(n-2)(n-3)\left[\sum_{i=0}^{n}\frac{(x-\mu)^2}{(n-1)}\right]^2} - \frac{3(n-1)^2}{(n-2)(n-3)}$$ (B-13)

The normal distribution has a Skewness of -0.5 and 0.5 and a Kurtosis of -3 and 3.

Appendix C

C.1. Modelling of the V_f^{tow} varianc

V_f^{tow} depends on width w and thickness t and can be calculated by Eq. C-1 Let us set $1/w=\alpha$ (unit of α becomes 1/mm) and set average α, $\mu_\alpha := E(\alpha)$ and average tow thickness t, $\mu_t := E(t)$, where $E()$ designates the mathematical expectation. Consider the first order Taylor expansion, around (μ_α, μ_t) for $V_f^{tow}(\alpha, t)$:

$$V_f^{tow} := V_f^{tow}(\alpha,t) = V_f^{tow}(\mu_\alpha, \mu_t)$$
$$+ \frac{dV_f^{tow}(\mu_\alpha, \mu_t)}{d\alpha}(\alpha - \mu_\alpha) + \frac{dV_f^{tow}(\mu_\alpha, \mu_t)}{dt}(t - \mu_t) \tag{C-1}$$

where $\dfrac{dV_f^{tow}}{d\alpha}$ and $\dfrac{dV_f^{tow}}{dt}$ are the 1th derivatives of V_f^{tow} with respect to α and t. In agreement with [196][197], the approximation for $\mu_{Vf}^{tow} := E(V_f^{tow})$ is given by:

$$\mu_{V_{ftow}} = E(V_f^{tow}(\mu_\alpha, \mu_t) + \frac{dV_f^{tow}(\mu_\alpha, \mu_t)}{d\alpha}(\alpha - \mu_\alpha) + \frac{dV_f^{tow}(\mu_\alpha, \mu_t)}{dt}(t - \mu_t) + ...)$$
$$\approx E(V_f^{tow}(\mu_\alpha, \mu_t)) + \frac{dV_f^{tow}(\mu_\alpha, \mu_t)}{d\alpha} E(\alpha - \mu_\alpha)$$
$$+ \frac{dV_f^{tow}(\mu_\alpha, \mu_t)}{dt} E(t - \mu_t) \tag{C-2}$$

By the definition of the variance, the variance of V_f^{tow}, $\sigma^2(V_f^{tow})$, can be written as:

$$\sigma^2(V_f^{tow}) = (4n_t r^2)^2 \sigma^2(\frac{\alpha}{t}) \tag{C-3}$$

Then, using the first order Taylor expansion once again around (μ_α, μ_t), the variance of V_{ftow} can be approximated as:

$$\sigma^2(V_f^{tow}) \approx E((V_f^{tow}(\alpha,t) - V_f^{tow}(\mu_\alpha, \mu_t))^2)) \tag{C-4}$$

Substitute Eq. C-6 in Eq. C-9, then Eq. C-8 can be recast as:

$$\sigma^2(V_f^{tow}) \approx (4n_t r^2)^2 \sigma^2(\frac{\mu_\alpha}{\mu_t} + \frac{1}{\mu_t}(\alpha - \mu_\alpha) - \frac{\mu_\alpha}{\mu_t^2}(t - \mu_t))$$

$$= (4n_t r^2)^2 \sigma^2(\frac{1}{\mu_t}\alpha - \frac{\mu_\alpha}{\mu_t^2}t)$$

$$= (4n_t r^2)^2(\frac{1}{\mu_t^2}\sigma^2(\alpha) + \frac{\mu_\alpha^2}{\mu_t^4}\sigma^2(t) - 2\frac{\mu_\alpha}{\mu_t^3}CV(\alpha,t))$$

$$= (4n_t r^2)^2 \frac{\mu_\alpha^2}{\mu_t^2} (\frac{1}{\mu_\alpha^2} \sigma^2(\alpha) + \frac{1}{\mu_t^2} \sigma^2(t) - 2\frac{1}{\mu_\alpha \mu_t} CV(\alpha,t)) \qquad \textbf{(C-5)}$$

In Eq. C-5, $CV(\alpha, t)$ is the covariance of α, t, $\sigma(\alpha)$ and $\sigma(t)$ are standard deviations of α, t, respectively. In the previous section, it was shown that w and t are dependent, and have a negative correlation coefficient ρ_{corr} (ca -0.6) with parameters (μ_w, μ_t, $\sigma^2(w)$, $\sigma^2(t)$, ρ_{corr}). With knowledge of $COV(t,w)$ and σ_t as well as σ_w, correlation coefficient ρ_{corr} (t,w) is estimated by Eq. C-11.

$$\rho_{corr} = \frac{CV(t,w)}{\sigma_t \sigma_w} \qquad \textbf{(C-6)}$$

In addition, the coefficient of variation (COV) of the random variable of V_f^{two}, $COV(V_f^{tow})$, is defined by Eq. C-7:

$$COV(V_f^{tow}) = \frac{\sigma(V_f^{tow})}{\mu_{V_f^{tow}}} \qquad \textbf{(C-7)}$$

Consequently, Eq. C-5, can be recast as:

$$\sigma^2(V_f^{tow}) \approx \mu_{V_f^{tow}}^2 (COV^2(\alpha) - 2COV(\alpha)COV(t)\rho_{corr} + COV^2(t)) \, \textbf{(C-8)}$$

Replace Eq. C-7 in Eq. C-6, then $COV(V_f^{tow})$ is given by Eq. C-9:

$$COV(V_{ftow}) \approx \sqrt{COV^2(\alpha) - 2COV(\alpha)COV(t)\rho_{corr} + COV^2(t)} \, \textbf{(C-9)}$$

Appendix D

D.1. Mould design

It is intended at this stage to design a RTM mould for the wing spar geometry. The study of mould design is an important task because the proper design of mould parameters including the location of injection gates as well as vents, sealing and the location and the size of the pinch-off allows injecting resin into mould cavity at high pressure coupling with the state of art hydraulic press. Possible alterations to the RTM injection machine were also studied in order to obtain an optimal mixture of resin and hardener at high pressures. The geometry for the case study is a U-beam as shown in Figure D-1.
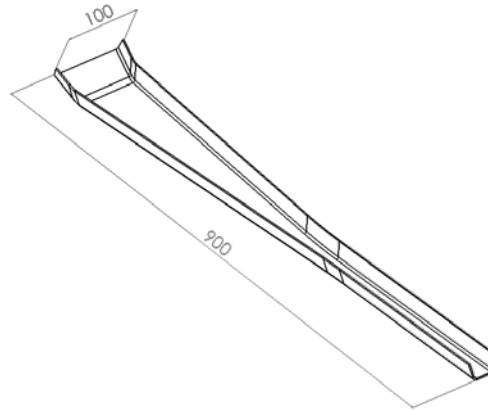
Figure D-1: U-shaped beam

D.2. Mould Assemblies

For the production of RTM parts, the RTM injection machine was used (Figure D-2). A vacuum pump (-900 / -800 mbar) is used to obtain optimum mixing proportion of resin and hardener.

Figure D-1: Vacuum machine

The opening and closing of the mold is assisted by the hydraulic press of 60 Ton (Figure D-3). Hence, supports are designed based on the required height for mold closing.
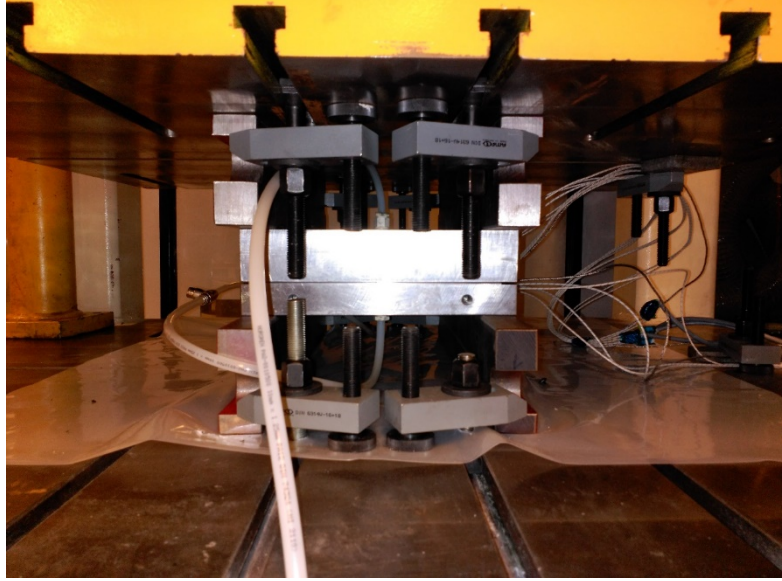
Figure D-2: The mould assembly with supports connected to the press

The HIPRTM process needs large clamping pressures to withstand the high injection pressures, not only compressing the laminate but also preventing resin leakages. The compaction pressures should be higher than injection pressures to prevent experiencing the resin leakages. The required mould clamping pressure depends on the size of the moulded component projected to press force. The author applied equal clamping pressures for the case of gap and without gap. The pressure on the mould is a total that shows that Clamping force (F_c)> Opening force (injection force +fibre expansion force) (F_o):

$$F_c = 60\,(\text{bar}) \times .81\,(\text{ton}) = 476.6\,\text{kN} \tag{D-1}$$
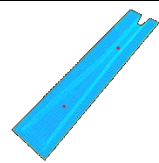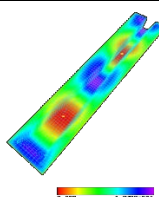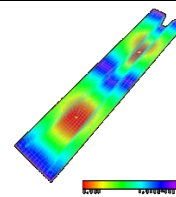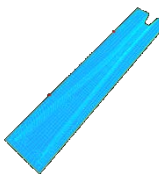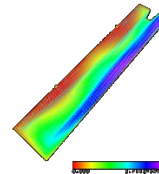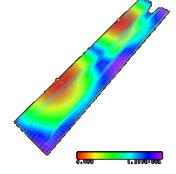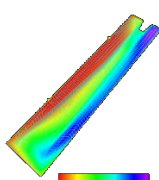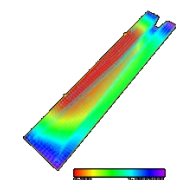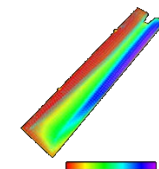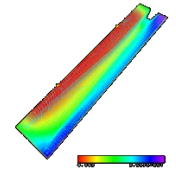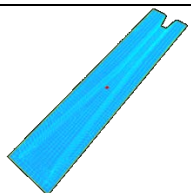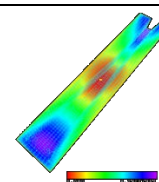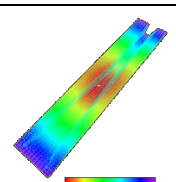
$$\text{Area of projection} = 170 \times 960\,(\text{mm}^2) \tag{D-2}$$

$$F_o = 25 \times 100000\,(\text{Nm}^{-2}) \times 170 \times 960 \times 10^{-6}\,(\text{m}^2) = 323\,\text{kN} \tag{D-3}$$

D.3. Tool design

By the use of LIMS software, the optimum injection geometry based on the filling time was selected. The results of simulations for different inlet geometries are summerised in table D-1. From Table D-1, it is observed that using two injection points and feed channel between these two points as well as 125 mm beyond the injection points provide the minimum filling time. As the LIMS required the permeability value as an input, an experiment for the in-plane measurement of permeability of a 2×2 twill woven carbon fabric was done.

Table D-1: Results of the simulations of the filling process for the spar wing.

Location of injection	Description	Rapid channel Type 1	T (min)	Rapid channel Type 2	T (min)
	a) Two central injection points		2.90		3.20
	b) Two injection points on the border of sample		1.60		5.90
	c) Two injection points on the border of sample along with feed channel between these two injection points		1.34		2.65
	d) two injection points and feed channel between these two points as well as 125 mm beyond the injection points		1.10		1.41
	e) One-point central injection		6.50		8.34

Based on the simulation results, the inlets and vents of mould were positioned as shown in Figure D-4.

Vents: Three points on the opposite side of the inlet gate.
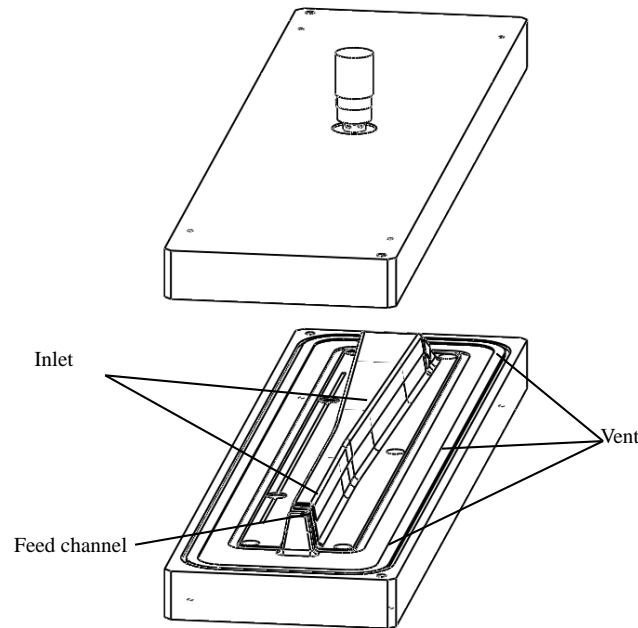
Figure D-3: RTM mould

D.4. Dimension of pinch-off

A strategy was applied to limit the reach of resin on the edges of the mould component, avoiding the formation of fast tracking between the fiber and the walls of the mold. To prevent the overlapping of the pinch-off and the edge of the fabric, this point was taken into account in the mold design in such a way as the edge of the fabric passes the pinch-of as shown in Figure D-5. The permeability tests also allowed to validate experimentally the decrease of the fast channels using the use of silicone with hardness 30 shore A for the pinch-off. The reason for the use of silicon is that this compressible material guarantees the compression of preform.
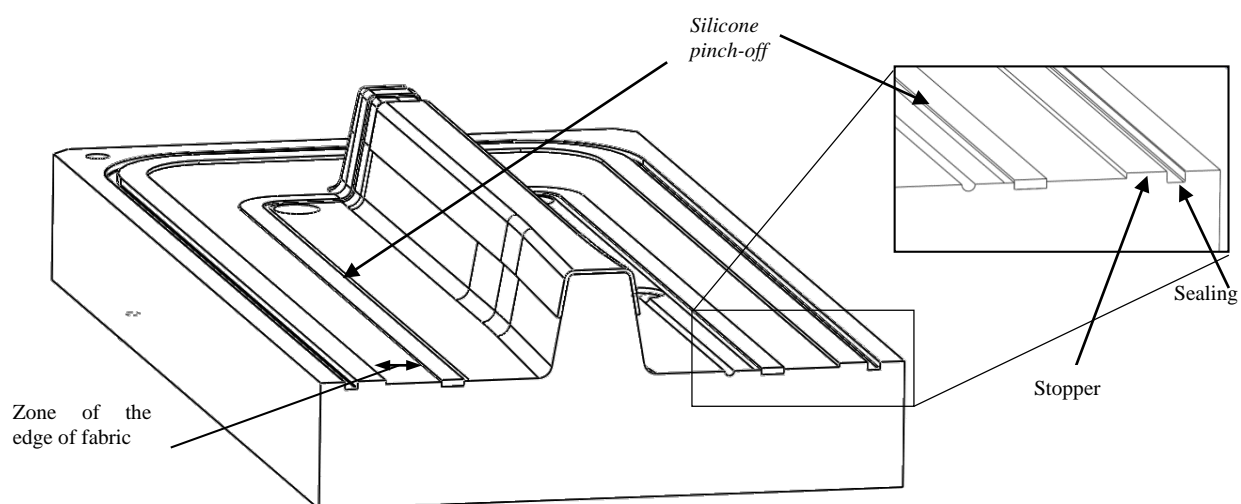
Figure D-4: Cutaway view of the male mould of the spar wing and detail of the pinch-

The following calculations show the required thickness of the pinch-off for the removal of the fast channels:

With the knowledge of the intended fibre volume fraction (70%), the areal density of 2by2 twill woven carbon fabric (280g/m^2) and the density of carbon fibre (1.8g/cm^3), the thickness of one layer fabric (h) is (Eq.D-4):

$$h = \frac{0.280}{1800} \times \frac{1}{0.7} = 0.22 \frac{mm}{layer}$$ **(D-4)**

For 7 layers, the laminate thickness becomes 1.54.The height left over of the pinch-off:

$$h_{pinch\text{-}off} = 2 - 1.54 = 0.46 \, mm$$ **(D-5)**

Figure D-6 shows the percentage of silicon compression as a function of the applied force. Then, the maximum compression of the considered silicone (300/9030) is 45%.
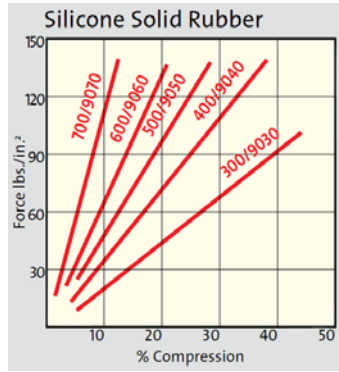

Figure D-5: The percentage of silicon compression versus applied force

And hence,

$$h_{pinch\text{-}off} = 0.5 \times 1.45 = 0.725 \, mm$$ **(D-6)**

There is therefore a gap of *ca* 0.7 mm after mould clamping, ensuring that the mould closes and always maintains pressure in the pinch-off zone. The width of the considered gap was 15 mm.

D.5. Dimension of O-ring

With reference to the Simrit catalog, the recommended dimensions for the O-ring channel are (Figure D-7):
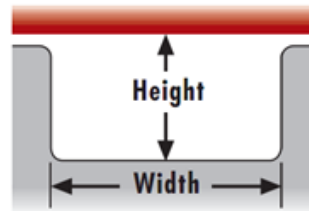

Figure D-6: Dimension of O-ring channel

For these values a channel fill of 76.2% was obtained.

(O-ring area) / (Area channel) × 100 = 76.2% (recommended range 60 to 85%)

For higher values of vacuum, an O-ring with 5.3mm for which would obtain a channel fill of 85.7% was used. It may also be necessary to use lubricants to aid the seal. The considered output angle for the design was 3° (range of advisable values between 0 and 5°) (Figure D-8).
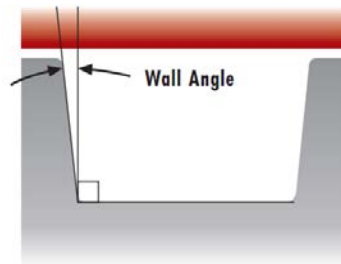

Figure D-7: Outlet angle of O-ring channel

The transverse radiuses were obtained from Table D-2.

Table D-2: Transverse radius of O-ring channel

TRANSITION RADII				
	Cross Section range		Radius 1	Radius 2
mm	1.0	2.0	0.10	0.30
inch	0.04	0.08	0.004	0.012
mm	2.0	3.0	0.20	0.30
inch	0.08	0.12	0.008	0.012
mm	3.0	4.0	0.20	0.50
inch	0.12	0.16	0.008	0.020
mm	4.0	5.0	0.20	0.60
inch	0.16	0.20	0.008	0.024
mm	5.0	6.0	0.20	0.60
inch	0.20	0.24	0.008	0.024
mm	6.0	8.0	0.20	0.80
inch	0.24	0.31	0.008	0.031
mm	8.0	10.0	0.20	1.00
inch	0.31	0.39	0.008	0.039
mm	10.0	12.0	0.20	1.00
inch	0.39	0.47	0.008	0.039
mm	12.0	15.0	0.20	1.20
inch	0.47	0.59	0.008	0.047
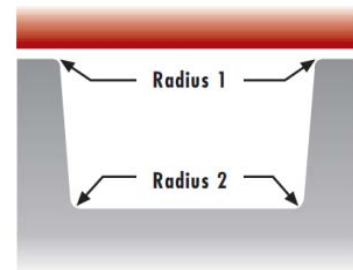
The top, A, and lower surfaces B as specified in the below Figure, as well as the side faces of the channel were obtained from the Table D-3.

Table D-3: Finishing type of O-ring channel surfaces

Sealing Surface A	μm	1.6	6.3	10.0
	μinch	64	256	400
Sealing Surface B	μm	3.2	10.0	12.5
	μinch	128	400	500
Containing Surfaces	μm	6.3	12.5	16.0
	μinch	256	500	640
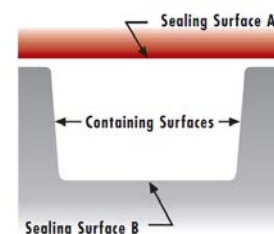
D.6. Inlet and vent

For the connection of the injection points and vents, standard MVP accessories used for the RTM light were utilised (Figure 9). In order to obtain higher injection pressures it was

necessary to develop a connection form between these accessories and the aluminum mould, Figures D-10 to D-12 show the threaded bush developed and assembly of the system
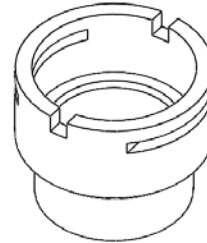

Figure D-8: MVP accessories

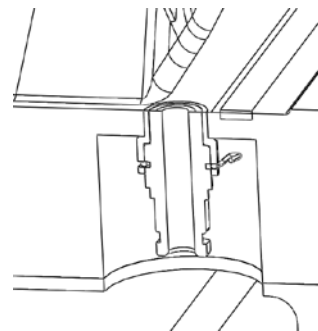
Figure D-9: Threaded bush

Figure D-10: Assembly detail

Figure D-11: Cut-off view of the assembly in the mould

Appendix E

E.1. The estimation of void content

The standard method to quantify the void content in a composite sample is ASTM D2734. However, this approach does not allow one to account the size of voids and their distribution. One way can be image processing. To do so, a code within Matlab environment was developed to distinguish voids from the matrix.

```matlab
close all
clear all
clc

for k =2
   %jpgFilename = strcat((num2str(k)),'(1)', '.jpg');
% the code read the image. The format of the image is JPG.
 jpgFilename  = strcat('1(', num2str(k), ').jpg');
    img    = imread(jpgFilename);
% img=imread('1 (7).tif');
%img = imcrop(img,[100 100 1000 1000]);

%imshow(img);
%imtool(img)

%img_grey=rgb2gray(img);
img_grey=img;
myfilter = fspecial('gaussian',[7 7], 0.25);
smooth_img = imfilter(img, myfilter, 'replicate');


  figure, imshow(smooth_img);

se = strel('disk',10);
closeBW = imclose(smooth_img,se);
 figure, imshow(closeBW)

bw = rgb2gray(closeBW);
%imtool(bw)
% wh_px=0;
% for i=1:size(bw,1)
%    for j=1:size(bw,1)
%        if (50<=bw(i,j))&&(bw(i,j)<=100)
%           wh_px=wh_px+1;
%        end
%    end
% end
myfilter = fspecial('gaussian',[1 1], 0.25);
bw = imfilter(bw, myfilter, 'replicate');
%imtool(bw)
bw(bw(:,:)>55)=255;
bw(bw(:,:)<=55)=0;


%imtool(bw)
```

```matlab
figure, imshow(bw)

[B,L] = bwboundaries(bw,'holes');

%figure, imshow(label2rgb(L, @jet, [.5 .5 .5]))
%imtool(label2rgb(L, @jet, [.5 .5 .5]))
hold on
for f= 1:length(B)
    boundary = B{f};
    plot(boundary(:,2), boundary(:,1), 'w', 'LineWidth', 2)
end

L2=L;
% im_process=zeros(size(img,1),size(img,2));
% for i=1:size(B,1)
%     for j=1:size(B{i},1)
%         im_process(B{i}(j,1), B{i}(j,2))=255;
%     end
% end
%
% imshow(L,[])
% fsfs
L(L(:,:)~=1)=255;
L(L(:,:)==1)=0;


% for i=1:size(bw,1)
%     for j=1:size(bw,2)
%         if L(i,j)==255
%             if (img_grey(i,j)>45)&&(img_grey(i,j)<50)
%                 L(i,j)=0;
%             end
%         end
%     end
% end
%

% wh_px=0;
% for i=1:size(L,1)
%     for j=1:size(L,1)
%         if L(i,j)==255
%             wh_px=wh_px+1;
%         end
%     end
% end
% counter=1;
% del{1}=0;
% for i=2:size(B,1)
%     for j=1:size(B{i},1)
%                                                 if
(img(B{i}(j,1),B{i}(j,2))>40)&&(img(B{i}(j,1),B{i}(j,2))<60)
%             del{counter}=L2(B{i}(j,1),B{i}(j,2));
%         end
%     end
%     counter=counter+1;
% end
%
%
% for i=1:size(del,2)
```

```matlab
%     if (~isempty(del{i}))
%         for j=1:size(L2,1)
%             for k=1:size(L2,2)
%                 if L2(j,k)==del{i}
%                     L2(j,k)=-1;
%                 end
%             end
%         end
%
%     end
% end
%
% L2(L2(:,:)~=-1)=0;
% L2(L2(:,:)==-1)=255;
%
% figure; imtool(L2,[]);


%xzczxc

counter=0;
for i=1:size(L,1)
    for j=1:size(L,2)
        if L(i,j)>0
            counter=counter+1;
        end
    end
end


voidcontent(k)=(counter)/(size(L,1)*size(L,2));

voidcontent'

% figure
% imshow(L,[])
%  fclose(jpgFilename);
end

xlswrite(strcat('check.xlsx'),voidcontent');
```